Hybrid static potentials, gluelumps and hybrid spin-dependent potentials from lattice gauge theory

Dissertation
zur Erlangung des Doktorgrades
der Naturwissenschaften

vorgelegt beim Fachbereich Physik
der Johann Wolfgang Goethe-Universität
in Frankfurt am Main

von
Carolin Viktoria Schlosser
aus Hildesheim

Frankfurt am Main 2025
D30

vom Fachbereich Physik der
Johann Wolfgang Goethe-Universität als Dissertation angenommen.

Dekan: Prof. Dr. Roger Erb

Gutachter: Prof. Dr. Marc Wagner
Apl. Prof. Dr. Antonio Vairo

Datum der Disputation: 10. Juli 2025

Deutsche Zusammenfassung

Die starke Wechselwirkung stellt eine der fundamentalen Kräfte im Standardmodell der Teilchenphysik dar und ist verantwortlich für die Bindung von Quarks zu Hadronen. Das Verständnis der starken Wechselwirkung ist dabei entscheidend für die Erklärung der Struktur hadronischer Materie. Bei Experimenten mit Hochenergiebeschleunigern wurde in den letzten Jahrzehnten ein ganzer Zoo von Hadronen gefunden. Dennoch bleiben viele Fragen bezüglich ihrer Erklärung offen, die weitere experimentelle und theoretische Fortschritte erfordern.

Die Quantenchromodynamik (QCD) als Theorie der starken Wechselwirkung sagt verschiedene Hadronenzustände voraus, von denen exotische Hadronen im Mittelpunkt theoretischer Untersuchungen stehen. Zu diesen exotischen Hadronen gehören schwere hybride Mesonen. Sie bestehen aus einem schweren Quark-Antiquark-Paar, das an ein angeregtes Gluonenfeld gekoppelt ist. Schwere hybride Mesonen wurden bisher noch nicht experimentell bestätigt, da ihre eindeutige Identifizierung in Experimenten nach wie vor schwierig ist, nicht zuletzt wegen ihrer möglichen Vermischung mit gewöhnlichen Quarkonium-Zuständen. Ein genaueres theoretisches Verständnis dieser Zustände und ihrer Eigenschaften ist daher entscheidend für die Interpretation experimenteller Ergebnisse und die gezielte Suche nach diesen exotischen Teilchen.

Der Fokus der vorliegenden Arbeit liegt auf der Untersuchung hybrider Mesonen im Rahmen der Born-Oppenheimer effektiven Feldtheorie (BOEFT). Dazu wird in dieser Arbeit die Gitterfeldtheorie verwendet, die eine nicht-störungstheoretische Methode zur Berechnung der QCD bietet. Mit dieser werden hybride Potentiale berechnet, welche die vollständige Dynamik des hybriden Mesons bis zu einer bestimmten Ordnung der Entwicklung der BOEFT in der inversen Quarkmasse $1/m_Q$ beschreiben. Die Potentiale gehen in gekoppelte Schrödingergleichungen ein und beeinflussen so die Berechnung der Massenspektren von hybriden Mesonen. In dieser Arbeit erweitern und verfeinern wir Ergebnisse für hybride Potentiale in der führenden und nachsthöheren Ordnung der BOEFT unter Verwendung reiner SU(3)-Gittereichtheorie. Die Resultate liefern wichtige Einblicke in die starke Wechselwirkung und erlauben genauere Vorhersagen von hybriden Mesonen und ebnen so den Weg für deren Identifizierung im experimentellen Spektrum.

In dieser Arbeit verwenden wir SU(3)-Gittereichtheorie und vier Gitterensembles mit feinen Gitterabständen im Bereich von $0.040\,\mathrm{fm} \ldots 0.093\,\mathrm{fm}$. Durch die Berechnung von Wilsonloops mit optimierten, hybriden Gitteroperatoren erhalten wir präzise Daten und Parametrisierungen für die niedrigsten hybriden statischen Potentiale Π_u und Σ_u^- sowie das normale statische Potential Σ_g^+. Dabei werden die a-abhängige Selbstenergie und Gitter-

diskretisierungsfehler in führender Ordnung in der Störungstheorie und in a^2 entfernt. Zusätzlich untersuchen wir mögliche systematische Fehlerquellen wie topologisches Einfrieren, das endliche Gittervolumen und Glueball-Zerfälle und schließen diese aus. Die Resultate für die hybriden statischen Potentiale werden durch gitterfeldtheoretische Ergebnisse für Gluelumps ergänzt, die deren Grenzfall bei verschwindendem Quark-Antiquark-Abstand darstellen. Wir bestimmen die Massen von Gluelump-Zuständen mit Gesamtdrehimpuls bis zu $J = 3$ und führen Kontinuumsextrapolationen von Gluelump-Massendifferenzen aus. Zudem diskutieren wir die Umrechnung der Gitter-Gluelump-Massen in das Renormalon Subtraction-Schema, da die umgerechneten Massen eine zentrale Rolle für die Bestimmung hybrider Mesonenmassen innerhalb der BOEFT spielen. Darüber hinaus untersuchen wir die spinabhängigen Korrekturen in der nächsthöheren Ordnung ($(1/m_Q)^1$) der BOEFT. Wir präsentieren die ersten gitterfeldtheoretischen Ergebnisse für die vier unbekannten Potentiale $V_{11}^{sa}(r)$, $V_{10}^{sb}(r)$, die für die Hyperfeinaufspaltung in Spektren schwerer hybrider Mesonen relevant sind, sowie $V_{\Sigma_u^-}^{\mathrm{mix}}(r)$ und $V_{\Pi_u}^{\mathrm{mix}}(r)$, welche die Vermischung schwerer hybrider Mesonen mit gewöhnlichem Quarkonium beschreiben. Wir drücken diese Potentiale durch Matrixelemente aus, die wir aus einer SU(3)-Gittereichtheorieberechnung von Wilsonloops mit einer chromomagnetischen Feldeinfügung extrahieren. Hierfür verwenden wir die Gradientflow-Methode, um eine Renormierung der Matrixelemente zu erleichtern und das statistische Rauschen erheblich zu reduzieren. Unsere Ergebnisse bei einem einzelnen Gitterabstand von $a = 0.060\,\mathrm{fm}$ zeigen, dass eine kombinierte Kontinuums- und Gradientflowzeit-Extrapolation mit den verwendeten Methoden möglich ist. Diese ist für zukünftige Untersuchungen notwendig, um die Hyperfeinaufspaltung in den Spektren schwerer hybrider Mesonen sowie deren Vermischung mit gewöhnlichem Quarkonium zuverlässig in der BOEFT vorherzusagen. Zusammen mit den hybriden statischen Potentialen und den Gluelump-Massen ermöglichen diese Ergebnisse ein besseres Verständnis schwerer hybrider Mesonen und ihrer Massenspektren.

Contents

1 Introduction

The strong interaction is one of the fundamental interactions described in the Standard Model for particle physics. The strong force is mediated by gluons and acts between quarks, which Gell-Mann and Zweig postulated in the 1960s [1, 2] as the fundamental elements of matter. The quarks are fermions with spin 1/2 and come in six different flavors, which have significantly different masses: up (u), down (d), strange (s), charm (c), bottom (b) and top (t).

The theory describing the strong interaction is Quantum Chromodynamics (QCD). QCD is formulated as an SU(3) gauge theory with the associated conserved charge being the color charge, which is carried by quarks and gluons. Due to the color charge of the gluons, a self-interaction is induced, which is reflected by the non-abelian nature of the SU(3) gauge theory for QCD. Self-interaction causes the running of the QCD coupling, implying that the interaction becomes weak at short distances (high energies) and strong at large distances (low energies). This explains an important phenomenon of the strong interaction known as confinement, which means that free quarks have never been observed. The quarks are bound into color-neutral hadrons. According to the quark model, these are classified into mesons and baryons. Mesons are integer-spin hadrons conventionally composed of a quark and an antiquark, while baryons are half-integer spin hadrons composed of three quarks. Typical examples of mesons are pions, which are bound states of light up and down quarks/antiquarks, with a mass of $\approx 140\,\mathrm{MeV}$[1] [3]. Prominent examples of baryons include the proton (uud) and the neutron (udd).

A zoo of hadrons has been detected in high-energy experiments over the last decades. These hadrons could successfully be explained by conventional hadrons for a long time. However, Belle discovered the exotic $X(3872)$ (also known as $\chi_{c1}(3872)$ [3]) state in the charmonium sector in 2003 [4], which does not fit into the quark model. Many more exotic states, the so-called XYZ-states, were discovered in the last two decades in high-energy collider experiments such as BESIII, Belle, BaBar, CLEO and the LHCb experiment. For a review see e.g. Refs. [3, 5–9]. The experimental effort to explore XYZ states in the quarkonium sector is matched by a high theoretical effort to explain their nature and predict further states. The exotic states may be attributed to other variations of color-neutral states allowed in QCD. These include multiquark composites such as tetraquarks and pentaquarks as well as states in which also gluons serve as constituents. Examples of the latter are glueballs, solely made from gluons, and hybrid mesons, which are composed of a quark-antiquark pair coupled to an excited gluon field. Due to the constituent gluons

[1] We use natural units, i.e. $\hbar = c = 1$.

contributing to the overall quantum numbers, exotic quantum numbers that are impossible for conventional hadrons are also realizable.

Heavy hybrid mesons, which are composed of a heavy quark-antiquark pair (either heavy c or b quarks) confined by an excited gluon field, have not yet been established experimentally [3]. The unambiguous identification of experimental states requires a complete theoretical understanding of the properties of heavy hybrid mesons, particularly their mixing with ordinary quarkonium. The theoretical investigation of hadron spectra in QCD necessitates non-perturbative methods due to the strong coupling of QCD in the low-energy regime. Lattice QCD, first suggested by Wilson in 1974 [10], is such a non-perturbative, first-principles approach to QCD. By discretizing the theory on a four-dimensional Euclidian spacetime lattice of finite size $T \times L^3$, lattice QCD, in principle, allows for the numerical calculation of hadron spectra using stochastic algorithms on high-performance computers. Direct lattice QCD calculations of heavy hybrid mesons are challenging and computationally expensive, thus, only a few full lattice QCD studies exist [11–13]. However, the heavy quark mass and the non-relativistic velocity of the heavy quarks within heavy hybrid mesons allow us to study them in a non-relativistic effective field theory framework, which incorporates essential input from lattice QCD. The Born-Oppenheimer Effective Field Theory (BOEFT) is a systematically improvable framework for studying various types of heavy exotic hadrons [14–20] and has recently been significantly advanced [19, 20]. The BOEFT enables the prediction of heavy hybrid meson spectra for both charmonium hybrids and bottomonium hybrids using a few hybrid potentials, which arise at each order in an expansion of the theory in terms of the inverse heavy quark mass $1/m_Q$. The potentials encode the full dynamics of the system at a given order and, once known, provide important insights into the strong interaction. Moreover, having precise knowledge of the potentials is crucial for predicting accurate heavy hybrid meson spectra [15, 17, 18, 21–23]. Lattice QCD offers an ideal method to determine the essential hybrid potentials, which can be calculated from Wilson loop-like correlation functions on the lattice.

In this work, we investigate the hybrid meson potentials at the leading and next-to-leading order of the Born-Oppenheimer Effective Field Theory using pure SU(3) lattice gauge theory. The main goal of this work is to improve and extend the range of precise lattice field theory results for investigating the lowest heavy hybrid mesons within the BOEFT framework. We investigate the small-r region of the lowest hybrid static potentials Π_u and Σ_u^- by performing lattice gauge theory computations of Wilson loop-like correlation functions with optimized hybrid lattice operators at four different small lattice spacings. We combine different ensembles to explore and remove lattice discretization errors, achieving final results consistent with the continuum limit. Thus, we improve upon previous investigations of hybrid static potentials in Refs. [24–51]. In addition, we complement these hybrid static potential results with SU(3) lattice gauge theory results for gluelumps, which represent the limit of vanishing quark-antiquark separation. We calculate up-to-date results for the continuum limit of 19 gluelump mass splittings and the renormalized mass of the lowest

gluelump associated with the lowest hybrid mesons in the Renormalon Subtraction (RS) scheme. We aim at a higher precision of gluelump masses entering the heavy hybrid meson spectra predictions through more accurate lattice gluelump results compared to previous studies in Refs. [44, 52]. Furthermore, we explore the lattice gauge theory calculation of heavy quark spin-dependent corrections at the next-to-leading order in the heavy quark mass expansion in the BOEFT. These hybrid potentials at order $(1/m_Q)^1$ have not yet been computed with lattice QCD, even though they are associated with spin-splitting in the heavy hybrid meson spectra and give insights into the mixing with ordinary quarkonia. We aim to provide the first lattice field theory results of hybrid spin-dependent potentials related to heavy quark spin effects and hybrid-quarkonium mixing of the lowest heavy hybrid mesons. Thus, we pave the way for refinements of heavy hybrid meson mass predictions as previously performed in Refs. [15, 17, 18, 23].

This thesis is structured in the following way: Chapter 2 introduces relevant concepts of lattice gauge theory calculations. The Born-Oppenheimer Effective Field Theory for heavy hybrid mesons up to order $(1/m_Q)^1$ in the heavy quark mass expansion is described in Chapter 3. In Chapter 4, we present our SU(3) lattice gauge theory results of the two lowest hybrid static potentials Π_u and Σ_u^-. In this chapter, we also present the details of the lattice gauge link ensembles employed throughout the thesis. We determine accurate parametrizations by eliminating discretization errors and other possible systematic errors. In Chapter 5, we extract the complete spectrum of SU(3) lattice gluelump states and extrapolate gluelump mass splittings to the continuum limit. Besides discussing the assignment of continuum spin to lattice gluelump results, we convert the lattice gluelump mass to the Renormalon Subtraction scheme. Chapter 6 provides the first lattice field theory determination of hybrid spin-dependent potentials at order $(1/m_Q)^1$ in the BOEFT. We compute the four unknown potentials $V_{11}^{sa}(r)$, $V_{10}^{sb}(r)$, which are relevant for the hyperfine splitting in heavy hybrid meson spectra, as well as $V_{\Sigma_u^-}^{\text{mix}}(r)$ and $V_{\Pi_u}^{\text{mix}}(r)$, which describe the mixing of heavy hybrid mesons with ordinary quarkonium. We explore the calculation of these potentials on the lattice using gradient flow and a single lattice spacing. This thesis ends with concluding remarks and an outlook in Chapter 7.

The research presented in Chapters 4-6 was primarily carried out by the author. Major parts of this work have been previously published in Refs. [53–58], and some sections may contain minor verbatim passages from these references. Any contributions from others are explicitly acknowledged in the text.

2 Lattice gauge theory

Lattice Quantum Chromodynamics (Lattice QCD) is a numerical first-principles approach to studying the strong interaction described by the theory of Quantum Chromodynamics (QCD). Through the discretization of spacetime and the path integral formalism, lattice QCD allows for numerical computations of quantum field theoretic observables with stochastic algorithms. This method is particularly useful for studying hadron energies in QCD since perturbative methods fail here due to the large coupling in the low-energy regime. In this chapter, we introduce important concepts based on standard textbooks such as [59–61], which are relevant to the lattice field theory calculations performed in this work.

2.1 Path integral formalism

In lattice field theory, the continuous spacetime is replaced with a four-dimensional hypercubic lattice. The discrete lattice sites are separated by a finite lattice spacing a, forming a grid of size $T \times L^3$. Classical field variables describe the degrees of freedom on the lattice with typically periodic boundary conditions. In this work, we consider pure SU(3) gauge theory, omitting fermionic degrees of freedom. The difference to the full theory of QCD with dynamical quarks is expected to be negligible in the gluonic observables studied in this work. Additionally, neglecting fermions allows for a more rigorous computation of observables with the methods of choice compared to their use in full QCD with dynamcial quarks. We discuss this approximation further in the context of systematic errors in Section 2.6. Moreover, quenched calculations, which ignore fermionic degrees of freedom, significantly reduce computational costs by avoiding the computationally expensive calculations related to the fermionic contribution.
The path integral sums all possible configurations of the gauge field A_μ weighted with the gauge action $S[A]$, introducing the quantization of SU(3) gauge theory in the path integral formalism. In this formalism, the expectation value of an observable O is expressed as

$$\langle O \rangle = \frac{1}{Z} \int DA_\mu O(A_\mu)\, e^{-S_E[A]}\,, \tag{2.1}$$

with the partition function

$$Z = \int dA_\mu\, e^{-S_E[A]}\,. \tag{2.2}$$

To facilitate numerical calculations using stochastic methods, one adopts Euclidean time

instead of Minkowski time ($e^{iS_M} \to e^{-S_E}$), which allows interpreting the exponential factor as a probability distribution.
The Euclidean gauge action is given by

$$S_E = \int d^4x \frac{1}{4g^2} F^b_{\mu\nu}(x) F_{b,\mu\nu}(x)\,, \tag{2.3}$$

where $F_{\mu\nu}$ is the field strength tensor. The trace over the color indices b ensures gauge invariance.
On the lattice, instead of the gauge field $A_\mu(n)$, we use variables $U_\mu(n) \in SU(3)$, which represent the parallel transporters of the gauge field between neighboring lattice sites n and $n + \hat{\mu}$, the lattice links. They are related to the gauge field via

$$U_\mu(n) = \exp(iaA_\mu(n)), \tag{2.4}$$

where a denotes the spacing between two neighboring lattice sites. The simplest and most commonly used discretization of the action in terms of lattice link variables is the Wilson plaquette action [62], given by

$$S = \beta \sum_{n\in\Gamma} \sum_{\mu<\nu} \frac{1}{2N} \operatorname{Re}\operatorname{Tr}\left[1 - P_{\mu\nu}(n)\right]\,, \tag{2.5}$$

where $P_{\mu\nu}(n)$ is the smallest closed loop of link variables, known as the plaquette

$$P_{\mu\nu}(n) = U_\mu(n) U_\nu(n+\hat{\mu}) U_{-\mu}(n+\hat{\mu}+\hat{\nu}) U_{-\nu}(n+\hat{\nu}). \tag{2.6}$$

The parameter β is related to the bare coupling as $\beta = \frac{6}{g^2}$ and, thus, the lattice spacing a. As the lattice spacing $a \to 0$, the Wilson plaquette action resembles the continuum Yang-Mills action (2.3) with a discretization error of $\mathcal{O}(a^2)$. The important gauge invariance of the underlying theory is maintained.

2.2 Statistical analysis

2.2.1 Generation of gauge link ensembles

The path integral in lattice gauge theory is evaluated using statistical methods, which requires the generation of many lattice gauge field configurations. These configurations are distributed according to the Boltzmann weight e^{-S}. When the number of gauge field configurations N is sufficiently large, the expectation value of an observable O can be approximated as

$$\langle O \rangle \approx \frac{1}{N} \sum_{U_n} O\left[U_n\right]\,, \tag{2.7}$$

where $O\left[U_n\right]$ denotes the observable measurement on the gauge field configuration U_n and the sum is taken over the whole ensemble of gauge field configurations.

Monte Carlo algorithms are used to generate these gauge field configurations. The process relies on Markov chains, where each updated gauge field configuration depends on the previous state. A Monte Carlo heat bath algorithm [63] is employed in this work to generate equilibrium ensembles of gauge field configurations. We combine it with an overrelaxation algorithm, which efficiently improves the step size in the Markov chain.
Thermalization is required to ensure the generated configurations form a statistically representative ensemble. The initial updates before reaching equilibrium are discarded and intermediate configurations are skipped to eliminate autocorrelation effects. Similarly, the number of intermediate overrelaxation steps can be tuned to reduce autocorrelations further. Evaluating simple observables, such as the plaquette, on each configuration allows to check thermalization and to estimate the autocorrelation time, which varies depending on the lattice setup. Once equilibrium is reached, the ensemble provides a valid statistical representation of the gauge theory, allowing for precise numerical evaluation of physical observables.

2.2.2 Statistical uncertainties

Given the limited number of gauge link configurations for statistical analysis, statistical methods introduce estimable errors. The jackknife and bootstrap methods are standard techniques for estimating the error of derived quantities and they will be introduced here shortly. This work uses the jackknife method for individual gauge link ensembles, while combined data sets employ both methods. The detailed strategy is explained in Appendix A.
The jackknife and bootstrap methods are typically performed on bin mean values, where the complete data sample is divided into small subsets. Binning minimizes correlations between measurements.

The jackknife method

Reduced jackknife samples are constructed from the full set of bin averages $\{X_n\}$ by deleting one bin at a time

$$X_i^{\text{jacknife}} = \frac{1}{N-1}\left[\sum_{n=1}^{N} X_n - X_i\right]. \tag{2.8}$$

The quantity of interest Q is then estimated on each reduced jackknife sample and its error estimate is given by

$$\sigma_Q = \sqrt{\frac{N-1}{N}\sum_{i=1}^{N}\left(Q_i - \bar{Q}\right)^2}, \tag{2.9}$$

where $\bar{Q}$ denotes the observable on the full sample and Q_i is the result on the i-th jackknife sample.

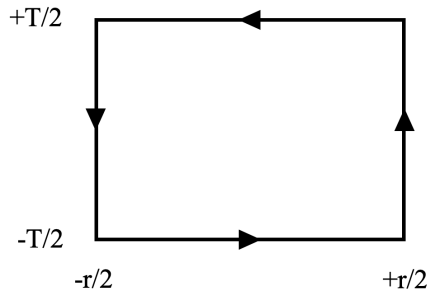

Figure 2.1: Wilson loop $W(r,T)$.

The bootstrap method

N randomly picked values from the complete set of data bin averages $\{X_n\}$ create a bootstrap sample, where data bin averages can be picked repeatedly. The quantity of interest Q is then computed for each of the K bootstrap samples and its error is estimated by

$$\sigma_Q = \sqrt{\frac{1}{K}\sum_{k=1}^{K}\left(Q_k - \bar{Q}\right)^2}, \tag{2.10}$$

where $\bar{Q}$ denotes the result on the full sample and Q_k is the result on the k-th bootstrap sample. K should be sufficiently large to avoid biased results.

2.3 Wilson loops

Wilson loops are the simplest gauge-invariant quantities constructed from a closed rectangular loop of lattice gauge links. In this thesis, Wilson loops with temporal extension T and spatial extension r play a crucial role, as they are directly related to the energy of a flux tube coupled to a static quark-antiquark pair. This connection can be understood from the temporal correlation function of a quark-antiquark pair linked to a flux tube in the static limit, i.e. the limit of infinitely heavy quark mass $m_Q \to \infty$.
A gauge-invariant operator that generates a quark-antiquark pair coupled to a flux tube is given by

$$\mathcal{O} = \bar{Q}(-r/2;t)U_z(-r/2,+r/2;t)Q(+r/2;t)\,, \tag{2.11}$$

where $Q(+r/2;t)$ and $\bar{Q}(-r/2;t)$ are operators creating a quark and an antiquark, respectively, separated by a distance r along the z-axis. $U_z(-r/2,+r/2;t)$ represents a gauge link path connecting the quark and the antiquark at spatial positions $r/2$ and $-r/2$ in a gauge-invariant way. The temporal correlation function describing the propagation of this state can be related to its energy levels by inserting the time evolution operator e^{-hT} and

a set of normalized energy eigenstates $|n\rangle$ to the Hamiltonian h, which results in

$$\langle\Omega|\mathcal{O}^\dagger(r,T/2)\mathcal{O}(r,-T/2)|\Omega\rangle = \sum_n |\langle n|\,\mathcal{O}|\Omega\rangle|^2\, e^{-E_n(r)T}\,. \tag{2.12}$$

This spectral decomposition shows that in the limit $T \to \infty$, the exponential decay of the correlation function is dominated by the lowest energy $E_0(r)$, corresponding to the ground-state energy. The prefactor $\langle n|\,\mathcal{O}|\Omega\rangle$ denotes the overlap of the trial state generated by $\mathcal{O}$ from the vacuum $|\Omega\rangle$ to the energy eigenstate $\langle n|$.
Within the path integral formalism, the quark degrees of freedom in the correlation function can be integrated out, leading to a propagator that can be evaluated analytically [60]. In the static limit, where the quark mass is taken to be infinitely heavy, the correlation function simplifies to the well-known Wilson loop

$$\begin{aligned} W(r,T) = \Big\langle \mathrm{Tr}\,[U_z(-r/2,+r/2;-T/2)U_t(r/2;-T/2,T/2) \\ \times U_z^\dagger(-r/2,+r/2;+T/2)U_t^\dagger(-r/2;-T/2,T/2)\,]\Big\rangle\,, \end{aligned} \tag{2.13}$$

which is sketched in Figure 2.1. It is given by the expectation value of the trace of a closed loop of gauge links with size $r \times T$. We can extract the ground-state energy of the flux tube in the presence of a static quark-antiquark pair from its asymptotic behavior according to Eq. (2.12), which is the static potential $V(r)$.

2.4 Improving the signal

In lattice field theory, short-distance fluctuations in the gauge fields show up as statistical noise in the observable of interest. They cancel each other when averaging over a large number of gauge field configurations. However, the relevant large T behavior of the correlation function is often challenging to extract with a limited number of configurations since the signal of the correlator decreases with $e^{-E_0 T}$ for large temporal distances while the statistical noise increases. Different methods were developed to improve the signal-to-noise ratio in lattice field theory calculations. Some methods aim to improve the overlap of the operator with the state of interest. The larger the overlap, the better the observable can be extracted at finite times. Other methods aim to increase statistics to dampen the noise in the correlator measurements. The methods are all based on averaging products of links. As long as the method is local, the large T behavior of correlation functions is not modified. In the following section, we will briefly introduce the methods we have applied throughout this work to improve the signal-to-noise ratio.

2.4.1 APE smearing

The APE-smearing method [64] takes a single link and adds its neighboring staples with a weight factor α_{APE}. This is performed iteratively, replacing the link $U_\mu^{N_{\mathrm{APE}}-1}$ in the

N_{APE}-th step by

$$U_\mu^{N_{\mathrm{APE}}}(n) = Proj_{SU(3)}\Big[U_\mu^{N_{\mathrm{APE}}-1}(n) + \alpha_{\mathrm{APE}} \sum_{\substack{\pm\nu \\ \mu\neq\nu}} U_\nu^{N_{\mathrm{APE}}-1}(n) U_\mu^{N_{\mathrm{APE}}-1}(n+\hat{\nu}) U_\mu^{N_{\mathrm{APE}}-1}(n+\hat{\nu}+\hat{\mu}) U_\nu^{N_{\mathrm{APE}}-1\dagger}(n+\hat{\mu})\Big]. \tag{2.14}$$

For SU(3), the smeared gauge link needs to be projected back to gauge group SU(3). We use APE smearing for operator optimization purposes throughout this work. The spatial operator extension is easily modified with a fine resolution by choosing an appropriate weight factor α_{APE} and level of smearing steps N_{APE}. When the lattice spacing is reduced, the size of operators built from elementary loops on the lattice decreases while the physical wave function keeps its extension. Adjusting the number of APE smearing steps to the lattice spacing can keep the size of the lattice operator constant.

2.4.2 HYP2 smearing

The HYP (hypercubic) smearing procedure [65–67] creates fat links from links inside a hypercube around the original link. The HYP-smeared link is defined via

$$U_\mu^{\mathrm{HYP}}(n) = Proj_{SU(3)}\Big[(1-\alpha_1)U_\mu(n) + \frac{\alpha_1}{6} \sum_{\substack{\pm\nu \\ \mu\neq\nu}} \tilde{U}_{\nu;\mu}(n) \tilde{U}_{\mu;\nu}(n+\hat{\nu}) \tilde{U}_{\nu;\mu}{}^\dagger(n+\hat{\mu})\Big]. \tag{2.15}$$

$\tilde{U}_{\mu;\nu}$ denotes a decorated link constructed from its neighboring staples without those extending in ν-direction

$$\tilde{U}_{\mu;\nu}(n) = Proj_{SU(3)}\Big[(1-\alpha_2)U_\mu(n) + \frac{\alpha_2}{4} \sum_{\substack{\pm\rho \\ \rho\neq\nu\mu}} \bar{U}_{\rho;\nu\mu}(n) \bar{U}_{\mu;\rho\nu}(n+\hat{\rho}) \bar{U}_{\rho;\nu\mu}{}^\dagger(n+\hat{\mu})\Big] \tag{2.16}$$

and $\bar{U}_{\rho;\nu\mu}(n)$ is built from an original link with a modified APE smearing step

$$\tilde{U}_{\mu;\nu}(n) = Proj_{SU(3)}\Big[(1-\alpha_3)U_\mu(n) + \frac{\alpha_3}{2} \sum_{\substack{\pm\eta \\ \eta\neq\rho\nu\mu}} U_\eta(n) U_\mu(n+\hat{\eta}) U_\eta{}^\dagger(n+\hat{\mu})\Big]. \tag{2.17}$$

HYP2 smearing relates to a specific combination of weight factors, i.e. $(\alpha_1, \alpha_2, \alpha_3) = (1.0, 1.0, 0.5)$ [67]. Using HYP2-smeared temporal gauge links significantly reduces the self-energy of static quarks, reducing statistical errors.

2.4.3 Gradient flow

The gradient flow is a modern method introduced in Ref. [68] that we employ for the efficient calculation of hybrid spin-dependent potentials (see Chapter 6). The gradient flow is a continuous smearing procedure that has some additional features. The defining

equations for the flowed gauge link V_{t_f} are

$$\dot{V}_{t_f}(x,\mu) = -g_0^2(\partial_{x,\mu}S(V_{t_f}))V_{t_f}(x,\mu) \tag{2.18}$$

$$V_{t_f}(x,\mu)|_{t=0} = U(x,\mu). \tag{2.19}$$

t_f denotes an extra dimension, the flow time. The so-called Wilson flow is obtained using the Wilson plaquette action S on the lattice. The above flow equations drive the gauge fields along the flow time toward the classical solution with minimal action. Numerical integration methods are used to calculate the solution of the differential equation, e.g. a third-order Runge Kutta method. This method has an integration error of $\mathcal{O}(\epsilon^3)$, where ϵ denotes the stepsize. In Ref. [69], optimized algorithms for efficient integration of the gradient flow are discussed. Other smoothing methods like APE, HYP and stout smearing can be perturbatively related by analytic expressions to the gradient flow smearing (see e.g. Refs. [68, 70]).

Furthermore, the gradient flow serves as a renormalization scheme for the correlators considered in this thesis. Refs. [71, 72] applied the gradient flow as a smoothing and renormalization procedure for related correlators, which contain chromomagnetic field insertions. Renormalized quantities are obtained by multiplying Wilson loop correlators with chromomagnetic insertions with the necessary matching coefficient $c_F(t_f,\mu)$, which is known for the conversion from gradient flow as a renormalization scheme with scale t_f to the $\overline{\text{MS}}$ scheme with the renormalization scale μ to one-loop order in perturbation theory and in the limit of small flow times [73, 74]. Remaining dependences on the scale t_f in the correlator, which are not canceled by $c_F(t_f)$ make a small-flow time-extrapolation necessary. The extrapolation is not trivial and is being investigated currently for related correlators [71, 72, 74–76]. It is convenient to perform this extrapolation after a continuum limit extrapolation of flowed observables with color field insertions because the gradient flow drastically reduces uncertainties due to a significantly weaker a-dependence in the observable. For this to be true, the gauge field must be smeared over a sphere of radius $r_f = \sqrt{8t_f} \geq 1.0\,a$. Moreover, to avoid discretization effects from overlapping gauge links in the Wilson loop, the minimal separation of operators in temporal and spatial directions should exceed $2r_f$.

2.4.4 Multilevel algorithm

The multilevel algorithm [77] significantly reduces statistical errors by averaging temporal links over multiple sublattice configurations. This algorithm is employed in Chapters 4 and 5 to compute hybrid static potentials and gluelump masses efficiently.

The multilevel algorithm begins with an ensemble of thermalized gauge link configurations. It divides each of the lattice configurations into n_{ts} timeslices with thicknesses $p_1, p_2, \ldots, p_{n_{\text{ts}}}$. If more than one level of the algorithm is applied, the timeslices are further subdivided for each level. A standard heat bath algorithm generates n_m independent

sublattice configurations for each timeslice. In order to minimize autocorrelations, these configurations are separated by n_u heat bath sweeps, in which only the interior links of the time slice are updated while spatial links on the boundaries remain fixed.
With the multilevel algorithm, temporal transporters appearing in observables are replaced by $[\mathbb{P}_k]$, which represents the average over n_m sublattice configurations of the product

$$\mathbb{P}_k = \{\mathbb{T}(x + (d_k - p_k)a\hat{0}, r\hat{j})\mathbb{T}(x + (d_k - p_k + 1)a\hat{0}, r\hat{j}) \dots \mathbb{T}(x + (d_k - 1)a\hat{0}, r\hat{j})\} \,. \quad (2.20)$$

This product of two-link operators $\mathbb{T}$ connects the boundaries of the k-th time slice, spanning from $t/a = d_{k-1}$ to $t/a = d_k$ with $d_k = \sum_{j=1}^{k} p_j$. The two-link operators are defined via $\mathbb{T}(x, r\hat{j})_{\alpha\beta\gamma\delta} = U_0^*(x)_{\alpha\beta} U_0(x + r\hat{j})_{\gamma\delta}$ ($\hat{j}$ denotes the spatial unit vector in j-direction). Consequently, a Wilson loop is computed from

$$W(r,T) = \left\langle U_z(-r/2, +r/2; x_0))_{\alpha\gamma} \{[\mathbb{P}_k][\mathbb{P}_{k+1}] \dots [\mathbb{P}_{k+n_t-1}]\}_{\alpha\beta\gamma\delta} \Big(U_z(-r/2, +r/2; x_0 + T)) \Big)^*_{\beta\delta} \right\rangle \,, \quad (2.21)$$

where n_t denotes the number of timeslices contributing to the temporal extent of the Wilson loop, $\sum_{j=1}^{n_t} p_{k+j} = T/a$, with $d_{k-1} = x_0$. The spatial transporters are located at the boundaries of the timeslices at the top level, which may constrain the allowed temporal extents of the Wilson loop. As in conventional computations without the multilevel algorithm, translational and rotational symmetries are exploited. Finally, the expectation value is obtained by averaging the Wilson loop over the whole ensemble of full gauge link configurations.
For a detailed technical discussion of the multilevel algorithm, see Section 3.2 of Ref. [78].

2.5 Renormalization and scale setting

In QCD, renormalization describes the procedure of relating the bare parameters of the Lagrangian, such as the coupling constant, to their physically measurable counterparts. Since bare parameters are not directly observable, they are redefined to ensure that computed physical quantities, like hadron masses, remain finite and well-defined. Renormalization addresses divergences that arise in quantum field theory due to contributions from very high momenta, i.e. ultraviolet (UV) divergencies.
In lattice QCD, introducing a finite lattice volume with lattice spacing a regulates these divergences by imposing a momentum cutoff $\Lambda \sim 1/a$. However, to obtain physically meaningful results from the regulated, dimensionless lattice quantities given in units of the lattice spacing, one must determine the lattice spacing a in physical units and remove the dependence on the regulator by taking the continuum limit $a \to 0$. A proper renormalization process ensures that physical observables remain finite.
Qualitatively, renormalization demands the equality of bare and renormalized quantities

at a characteristic energy scale. This condition is implied at a fixed order in a perturbative renormalization scheme. For example, the renormalized coupling g_R at a characteristic energy scale μ_E is related to the bare coupling g via a multiplicative renormalization factor

$$g_R(\mu_E) = Z_g(\mu_E, \Lambda) g(\Lambda)\,. \tag{2.22}$$

As the regulator is removed by sending the momentum cutoff $\Lambda \to \infty$, the bare coupling diverges, but the renormalization factor compensates for this divergence, yielding a finite renormalized coupling that depends only on the energy scale. The energy scale dependence is described by the renormalization group equation, determined by the β-function

$$\mu_E \frac{\partial \alpha_s}{\partial \mu_E} = \beta_{\text{ren}}(\alpha_s)\,, \tag{2.23}$$

where α_s is the normalized coupling constant. The QCD β-function causes the coupling to decrease at high energies, meaning that the interaction becomes weaker and the quarks become free, which is known as asymptotic freedom. At low energies, the coupling becomes strong, making perturbative methods unreliable and requiring non-perturbative approaches like lattice QCD.

In pure lattice gauge theory, the bare coupling g is connected to the lattice spacing a. Setting the scale a in lattice gauge theory is an example of renormalizing the bare coupling. There are several methods to set the scale, a common one is to relate a to the Sommer scale r_0. The Sommer scale is defined in terms of the force between a static quark and antiquark, $F(r) = \partial_r V(r)$, via

$$r^2 F(r)|_{r=r_c} = c\,, \tag{2.24}$$

with $c = 1.65$ and $r_{1.65} = r_0$ being the common choice for r_c [79]. From a parametrization of the ordinary static potential Σ_g^+, $aV(r) = aV_0 - \alpha/r + a^2\sigma r$, in the region of r_0 the lattice spacing a can be determined via

$$a = r_0 \sqrt{\frac{a^2\sigma}{1.65 + \alpha}}. \tag{2.25}$$

Throughout this work, we use $r_0 = 0.5\,\text{fm}$ to convert lattice results to physical units, which is a simple and common choice for r_0 but larger than the physical value for QCD [80].

2.6 Possible systematic errors

Although lattice QCD is a first-principles approach to QCD, it introduces systematic effects that must be carefully considered and successively eliminated. In this section, we discuss several typical sources of systematic errors, including autocorrelations, topological freezing, finite lattice volume effects and discretization errors, for which we develop strategies to avoid these issues in the following chapters.

Additionally, our calculations omit light dynamical quarks, which introduces systematic

differences compared to full QCD calculations. However, these differences are expected to be small. For instance, lattice computations of hybrid static potentials with and without dynamical quarks from Ref. [38] show no statistically significant difference. Furthermore, due to the necessity of resolving several multiparticle states with the same quantum numbers below the state of interest, rigorous methods such as the Lüscher method [81] are computationally demanding in full lattice QCD calculations, particularly for heavy exotic hadrons. Ignoring these effects could introduce more significant systematic errors than those coming from the quenched approximation. The possible multiparticle states in pure gauge theory that may appear below heavy hybrid mesons are discussed in Section 4.4.3.

2.6.1 Autocorrelations

When simulating QCD on the lattice, the computations are based on Monte Carlo Markov chain algorithms generating a series of gauge field configurations. Understanding the time scales of the system is essential for two main reasons. First, the distribution of gauge field configurations must be sampled correctly by the simulation. The observable estimates will be biased if the ensemble of gauge field configurations is not representative. Second, knowing the time scales is necessary for accurately estimating statistical errors, notably when measurements are correlated. For reliable results, simulation runs must be longer than the autocorrelation times in the system.
The autocorrelation between two observables measured at different times in the Monte Carlo (MC) series is defined as

$$\Gamma_{\alpha\beta}(t) = \langle O_\alpha(t) O_\beta(0) \rangle - \langle O_\alpha(t) \rangle \langle O_\beta(0) \rangle \,, \tag{2.26}$$

where t denotes the separation in the Monte Carlo series. For a function F of the observables, the normalized autocorrelation function is given by

$$\rho_F(t) = \frac{\Gamma_F(t)}{\Gamma_F(0)} \,, \tag{2.27}$$

where

$$\Gamma_F(t) = \sum_{\alpha,\beta} \frac{\partial F}{\partial \langle O_\alpha \rangle} \Gamma_{\alpha\beta}(t) \frac{\partial F}{\partial \langle O_\beta \rangle} \,. \tag{2.28}$$

The integrated autocorrelation time τ_{int}, which characterizes the dynamics of the Monte Carlo simulation which is relevant for the observable F, is given by an infinite sum over the autocorrelation function

$$\tau_{\text{int}}(F) = \frac{1}{2} + \sum_{t=1}^{\infty} \rho_F(t). \tag{2.29}$$

If measurements are correlated, the statistical error of the observable receives a correction

factor given by the integrated autocorrelation time

$$(\partial \bar{F})^2 = \frac{\sigma_F^2}{N} 2\,\tau_{\mathrm{int}}(F). \tag{2.30}$$

However, determining autocorrelation times is challenging, as they depend on various simulation details, such as the discretization of the theory, the algorithms used, the choice of observables and the lattice spacing.
The dependence of the autocorrelation time on the lattice spacing a is characterized by the dynamical critical exponent z

$$\tau_{\mathrm{int}}(F) \propto a^{-z}. \tag{2.31}$$

This exponent has been studied, e.g. in Ref. [82]. Notably, for the topological charge, the critical dynamical exponent is $z \approx 5$ and the increase in autocorrelation time with decreasing lattice spacing is much more severe than for an ordinary Wilson loop, which has $z \approx 0.6$. Therefore, the large autocorrelation times for the topological charge related to the critical slowing down of the algorithm are addressed in detail in a separate discussion below.
In practice, we aim to eliminate correlations in the calculation of observables. We avoid using close configurations in the MC series by leaving out a sufficient number of sweeps N_{sep} between subsequent gauge field configurations. The value of N_{sep} depends on the simulation details and the observable under consideration. The values of N_{sep} used in this work (see Table 4.3) are expected to be much larger than the autocorrelation time of the Wilson loop-like observables, ensuring reliable measurements. Furthermore, we run independent, parallel Monte Carlo simulations to generate more gauge link configurations, which are mainly uncorrelated. Finally, we further reduce correlations by binning measurements into groups larger than the autocorrelation time, using the bin averages in the subsequent statistical analysis.

2.6.2 Topological freezing

Topology classifies equivalent objects, such as gauge field configurations, under continuous transformations. In lattice gauge theory, the field space is divided into topological sectors characterized by the topological charge Q. These sectors are separated by an infinite action barrier in the continuum [83]. However, on the lattice, the barrier is finite, allowing for a change of sectors in Monte Carlo algorithms.
As the lattice spacing a decreases, the probability of tunneling between topological sectors becomes smaller due to an increasing barrier. For small lattice spacings $a \lesssim 0.05\,\mathrm{fm}$ [82], it becomes increasingly difficult for the algorithm to change the topological sector. This phenomenon is known as topological slowing down, meaning that the simulation remains trapped in a single sector for extended periods of the Monte Carlo simulation, increasing autocorrelation times. As a result, the gauge field distribution $\propto e^{-S}$ and the topological

charge are poorly sampled. At very fine lattice spacings, the algorithm may remain confined to one sector, a phenomenon known as topological freezing, which introduces a bias in observables. When a simulation is trapped in a single topological sector, observables receive an additional dependence on the finite lattice volume proportional to powers of the inverse spacetime volume $1/V$ (see e. g. Refs. [84–86]). Several strategies exist to avoid these corrections, like introducing open boundary conditions in one direction or relating the observables at fixed topology to the physical counterparts [86].

The topological charge is quantized on a lattice with periodic boundary conditions in all four directions for the gauge field, which is equivalent to a torus. The topological charge on such a torus is restricted to integer-valued topological sectors. Tunneling events between topological sectors are associated with non-trivial configurations, which are interpreted as instantons in the instanton picture [83]. Instantons can propagate freely around the lattice with periodic boundary conditions, but their net number is conserved. The net number gives the integer topological charge, $n_+ - n_- = Q \in \mathbb{Z}$, where n_+ and n_- are the numbers of instantons and anti-instantons, respectively.

Omitting the distinction between instantons and anti-instantons, the probability of finding a configuration with charge Q can be approximated by a normal distribution. It reads

$$p(Q) = \frac{1}{\sqrt{2\pi\sigma^2}} \exp\left(-\frac{Q^2}{2\sigma^2}\right) \tag{2.32}$$

with $\sigma^2 = \langle Q^2 \rangle$ containing all relevant information about the distribution. The parameter is related to the topological susceptibility χ_{top}, which quantifies topological charge fluctuations in a given spacetime volume V

$$\chi_{top} = \frac{\langle Q^2 \rangle}{V}. \tag{2.33}$$

The literature value for the topological susceptibility is $\approxeq (200\,\mathrm{MeV})^4$ [87].

In the following, we introduce the field-theoretic definition of the topological charge, which is later used to assess whether the gauge link ensembles used in this work are affected by topological freezing. For a review of different definitions of the topological charge, see e. g. Ref. [70].

On the lattice, the continuum expression

$$Q = \int \mathrm{d}^4x\, q(x), \tag{2.34}$$

with the field-theoretic definition of the topological charge density

$$q(x) = \frac{1}{32\pi^2} \epsilon_{\mu\nu\rho\sigma} \,\mathrm{Tr}\left(F_{\mu\nu} F_{\rho\sigma}\right), \tag{2.35}$$

is replaced by a discretized sum over all lattice sites,

$$Q = a^4 \sum_x q_L(x)\,. \tag{2.36}$$

Here, $q_L(x)$ represents a valid lattice discretization of the topological charge density, whose choice affects lattice artifacts in the total topological charge Q.
The simplest discretization of q uses the plaquette, $P_{\mu\nu}(x)$, the smallest closed loop on the lattice,

$$q_L(x) = \frac{1}{32\pi^2}\epsilon_{\mu\nu\rho\sigma}\,\mathrm{Tr}\left(C_{\mu\nu}(x)C_{\rho\sigma}(x)\right), \tag{2.37}$$

where

$$C_{\mu\nu}(x) = \frac{1}{2}\left(P_{\mu\nu}(x) - P^\dagger_{\mu\nu}(x)\right)\,. \tag{2.38}$$

An improved discretization replaces $P_{\mu\nu}(x)$ with the clover-leaf

$$P^{\mathrm{clov}}_{\mu\nu}(x) = \frac{1}{4}\left[P_{\mu\nu}(x) + P_{\nu-\mu}(x) + P_{-\mu-\nu}(x) + P_{-\nu\mu}(x)\right]. \tag{2.39}$$

This version reduces lattice artifacts to $\mathcal{O}\left(a^2\right)$. Due to the lattice artifacts and ultraviolet (UV) fluctuations, the lattice topological charge deviates from their integer values. In order to suppress these fluctuations, smoothing procedures must be applied before computing the topological charge.
A common smoothing technique is APE-smearing, which can also be related to other methods, such as gradient flow or cooling (see Ref. [70]). It needs to be applied to all four dimensions. The number of smearing steps N_{APE} should be large enough to suppress UV fluctuations but small enough to preserve the topological structure of the gauge field. N_{APE} must be tuned for each lattice spacing.
Since the lattice spacings in this work are relatively small, we explicitly check the Monte Carlo history of the topological charge and verify proper sampling of its distribution in Section 4.4.1 to exclude bias due to topological freezing.

2.6.3 Finite volume effects

Lattice observables depend on the lattice spacing a and the discretized spacetime volume in which they are computed. To properly connect to the continuum, one must take the limit $a \to 0$ while ensuring that the volume V is large enough for finite-volume effects to be negligible within statistical uncertainties.
If the lattice volume is too small, two effects can cause a shift in the energy levels. Particles propagating around the lattice interact with their periodic copies and induce a negative energy shift proportional to $\exp(-mL)$ [88], where m is the mass of the particle. For asymptotically large lattice extents L, the effect is dominated by the lightest particle of the theory. In pure gauge theory, the lightest particle is the relatively heavy glueball (the lightest glueball with quantum numbers $J^{PC} = 0^{++}$ has a mass of $m_{0^{++}} = 1730(50)\,\mathrm{MeV}$

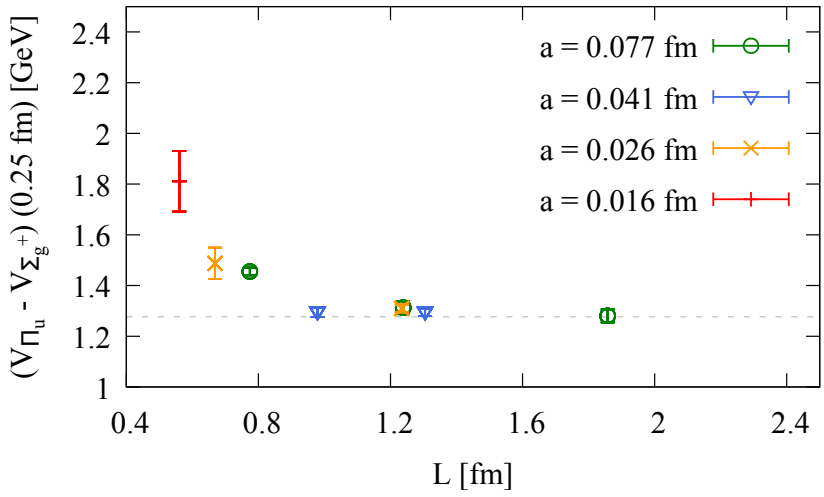

Figure 2.2: Lattice volume dependence of SU(2) lattice results for the static potentials. Details on the used gauge field ensembles can be found in Appendix B.

[89]). Due to its large mass, this effect is less severe than in full QCD with light quarks, where the lightest particles are the much lighter pions.

Furthermore, the lattice must be large enough to accommodate the particle's wave function. If the volume is too small, the wave function becomes compressed, resulting in a squeezed wavelength and a positive shift in the energy levels.

For an exemplary computation of the ordinary and hybrid static potentials, which we performed in SU(2) lattice gauge theory, a sizeable lattice volume dependence can be observed in the difference of the lowest hybrid and the ordinary static potential for $L < 1.0\,\mathrm{fm}$, shown in Figure 2.2. The volume effects are negligible for lattice volumes $L^3 \gg (1.0\,\mathrm{fm})^3$ in both the ordinary and the hybrid static potentials with the precision achieved in conventional computations. For smaller lattice volumes, the ordinary static potential values experience a small negative shift, probably caused by the traveling of a glueball, whereas we observe a relatively large positive shift for the hybrid static potentials originating in the squeezed wavelength.

2.6.4 Discretization effects

Lattice calculations introduce discretization errors due to the finite lattice spacing a. Unlike in the continuum, where rotational symmetry is exact, the rotational symmetry is violated on the lattice since only rotations by multiples of 90 degrees are allowed. As a result, lattice observables differ from their continuum counterparts, requiring careful corrections for accurate results.

Different discretizations of the Yang-Mills theory and observables lead to varying discretization errors. For instance, the Wilson plaquette action has $\mathcal{O}(a^2)$ errors, but all formulations should converge to the same continuum result as $a \to 0$.

Several strategies exist to reduce discretization errors. One approach is to employ improved actions such as the Symanzik improved gauge action [90], where additional operators are added to cancel leading lattice discretization errors compared to the Wilson plaquette action. Another strategy for discretization errors is a tree-level improvement applicable to observables like the static force or static potentials. This method involves matching the tree-level lattice propagator to its continuum counterpart. The latter method is particularly relevant for our parametrization of hybrid static potentials (see Chapter 4) and will be discussed in detail in the following.

In leading-order perturbation theory, the continuum static potential is given by a one-gluon exchange and, thus, is proportional to $1/r$. The lattice counterpart is determined by the Green's function of the Wilson plaquette gauge action and Eichten-Hill static action

$$\left(\frac{1}{r}\right)_{\text{lat}} = 4\pi G(r/a, 0, 0), \tag{2.40}$$

where the Green's function is

$$G(\mathbf{R}) = \frac{1}{(2\pi)^3} \int_{-\pi}^{\pi} \mathrm{d}^3k \, \frac{\prod_{j=1}^{3} \cos(k_j R_j)}{4 \sum_{j=1}^{3} \sin^2(k_j/2)} \,. \tag{2.41}$$

For the HYP2 static action [66, 67, 91], where HYP2 smeared temporal links replace unsmeared links, the Greens function (2.41) is modified by an additional factor,

$$G^{\text{HYP}}(\mathbf{R}) = \frac{1}{(2\pi)^3} \int_{-\pi}^{\pi} \mathrm{d}^3k \, \frac{\prod_{j=1}^{3} \cos(k_j R_j) \times \left(1 - (\alpha_1/6) \sum_{i=1}^{3} 4 \sin^2(k_i) \Omega_{i0}\right)^2}{4 \sum_{j=1}^{3} \sin^2(k_j/2)}, \tag{2.42}$$

where $\Omega_{\mu\nu}$ is [65]

$$\begin{aligned} \Omega_{\mu\nu} = 1 + \alpha_2(1+\alpha_3) - \frac{\alpha_2}{4}(1+2\alpha_3)\left(\sum_{j=1}^{3} 4\sin^2(p_j/2) - 4\sin^2(p_\mu/2) - 4\sin^2(p_\nu/2)\right) \\ + \frac{\alpha_2\alpha_3}{4} \prod_{\eta \neq \mu,\nu} 4\sin^2(p_\mu/2) \,. \end{aligned} \tag{2.43}$$

The Green's function for the Eichten-Hill static action can be efficiently computed using a recursion relation [92, 93]. In contrast, for the HYP2 static action, the integral is evaluated using standard Monte Carlo integration techniques.

The difference between the continuum and lattice tree-level static potential can be used to quantify the discretization error. Notably, the HYP2 action shows more significant discretization errors at small quark-antiquark separations r/a compared to the Eichten-Hill static action.

Two common methods exist to correct the static potential for the discretization error quantified at the tree level of perturbation theory. They are referred to by r-method and V-method, respectively. Both methods were studied in the context of a bachelor thesis [94]

and extensively discussed and compared in Ref. [56]. Here, SU(2) lattice field theory data for the ordinary static potential at on- and off-axis separations with two different discretizations of the static action, the HYP2 static action and the standard Eichten-Hill static action, were investigated.

Initially introduced for the static force [79] and later applied to the static potential [93], the r-method shifts lattice data points computed at r to an improved separation r_{impr} defined via $(4\pi r_{\mathrm{impr}})^{-1} = G(\mathbf{r}/a)/a$, where $G(\mathbf{r}/a)$ is the tree-level lattice propagator, dependent on the static action discretization. However, applying the r-method to the static potential introduces an overcorrection, which can be parametrized as $\bar{\Delta}^{\mathrm{lat}} = \sigma(r - r_{\mathrm{impr}})$, where σ denotes a fit parameter closely related to the string tension. This overcorrection arises because one-gluon exchange primarily affects the α/r term in a Cornell potential $V_0 - \alpha/r + \sigma r$, describing the ordinary static potential, while the linear term σr remains unchanged. The r-method without correcting for this overcorrection is commonly used due to its simplicity. However, the overcorrection term should be subtracted after improving the separation r, even though it complicates the procedure.

Therefore, the alternative V-method [65, 95] is better suited for the static potential. It corrects the lattice static potential by subtracting the difference between the lattice static potential at the tree level, which is proportional to $G(\mathbf{r}/a)/a$, and the continuum static potential at the tree level, which is proportional to $1/r$,

$$V^e_{\Sigma_g^+}(r) \to V^e_{\Sigma_g^+}(r) - \Delta V^{\mathrm{lat},e}_{\Sigma_g^+}(r) = V^e_{\Sigma_g^+}(r) - \alpha' \left(\frac{1}{r} - \frac{G^e(\mathbf{r}/a)}{a} \right). \tag{2.44}$$

Here, α' is determined by a fit to the unimproved data (see Section 4.3) and is related to the strong coupling constant. Improved data can be defined through $V^e_{\Sigma_g^+}(r) - \Delta V^{\mathrm{lat},e}_{\Sigma_g^+}(r)$. Similarly, hybrid static potentials can be improved by subtracting $\Delta V^{\mathrm{lat},e}_{\mathrm{hybrid}}(r) = -(1/8)\Delta V^{\mathrm{lat},e}_{\Sigma_g^+}(r)$ from the lattice data points. The prefactor originates in the repulsive behavior of hybrid static potentials and, in leading-order perturbation theory, they are suppressed by a factor 1/8 relative to the ordinary static potential.

The benefit of applying tree-level improvement when combining lattice field theory results obtained at different lattice spacings and with different static actions is demonstrated in Figure 2.3, where we compare unimproved and improved data points for the Σ_g^+ potential from our five ensembles (see Table 4.3). The two plots show that most improved data points are consistent with a single curve, while unimproved data points from different ensembles exhibit substantial discrepancies for $r \lesssim 0.4\,\mathrm{fm}$.

Given the current statistical precision of lattice static potential computations, tree-level improvement is essential. As shown in Section 4.3, the lattice potential data improved using the V-method can be consistently described by a smooth curve, restoring rotational symmetry within statistical errors.

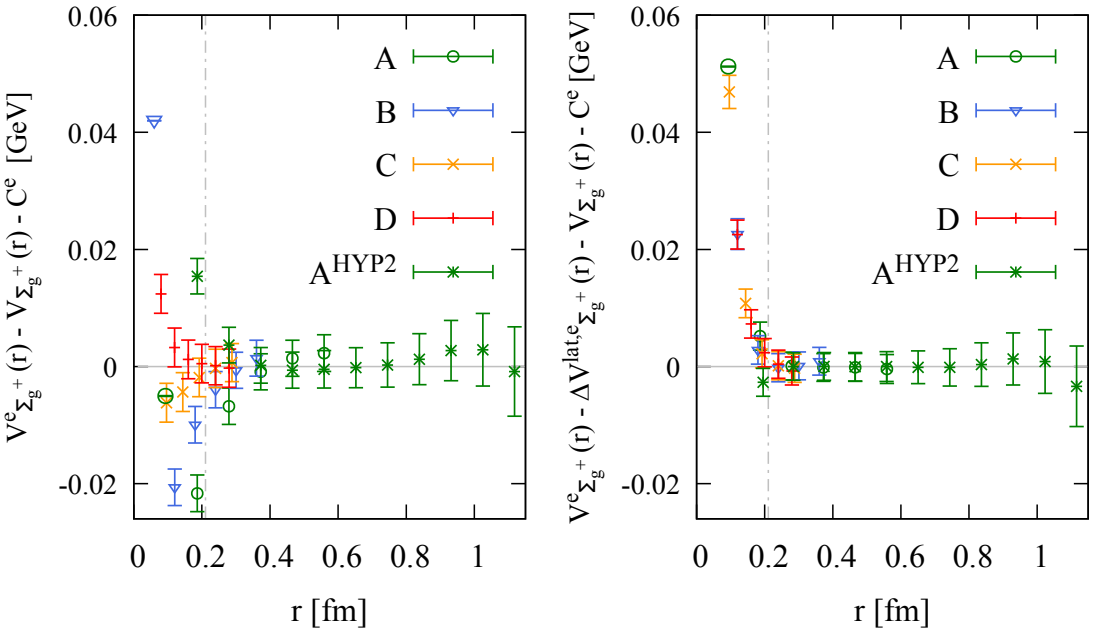

Figure 2.3: Comparison of unimproved (left) and improved (right) lattice data points for the Σ_g^+ static potential from our five ensembles A, B, C, D and A^{HYP2} (see Table 4.3). We subtract $V_{\Sigma_g^+}(r) + C^e$ with $V_{\Sigma_g^+}(r)$ being the Cornell potential and parameters obtained by a fit to data points with $r \geq 0.2\,\mathrm{fm}$ (indicated by the vertical dashed line), see Section 4.3.

3 Heavy hybrid mesons in an effective field theory framework

Heavy hybrid mesons, also called quarkonium hybrids, are composed of a heavy quark and a heavy antiquark coupled to an excited gluonic field. Due to the large mass of the heavy quarks (m_Q), the quark-antiquark pair motion can be treated non-relativistically, while the gluons, the system's light degrees of freedom, move much faster. The distinct scale separation enables the effective description of heavy hybrid mesons using the Born-Oppenheimer approximation, which was first applied in molecular physics [96], where one can exploit a similar hierarchy of scales. In hybrid mesons, the heavy quark-antiquark pair is considered static on the timescale of the excited gluons, allowing the gluonic field to be treated adiabatically. This approximation is especially applicable to hybrid mesons consisting of heavy charm or bottom quarks ($m_c = 1628\,\text{MeV}$ and $m_b = 4977\,\text{MeV}$ from quark models [97]). The Born-Oppenheimer approximation has been applied to heavy hybrid mesons, e.g. in Refs. [36, 40, 98, 99].

Recent advancements have extended this approximation into a systematic effective field theory framework for exotic hadrons such as heavy hybrid mesons, but also tetraquarks, doubly heavy baryons and pentaquarks [14–16, 18–20, 100], now known as the Born-Oppenheimer Effective Field Theory (BOEFT). Effective field theories are powerful tools in physics. They allow us to describe complex systems by focusing only on the relevant degrees of freedom at a particular energy scale. The scale Λ_{QCD} plays a crucial role as it separates the perturbative from non-perturbative effects in Quantum Chromodynamics (QCD). For systems involving heavy quarks, however, the quark mass m_Q is much larger than $\Lambda_{\text{QCD}} \approx 300\,\text{MeV}$ [101]. The heavy quark mass and the non-relativistic velocity enable the separation of scales: $m_Q \gg m_Q v \gg m_Q v^2$, where v is the relative velocity between the heavy quark and antiquark (in the rest frame of the meson $v^2 \approx 0.1$ for $\bar{b}b$, $v^2 \approx 0.3$ for $\bar{c}c$ systems [20]), $m_Q v$ is related to the inverse size of the system and $m_Q v^2$ is the scale of the binding energy. This hierarchy enables the factorization of scales such that one arrives at a series of effective field theories. Non-relativistic QCD (NRQCD) is obtained from QCD by an expansion in terms of the inverse heavy quark mass $1/m_Q$. Moreover, BOEFT exploits the scale hierarchy $m_Q v^2 \ll \Lambda_{QCD}$, meaning that the gluonic binding energy can be treated adiabatically. Further factorization in the case of small quark-antiquark separations ($1/r \approx m_Q v \gg \Lambda_{QCD}$) leads to weakly-coupled potential NRQCD (pNRQCD) [100]. The effective field theory describes the system up to some matching coefficients that relate it to the previous effective field theory in the series. NRQCD is matched to QCD and

BOEFT is matched to NRQCD after successively integrating out scales. Some of these matching coefficients, the potentials, involve non-perturbative terms and require input from lattice field theory. Thus, effective field theory and lattice gauge theory complement each other in enhancing the knowledge about exotic hadrons.

This chapter explains relevant aspects of the BOEFT description of heavy hybrid mesons, mainly based on Refs. [15, 19, 20]. The introduction shall motivate the lattice field theory calculations presented in the following chapters. For a detailed, comprehensive presentation, see Refs. [14, 18–20] and references therein.

3.1 Lagrangian and potentials

The BOEFT, as formulated in Refs. [19, 20], is capable of describing all sorts of general exotic hadrons consisting of two heavy quarks such as hybrid quarkonium, tetraquarks, double heavy baryons and pentaquarks. The BOEFT Lagrangian is organized in an expansion in the inverse heavy quark mass, $1/m_Q$, which is rooted in integrating out the energy scale of the heavy quarks.

The general BOEFT Lagrangian describing heavy hybrid mesons reads [19]

$$\mathcal{L} = {\Psi^\dagger_{\kappa^{PC}}}^{n'A'} \left[i\partial_t - h_{\kappa^{PC}} \right]^{n'A';nA} {\Psi_{\kappa^{PC}}}^{nA} \tag{3.1}$$

with the Hamiltonian given as an expansion in powers of $1/m_Q$

$$\left[h_{\kappa^{PC}}(\mathbf{r})\right]^{n'A';nA} = -\frac{\Delta_{\mathbf{r}}}{m_Q}\delta^{n'n}\delta^{A'A} + V_{\kappa^{PC}}^{(0)n'A';nA}(\mathbf{r}) + \frac{1}{m_Q}V_{\kappa^{PC}}^{(1)n'A';nA}(\mathbf{r},\mathbf{p}) + \mathcal{O}\left(\frac{1}{m_Q^2}\right). \tag{3.2}$$

The Lagrangian is specific to hybrid mesons composed of a quark-antiquark pair and an excited gluon field characterized by the gluonic spin κ, parity P and charge conjugation behavior C. The hybrid fields $\Psi_{\kappa^{PC}} \equiv {\Psi_{\kappa^{PC}}}^{nA}$ live both in the gluon spin space and the heavy quark spin space. The first index n corresponds to the $2\kappa+1$ components of the gluon spin. The second index $A = 1, 2, 3, 4$ corresponds to the heavy quark pair spin. The spin of $1/2$ of each quark can either couple to heavy quark pair spin 0 (singlet) or 1 (triplet) and the heavy quark spin operator is defined as $2\mathbf{S}_{Q\bar{Q}} = \boldsymbol{\sigma}_Q I_{2\bar{Q}} + \boldsymbol{\sigma}_{\bar{Q}} I_{2Q}$. The trace over spin indices is implicit in the Lagrangian.

The Lagrangian can be systematically extended to describe several sorts of heavy hadrons and their mixing. In the following, we give details on the leading order, order $(1/m_Q)^0$, and next-to-leading order, order $(1/m_Q)^1$, potentials for hybrid mesons.

3.1.1 Order $(1/m_Q)^0$

The Lagrangian at leading order in the heavy quark mass expansion includes, besides the kinetic term, all terms proportional to $(1/m_Q)^0$. The leading order potential in Eq. (3.2)

is given by $V^{(0)}_{\kappa^{PC}}(\mathbf{r})$. $V^{(0)}_{\kappa^{PC}} \equiv V^{(0)\,n'A';nA}_{\kappa^{PC}} = \delta^{A'A} V^{(0)\,n'n}_{\kappa^{PC}}$ is a 12×12 matrix, while $\delta^{A'A}$ indicates that at order $(1/m_Q)^0$ the spin of the heavy quarks is irrelevant. The leading order potential matrix $V^{(0)\,n'n}_{\kappa^{PC}}$ can be organized in terms of specific configurations of the gluonic field.

In the full rotation group, the gluon field is characterized by the orbital angular momentum κ, the behavior under parity transformation P and the behavior under charge conjugation C. The non-vanishing separation of the quark and antiquark to which the gluons are coupled breaks the full rotational symmetry to a cylindrical symmetry. The representations of this symmetry group, the dihedral group $D_{\infty h}$, are conventionally characterized by $\Lambda^{\epsilon}_{\eta}$:

- $\Lambda = \Sigma(=0), \Pi(=1), \Delta(=2), \ldots$ denotes the total angular momentum with respect to the quark-antiquark separation axis, i.e. a non-negative integer (w.l.o.g. we separate the static quark and antiquark along the z-axis).
- $\eta = g(=+), u(=-)$ describes the even (g) or odd (u) behavior under the combined parity and charge conjugation transformation $\mathcal{P} \circ \mathcal{C}$.
- $\epsilon = +, -$ is the eigenvalue of a reflection $\mathcal{P}_x$ along an axis perpendicular to the quark-antiquark separation axis (for definiteness, we use the x-axis). For $\Lambda \geq 1$, hybrid potentials are degenerate with respect to ϵ and ϵ is typically omitted. However, states with different ϵ are not equal and need to be differentiated.

Each representation κ^{PC} of the full rotation group corresponds to certain subduced representations $\Lambda^{\epsilon}_{\eta}$ of the subgroup. $\Lambda = |\lambda|$ can take values $0, \ldots, \kappa$ and η and ϵ are restricted by P and C. When the distance between quark and antiquark in a hybrid meson is sent to zero, the full rotational symmetry of the gluons is restored. In the limit of vanishing separation, the quark-antiquark pair represents an adjoint color source coupled to the gluon field, corresponding to a gluelump state (see Chapter 5). The gluelump with the lowest mass is associated to the gluonic quantum numbers $\kappa^{PC} = 1^{+-}$. The subduced representations for these quantum numbers are $\Pi^{\pm}_{u}$ and Σ^{-}_{u}, which are the quantum numbers of the lowest hybrid static potentials (see Chapter 4).

The representations of the subgroup could be characterized alternatively by λ_η, where λ denotes the gluon spin projection along the quark-antiquark separation axis $\lambda = -\kappa, \ldots, 0, \ldots, \kappa$. For $|\lambda| = \Lambda \geq 1$, hybrid static potentials are degenerate with respect to the sign of λ. This labeling is also common in the literature (e.g. Ref. [19]). However, in this work, we will primarily use the notation $\Lambda^{\epsilon}_{\eta}$ to label the representations, as is standard in lattice field theory.

Consequently, the leading order potential $V^{(0)}_{\kappa^{PC}}(\mathbf{r})$ can be decomposed as

$$V^{(0)\,n'n}_{\kappa^{PC}}(\mathbf{r}) = \sum_{\Lambda^{\epsilon}_{\eta}} V_{\Lambda^{\epsilon}_{\eta}}(r) \mathcal{P}^{n'n}_{\kappa\Lambda}. \tag{3.3}$$

$\mathcal{P}_{\kappa\Lambda^{\epsilon}_{\eta}}$ is a $(2\kappa+1) \times (2\kappa+1)$ projection matrix that projects onto a representation $\Lambda^{\epsilon}_{\eta}$ of

the dihedral group $D_{\infty h}$. The projection matrices for $\kappa^{PC} = 1^{+-}$ can be represented by

$$\mathcal{P}_{1\Sigma} = \mathcal{P}_{10} = \mathbf{e}_r \otimes \mathbf{e}_r \quad , \quad \mathcal{P}_{1\Pi} = \mathcal{P}_{11} = 1 - \mathbf{e}_r \otimes \mathbf{e}_r \,, \tag{3.4}$$

where $\mathbf{e}_r$ denotes the unit vector along the quark-antiquark separation axis. $\mathcal{P}_{1\Sigma}$ relates the components of the spin-1 gluon fields parallel to the separation axis of the quark-antiquark pair to the static potential $V_{\Sigma_u^-}(r)$, while $\mathcal{P}_{1\Pi}$ relates the gluon spin components of the gluon field which are orthogonal to the separation axis to the static potential $V_{\Pi_u}(r)$. $V_{\Lambda_\eta^\epsilon}(r)$ describes the static energy of the gluon field in the configuration Λ_η^ϵ as a function of the absolute separation distance r of the quark and antiquark. The lattice calculation and parametrization of the lowest hybrid static potentials $V_{\Pi_u}(r)$ and $V_{\Sigma_u^-}(r)$ is the main focus of Chapter 4.
The static potentials $V_{\Lambda_\eta^\epsilon}(r)$ are those matching coefficients of the BOEFT appearing at leading order in the inverse heavy quark mass expansion.

Weakly-coupled pNRQCD exploits an additional multipole expansion in r for short distances, which yields a prediction for the hybrid static potentials for small separations $r \ll 1/\Lambda_{\text{QCD}}$ [14, 100],

$$V_{\Lambda_\eta^\epsilon}^{\text{pNRQCD}}(r) = V_o(r) + \Lambda_H + b_{\Lambda_\eta^\epsilon} r^2 + \mathcal{O}\big(r^3\big). \tag{3.5}$$

$V_o(r)$ denotes the perturbative octet potential. At leading order in perturbation theory, it is a repulsive Coulombic potential $V_o(r) = \alpha_s/(6r)$, where α_s denotes the strong coupling constant at a reasonable scale. The perturbative octet potential is known up to next-to-next-to-next-to-leading order in α_s (see e.g. Ref. [102]). Λ_H denotes a constant corresponding to the gluelump mass associated with the quantum number sector. Both the gluelump mass and the next-to-leading order term in the multipole expansion proportional to r^2 denote non-perturbative quantities. Their determination requires non-perturbative methods such as lattice gauge theory. The lattice calculation and continuum extrapolation of gluelump masses is the main focus of Chapter 5.

3.1.2 Order $(1/m_Q)^1$

Corrections to the leading order arise as additional terms in the heavy quark mass expansion of the Hamiltonians and as supplementary terms in the Lagrangian,

$$\mathcal{L} = \sum_{\kappa} \Psi^\dagger_{\kappa^{PC}}{}^{n'A'} \left[i\partial_t - \left(-\frac{\Delta_{\mathbf{r}}}{m_Q} + V^{(0)}_{\kappa^{PC}}(\mathbf{r}) + \frac{1}{m_Q} V^{(1)}_{\kappa^{PC}}(\mathbf{r},\mathbf{p}) \right) \right]^{n'A';nA} \Psi_{\kappa^{PC}}{}^{nA} + \mathcal{L}_{\mathcal{O}(1/m_Q)} \,. \tag{3.6}$$

For ordinary quarkonium ($\kappa^{PC} = 0^{++}$), the potential $V^{(1)}_{0^{++}}(\mathbf{r},\mathbf{p})$ does not depend on the heavy quark spin $S_{Q\bar{Q}}$. Spin-dependent potentials for ordinary quarkonium only ap-

pear beyond order $(1/m_Q)^2$. Some of them have been studied in the literature (see e.g. Refs. [103–106]).

In contrast, for heavy hybrid mesons, spin-dependent effects start to show up at a lower order, specifically at $(1/m_Q)^1$. This makes these effects especially important for hybrid mesons. The next-to-leading order potential for hybrid mesons can be divided into spin-dependent and spin-independent contributions,

$$V^{(1)}_{\kappa^{PC}}(\mathbf{r},\mathbf{p}) = V^{(1),\mathrm{SD}}_{\kappa^{PC}}(\mathbf{r}) + V^{(1),\mathrm{SI}}_{\kappa^{PC}}(\mathbf{r},\mathbf{p})\,. \tag{3.7}$$

The spin-independent corrections are not considered in this work because matching expressions are mostly not available for heavy hybrid mesons (only the angular momentum-dependent potential $V^l_{\Lambda\Lambda'}$ has been derived, see Ref. [19] for details, and matching equations for spin-independent potentials have been obtained in weakly-coupled pNRQCD only for short r, see Ref. [18] for details). Even when spin-independent terms are neglected, computations of heavy hybrid meson masses (as outlined in the next section) remain relevant, as spin-dependent terms determine the spin splittings in the spectra of heavy hybrid mesons.

Hybrid spin-dependent potentials

The spin-dependent part of the hybrid potential at order $(1/m_Q)^1$ was derived in Refs. [17–19]

$$\begin{aligned}[V^{(1)SD}_{\kappa^{PC}}(\mathbf{r})]^{n'A;nA} = \sum_{\Lambda\Lambda'} \mathcal{P}^{n'k}_{\kappa\Lambda} \Big[& V^{sa}_{\kappa^{PC}\Lambda\Lambda'}(r)(\boldsymbol{S}^i_{Q\bar{Q}})^{A'A} \cdot \left(\mathcal{P}^{ir}_{10}\cdot(\boldsymbol{S}^r_\kappa)^{kj}\right) \\ & + V^{sb}_{\kappa^{PC}\Lambda\Lambda'}(r)(\boldsymbol{S}^i_{Q\bar{Q}})^{A'A} \cdot \left(\mathcal{P}^{ir}_{11}\cdot(\boldsymbol{S}^r_\kappa)^{kj}\right)\Big] \mathcal{P}^{jn}_{\kappa\Lambda'}\,. \end{aligned} \tag{3.8}$$

$\boldsymbol{S}_\kappa$ denotes the spin operator of the gluons with spin κ, which couples to the heavy quark pair spin $\boldsymbol{S}_{Q\bar{Q}}$. The hybrid spin-dependent potentials $V^{sa}_{\kappa^{PC}\Lambda\Lambda'}(r)$ and $V^{sb}_{\kappa^{PC}\Lambda\Lambda'}(r)$ are matching coefficients of the BOEFT at next-to-leading order. These r-dependent coefficients require determination with non-perturbative methods such as lattice field theory. A matching calculation between NRQCD and BOEFT correlators provides expressions for these coefficients in terms of generalized Wilson loops. We provide a detailed discussion of the matching expressions and their lattice calculation in Chapter 6. For small separations ($r \ll 1/\Lambda_{\mathrm{QCD}}$), pNRQCD exploits an additional multipole expansion which yields a prediction for the hybrid spin-dependent potentials. For the potentials $V^{sa}_{11}(r)$ and $V^{sb}_{10}(r)$ related to the lowest hybrid mesons with gluon spin $\kappa^{PC} = 1^{+-}$, it reads [18, 19]

$$V^{sa}_{11}(r) = V^{np\,(0)}_{SK} + V^{np\,(1)}_{SK} r^2 + \cdots \tag{3.9}$$

$$V^{sb}_{10}(r) = V^{np\,(0)}_{SK} + (V^{np\,(0)}_{SKb} + V^{np\,(1)}_{SK}) r^2 + \cdots\,. \tag{3.10}$$

$V^{np\,(1)}_{SK}$, $V^{np\,(1)}_{SK}$ $V^{np\,(1)}_{SK}$ are unknown non-perturbative coefficients. Ref. [18] derived expressions for these coefficients in terms of gluelump-like correlators with chromomagnetic inser-

tions, which could also be evaluated with lattice field theory. These predictions, however, are limited to short distances.

Hybrid-quarkonium mixing potentials

In addition, interactions between hybrid mesons and ordinary quarkonium states with the same quantum numbers are possible due to the coupling between gluon spin and heavy quark spin. This hybrid-quarkonium mixing is also suppressed by a factor of $1/m_Q$ and is incorporated in the Lagrangian as an additional term $\mathcal{L}_{\mathcal{O}(1/m_Q)}$, which was derived in Ref. [15]. For the mixing between ordinary quarkonium and the lowest hybrid mesons related to gluon spin $\kappa = 1$, the hybrid-quarkonium mixing Lagrangian reads

$$\mathcal{L}_{\text{mixing}} = 2V_{\text{mix}}^{n'n}\Big(\Psi_{0^{++}}^{n'\dagger}\Psi_{1^{+-}}^{n0} + \Psi_{0^{++}}^{0\dagger}\Psi_{1^{+-}}^{nn'} + \text{H.c.}\Big). \tag{3.11}$$

The mixing term in the Lagrangian has no apparent $1/m_Q$ factor due to local field redefinitions [15]. Nevertheless, it is of order $(1/m_Q)^1$ because of its dependence on the heavy-quark spin.
In this notation, $\Psi_{0^{++}}^{A\dagger}$ denotes the ordinary quarkonium field and it has four components, where $A = 0$ refers to heavy quark-antiquark spin $S_{Q\bar{Q}} = 0$ and $A = j$ with $j = 1, 2, 3$ to the eigenstates of the three Cartesian x-, y- and z-components of the heavy quark spin-1 operator. $\Psi_{1^{+-}}^{nA}$ represents the hybrid meson field, where the first index corresponds to the gluon spin components and the second is associated with the heavy quark spin components similar to the ordinary quarkonium field. Note that the notation in Ref. [15] differs from that used here, which aligns with the notation in Refs. [19, 23]. The correspondence between both notations is explained in Appendix C.
Regardless of the Lagrangian formulation, the potential matrix $V_{\text{mix}}^{n'n}$ can be decomposed in terms of the irreducible representations of $D_{\infty h}$

$$V_{\text{mix}}^{n'n}(\mathbf{r}) = \sum_{\Lambda_\eta^\epsilon = \Sigma_u^-, \Pi_u} V_{\Lambda_\eta^\epsilon}^{\text{mix}}(r)\mathcal{P}_{1\Lambda}^{n'n} \tag{3.12}$$

$$= V_{\Sigma_u^-}^{\text{mix}}(r)\Big(\mathbf{e}_r \otimes \mathbf{e}_r\Big)^{n'n} + V_{\Pi_u}^{\text{mix}}(r)\Big(1 - \mathbf{e}_r \otimes \mathbf{e}_r\Big)^{n'n}. \tag{3.13}$$

The mixing potentials $V_{\Pi_u}^{\text{mix}}(r)$ and $V_{\Sigma_u^-}^{\text{mix}}(r)$ are matching coefficients of the BOEFT at next-to-leading order, which require determination via lattice field theory. These coefficients can be expressed in terms of generalized Wilson loops after matching calculations between NRQCD and BOEFT correlators [15]. The Wilson loop expressions and their calculation with lattice field theory will be discussed in detail in Chapter 6. At short distances, pNRQCD predicts that the potentials $V_{\Sigma_u^-}^{\text{mix}}(r)$ and $V_{\Pi_u}^{\text{mix}}(r)$ are degenerate for small separations [15].

3.2 Schrödinger-like equations

The Born-Oppenheimer Effective Field Theory originates in the Born-Oppenheimer approximation, first introduced in Ref. [96] and successfully applied to diatomic molecules. Its extension to hybrid mesons, which exhibit a similar hierarchy of energy scales, was pioneered in Refs. [29, 36, 107] and is comprehensively discussed in Ref. [99].
In the following, we outline the Born-Oppenheimer approximation as applied to hybrid mesons and present the corresponding radial Schrödinger equations. We then discuss refined formulations based on the Born-Oppenheimer Effective Field Theory framework [14, 15, 23], which incorporates systematic corrections and, thereby, improves the theoretical prediction of the hybrid meson spectrum.

3.2.1 Born-Oppenheimer approximation

The Born-Oppenheimer approximation exploits the existence of slow and fast degrees of freedom, typically arising in systems where particle masses differ by orders of magnitude, leading to separate timescales. Its application to hybrid mesons relies on several assumptions. The heavy quarks are treated as static on the timescale of gluon dynamics and their spin is neglected. Under this assumption, the gluonic energy levels are determined in the presence of static color sources, yielding the so-called static potentials. Secondly, it is assumed that the gluonic field adjusts instantaneously to variations in the heavy quark positions while remaining in its configuration. This is the adiabatic approximation. These assumptions hold well for heavy quarks, as corrections are of order $1/m_Q$. Subsequently, within the single-channel approximation, contributions from other quantum number sectors Λ_η^ϵ are neglected, which is justified as long as the static potentials do not cross with other static potentials.
The simplest Schrödinger equation is the one for ordinary quarkonium, where a heavy quark-antiquark pair binds within an interaction potential given by the ordinary static potential Σ_g^+

$$\left[-\frac{\Delta_{\mathbf{r}}}{m_Q} + V_{\Sigma_g^+}(r)\right] \Psi(\mathbf{r}) = E_{\Sigma_g^+} \Psi(\mathbf{r})\,. \tag{3.14}$$

Here, $\Psi(\mathbf{r})$ represents the wave function of the quarkonium system. The kinetic term consists of a radial derivative and a centrifugal term proportional to the orbital angular momentum operator of the heavy quark-antiquark pair

$$\frac{\Delta_{\mathbf{r}}}{m_Q} = \frac{1}{m_Q}\left(\frac{d}{dr}\right)^2 - \frac{\mathbf{L}_{Q\bar{Q}}^2}{m_Q r^2}\,. \tag{3.15}$$

For ordinary quarkonium, the quark-antiquark orbital angular momentum $\mathbf{L}_{Q\bar{Q}}$ coincides with the total orbital angular momentum $\mathbf{L}$.
Applying a separation ansatz, $\Psi(\mathbf{r}) = (1/r) P_{\Sigma_g^+;L,n}(r) Y_{LM}(\theta,\phi)$, where Y_{LM} are spherical harmonics, the equation reduces to a radial Schrödinger equation for the heavy quark-

antiquark relative coordinate in the static potential $V_{\Sigma_g^+}(r)$

$$\left(-\frac{1}{m_Q}\left(\frac{d}{dr}\right)^2+\frac{L(L+1)}{m_Q r^2}+V_{\Sigma_g^+}(r)\right)P_{\Sigma_g^+;L,n}(r) \;=\; E_{\Sigma_g^+;L,n}P_{\Sigma_g^+;L,n}(r)\,. \tag{3.16}$$

For hybrid mesons, the wave function has $2\kappa+1$ components due to the corresponding gluon spin κ. It can be expanded in terms of static eigenstates. As opposed to the case of ordinary quarkonium, the centrifugal term of the derivative, the orbital angular momentum operator $\mathbf{L}_{Q\bar{Q}}$, acts non-trivially on the static eigenstates, which introduces mixing between channels corresponding to the same gluon spin κ. For details, see e.g. Refs. [14, 108]. Under the single-channel approximation, the radial Schrödinger equation for hybrid mesons with a static potential $V_{\Lambda_\eta^\epsilon}(r)$ takes the form

$$\left(\frac{-1}{m}\frac{d^2}{dr^2}+\frac{L(L+1)-2\Lambda^2+\kappa(\kappa+1)}{mr^2}+V_{\Lambda_\eta^\epsilon}(r)\right)P_{\Lambda_\eta^\epsilon;L,n}(r) \;=\; E_{\Lambda_\eta^\epsilon;L,n}P_{\Lambda_\eta^\epsilon;L,n}(r). \tag{3.17}$$

Here, L is the total orbital angular momentum, given by $\mathbf{L}=\mathbf{L}_{Q\bar{Q}}+\boldsymbol{\kappa}$. The term $L(L+1)-2\Lambda^2+\kappa(\kappa+1)$ arises from the expectation value of the quark-antiquark orbital angular momentum operator in the gluonic static eigenstates Λ_η^ϵ (for details see Ref. [99]). This one-dimensional, non-relativistic Schrödinger equation for the radial quark-antiquark wavefunction has been used in Refs. [29, 36, 51, 55, 99, 107] to compute energy levels of heavy hybrid mesons. Since the heavy quark spin is neglected, the resulting energy levels correspond to heavy-quark spin multiplets. The quantum numbers J^{PC} of hybrid mesons within these spin multiplets can be determined via

$$J \;=\; \begin{cases} L & \text{if } S=0 \\ 1 & \text{if } S=1 \text{ and } L=0 \\ \{L-1,L,L+1\} & \text{if } S=1 \text{ and } L\geq 1 \end{cases} \tag{3.18}$$

$$P \;=\; \epsilon(-1)^{\Lambda+L+1} \tag{3.19}$$

$$C \;=\; \eta\epsilon(-1)^{\Lambda+L+S} \tag{3.20}$$

as discussed in [99].

3.2.2 Coupled-channel Schrödinger equations including heavy quark spin effects

The Born-Oppenheimer Effective Field Theory systematically extends the Born-Oppenheimer approximation by incorporating corrections in inverse powers of the heavy quark mass, such as heavy quark spin effects. These corrections are included through Schrödinger-like multi-channel equations, which are derived from the equations of motion using the Lagrangian at a given order in the heavy quark mass expansion.

At leading order, the general Schrödinger-like equation takes the form

$$\left[-\frac{\Delta_{\mathbf{r}}}{m_Q}\delta^{n'n}+V_{\kappa^{PC}}^{(0)\,n'n}(\mathbf{r})\right]\Psi_{\kappa^{PC}}^{n}(\mathbf{r})=E\Psi_{\kappa^{PC}}^{n'}(\mathbf{r})\,. \tag{3.21}$$

For ordinary quarkonium with $\kappa=0$, this is a single-component matrix equation and the resulting radial Schrödinger equation reduces to the one obtained in the Born-Oppenheimer approximation for the Σ_g^+ potential (3.16).
The situation is more complex for the lowest hybrid mesons, where the gluon spin is $\kappa=1$. The wave function consists of three components corresponding to the gluonic configurations Π_u and Σ_u^-. Without the single-channel approximation, this leads to a system of 3×3 coupled Schrödinger-like equations [14, 15]. Such coupled equations are obtained by expanding the hybrid wave function in terms of eigenstates of the total orbital angular momentum $\mathbf{L}=\mathbf{L}_{Q\bar{Q}}+\boldsymbol{\kappa}$, following Ref. [15]

$$\begin{aligned}\boldsymbol{\Psi}(\mathbf{r})=&\frac{1}{r}P_0^+(r)\mathbf{Y}_{00}^{L_{Q\bar{Q}}=1}\\&+\frac{1}{r}\sum_{L=1}^{\infty}\sum_{M=-L}^{L}[P_L^+(r)\mathbf{Y}_{LM}^{L_{Q\bar{Q}}=L+1}+P_L^0(r)\mathbf{Y}_{LM}^{L_{Q\bar{Q}}=L}+P_L^-(r)\mathbf{Y}_{LM}^{L_{Q\bar{Q}}=|L-1|}]\,.\end{aligned} \tag{3.22}$$

Here, $P_L^{L_{Q\bar{Q}}}(r)$ are the radial wave functions for the heavy quark-antiquark pair, with the upper index indicating $L_{Q\bar{Q}}$, where $L_{Q\bar{Q}}=L,L\pm1$ are represented by $0,\pm1$. $\mathbf{Y}_{L\,M}^{L_{Q\bar{Q}}}$ are vector spherical harmonics, defined as

$$Y_{L\,M}^{iL_{Q\bar{Q}}}=\sum_{\mu=0,\pm1}C(L_{Q\bar{Q}}1L;M-\mu\,\mu)Y_{L_{Q\bar{Q}}}^{M-\mu}\chi_\mu^i, \tag{3.23}$$

where $Y_{L_{Q\bar{Q}}}^M$ are standard spherical harmonics, $C(L_1L_2L;M_1M_2)$ are Clebsch-Gordan coefficients and $\boldsymbol{\chi}_{\pm1}=\mp\frac{1}{\sqrt{2}}(1,\pm i,0)^T$ and $\boldsymbol{\chi}_0=(0,0,1)^T$ are the gluon spin functions.
In the basis introduced above, the coupled-channel radial Schrödinger equations for $L\neq0$ are

$$\begin{aligned}&\left[-\frac{1}{m_Q}\frac{\partial^2}{\partial r^2}+\begin{pmatrix}\frac{(L-1)L}{m_Qr^2}&0\\0&\frac{(L+1)(L+2)}{m_Qr^2}\end{pmatrix}+V_{\Sigma_u^-}(r)+\right.\\&\left.(V_{\Pi_u}(r)-V_{\Sigma_u^-}(r))\begin{pmatrix}\frac{L+1}{2L+1}&\frac{\sqrt{(L+1)L}}{2L+1}\\\frac{\sqrt{(L+1)L}}{2L+1}&\frac{L}{2L+1}\end{pmatrix}\right]\begin{pmatrix}P_L^-(r)\\P_L^+(r)\end{pmatrix}=E_{LL_{Q\bar{Q}}}\begin{pmatrix}P_L^-(r)\\P_L^+(r)\end{pmatrix}\end{aligned} \tag{3.24}$$

$$\left(-\frac{1}{m_Q}\frac{\partial^2}{\partial r^2}+\frac{L(L+1)}{m_Qr^2}+V_{\Pi_u}(r)\right)P_L^0(r)=E_{LL_{Q\bar{Q}}}P_L^0(r)\,, \tag{3.25}$$

and for $L = 0$

$$\left(-\frac{1}{m_Q}\frac{\partial^2}{\partial r^2} + \frac{2}{m_Q r^2} + V_{\Sigma_u^-}(r)\right) P_0^+(r) = E_{01} P_0^+(r)\,. \tag{3.26}$$

These coupled equations are equivalent to those formulated in an alternative basis in Ref. [14].

By applying the single-channel approximation to the leading-order hybrid Schrödinger-like equations and using the gluonic eigenstates as the basis, one recovers the hybrid single-channel Schrödinger equations of the Born-Oppenheimer approximation (3.17). Masses of heavy quark spin multiplets have been computed from the leading-order coupled-channel Schrödinger equations in Refs. [14, 15].

While the leading-order equations are independent of the heavy quark-antiquark pair spin, the next-to-leading-order spin-dependent potential, $V_{1^{+-}}^{(1),SD}$ (Eq. (6.1)), arising at order $(1/m_Q)^1$, induces the hyperfine splitting in the heavy hybrid meson spectrum. The inclusion of the next-to-leading-order potential matrix leads to coupled channel Schrödinger equations with a matrix structure of size 3×3, 7×7 and 9×9 for total angular momentum of the heavy hybrid meson $J = 0$, $J = 1$ and $J > 1$, respectively, where $\mathbf{J} = \mathbf{L} + \mathbf{S}_{Q\bar{Q}}$. These complicated equations have been derived in Ref. [23], where explicit equations can be found.

The hybrid-quarkonium mixing potential V_{mix} (Eq. (6.2)), also appearing at order $(1/m_Q)^1$, couples ordinary quarkonium and heavy hybrid mesons. Schrödinger-like equations incorporating V_{mix} but neglecting the spin-dependent potential $V_{1^{+-}}^{(1),SD}$ were derived in Ref. [15]. The resulting coupled channel Schrödinger equations are of size 2×2, 4×4 and 6×6. An illustrative example of such a coupled-channel Schrödinger equation, which demonstrates the mixing of ordinary quarkonium and heavy hybrid mesons, is

$$\left(-\frac{1}{m_Q}\frac{d^2}{dr^2} + \frac{J(J+1)}{m_Q r^2} + \begin{pmatrix} V_{\Sigma_g^+} & 2V_{\Pi_u}^{\text{mix}} \\ 2V_{\Pi_u}^{\text{mix}} & V_{\Pi_u} \end{pmatrix}\right) \begin{pmatrix} S_{1JM}^0(r) \\ P_{0JM}^0(r) \end{pmatrix} = E \begin{pmatrix} S_{1JM}^0(r) \\ P_{0JM}^0(r) \end{pmatrix} \tag{3.27}$$

for total angular momentum $J \neq 0$, where M is the third component of J. Here, the mixing potential $V_{\Pi_u}^{\text{mix}}$, appearing in the off-diagonal elements of the potential matrix, couples the radial wave functions S_{1JM}^0 and P_{0JM}^0. S_{1JM}^0 represents quarkonium with $S_{Q\bar{Q}} = 1$, while P_{0JM}^0 represents a heavy hybrid meson with $S_{Q\bar{Q}} = 0$. The upper index denotes $L_{Q\bar{Q}}$, where $L_{Q\bar{Q}} = L, L \pm 1$ is represented by $0, \pm1$.

4 Hybrid static potentials Π_u and Σ_u^-

Static potentials describe the energy of the gluonic field in the presence of a static quark-antiquark pair as a function of its separation. In ordinary quarkonium, the gluonic field is in a trivial, non-excited configuration and its energy is described by the ordinary static potential. In hybrid mesons, however, the gluonic field is excited and the field configuration is characterized by quantum numbers Λ_η^ϵ different from the quantum numbers Σ_g^+ of the ordinary static potential. The hybrid static potential describes the energy of the excited gluonic field. This chapter focuses on the two lowest hybrid static potentials, Π_u and Σ_u^-, which play a crucial role within the Born-Oppenheimer Effective Field Theory (BOEFT) as they provide the leading-order contribution in the heavy quark mass expansion of the BOEFT Lagrangian for the lowest heavy hybrid mesons (see Chapter 3).

The leading order of the heavy quark mass expansion, order $(1/m_Q)^0$, where the potentials are solely given by the static potentials, corresponds to the well-known Born-Oppenheimer approximation, which has been used for a long time to study heavy hybrid mesons [14, 15, 17, 18, 29, 30, 36, 51, 98, 99]. Perturbation theory determines the static potentials at very short quark-antiquark separations and QCD effective string theory can describe them at large separations [109, 110], but non-perturbative methods such as lattice gauge theory are required to determine the potentials in a broader separation range from first principles. Lattice results for hybrid static potentials were computed in Refs. [24–51, 111, 112]. Frequently used lattice results cover quark-antiquark separations of $r \gtrsim 0.16\,\text{fm}$ [40, 44, 51], where the lattice results are considered trustworthy. To make a connection to perturbation theory, lattice data at much smaller separations is needed.

In this chapter, we present our investigations of hybrid static potentials, which were previously published in Refs. [53–56]. We extend lattice field theory results for the two lowest hybrid static potentials Π_u and Σ_u^- to smaller quark-antiquark separations by using several rather fine lattice spacings. We discuss the lattice calculation of Wilson loop correlation functions with suitable hybrid operators, present details on the four gauge link ensembles generated for this work and discuss the use of the multilevel algorithm for statistical error reduction. Hybrid static potentials are extracted from plateau fits of effective potentials for all four lattice ensembles, reaching separations of $r = 0.04\,\text{fm}$. We determine accurate parametrizations for the hybrid static potentials Π_u and Σ_u^- by quantifying and eliminating discretization errors. The parametrizations provide a continuum limit description and can be directly used in Schrödinger equations solved for the masses of heavy hybrid mesons. We investigate the effects of our improvements for heavy hybrid meson masses computed in the Born-Oppenheimer approximation. Moreover, we discuss and exclude systematic

errors from topology, the finite lattice volume and glueball decay.

4.1 Lattice computation

In this section, we outline the computational setup and methodology employed for the lattice determination of hybrid static potentials. We use methods introduced in Ref. [51] and extend the results from this reference to finer lattice spacings to obtain hybrid static potentials at shorter separation distances. Our study utilizes newly generated gauge link ensembles, which are also applied in subsequent chapters for the computation of gluelump masses (Chapter 5) and hybrid spin-dependent potentials (Chapter 6).

4.1.1 Wilson loop correlation functions

In this work, we focus primarily on the two lowest hybrid static potentials, Π_u and Σ_u^-, both of which correspond to gluon quantum numbers $\kappa^{PC} = 1^{+-}$. Additionally, we compute the ordinary static potential with quantum numbers Σ_g^+ to control discretization effects. The static potential $V_{\Lambda_\eta^\epsilon}(r)$, as the ground-state gluonic energy in the specific quantum number sector Λ_η^ϵ, can be obtained from the large-time limit of a Wilson loop-like correlation function,

$$\lim_{T\to\infty} W_{\Lambda_\eta^\epsilon}(r,T) \propto \exp\Big(-V_{\Lambda_\eta^\epsilon}(r)T\Big)\,, \tag{4.1}$$

which follows from the spectral decomposition. The Wilson loop-like correlation function is defined as

$$\begin{aligned} W_{\Lambda_\eta^\epsilon}(r,T) &= \langle\Omega|(\mathcal{O}^{\text{lattice}}_{\Lambda_\eta^\epsilon})^\dagger(r,T/2)\mathcal{O}^{\text{lattice}}_{\Lambda_\eta^\epsilon}(r,-T/2)|\Omega\rangle \\ &= \Big\langle \mathrm{Tr}\Big(a_{S;\Lambda_\eta^\epsilon}(-r/2,+r/2;-T/2)U(+r/2;-T/2,T/2)\Big(a_{S;\Lambda_\eta^\epsilon}(-r/2,+r/2;T/2)\Big)^\dagger \\ &\qquad U(-r/2;T/2,-T/2)\Big)\Big\rangle_U, \end{aligned} \tag{4.2}$$

where $\mathcal{O}^{\text{lattice}}_{\Lambda_\eta^\epsilon}$ denotes the operator generating a (hybrid) trial state with definite quantum numbers Λ_η^ϵ,

$$\mathcal{O}^{\text{lattice}}_{\Lambda_\eta^\epsilon} = \bar{Q}(-r/2)a_{S;\Lambda_\eta^\epsilon}(-r/2,+r/2)Q(+r/2)\,. \tag{4.3}$$

The static quark and antiquark, Q and $\bar{Q}$, are separated along the z-axis without loss of generality in the following analysis. Thus, we use a simplified notation $r/2 \equiv (0,0,r/2)$. $U(+r/2;-T/2,T/2)$ represents the temporal gauge link connecting times $-T/2$ and $T/2$ and $\langle\dots\rangle_U$ denotes the ensemble average over gauge link configurations.
The creation operator $a_{S;\Lambda_\eta^\epsilon}$ for Λ_η^ϵ is a sum of properly transformed spatial insertions

$S(r_1, r_2)$, defined as

$$a_{S;\Lambda_\eta^\epsilon}(-r/2, +r/2) = \frac{1}{4}\Big(1 + \eta(\mathcal{P}\circ\mathcal{C}) + \epsilon\mathcal{P}_x + \eta\epsilon(\mathcal{P}\circ\mathcal{C})\mathcal{P}_x\Big)$$
$$\times \sum_{k=0}^{3} \frac{1}{2}\left(\exp\left(\frac{+i\pi\Lambda k}{2}\right) + \exp\left(\frac{-i\pi\Lambda k}{2}\right)\right) R\left(\frac{\pi k}{2}\right)\Big(U(-r/2, r_1)S(r_1, r_2)U(r_2, +r/2)\Big). \tag{4.4}$$

$U(r_1, r_2)$ is a spatial gauge link connecting lattice sites r_1 and r_2. $R\left(\frac{\pi k}{2}\right)$ denotes a rotation around the quark-antiquark separation axis by discrete multiples of $\pi/2$. Due to the restriction to discrete rotations on the discretized spacetime volume, the lattice hybrid trial states, which correspond to lattice representations $\Gamma \in D_{4h}$, do not have definite continuum angular momentum Λ. They receive contributions from an infinite number of continuum angular momentum. However, we assume that the ground states generated with $a_{S;\Lambda_\eta^\epsilon}$ correspond to the lowest continuum angular momentum of this infinite set, which would be given by Λ. $\mathcal{P}_x$ and $\mathcal{P}\circ\mathcal{C}$ represent a parity transformation and a combined parity and charge conjugation transformation of the gauge link paths, respectively.

In Ref. [51], optimized insertion paths S were identified to enhance the ground-state overlap in each of the considered quantum number sectors Λ_η^ϵ. Optimized operators are crucial for reducing excited-state contamination and obtaining precise and reliable potentials from Wilson loop correlators at large but finite temporal extents.

We employ one operator for each quantum number $\Lambda_\eta^\epsilon \in \{\Sigma_g^+, \Pi_u^+, \Sigma_u^-\}$. For Σ_g^+, S is a straight path of spatial gauge links. We select $S = S_{\mathrm{III},1}$ for Π_u^+ and $S = S_{\mathrm{IV},2}$ for Σ_u^-, as defined in Ref. [51] or in Tables 4.1 and 4.2. The spatial extent of these operators was optimized in Ref. [51] for a lattice spacing of $a = 0.093\,\mathrm{fm}$. We increase the operator extents E_x and E_y (see Tables 4.1 and 4.2) consistently when reducing the lattice spacing to maintain their physical length, ensuring a rather large overlap with the ground state. We validated this scaling in a SU(2) exploratory study of the hybrid operators at different lattice spacings [53].

Note that the definition of creation operators (4.4) differs slightly from the one given in Ref. [51]. Eq. (4.4) ensures exclusively real weight factors simplifying lattice calculations. This definition was also used in calculations in Ref. [51]. It is important to note that the use of solely real weights as in Eq. (4.4) alters the exact operator structure while still generating a state with quantum numbers Λ_η^ϵ. Because of this, $a_{S;\Pi_u^+}$ is not related to $a_{S;\Pi_u^-}$ by a simple $\pi/2$ rotation around the separation axis, despite their identical insertion S and the fact that the static potentials are degenerate, $V_{\Pi_u^+} = V_{\Pi_u^-} = V_{\Pi_u}$. The choice of operator structure may introduce relative phases between operators. However, this is relevant only if we are interested in matrix elements between different hybrid operators. These are associated with hybrid spin-dependent potentials, which are investigated in Chapter 6.

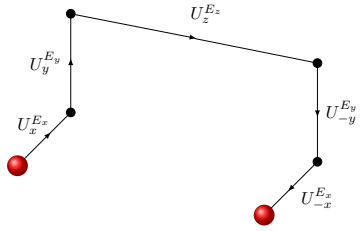

$US_{\mathrm{III},1}U = U_x^{E_x} U_y^{E_y} U_z^{E_z} U_{-y}^{E_y} U_{-x}^{E_x}$

r/a	2	3	4	5	6	7	8	9	10	11	12
E_z	2	3	4	5	6	7	8	9	10	11	12
E_x	1	1	1	1	1	1	1	1	1	1	1
E_y	3	3	3	3	3	3	3	3	3	3	3

Table 4.1: Optimized creation operator for Π_u^+ [51].

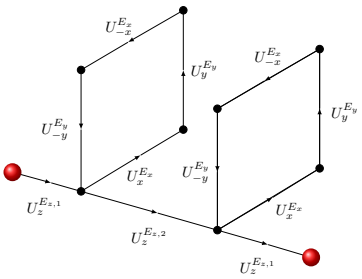

$US_{\mathrm{IV},2}U = U_z^{E_{z,1}} U_x^{E_x} U_y^{E_y} U_{-x}^{E_x} U_{-y}^{E_y} U_z^{E_{z,2}}$
$\times U_x^{E_x} U_y^{E_y} U_{-x}^{E_x} U_{-y}^{E_y} U_z^{E_{z,1}}$

r/a	2	3	4	5	6	7	8	9	10	11	12
$E_{z,1}$	0	0	0	1	1	2	2	3	3	4	4
$E_{z,2}$	2	3	4	3	4	3	4	3	4	3	4
E_x	3	3	3	3	3	3	3	3	3	3	3
E_y	3	3	3	3	3	3	3	3	3	3	3

Table 4.2: Optimized creation operator for Σ_u^- [51].

4.1.2 Gauge link ensembles

We employ four SU(3) gauge link ensembles with fine lattice spacings to investigate the short-distance regime of hybrid static potentials. We generated the gauge link ensembles with the standard Wilson plaquette action and a heat bath algorithm implemented in the CL2QCD software package [63]. Each ensemble was produced with N_{sim} independent Monte Carlo simulations, each consisting of N_{total} updates. Each update includes a heat bath sweep followed by N_{or} overrelaxation sweeps to minimize correlations between consecutive gauge link configurations. After discarding the initial N_{therm} thermalization updates, correlation functions were measured using gauge link configurations separated by N_{sep} updates. The total number of gauge link configurations used for measurements is given by $N_{\mathrm{meas}} = N_{\mathrm{sim}} \frac{(N_{\mathrm{total}} - N_{\mathrm{therm}})}{N_{\mathrm{sep}}}$. The ensemble-specific parameters are listed in Table 4.3.
The four gauge link ensembles have gauge couplings $\beta = 6.594\,,\ 6.451\,,\ 6.284\,,\ 6.000$. The gauge couplings are related to lattice spacings a via a parametrization of $\ln(a/r_0)$ provided in Ref. [93], where the Sommer scale r_0 and a related scale r_c were determined. In order to introduce physical units, we set $r_0 = 0.5\,\mathrm{fm}$, which is a simple and common choice in pure gauge theory but is slightly larger than QCD results [80]. The lattice volume $L^3 \times T$ for all ensembles is approximately $(1.2\,\mathrm{fm})^3 \times 2.4\,\mathrm{fm}$ in physical units. Due to technical constraints in the CL2QCD software, both spatial and temporal lattice extents must have an even number of lattice sites, so the ratio T/L is not exactly the same across ensembles. Additionally, some configurations from ensembles C and D were reused from a previous study [78]. Nevertheless, the volumes are sufficiently large to neglect finite volume

corrections, as discussed in Section 4.4.2.

To eliminate autocorrelations, the N_{meas} gauge link configurations were grouped into smaller bins. Statistical errors for individual ensemble results were determined using the jackknife method. For analyses involving data from multiple ensembles, we developed a consistent error analysis strategy described in detail in Appendix A. This approach utilizes the bootstrap method when combining data from ensembles with different numbers of jackknife-reduced samples. The same strategy is applied in subsequent chapters. The computations in this chapter were performed using $N^A = 320$, $N^B = N^C = N^D = 160$ jackknife reduced samples. In the parametrizations of hybrid static potentials, we incorporate an additional ensemble from Ref. [51] with $N^{A^{\text{HYP2}}} = 5000$ jackknife reduced samples. The ensemble details are further discussed in Section 4.3. Ultimately, we employ $K = 10000$ bootstrap samples for the final analysis.

ensemble	β	a in fm [93]	$(L/a)^3 \times T/a$	N_{sim}	N_{total}	N_{or}	N_{therm}	N_{sep}	N_{meas}
A	6.000	0.093	$12^3 \times 26$	2	60000	4	20000	50	1600
B	6.284	0.060	$20^3 \times 40$	2	60000	12	20000	100	800
C	6.451	0.048	$26^3 \times 50$	4	80000	15	40000	200	800
D	6.594	0.040	$30^3 \times 60$	4	80000	15	40000	200	800

Table 4.3: Gauge link ensembles.

4.1.3 Computational details

We utilize the multilevel algorithm to enhance computational efficiency for Wilson loop-like correlation functions [77]. The implementation of the multilevel algorithm has already been carried out in the context of Ref. [78]. For a detailed explanation of the algorithm and its technical aspects, we refer to Section 2.4.4 and Refs. [55, 78]. In our calculation, we choose a single level of partitioning with a uniform pattern, where each time-slice has a thickness of 2, i.e. $p_1 = p_2 = \cdots = p_{n_{\text{ts}}} = 2$. This choice simplifies the algorithm and maximizes efficiency by fully exploiting translational invariance in the temporal direction. Additionally, we set the number of sublattice configurations n_m to 400, each separated by $n_u = 30$ updates.

Furthermore, APE smearing is applied to the spatial gauge links to adjust the size of the operators and improve the signal quality. We use a smearing coefficient of $\alpha_{\text{APE}} = 0.5$, a commonly chosen value in lattice gauge theory. The number of APE smearing steps was increased as the lattice spacing decreased, based on a study in SU(2) that investigated the dependence of the effective potential for both the ordinary and the lowest hybrid static potential on the number of smearing levels. The chosen smearing levels, summarized in Table 4.4, are consistently applied across all static potential quantum numbers.

a in fm	0.093	0.060	0.048	0.040
N_{APE} for SU(3)	20	50	75	100

Table 4.4: Smearing parameter N_{APE} for various lattice spacings for gauge group SU(3).

4.2 Numerical results

We aim to compute lattice field theory results for static potentials $V^e_{\Lambda^\epsilon_\eta}(r)$ with quantum numbers $\Lambda^\epsilon_\eta = \Sigma^+_g$ (the ordinary static potential) and $\Lambda^\epsilon_\eta = \Pi_u, \Sigma^-_u$ (the two lowest hybrid static potentials) for all four lattice ensembles $e \in \{A, B, C, D\}$ listed in Table 4.3. We extract the potential values from the large-time behavior of effective potentials, which we define as

$$V^e_{\mathrm{eff};\Lambda^\epsilon_\eta}(r,T) = \frac{1}{2a}\ln\left(\frac{W^e_{\Lambda^\epsilon_\eta}(r,T)}{W^e_{\Lambda^\epsilon_\eta}(r,T+2a)}\right), \tag{4.5}$$

where $W^e_{\Lambda^\epsilon_\eta}(r,T)$ denotes the Wilson loop correlation function (4.2) on ensemble e. We exploit rotational and translational symmetry for calculating $W^e_{\Lambda^\epsilon_\eta}(r,T)$. The calculated temporal extents T are multiples of $2a$, which is a constraint originating in the partitioning for the multilevel algorithm. In the large T limit, the effective potential approaches a plateau,

$$\lim_{T\to\infty} V^e_{\mathrm{eff};\Lambda^\epsilon_\eta}(r,T) = V^e_{\Lambda^\epsilon_\eta}(r)\,, \tag{4.6}$$

which corresponds to the lattice static potential value $V^e_{\Lambda^\epsilon_\eta}$ at quark-antiquark separation r.

The plateaus in the effective potentials are extracted through uncorrelated χ^2 minimizing fits of constants in the range $T'_{\mathrm{min}} \le T \le T'_{\mathrm{max}}$. We employ a fit algorithm inspired by the one used in Ref. [51] to ensure a systematic and consistent extraction of static potentials for each combination of quantum numbers Λ^ϵ_η and quark-antiquark separation r. The fit procedure is described as follows:

1. A lower bound T_{min} is defined as the smallest T where the difference between the consecutive values $aV^e_{\mathrm{eff};\Lambda^\epsilon_\eta}(r,T-2a)$ and $aV^e_{\mathrm{eff};\Lambda^\epsilon_\eta}(r,T)$ is within 1σ.

2. An upper bound T_{max} is defined as the largest T for which the Wilson loop $W^e_{\Lambda^\epsilon_\eta}(r,T+2a)$ is computed, i.e. $T_{\mathrm{max}} = 12a, 20a, 22a, 22a$ for ensembles A, B, C, D, respectively.

3. Fits are performed for all intervals $T'_{\mathrm{min}} \le T \le T'_{\mathrm{max}}$ satisfying:

$$T'_{\mathrm{min}} \ge T_{\mathrm{min}}\,, \qquad T'_{\mathrm{max}} \le T_{\mathrm{max}} \quad \text{and} \qquad T'_{\mathrm{max}} - T'_{\mathrm{min}} \ge 6\,a\,. \tag{4.7}$$

4. The fit yielding the longest plateau with $\chi^2_{\mathrm{red}} \le 1$ is chosen as the final result for

$aV^e_{\Lambda^\epsilon_\eta}(r)$. The reduced χ^2 is computed as

$$\chi^2_{\text{red}} = \frac{2a}{T'_{\text{max}} - T'_{\text{min}}} \sum_{T=T'_{\text{min}},T'_{\text{min}}+2a,\ldots,T'_{\text{max}}} \frac{\left(aV^e_{\text{eff};\Lambda^\epsilon_\eta}(r,T) - aV^e_{\Lambda^\epsilon_\eta}(r)\right)^2}{\left(a\sigma[V^e_{\text{eff};\Lambda^\epsilon_\eta}](r,T)\right)^2}, \tag{4.8}$$

where $a\sigma[V^e_{\text{eff};\Lambda^\epsilon_\eta}](r,T)$ represents the statistical uncertainty of $aV^e_{\text{eff};\Lambda^\epsilon_\eta}(r,T)$.

To confirm the reliability of our results, we numerically validated that the extracted potential results $aV^e_{\Lambda^\epsilon_\eta}(r)$ are stable within statistical errors when the fit range is manually changed to $T'_{\text{min}} + 2a \leq T \leq T'_{\text{max}}$. Figure 4.1 presents exemplary effective potentials $aV^e_{\text{eff};\Lambda^\epsilon_\eta}(r = 4a, T)$ for $\Lambda^\epsilon_\eta = \Sigma^+_g$ and $\Lambda^\epsilon_\eta = \Pi_u, \Sigma^-_u$ and the four different ensembles. The horizontal gray bands indicate the fitted plateau and its statistical error.

The resulting static potentials $V^e_{\Lambda^\epsilon_\eta}(r)$ for $\Lambda^\epsilon_\eta = \Sigma^+_g, \Pi_u, \Sigma^-_u$ and separations $r \geq 1a$ are shown in Figure 4.2 and collected in Table E.1. Due to the self-energy of static quarks, which depends on the lattice spacing a, potentials computed on different ensembles are shifted relative to one another. To enable a meaningful comparison of results across different ensembles in Figure 4.2, we normalize the static potentials by setting $V^e_{\Sigma^+_g}(r = 0.5r_0) = 0$ for $e \in \{A, B, C, D\}$ to compensate for the ensemble-dependent self-energy of the static quarks. $V^e_{\Sigma^+_g}(r = 0.5r_0)$ is computed via a simple interpolation of $V^e_{\Sigma^+_g}(r)$ via the Cornell potential.

In the continuum limit, results from all ensembles should coincide. However, at the current level of statistical precision, discretization effects lead to noticeable deviations between different lattice ensembles for the same physical quark-antiquark separations of the ordinary as well as hybrid static potentials. This effect is illustrated in Figure 4.3 for the ordinary static potential. Here, we show the deviation of $V^e_{\Sigma^+_g}(r) - V^e_{\Sigma^+_g}(r = 0.5r_0)$ from a simple Cornell potential fit $V_{\Sigma^+_g}(r)$. The fact that data points from different ensembles do not lie on top of each other particularly at small r/a illustrates the presence of discretization effects. In Section 4.3, we will discuss how to systematically reduce discretization effects by correcting for discretization errors at tree level and partially proportional to a^2. This approach will allow us to find a parametrization of the static potentials consistent with the continuum limit, which can then directly be used as input for Born-Oppenheimer predictions of heavy hybrid meson masses as previously done in Refs. [14, 15, 17, 18, 29, 30, 36, 51, 98, 99].

Unlike previous lattice studies of hybrid static potentials [27–30, 32, 40, 44, 45, 51], which used lattice spacings $a \gtrsim 0.07\,\text{fm}$, our analysis employs four ensembles with lattice spacings as small as $0.04\,\text{fm}$. Thus, much smaller quark-antiquark separations can be reached. Furthermore, we are able to quantify discretization errors and will eliminate these from the lattice results to a large extent in the next section.

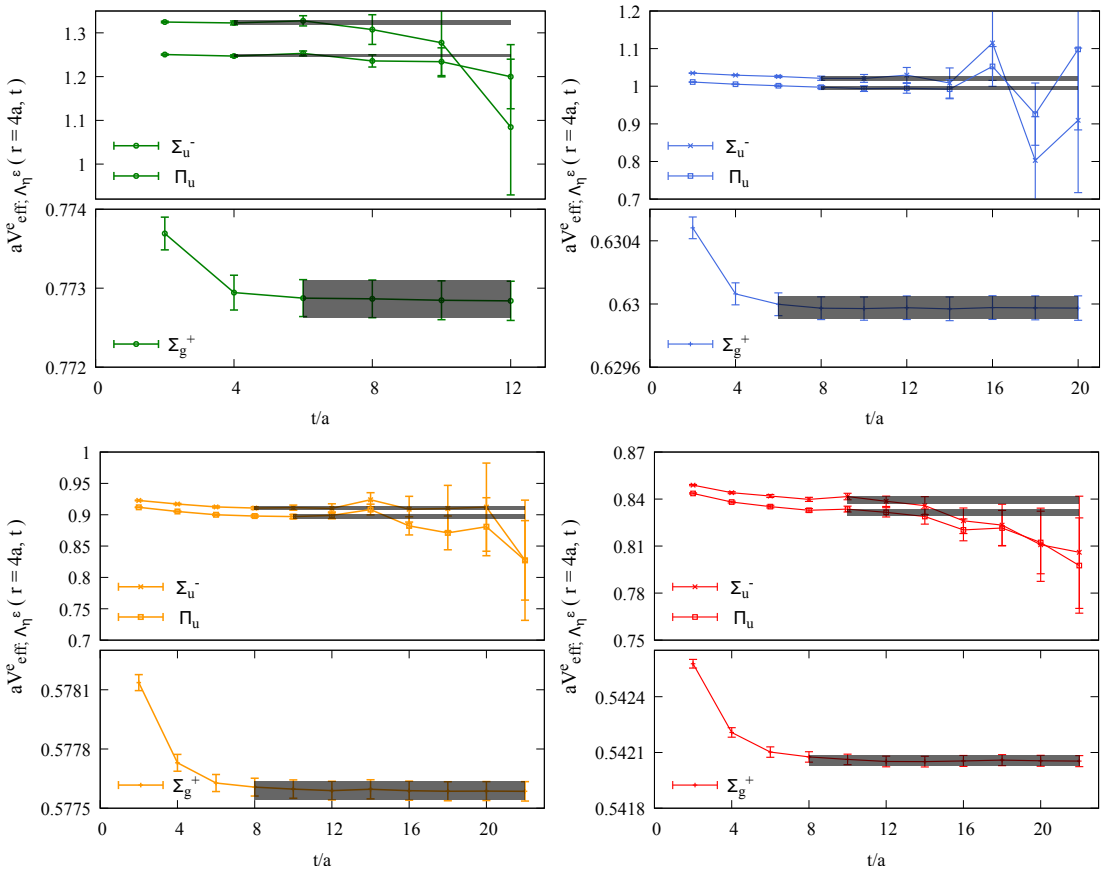

Figure 4.1: Exemplary plots of effective potentials $aV^e_{\text{eff};\Lambda^\epsilon_\eta}(r,t)$ with $\Lambda^\epsilon_\eta = \Sigma_g^+, \Pi_u, \Sigma_u^-$ for $r = 4a$ (Top left: ensemble A; Top right: ensemble B; Bottom left: ensemble C; Bottom right: ensemble D).

4.3 Parametrization

In this section, we aim to obtain continuum-extrapolated results and parametrizations of the ordinary static potential $V_{\Sigma_g^+}(r)$ and the two lowest hybrid static potentials, $V_{\Pi_u}(r)$ and $V_{\Sigma_u^-}(r)$, based on the lattice field theory results computed in the previous section.
A direct approach to achieving continuum results would involve extrapolating individual data points $V^e(r)$ at fixed r to $a = 0$. The resulting extrapolated lattice data points could then be parametrized using a continuous function. However, since our ensembles have very different lattice spacings, the resolution of $V^e(r)$ in r varies across ensembles. Fixing r for the extrapolation in a would require interpolation between data points at neighboring r, introducing possible systematic errors due to interpolation choices. To mitigate this issue, we adopt an alternative approach. This method quantifies lattice discretization errors at tree level in perturbation theory and partially at order a^2, accounts for the a-dependent self-energy and eliminates them from the parametrization. We describe this approach in the following.
First, we add lattice data from Ref. [51] to our set of lattice data to extend the range

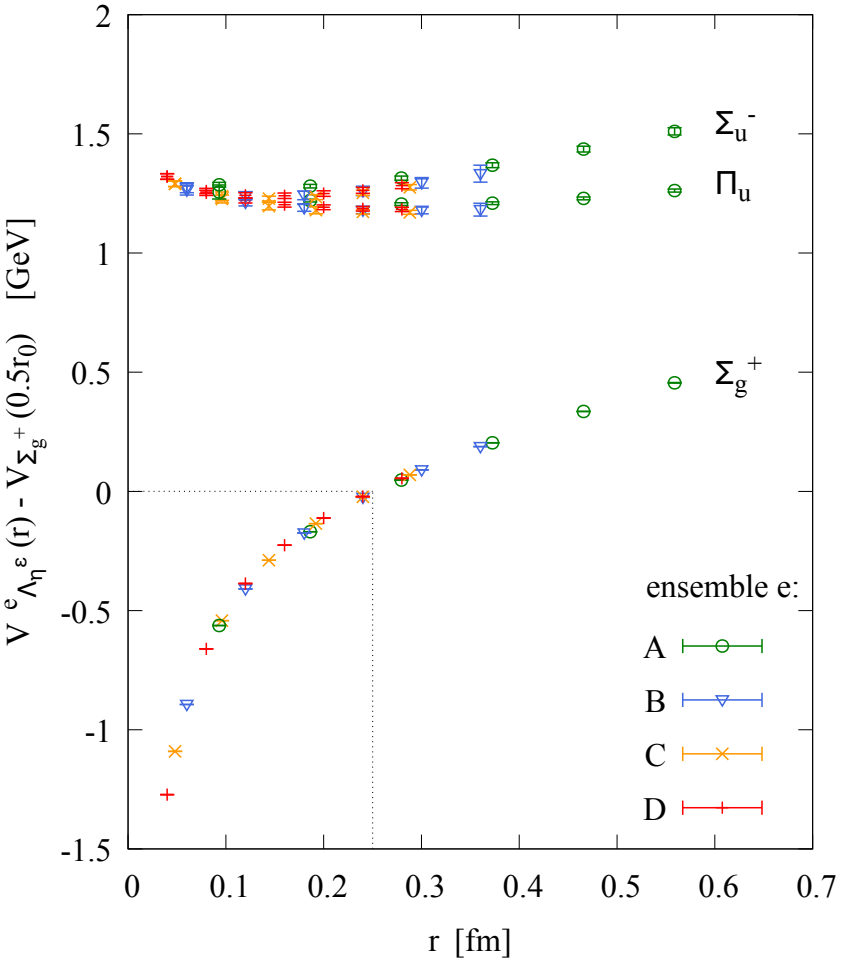

Figure 4.2: SU(3) lattice field theory results for the ordinary static potential Σ_g^+ and the hybrid static potentials Π_u and Σ_u^- from the four ensembles $e \in \{A, B, C, D\}$.

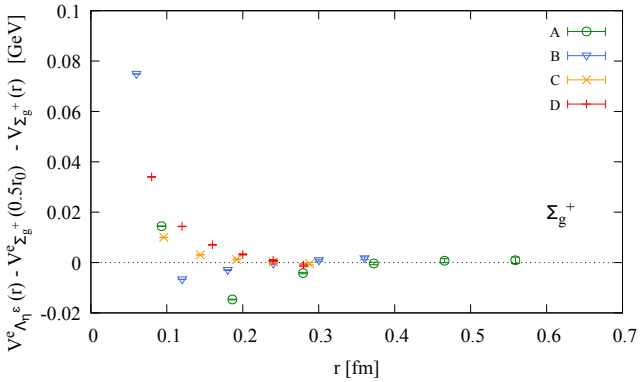

Figure 4.3: Visualization of lattice discretization errors in the lattice data for Σ_g^+. $V_{\Sigma_g^+}(r)$ as defined in Eq. (4.9) and fitted to $r > 0.2\,\mathrm{fm}$ is subtracted from the lattice data.

of available quark-antiquark separations to $0.19\,\text{fm} \lesssim r \lesssim 1.12\,\text{fm}$. This additional dataset, labeled A^{HYP2}, was obtained on a lattice volume of $(L/a)^3 \times T/a = 24^3 \times 48$ with a lattice spacing of $a = 0.093\,\text{fm}$, matching that of our ensemble A (see Table 4.3). The results were computed in Ref. [51] using HYP2-smeared temporal links, which significantly reduce the self-energy and lead to smaller statistical errors, though at the cost of increased discretization effects at small r/a. Consequently, our dataset consists of lattice results from five ensembles, $e \in \{A, B, C, D, A^{\text{HYP2}}\}$, including separations $0.04\,\text{fm} \leq r \leq 1.12\,\text{fm}$.
We now derive the parametrizations used to fit our lattice data. We begin with the ordinary static potential Σ_g^+. It is known that the Cornell ansatz

$$V_{\Sigma_g^+}(r) = -\frac{\alpha}{r} + \sigma r \tag{4.9}$$

describes the ordinary static potential for $r \gtrsim 0.2\,\text{fm}$ in the continuum (see e.g. Ref. [113]). The parameters α and σ related to the strong coupling constant and the string tension, respectively, are determined via a fit to our lattice data. To match the lattice results, the fit function must account for the self-energy of the static quark-antiquark pair, which appears as an unphysical offset in the static potentials. Since the self-energy depends on the discretization of the static action and the lattice spacing a, an ensemble-dependent constant term C^e is included in the fit.
As observed in Figure 4.3, the lattice results for the static potentials from the five ensembles are not consistent with a single curve. These deviations are attributed to lattice artifacts, which can be estimated by comparing the lattice Green's function to its continuum counterpart at tree level in perturbation theory, as discussed in Section 2.6.4. We use the so-called V-method (see Section 2.6.4 and Refs. [56, 65]) to account for discretization effects at tree-level by incorporating an additional correction term

$$\Delta V_{\Sigma_g^+}^{\text{lat},e}(r) = \alpha' \left(\frac{1}{r} - \frac{G^e(r/a)}{a} \right), \tag{4.10}$$

where α' is a fit parameter related to the strong coupling constant and G^e is the lattice propagator as defined in Section 2.6.4. Since the lattice propagator depends on the discretization of the static action used to generate the ensemble, it differs between ensembles with and without HYP2-smearing.
Consequently, the final 8-parameter fit function describing our lattice data for Σ_g^+ is given by

$$V_{\Sigma_g^+}^{\text{fit},e}(r) = V_{\Sigma_g^+}(r) + C^e + \Delta V_{\Sigma_g^+}^{\text{lat},e}(r) \tag{4.11}$$

$$= -\frac{\alpha}{r} + \sigma r + C^e + \alpha' \left(\frac{1}{r} - \frac{G^e(r/a)}{a} \right). \tag{4.12}$$

Similarly, based on a prediction of pNRQCD for the hybrid static potentials [14] (see Chapter 3), a physical meaningful description of the hybrid static potentials Π_u and Σ_u^-

already proposed in Ref. [51] is given by

$$V_{\Pi_u}(r) = \frac{A_1}{r} + A_2 + A_3 r^2 \tag{4.13}$$

$$V_{\Sigma_u^-}(r) = \frac{A_1}{r} + A_2 + A_3 r^2 + \frac{B_1 r^2}{1 + B_2 r + B_3 r^2}\,. \tag{4.14}$$

This ansatz captures the degeneracy of Π_u and Σ_u^- at $r \to 0$ and their repulsive behavior at short distances expected from the perturbative octet potential. Inspired by the multipole expansion of pNRQCD, quadratic corrections in r are incorporated with different parameters for Π_u and Σ_u^-. In Ref. [51], it was found that Σ_u^- is best described for intermediate separations through an additional term with parameters B_1, B_2 and B_3. For even larger r than the separations considered in this work, one expects a linear string-like behavior in the hybrid static potentials [112, 114].

Self-energy and tree-level lattice artifacts affect both hybrid and ordinary static potentials. As discussed in Section 2.6.4, discretization artifacts at tree level in hybrid static potentials are similar to those in the ordinary static potential up to a factor of $-1/8$. Thus, we include the correction term

$$\Delta V_{\text{hybrid}}^{\text{lat},e}(r) = -\frac{1}{8}\Delta V_{\Sigma_g^+}^{\text{lat},e}(r) = -\frac{\alpha'}{8}\left(\frac{1}{r} - \frac{G^e(r/a)}{a}\right), \tag{4.15}$$

into the fit function. The self-energy constant C^e is also incorporated. Since the Σ_g^+ lattice data has smaller statistical errors due to its lower energy, we determine the parameters C^e and α' in the fit to the ordinary static potential.

Moreover, each parameter exhibits a dependence on the lattice spacing. Within the current precision, the lattice spacing dependence is most noticeable in A_2 due to a small ensemble dependent offset particularly prominent at large a in the lattice data, see Figure 4.2. To account for this, we introduce an additional term $A'^e_{2,\Lambda_\eta^\epsilon} a^2$. The new parameter differs for the Π_u and Σ_u^- hybrid static potentials and varies based on whether HYP2-smeared temporal links are used. However, it remains the same across different lattice spacings. Thus, we have $A'^A_{2,\Pi_u} = A'^B_{2,\Pi_u} = A'^C_{2,\Pi_u} = A'^D_{2,\Pi_u}$ and $A'^A_{2,\Sigma_u^-} = A'^B_{2,\Sigma_u^-} = A'^C_{2,\Sigma_u^-} = A'^D_{2,\Sigma_u^-}$.

Finally, the fit functions describing the lattice data of the hybrid static potentials Π_u and Σ_u^- are given by

$$V_{\Pi_u}^{\text{fit},e}(r) = V_{\Pi_u}(r) + C^e + \Delta V_{\text{hybrid}}^{\text{lat},e}(r) + A'^e_{2,\Pi_u} a^2 \tag{4.16}$$

$$V_{\Sigma_u^-}^{\text{fit},e}(r) = V_{\Sigma_u^-}(r) + C^e + \Delta V_{\text{hybrid}}^{\text{lat},e}(r) + A'^e_{2,\Sigma_u^-} a^2\,, \tag{4.17}$$

which includes 10 fit parameters.

The parametrization strategy is as follows: First, we perform an 8-parameter uncorrelated χ^2-minimizing fit of $V_{\Sigma_g^+}^{\text{fit},e}(r)$ (4.12) using all lattice data points $V_{\Sigma_g^+}^e(r)$ from the five ensembles $e \in \{A, B, C, D, A^{\text{HYP2}}\}$ with $0.2\,\text{fm} \leq r$. The primary purpose of this fit is to accurately determine the parameters C^e and α'. The resulting parameters can be

α [GeV fm]	σ [GeV/fm]	α' [GeV fm]	χ^2_{red}
0.0571(4)	1.064(4)	0.0735(23)	0.7

	A_1 [GeV fm]	A_2 [GeV]	A_3 [GeV fm^2]	B_1 [GeV fm^2]	B_2 [fm^{-1}]	B_3 [fm^{-2}]	χ^2_{red}
Fit 1	0.0124(9)	1.135(8)	0.372(7)	1.56(15)	1.2(3)	2.1(2)	1.2
Fit 2	0.0147(18)	1.126(11)	0.381(7)	1.57(17)	1.0(4)	2.3(2)	0.8
Fit 3	0.0065(16)	1.190(14)	−0.092(91)	1.15(4)	-	-	0.5

		Fit 1		Fit 2		Fit 3		
ensemble	C^e [GeV]	A'^e_{2,Π_u}	A'^e_{2,Σ_u^-}	A'^e_{2,Π_u}	A'^e_{2,Σ_u^-}	A'^e_{2,Π_u}	A'^e_{2,Σ_u^-}	[GeV/fm^2]
A	1.398(2)	3.1(7)	6.7(8)	3.0(9)	6.5(9)	3.4(8)	5.7(9)	
B	2.059(2)							
C	2.472(2)							
D	2.862(2)							
A^{HYP2}	0.340(2)	1.0(7)	5.0(5)	0.9(9)	4.7(9)	1.6(7)	4.4(6)	

Table 4.5: Resulting fit parameters. Fit 1 and Fit 2 correspond to the parametrizations (4.13) and (4.14) and fit ranges $2a \leq r$ and $3a \leq r$, respectively. Fit 3 corresponds to the parametrizations (4.13) and (4.14) with $B_2 = B_3 = 0$ and fit range $2a \leq r \leq 0.3\,\text{fm}$, where $A_{3,\Pi_u} = A_3$ and $A_{3,\Sigma_u^-} = A_3 + B_1$.

found in Table 4.5. $\alpha = 0.289(2) = 0.0571(4)\,\text{GeV fm}$ and $\sigma = 1.064(4)\,\text{GeV/fm}$ are in reasonable agreement with results from the literature [115]. In a second step, we perform a 10-parameter uncorrelated χ^2 minimizing fit of $V^{\text{fit},e}_{\Pi_u}(r)$ (4.16) and $V^{\text{fit},e}_{\Sigma_u^-}(r)$ (4.17) simultaneously to both hybrid static potentials $V^e_{\Pi_u}(r)$ and $V^e_{\Sigma_u^-}(r)$ from all five ensembles $e \in \{A, B, C, D, A^{\text{HYP2}}\}$. The resulting parameters can also be found in Table 4.5. Finally, we can define improved lattice data points via

$$\tilde{V}^e_{\Sigma_g^+}(r) = V^e_{\Sigma_g^+}(r) - C^e - \Delta V^{\text{lat},e}_{\Sigma_g^+}(r), \tag{4.18}$$

$$\tilde{V}^e_{\Lambda_\eta^\epsilon}(r) = V^e_{\Lambda_\eta^\epsilon}(r) - C^e - \Delta V^{\text{lat},e}_{\text{hybrid}}(r) - A'^e_{2,\Lambda_\eta^\epsilon} a^2\,, \tag{4.19}$$

where the discretization errors and the self-energy are subtracted. The improved lattice data is collected in Table E.2. We present the parametrizations alongside the improved data points in Figure 4.4.

The main result for the parametrizations is obtained from a fit to separations $r \geq 2a$ (Fit 1). The inclusion of data at $r = 2a$ is crucial for constraining the short-range behavior ($r \lesssim 0.15\,\text{fm}$), while the long-range behavior remains stable even when restricting the data to $r \geq 3a$ (Fit 2). However, data at $r = 1a$ is excluded, as it may be affected by discretization errors that cannot be fully corrected through tree-level improvement.

At small separations, the lattice results clearly exhibit the repulsive behavior predicted by perturbation theory and indicate the expected degeneracy. To further investigate the short-distance behavior, we additionally restrict the fit to $2a \leq r \leq 0.3\,\text{fm}$ and set $B_2 = B_3 = 0$

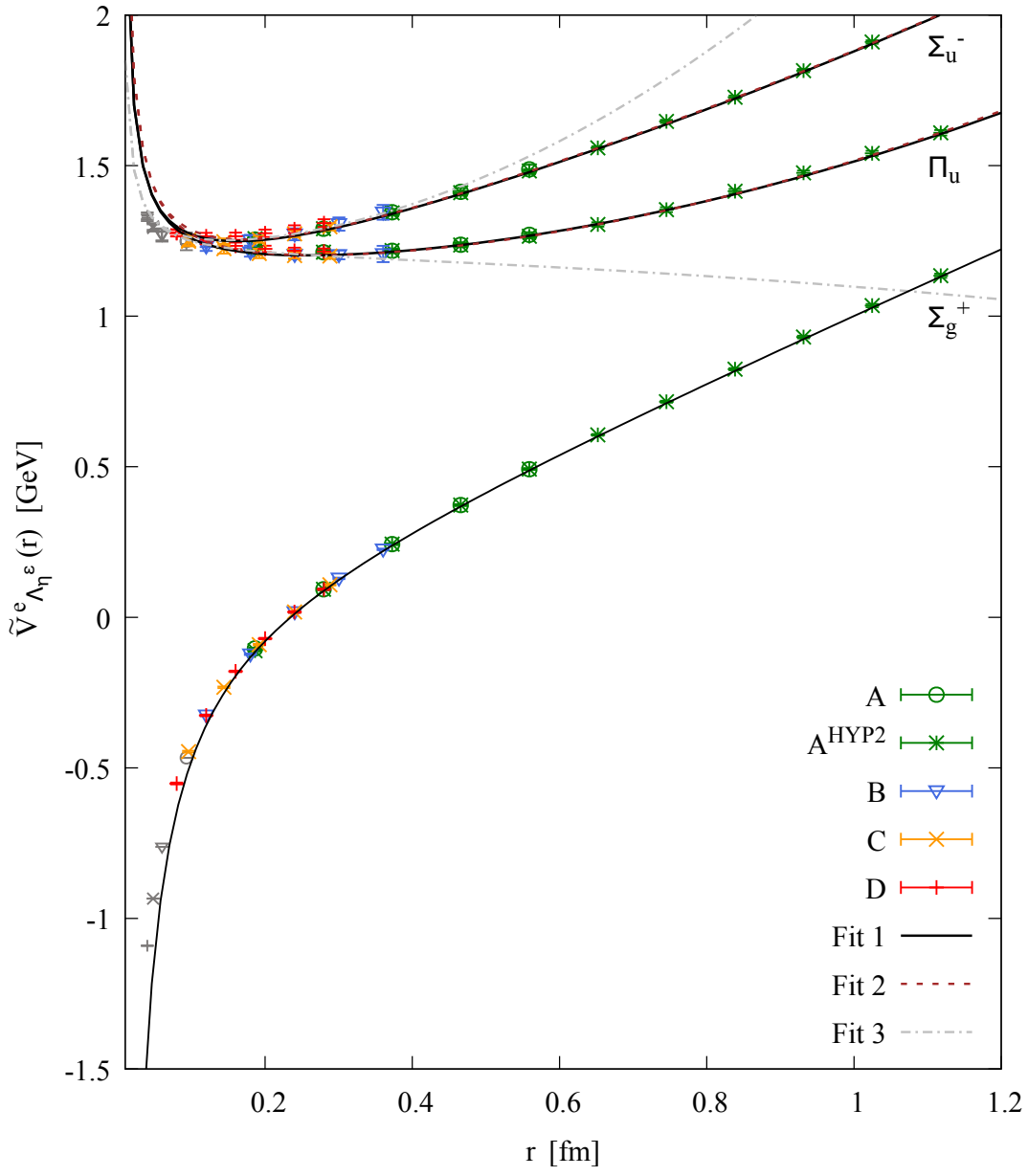

Figure 4.4: Lattice data points $\tilde{V}^e_{\Lambda_\eta^\epsilon}(r)$ in GeV and corresponding parametrizations (4.9),(4.13) and (4.14) as functions of the quark-antiquark separation r in fm. The colors green, blue, yellow and red indicate different lattice spacings $a = 0.093\,\text{fm}$, $a = 0.060\,\text{fm}$, $a = 0.048\,\text{fm}$ and $a = 0.040\,\text{fm}$. Data points $\tilde{V}^e_{\Lambda_\eta^\epsilon}(r = 1a)$ are shown in gray as they are excluded from all fits.

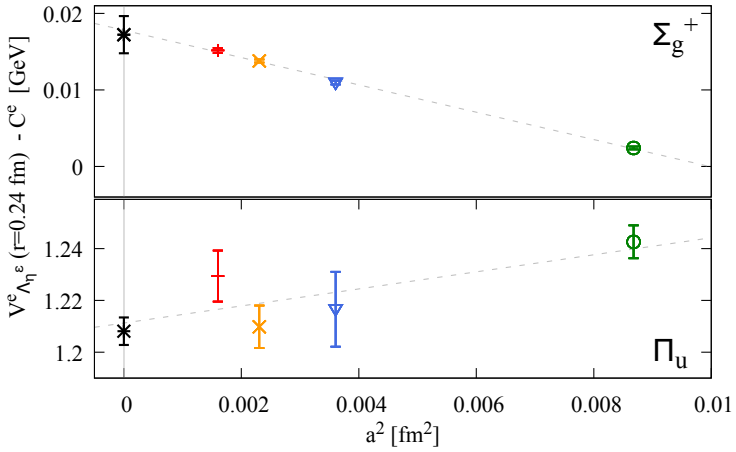

Figure 4.5: Continuum extrapolations linear in a^2 using lattice data $V^e_{\Lambda^\epsilon_\eta}(r = 0.24\,\text{fm}) - C^e$, $e = A, B, C, D$ for $\Lambda^\epsilon_\eta = \Sigma_g^+$ (top) and $\Lambda^\epsilon_\eta = \Pi_u$ (bottom). The results are consistent with the parametrizations (4.9) and (4.13) with parameters corresponding to Fit 1 as listed in Table 4.5 (the black points).

(Fit 3) to align with the pNRQCD prediction. The pNRQCD parameter proportional to r^2 in the multipole expansion, corresponds to A_3 in Eq. (4.13) for Π_u and $A_3 + B_1$ in Eq. (4.14) for Σ_u^-. This fit results in a significantly smaller coefficient for the repulsive $1/r$ term, $A_1 = 0.0065(16)$ GeV fm (see Table 4.5), in agreement with Refs. [14, 15]. Although the data points at $r = 1a$ should be treated with caution, they align well with the parametrization of Fit 3.

In Ref. [116] the lattice data for Π_u from Ref. [40] was parametrized using a similar fit function as Eq. (4.13) yielding $A_1 = 0.022\,\text{GeV fm}$, which is also larger than our results for A_1 from Fit 1. Our value for A_1 agrees with the results from Refs. [14, 15]. Specifically, in Ref. [15], the $1/r$-coefficient was fixed to $\alpha/8$ following the perturbative prediction. α was determined by fitting a Cornell potential similar to Eq. (4.9) to Σ_g^+ lattice data from Ref. [40] in the range $0.2\,\text{fm} \leq r \leq 2.4\,\text{fm}$. The resulting $1/r$-coefficient for the hybrid potentials, $0.012\,\text{GeV fm}$, aligns with our fit results for the parameter A_1 for Fit 1 and Fit 2. Ref. [14] determined the $1/r$-coefficient to be $\approx 0.01\,\text{GeV fm}$ based on the perturbative octet potential computed in the Renormalon Subtraction scheme up to α_s^3. This value is within the range of our fit results for A_1.

The parametrization strategy effectively removes discretization errors and self-energy contributions, producing a result equivalent to a continuum extrapolation, which is confirmed by Figure 4.5. Here, we present data points $V^e_{\Lambda^\epsilon_\eta}(r) - C^e$, where only the ensemble dependent self-energy is subtracted, at an exemplary separation $r = 0.24\,\text{fm}$ as a function of the squared lattice spacing a^2. Note that we only have lattice data at this specific r for ensembles B, C and D such that we need an interpolating function for data points $V^A_{\Lambda^\epsilon_\eta}(r)$ close to $r = 0.24\,\text{fm}$. The data points show a linear behavior in a^2 and when extrapolated to $a = 0$ coincide with the parametrization $V_{\Lambda^\epsilon_\eta}(r = 0.24\,\text{fm})$ (shown at $a = 0$ in Figure

4.5). The agreement confirms that our strategy to account for discretization errors to a large extent in the parametrizations (4.12), (4.16) and (4.17) is successful and superior to a naive continuum limit. In Refs. [56, 94] it was also shown that tree-level improvement via the subtraction of $\Delta V_{\Sigma_g^+}^{\mathrm{lat},e}(r)$ is preferable to the introduction of an improved separation $r \to r_{\mathrm{impr}}$ (see the discussion in Section 2.6.4).

4.4 Exclusion of systematic effects

In addition to discretization errors addressed in the previous section, we aim to exclude other possible sources of systematic errors from our precise hybrid static potential data and parametrizations. This section focuses on excluding systematic effects arising from topological freezing, the finite lattice volume and glueball decay. This discussion was previously published in Refs. [53–55, 117].

4.4.1 Topological freezing

To exclude volume effects in our results and avoid unreliable error analysis due to topological freezing and long autocorrelation times in the sets of gauge link configurations, we investigate the topological charge and the topological susceptibility.

We compute the topological charge history for the four lattice ensembles $e \in \{A, B, C, D\}$ used in this work, employing the field strength definition of the lattice topological charge with the clover-leaf discretization (see Section 2.6.2). For this purpose, we apply four-dimensional APE smearing, similar to the three-dimensional version used for static potential operators (see Section 2.4.1), with a smearing parameter of $\alpha_{\mathrm{APE}} = 0.3$. The number of smearing iterations is adapted to each lattice spacing to ensure that the topological charge Q stabilizes across multiple smearing steps for most gauge link configurations. Figure 4.6a illustrates the Monte Carlo histories of the topological charge for a subset of gauge configurations from ensembles B ($a = 0.06\,\mathrm{fm}$) and D ($a = 0.04\,\mathrm{fm}$). For $a = 0.06\,\mathrm{fm}$, the topological charge fluctuates frequently, indicating no issue with topological freezing. However, for $a = 0.04\,\mathrm{fm}$, the autocorrelation time of Q is significantly longer, consistent with expectations for smaller lattice spacings (see e.g. Ref. [82]). Despite this, there are sufficient changes in Q to ensure that our statistical error analysis, which involves four independent simulation runs and appropriate binning, yields reliable uncertainties for the observables.

Figure 4.6b presents normalized and symmetrized histograms of the topological charge distribution for ensembles B and D. Both distributions align well with a Gaussian shape, as expected for large, finite spacetime volumes. From their squared widths, $\langle Q^2 \rangle$, we estimate the corresponding topological susceptibilities via $\chi_{\mathrm{top}} = \langle Q^2 \rangle / V$, which provides insight into whether the topological charge sectors are adequately sampled. The results for all four ensembles agree with literature values [118], further indicating that topological freezing does not affect our computations.

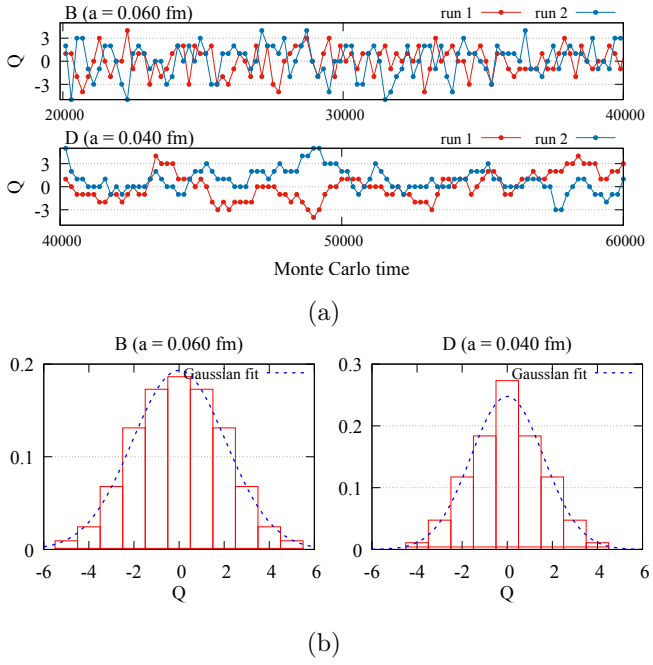

Figure 4.6: (a) Monte Carlo histories of the topological charge for ensemble B ($a = 0.06\,\text{fm}$) and D ($a = 0.04\,\text{fm}$) for two independent simulation runs. (b) Normalized and symmetrized histograms reflecting the topological charge distribution for ensemble B and ensemble D.

4.4.2 Finite volume corrections

The gauge link ensembles employed in the calculation have a finite spacetime volume of $L^3 \approx (1.2\,\text{fm})^3$. Given the relatively small volume, it is curcial to verify that finite volume corrections do not significantly impact these results. Previous studies in SU(2) (see Section 2.6.3) have shown that for $L \ll 1.0\,\text{fm}$, static potential results are systematically shifted. In the case of ordinary static potentials, glueball interactions across the periodic lattice induce a slight negative shift. For the larger hybrid states, however, wave function squeezing inside the finite lattice volume is expected to become the dominant effect in small lattice volumes, leading to a significant positive shift in the static potential. For our SU(3) gauge link ensembles, we compared lattice data for the difference between static potentials at a fixed separation, $(V_{\Pi_u}(0.25\,\text{fm}) - V_{\Sigma_g^+}(0.25\,\text{fm}))$, from ensemble A with lattice spacing $a = 0.093\,\text{fm}$ with results from a similar computation performed with a larger spatial lattice extent, i.e. $L = 2.4\,\text{fm}$. As shown in Figure 4.7, no statistically significant deviations were observed. The figure also presents data points from the other ensembles, reinforcing this conclusion. Overall, our analyses indicate that finite volume corrections at the chosen spacetime volume $L^3 \times T \approx (1.2\,\text{fm})^3 \times 2.4\,\text{fm}$ are negligible compared to current statistical uncertainties.

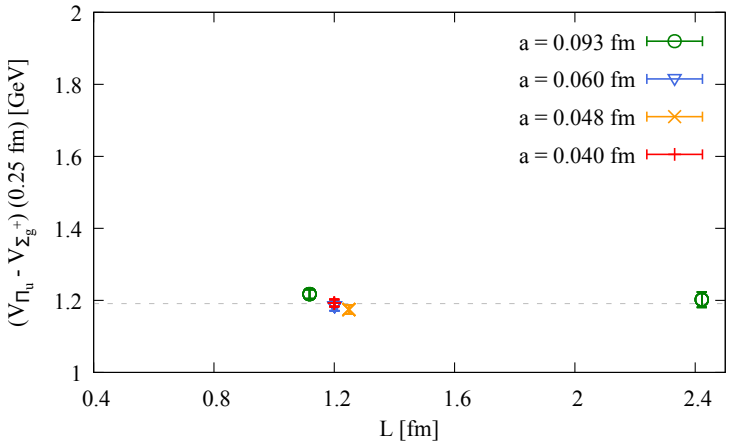

Figure 4.7: $(V_{\Pi_u}(0.25\,\mathrm{fm}) - V_{\Sigma_g^+}(0.25\,\mathrm{fm}))$ as function of the spatial lattice extent L for gauge group SU(3).

4.4.3 Glueball decay

For each hybrid state, we compute a single operator. We assume that its ground-state overlap with the hybrid state with quantum numbers Λ_η^ϵ is sufficiently large for the extracted effective potential plateau to correspond to the ground-state energy of the hybrid static potential. However, in principle, this operator may also overlap with other states sharing the same quantum numbers, such as the scattering state of a glueball and the Σ_g^+ ground-state flux tube.

Given the energy gap of $\approx 1000\,\mathrm{MeV}$ between hybrid and ordinary quarkonium, several multiparticle states are lighter than the hybrid ground states. In pure gauge theory, such scattering states are limited to multiparticle states involving a non-excited flux tube and relatively heavy glueballs. In contrast, including dynamical light quarks introduces additional multiparticle states involving quarkonium and pions with Σ_u^- and $\Pi_u^\pm$ quantum numbers, which are lighter than the ground states $|0, \Sigma_u^-\rangle$ and $|0, \Pi_u^\pm\rangle$ in the pure SU(3) gauge theory. Resolving these states in a lattice QCD computation would be highly challenging. Conversely, neglecting their effects also introduces systematic errors, which might be larger than those arising from a calculation, where light dynamical quarks are ignored but a rigorouos ground state extraction is possible. In the following section, we discuss cases in pure SU(3) gauge theory where the extracted ground state may be contaminated by scattering states.

The hybrid flux tube can decay into a glueball and the Σ_g^+ ground state when the energy difference to the ordinary static potential is sufficiently large. This occurs at small separations r where the ordinary static potential is attractive while the hybrid static potential is repulsive. This is illustrated in Figure 4.8, where we plot the lightest glueball mass ($m_{0^{++}} = 1.73(5)\,\mathrm{GeV}$ [89]) plus the Σ_g^+ ground state as a function of separation alongside hybrid static potentials up to $\Lambda = 2$ from Ref. [51]. The critical separation $r_{\mathrm{crit}}^{\Lambda_\eta^\epsilon}$ is defined

as the point where this energy intersects with the hybrid static potentials, which marks the threshold below which a decay is energetically allowed. The critical separations have been previously discussed in Refs. [53, 55, 117] and are listed in Table 4.6.

However, such decays may be restricted due to quantum number constraints. A thorough and general analysis of selection rules for both hybrid states and tetraquarks is provided in Ref. [108]. Here, we specifically examine hybrid static potentials characterized by quantum numbers Λ_η^ϵ and assess whether transitions to the Σ_g^+ ground state accompanied by a $J^{PC} = 0^{++}$ glueball are possible.

Since the glueball under consideration has total angular momentum $J = 0$, its angular momentum projection along the z-axis must also be zero, i.e., $J_z = 0$. Consequently, the glueball's orbital angular momentum component along the quark-antiquark separation axis (the z-direction) must satisfy $L_z = \Lambda$. The quantum number η does not restrict the glueball, as its distribution along the z-direction can be either symmetric ($\eta = g$) or antisymmetric ($\eta = u$).

In contrast, the quantum number ϵ introduces an important restriction. The 0^{++} glueball is symmetric under a $\mathcal{P}_x$ transformation. When $L_z = \Lambda = \Sigma = 0$, its orbital angular momentum wave function is also symmetric, meaning that scattering states with $\epsilon = -$ are impossible. As a result, decays involving a 0^{++} glueball are forbidden for Σ_u^- and Σ_g^-. For cases where $L_z = \Lambda > 0$, the glueball's wave function can either be symmetric or antisymmetric such that transitions are allowed for all other hybrid flux tubes.

Decays involving heavier glueballs with quantum numbers $J^{PC} \neq 0^{++}$ are possible in certain cases, particularly when the glueball wave functions are antisymmetric with respect to $\mathcal{P}_x$. However, these decays are only energetically viable at much smaller separations than those listed in Table 4.6, making them irrelevant to our analysis.

In Sections 4.2 and 4.3, we have presented and utilized lattice results for separations down to $r = 0.04\,\text{fm}$. Since the critical separation for Π_u is $r_{\text{crit}}^{\Pi_u} = 0.11\,\text{fm}$, results for this state at smaller separations might, in principle, be affected by mixing with a Σ_g^+ plus glueball scattering state. However, as shown in Figure 4.4, the Π_u hybrid static potential exhibits the expected upward curvature. Furthermore, at small separations, the Π_u and Σ_u^- hybrid static potentials converge, consistent with the anticipated degeneracy in the limit $r \to 0$. These observations indicate that any possible contamination in the Π_u hybrid static potential is negligible compared to the statistical uncertainties.

Λ_η^ϵ	Π_u	Π_g	Δ_g	Δ_u	$\Sigma_g^{+\prime}$	Σ_u^+	Σ_u^-	Σ_g^-
$r_{\text{crit}}^{\Lambda_\eta^\epsilon}$ [fm]	0.11	0.23	0.28	0.58	0.19	0.46	0.11	0.3

Table 4.6: Maximal separation $r_{\text{crit}}^{\Lambda_\eta^\epsilon}$, where a decay of a Λ_η^ϵ hybrid flux tube into the Σ_g^+ ground state and a 0^{++} glueball is energetically possible. For Σ_u^- and Σ_g^-, such decays are excluded because of quantum numbers.

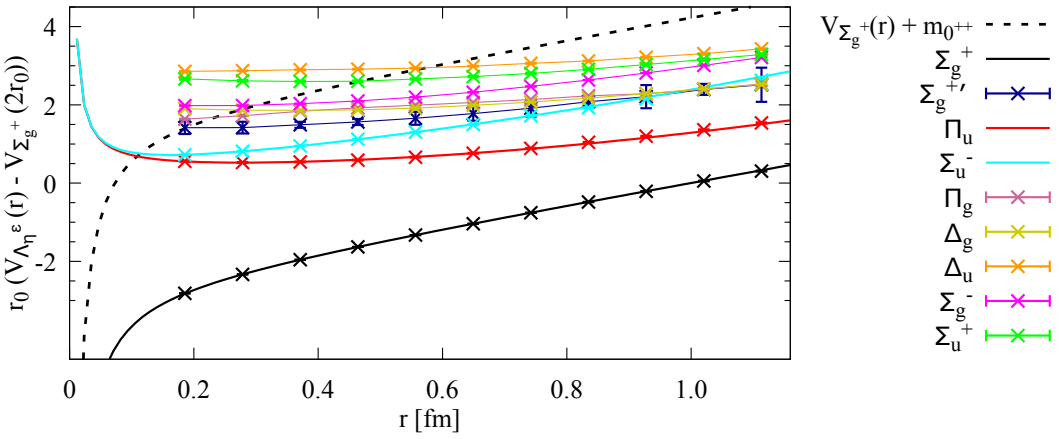

Figure 4.8: Threshold energy for decays of hybrid flux tubes into the Σ_g^+ ground state and a 0^{++} glueball (dashed line) and hybrid static potentials for various quantum numbers Λ_η^ϵ. Static potentials are taken from Ref. [51], the 0^{++} glueball mass from Ref. [89].

4.5 Hybrid meson masses in the Born-Oppenheimer approximation

The primary objective of this chapter is to obtain precise hybrid static potential data and parametrizations, which provide valuable insight into the gluonic energy in the presence of a static quark-antiquark pair. This was addressed in the previous sections. However, the ultimate aim is a comparison of theoretical mass predictions with experiments. Hybrid meson masses can be obtained by solving Schrödinger-like equations, which, as outlined in Section 3.2, can be systematically derived within BOEFT at different orders in the heavy-quark mass expansion. At leading order, this approach corresponds to the Born-Oppenheimer approximation [96], initially used for diatomic molecules, where the motion of the heavy quark and antiquark in a hybrid meson is treated within the static energy of the excited gluon field. The hybrid potentials play a crucial role as input for these differential equations, ultimately solved for the heavy hybrid meson spectrum.
In this section, we investigate how our improved hybrid static potential results impact the prediction of heavy hybrid meson masses. Specifically, we solve the leading-order Schrödinger equations within the BOEFT framework, employing the common simplifying Born-Oppenheimer approximation. The Born-Oppenheimer approximation has been extensively used in the literature [29, 36, 99, 107]. While this provides an initial estimate of the mass spectrum, a more precise determination requires corrections beyond leading order. These refinements involve coupled channels and higher-order potentials in the $1/m_Q$ expansion, including spin-dependent contributions, which will be computed in Chapter 6. More advanced Schrödinger-like equations incorporating mixing and spin effects have been solved recently in Refs. [14, 15, 17, 18, 23]. Our analysis in this section highlights the im-

portance of accurate lattice data for reliable heavy hybrid meson mass calculations.

To compute the masses of heavy hybrid mesons containing either $b\bar{b}$ or $c\bar{c}$ quark pairs, we use the BOEFT at leading order in $1/m_Q$, adopting the single-channel approximation, which neglects the mixing between different static potential sectors. This follows the approach of a previous work [51], where hybrid meson masses were obtained using a parametrization based on the hybrid static potential lattice data from ensemble A^{HYP2} (for details on this ensemble see Section 4.3). By following the same methodology, we can directly assess the impact of our improved hybrid static potential results on mass predictions.

At leading order in the BOEFT and within the single-channel approximation, the radial Schrödinger equation is given by

$$\left(-\frac{1}{2\mu}\frac{d^2}{dr^2} + \frac{L(L+1) - 2\Lambda^2 + \kappa(\kappa+1)}{2\mu r^2} + V_{\Lambda_\eta^\epsilon}(r) \right) u_{\Lambda_\eta^\epsilon;L,n}(r) \quad = \quad E_{\Lambda_\eta^\epsilon;L,n} u_{\Lambda_\eta^\epsilon;L,n}(r), \tag{4.20}$$

where $\mu = m_{\bar{Q}} m_Q/(m_{\bar{Q}} + m_Q)$ is the reduced mass of the heavy $\bar{Q}Q$ pair. The total angular momentum excluding the heavy quark pair spin $\mathbf{S}_{\bar{Q}Q}$ is denoted by $\mathbf{L}$, with $L \in \{\Lambda, \Lambda+1, \ldots\}$. So the total angular momentum of the meson is $\mathbf{J} = \mathbf{L} + \mathbf{S}_{\bar{Q}Q}$. κ represents the gluon spin quantum number of the associated gluelump, which corresponds to the $r \to 0$ limit of the specific hybrid static potential Λ_η^ϵ. For Π_u and Σ_u^-, it is given by $\kappa = 1$. The wave function of the relative coordinate of the $\bar{Q}Q$ pair is $\psi_{\Lambda_\eta^\epsilon;L,n,m_L}(r,\vartheta,\varphi) = (u_{\Lambda_\eta^\epsilon;L,n}(r)/r) Y_{L,m_L}(\vartheta,\varphi)$. The static potential $V_{\Lambda_\eta^\epsilon}(r)$ corresponds to one of our parametrizations (4.9), (4.13) or (4.14) with parameters listed as Fit 1 in Table 4.5. We use quark model values for the charm and bottom quark masses, $m_c = 1628\,\mathrm{MeV}$ and $m_b = 4977\,\mathrm{MeV}$ [97].

We numerically solve the Schrödinger equation using standard methods, specifically a fourth-order Runge-Kutta shooting method combined with Newton's root-finding method. To eliminate the unphysical offset inherent in the energy levels, we subtract the lowest energy level computed with the ordinary static potential, $E_{\Lambda_\eta^\epsilon=\Sigma_g^+;n=1,L=0}$, and add the associated spin-averaged mass of the lightest quarkonium from experiment, $\overline{m} = (m_{\eta_c(1S),\mathrm{exp}} + 3m_{J/\Psi(1S),\mathrm{exp}})/4 = 3.069(1)\,\mathrm{GeV}$ for $\bar{c}c$ or $\overline{m} = (m_{\eta_b(1S),\mathrm{exp}} + 3m_{\Upsilon(1S),\mathrm{exp}})/4 = 9.445(1)\,\mathrm{GeV}$ for $\bar{b}b$ [119], i.e.

$$m_{\Lambda_\eta^\epsilon;L,n} \quad = \quad E_{\Lambda_\eta^\epsilon;L,n} - E_{\Lambda_\eta^\epsilon=\Sigma_g^+;n=1,L=0} + \overline{m}\,. \tag{4.21}$$

Alternatively, the renormalized mass of the associated gluelump can also be utilized to determine the absolute value of the static potentials and, consequently, the energy levels. Ref. [14] employed the gluelump mass in the Renormalon Subtraction (RS) scheme at a scale of 1 GeV, specifically $\Lambda_B^{\mathrm{RS}}(\nu_f = 2.5/r_0 \approx 1\,\mathrm{GeV})$. In Chapter 5, we will provide an updated estimate of this quantity based on more precise lattice data.

The computed energy levels $m_{\Lambda_\eta^\epsilon;L,n}$ correspond to spin multiplets of heavy hybrid mesons, with associated quantum numbers J^{PC} are discussed in Section 3.2. The final mass results

are listed in Table 4.7 and can be directly compared to Ref. [51].

We find that the obtained mass values are lower by $\mathcal{O}(10\ldots45\,\text{MeV})$ than those from our previous results in Ref. [51]. These deviations are comparable in magnitude to the term $A'^e_{2,\Lambda_\eta^\epsilon} a^2$, which is, evaluated for $e = A^{\text{HYP2}}$, 43(4) MeV for $\Lambda_\eta^\epsilon = \Sigma_u^-$ and 9(6) MeV for $\Lambda_\eta^\epsilon = \Pi_u$. This term represents parts of the lattice discretization errors, which we systematically assessed through static potential data at multiple lattice spacings in the previous sections.

A significant portion of the remaining discrepancies in the masses can likely be attributed to the parameter α in the parametrization of $V_{\Sigma_g^+}(r)$ (4.9). The improvements in parametrizations and the removal of lattice discretization errors lead to a slightly larger value of α compared to the previous study.

These findings highlight that the improved lattice data and parametrizations presented here are an important step toward more precise Born-Oppenheimer predictions of heavy hybrid meson masses. Future studies could refine the Born-Oppenheimer calculations performed in Refs. [14, 15, 17, 18] by incorporating not only our updated static potential results, but also the gluelump results of Chapter 5 and the order hybrid spin-dependent potentials at order $(1/m_Q)^1$ calculated in Chapter 6.

Λ_η^ϵ	L	n	$m_{\Lambda_\eta^\epsilon;L,n}$ in GeV for $Q\bar{Q} = c\bar{c}$	$m_{\Lambda_\eta^\epsilon;L,n}$ in GeV for $Q\bar{Q} = b\bar{b}$
Π_u	1	1	4.175 (6)	10.682 (6)
	1	2	4.550 (8)	10.895 (6)
	2	1	4.360 (7)	10.785 (6)
	3	1	4.546 (8)	10.890 (7)
Σ_u^-	0	1	4.439 (5)	10.876 (5)
	0	2	4.878 (5)	11.153 (5)
	1	1	4.574 (5)	10.960 (5)
	1	2	5.001 (6)	11.228 (5)
	2	1	4.762 (5)	11.078 (5)
	3	1	4.964 (5)	11.205 (5)

Table 4.7: Predictions for heavy hybrid meson masses.

4.6 Summary

In this chapter, we presented precise lattice field theory results for the hybrid static potentials Π_u and Σ_u^- and the ordinary static potential Σ_g^+. Our study significantly extended the available range of lattice data for hybrid static potentials, reaching quark-antiquark separations as small as 0.04 fm compared to the previous limit of 0.07 fm. Our approach, using significantly smaller lattice spacings, as small as 0.04 fm, than e.g. in Refs. [27, 30, 32, 40, 44, 45, 51, 89, 120], provides unprecedented resolution at short quark-antiquark separations and allowed for a more detailed analysis of systematic uncertainties.

Through exploratory studies at very small lattice spacings in SU(2) lattice gauge theory [53, 56], we investigated the possible sources of systematic errors, such as topological freezing, finite lattice volume effects, possible glueball decays and lattice discretization errors. All these findings were applied and extended to our SU(3) gauge link ensembles to exclude systematic errors. Hybrid static potential data at four different lattice spacings were extracted from reliable plateaus in the effective potentials. We incorporated a fifth gauge link ensemble from Ref. [51] using a HYP2 static action in order to extend the separation range to larger r values and reliably quantify discretization errors at the tree level and those proportional to a^2.

The final result of these investigations is a precise parametrization of the hybrid static potentials Π_u and Σ_u^- over the range $0.08\,\text{fm} \leq r \leq 1.2\,\text{fm}$ (see Table 4.5) along with improved hybrid static potential data (see Table E.2) consistent with a continuum limit. We further demonstrated the impact of these refinements by evaluating their effect on the calculation of heavy hybrid meson masses within a simple Born-Oppenheimer approximation.

5 Gluelumps

A gluelump is a color-neutral state composed of a static adjoint color charge bound to gluons. A static quark-antiquark pair effectively constitutes a color source in the adjoint (octet) representation in the limit of vanishing relative separation. Consequently, a gluelump can be regarded as the short-distance limit of a heavy hybrid meson, which consists of a heavy quark-antiquark pair coupled to an excited gluonic field. Although not directly observed in nature, gluelumps play a significant role in various Quantum Chromodynamics (QCD) calculations.

In weakly-coupled potential Non-Relativistic QCD (pNRQCD), gluelumps constitute non-perturbative coefficients that define the potentials required to solve Schrödinger-like equations for heavy hybrid meson masses (see Chapter 3). Beyond the Standard Model, gluelumps are considered as additional bound states, where the color charge may also be in higher representations than the octet (see e.g. Ref. [121]).

Gluelumps have been explored using various models and approximations of QCD, including the bag model, potential models and the variational approach in Coulomb gauge QCD (see e.g., Refs. [122–126]). However, the resulting gluelump spectra depend significantly on the model applied. In contrast, lattice gauge theory provides a first-principles approach. However, only a limited number of lattice computations of gluelump spectra exist in the literature. In Ref. [52], the masses of ten gluelump states were determined within SU(3) gauge theory, with five gluelump mass splittings extrapolated to the continuum. A more recent lattice study is a full lattice QCD study in Ref. [127], where they examined the gluelump spectrum and determined the masses of twenty gluelump states in the color octet representation, as well as an even larger number in higher color representations. As a result of the inclusion of dynamical quarks, mixings with static adjoint mesons, states composed of a static adjoint color charge and a light quark-antiquark pair, are possible. Such mixings might introduce systematic errors. Consequently, despite its technical advancements, Ref. [127] cannot be directly compared to Ref. [52] or serve as a replacement for it. We note that a more recent preliminary calculation of gluelump masses in full QCD has been performed in Ref. [128].

In lattice gauge theory, gluelump masses are divergent in the limit $a \to 0$ due to the inherent self-energy of the static adjoint color charge. Thus, only mass splittings to a reference mass can be extrapolated to the continuum limit. In general, absolute gluelump masses depend on the chosen regularization scheme and the specific value of the regulator. Ref. [44] converted the lightest lattice gluelump mass from Ref. [52], conventionally used as a reference, into the Renormalon Subtraction (RS) scheme, which is frequently employed

in perturbative calculations. The results from Refs. [44, 52] have since been widely utilized, both for comparison with model predictions and for computing heavy hybrid meson spectra in the Born-Oppenheimer Effective Field Theory (BOEFT) [14]. However, the precision of such applications is constrained not only by perturbative uncertainties but also by the relatively outdated lattice data from Ref. [52], which was generated over two decades ago. In this chapter, we aim to improve the lattice results for the gluelump spectrum in the color octet representation. We present a lattice calculation of gluelump correlators using chair-shaped operators on four SU(3) lattice ensembles with fine lattice spacings, performed in the context of a master's thesis [129]. Using these results, we extract the complete spectrum of gluelump states formed by a static color charge in the octet representation coupled to gluons and extrapolate gluelump mass splittings to the continuum limit. A detailed analysis is conducted to estimate systematic uncertainties associated with lattice discretization effects and the large-time behavior of correlators. Finally, we perform a renormalization and convert our result for the reference gluelump mass, $m_{T_1^{+-}}$, to the Renormalon Subtraction (RS) scheme investigating the effect of our improved lattice results on the renormalized gluelump mass. This work has been published previously in Ref. [57].

5.1 Connection to hybrid static potentials

Hybrid static potentials and gluelumps have both been explored in various studies as part of investigations of hybrid mesons, see Refs. [14, 17, 18, 44, 98, 99].
The relationship between gluelumps and hybrid static potentials is established in pNRQCD [14, 100], where the hybrid static potentials are expressed as

$$V_{\Lambda_\eta^\epsilon}(r) = \Lambda_H + V_o(r) + \mathcal{O}\big(r^2\big), \tag{5.1}$$

at leading order in a multipole expansion. Here, Λ_H represents the gluelump mass associated with the hybrid static potential Λ_η^ϵ. Extracting the gluelump mass from a fit to lattice data for the static potential is challenging, as the data includes the self-energy of the static quarks. An adjoint self-energy is also present in direct lattice results for gluelump masses. Thus, determining the absolute value of Λ_H requires a careful renormalization procedure in both cases, which we discuss later for direct lattice gluelump calculations.
The connection between gluelumps and hybrid static potentials is also evident from a group-theoretical perspective. The symmetry group of gluelumps is the full rotational group and their representations are classified by J^{PC}, where J represents the total angular momentum, P and C denote parity and charge conjugation behavior, respectively. The total angular momentum of the gluelump J corresponds to the spin of the gluons κ (see Chapter 3). In hybrid mesons, the quark-antiquark separation axis reduces the full rotational symmetry of the gluons to the cylindrical symmetry group $D_{\infty h}$, which characterizes hybrid static potentials labeled by Λ_η^ϵ (see Chapter 3). Thus, the full rotational symmetry representations κ^{PC} decompose into multiple representations Λ_η^ϵ of its subgroup. As

$r \to 0$, the rotational symmetry is restored, which implies the formation of multiplets of hybrid static potentials, related to specific gluelumps with $J^{PC} = \kappa^{PC}$.
In general, the hybrid static potential representations Λ_η^ϵ contribute to an infinite number of gluelump representations J^{PC}. By assuming that the lowest energy state within a representation Λ_η^ϵ corresponds to the lowest gluelump state and that the first excitation $\Lambda_\eta^{\epsilon\prime}$ corresponds to the second lowest gluelump state, one can establish a correspondence between hybrid static potentials, their excitations and gluelump states. For hybrid static potentials up to angular momentum $\Lambda = 2$, these degeneracies are summarized in Table 5.1. These degeneracies are supported by Ref. [100], where the symmetry properties of

J^{PC}	Λ_η^ϵ
1^{+-}	Π_u, Σ_u^-
1^{--}	Π_g, $\Sigma_g^{+\prime}$
2^{--}	Π_g', Σ_g^-, Δ_g
2^{+-}	Π_u', Σ_u^+, Δ_u

Table 5.1: Correspondence between gluelump quantum numbers J^{PC} and hybrid static potential quantum numbers Λ_η^ϵ in the limit $r \to 0$.

gluonic operators for hybrid static states were analyzed in the short-distance limit. For this analysis, it was assumed that higher-dimensional operators in a given Λ_η^ϵ representation generate the first excited states in this sector.
Using these degeneracies alongside perturbative expressions for the static potentials, one can use lattice data for the lowest hybrid static potentials and the ordinary static potential to extract the lowest gluelump mass in the RS scheme. This approach was employed in Ref. [44]. This reference also explored an alternative method based on direct lattice computations of the lowest gluelump mass. In this chapter, we adopt the latter approach, computing gluelump masses directly from gluonic correlators on the lattice and converting them to the RS scheme, as outlined in the following sections.

5.2 Lattice computation

In the following, we summarize lattice gluelump quantum numbers, operators and correlation functions needed for the lattice determination of gluelump masses. We also describe the lattice setups and computational details of the lattice calculation performed in the context of a master's thesis [129]. The subsequent analysis of this lattice data, which is discussed in the following sections, was performed in the context of this work and published in Ref. [57].

5.2.1 Gluelump correlation functions

Gluelumps in the continuum are characterized by their continuum quantum numbers J^{PC}. On the lattice, rotations are restricted to multiples of 90°, reducing the symmetry group to the full cubic group O_h. Consequently, gluelumps on the lattice are classified according to the irreducible representations of O_h, which includes four one-dimensional representations, $A_1^{\pm}$, $A_2^{\pm}$, two two-dimensional representations, $E^{\pm}$ and four three-dimensional representations, $T_1^{\pm}$, $T_2^{\pm}$. In Section 5.3.5, we discuss the assignment of continuum spin to the lattice representations.

The temporal correlation function for a gluelump in one of the twenty lattice representations $\mathcal{R}^{PC}$ is defined as

$$C_{\mathcal{R}^{PC}}(t_2 - t_1) = H^a_{\mathcal{R}^{PC}}(\mathbf{r}_Q; t_1) G^{ab}(\mathbf{r}_Q; t_1, t_2) H^{b\dagger}_{\mathcal{R}^{PC}}(\mathbf{r}_Q; t_2). \tag{5.2}$$

$\mathbf{r}_Q$ denotes the spatial position of the static adjoint quark. Due to translational invariance, the correlation function is independent of $\mathbf{r}_Q$. This allows averaging the right-hand side of Eq. (5.2) over all possible quark positions to enhance statistical precision. We omit the spatial coordinate $\mathbf{r}_Q$ in the notation for simplicity.

G denotes the static quark propagator in the adjoint representation. It is given by a product of adjoint temporal gauge links (represented in SU(3) gauge theory by 8×8 matrices, where rows and columns are labeled by upper indices $a, b, c, \ldots = 1, \ldots, 8$) connecting time t_1 and time t_2,

$$G^{ab}(t_1, t_2) = U_t^{(8),ac}(t_1) U_t^{(8),cd}(t_1 + a) U_t^{(8),de}(t_1 + 2a) \ldots U_t^{(8),fb}(t_2). \tag{5.3}$$

Adjoint gauge links are related to ordinary gauge links in the fundamental representation via $U_t^{(8),ab} = \mathrm{Tr}[T^a U_t T^b U_t^\dagger]$, where $T^a = \lambda^a/\sqrt{2}$ are the SU(3) generators with the Gell-Mann matrices λ^a.

The operators $H_{\mathcal{R}^{PC}}$ at time t_1 and time t_2 are built from gauge links in the fundamental representation generating gluons with definite lattice quantum numbers $\mathcal{R}^{PC}$. The gluonic operators on the lattice are not unique. First lattice studies of gluelumps employed simple operators built from clover-leaf plaquettes [52, 130]. Lattice results used in this work were computed from improved chair-like operators constructed and discussed in detail in Ref. [127].

The operators are constructed as linear combinations of closed gauge link paths. There are 24 basic building blocks L_n, $n = 1, \ldots, 24$, which have a chair-like shape, i.e. are 1×2

rectangles bent by $\pi/2$:

$$
\begin{aligned}
L_1 &= U^N_{+x}U^N_{+y}U^N_{+z}U^N_{-x}U^N_{-z}U^N_{-y} & L_2 &= U^N_{-y}U^N_{+x}U^N_{+z}U^N_{+y}U^N_{-z}U^N_{-x}\,,\\
L_3 &= U^N_{-x}U^N_{-y}U^N_{+z}U^N_{+x}U^N_{-z}U^N_{+y} & L_4 &= U^N_{+y}U^N_{-x}U^N_{+z}U^N_{-y}U^N_{-z}U^N_{+x}\,,\\
L_5 &= U^N_{+y}U^N_{+z}U^N_{+x}U^N_{-y}U^N_{-x}U^N_{-z} & L_6 &= U^N_{+x}U^N_{+z}U^N_{-y}U^N_{-x}U^N_{+y}U^N_{-z}\,,\\
L_7 &= U^N_{-y}U^N_{+z}U^N_{-x}U^N_{+y}U^N_{-x}U^N_{-z} & L_8 &= U^N_{-x}U^N_{+z}U^N_{+y}U^N_{+x}U^N_{-y}U^N_{-z}\\
L_9 &= U^N_{+z}U^N_{+x}U^N_{+y}U^N_{-z}U^N_{-y}U^N_{-x} & L_{10} &= U^N_{+z}U^N_{-y}U^N_{+x}U^N_{-z}U^N_{-x}U^N_{+y}\\
L_{11} &= U^N_{+z}U^N_{-x}U^N_{-y}U^N_{-z}U^N_{+y}U^N_{+x} & L_{12} &= U^N_{+z}U^N_{+y}U^N_{-x}U^N_{-z}U^N_{+x}U^N_{-y}\\
L_{13} &= U^N_{-y}U^N_{-x}U^N_{-z}U^N_{+y}U^N_{+z}U^N_{+x} & L_{14} &= U^N_{-x}U^N_{+y}U^N_{-z}U^N_{+x}U^N_{+z}U^N_{-y}\\
L_{15} &= U^N_{+y}U^N_{+x}U^N_{-z}U^N_{-y}U^N_{+z}U^N_{-x} & L_{16} &= U^N_{+x}U^N_{-y}U^N_{-z}U^N_{-x}U^N_{+z}U^N_{+y}\\
L_{17} &= U^N_{-z}U^N_{-y}U^N_{-x}U^N_{+z}U^N_{+x}U^N_{+y} & L_{18} &= U^N_{-z}U^N_{-x}U^N_{+y}U^N_{+z}U^N_{-y}U^N_{+x}\\
L_{19} &= U^N_{-z}U^N_{+y}U^N_{+x}U^N_{+z}U^N_{-x}U^N_{-y} & L_{20} &= U^N_{-z}U^N_{+x}U^N_{-y}U^N_{+z}U^N_{+y}U^N_{-x}\\
L_{21} &= U^N_{-x}U^N_{-z}U^N_{-y}U^N_{+x}U^N_{+y}U^N_{+z} & L_{22} &= U^N_{+y}U^N_{-z}U^N_{-x}U^N_{-y}U^N_{+x}U^N_{+z}\\
L_{23} &= U^N_{+x}U^N_{-z}U^N_{+y}U^N_{-x}U^N_{-y}U^N_{+z} & L_{24} &= U^N_{-y}U^N_{-z}U^N_{+x}U^N_{+y}U^N_{-x}U^N_{+z}\,,
\end{aligned}
\tag{5.4}
$$

with $U^N_{\pm j}$ denoting a product of N gauge links in the fundamental representation in $\pm j$-direction. All 24 chair-like building blocks are also defined graphically in Figure 1 of Ref. [127] (the red chair-shaped paths).

Linear combinations of L_n that correspond to the five representations, A_1, A_2, T_1, T_2 and E, have been worked out in Ref. [127] and are given by

$$H^a_{A_1} = \left(\tilde{H}_{A_1}\right)_{\alpha\beta} T^a_{\alpha\beta} = \left(\sum_{n=1}^{24} L_n\right)_{\alpha\beta} T^a_{\alpha\beta} \tag{5.5}$$

$$H^a_{A_2} = \left(\tilde{H}_{A_2}\right)_{\alpha\beta} T^a_{\alpha\beta} = \left(\sum_{n=1}^{12}(-1)^a L_n - \sum_{n=13}^{24}(-1)^a L_n\right)_{\alpha\beta} T^a_{\alpha\beta} \tag{5.6}$$

$$H^a_{T_1^x} = \left(\tilde{H}_{T_1^x}\right)_{\alpha\beta} T^a_{\alpha\beta} = (L_6 + L_{20} + L_{21} + L_{11} - L_{18} - L_8 - L_9 - L_{23})_{\alpha\beta}\, T^a_{\alpha\beta} \tag{5.7}$$

$$H^a_{T_1^y} = \left(\tilde{H}_{T_1^y}\right)_{\alpha\beta} T^a_{\alpha\beta} = (L_5 + L_{19} + L_{24} + L_{10} - L_{17} - L_7 - L_{12} - L_{22})_{\alpha\beta}\, T^a_{\alpha\beta} \tag{5.8}$$

$$H^a_{T_1^z} = \left(\tilde{H}_{T_1^z}\right)_{\alpha\beta} T^a_{\alpha\beta} = (L_1 + L_2 + L_3 + L_4 - L_{13} - L_{14} - L_{15} - L_{16})_{\alpha\beta}\, T^a_{\alpha\beta} \tag{5.9}$$

$$H^a_{T_2^x} = \left(\tilde{H}_{T_2^x}\right)_{\alpha\beta} T^a_{\alpha\beta} = (L_6 - L_{20} + L_{21} - L_{11} + L_{18} - L_8 + L_9 - L_{23})_{\alpha\beta}\, T^a_{\alpha\beta} \tag{5.10}$$

$$H^a_{T_2^y} = \left(\tilde{H}_{T_2^y}\right)_{\alpha\beta} T^a_{\alpha\beta} = (L_5 - L_{19} + L_{24} - L_{10} + L_{17} - L_7 + L_{12} - L_{22})_{\alpha\beta}\, T^a_{\alpha\beta} \tag{5.11}$$

$$H^a_{T_2^z} = \left(\tilde{H}_{T_2^z}\right)_{\alpha\beta} T^a_{\alpha\beta} = (L_1 - L_2 + L_3 - L_4 + L_{13} - L_{14} + L_{15} - L_{16})_{\alpha\beta}\, T^a_{\alpha\beta} \tag{5.12}$$

$$H^a_{E_1} = \left(\tilde{H}_{E^1}\right)_{\alpha\beta} T^a_{\alpha\beta} = (v^x - v^y)_{\alpha\beta}\, T^a_{\alpha\beta} \tag{5.13}$$

$$H^a_{E_2} = \left(\tilde{H}_{E^2}\right)_{\alpha\beta} T^a_{\alpha\beta} = (v^x + v^y - 2v^z)_{\alpha\beta}\, T^a_{\alpha\beta}\,, \tag{5.14}$$

with

$$v^x = L_6 + L_{20} + L_{21} + L_{11} + L_{18} + L_8 + L_9 + L_{23} \tag{5.15}$$

$$v^y = L_5 + L_{19} + L_{24} + L_{10} + L_{17} + L_7 + L_{12} + L_{22} \tag{5.16}$$

$$v^z = L_1 + L_2 + L_3 + L_4 + L_{13} + L_{14} + L_{15} + L_{16}\,, \tag{5.17}$$

where lower indices $\alpha, \beta = 1, \ldots, 3$ refer to the rows and columns of the 3×3 matrices L_n, which are defined in Eq. (5.4). An operator generating a state, which also has definite parity and charge conjugation, is given by

$$H^a_{\mathcal{R}^{PC}} = H^a_{\mathcal{R}^{\pm\pm}} = \frac{1}{4}\Big(\Big(H^a_{\mathcal{R}} \pm (\mathcal{P} H^a_{\mathcal{R}})\Big) \pm \mathcal{C}\Big(H^a_{\mathcal{R}} \pm (\mathcal{P} H^a_{\mathcal{R}})\Big)\Big). \tag{5.18}$$

The correlation function (5.2) can be simplified analytically,

$$C_{\mathcal{R}^{PC}}(t_2 - t_1) = \\ \mathrm{Tr}\left[\tilde{H}_{\mathcal{R}^{PC}}(t_1) Q(t_1, t_2) \tilde{H}^\dagger_{\mathcal{R}^{PC}}(t_2) (Q(t_1, t_2))^\dagger\right] - \frac{1}{3}\mathrm{Tr}\left[\tilde{H}_{\mathcal{R}^{PC}}(t_1)\right] \mathrm{Tr}\left[\tilde{H}^\dagger_{\mathcal{R}^{PC}}(t_2)\right], \tag{5.19}$$

by exploiting $T^a_{\alpha\beta} T^a_{\gamma\delta} = \delta_{\alpha\delta}\delta_{\beta\gamma} - \delta_{\alpha\beta}\delta_{\gamma\delta}/3$. $Q(t_1, t_2)$ denotes a product of temporal gauge links in the fundamental representation connecting time t_1 and time t_2.
The size of the chair-like building blocks can be adjusted through both N (see Eq. (5.4)) and the number of APE smearing steps applied to the spatial gauge links appearing in the operators $\tilde{H}_{\mathcal{R}^{PC}}$. An optimal value of $N = 2$ was determined and the number of smearing steps was optimized on ensemble B (see Table 4.3) in Ref. [129]. For the other three ensembles, the APE step numbers N_{APE} were selected based on the optimization performed in Chapter 4 and Ref. [55]. Ultimately, the chosen values were $N_{\mathrm{APE}} = 33$, 82, 115 and 164 for ensembles A, B, C and D, respectively.

5.2.2 Lattice setup

Lattice results for the gluelump correlation functions (5.19) were obtained as part of a master's thesis [129]. However, these calculations were performed on the same four SU(3) gauge link ensembles, denoted as A, B, C and D, used for computing hybrid static potentials in Chapter 4. The parameters for these ensembles are summarized in Table 4.3 and further detailed in Section 4.1.2. Employing the same lattice setup ensures consistency and enables direct comparisons between hybrid static potentials and the gluelump spectrum.
To reduce statistical errors in the gluelump correlation functions, the multilevel algorithm [77] was employed as previously for the lattice calculation of hybrid static potentials in Chapter 4. The technical details of this method are discussed in Sections 2.4.4 as well as in Refs. [55, 78]. Here, a single level of time-slice partitioning was implemented, using a regular pattern with time-slice thickness $p_1 = p_2 = \cdots = p_{n_{ts}} = a$ and $n_m = 10$ sublattice

configurations, separated by $n_u = 30$ standard heat bath sweeps. These parameters were optimized specifically for the computations of gluelumps, as discussed in Ref. [129].
For the analysis, we consider two sets of gluelump correlation function computations: one using unsmeared temporal links and the other using HYP2-smeared temporal links. HYP2 smearing reduces the self-energy of the static adjoint quark, leading to smaller statistical errors. However, results from unsmeared temporal links remain crucial, as they provide direct consistency with our previous hybrid static potential calculations (see Chapter 4) and are required for converting gluelump masses from the lattice scheme to the Renormalon Subtraction scheme, following the procedure in Ref. [44] (see Section 5.4).
Statistical uncertainties for individual ensemble results were estimated using the jackknife method. We applied the bootstrap method for continuum extrapolations, which combine data from multiple ensembles, following the approach described in Appendix A. Specifically, we used $N^A = 640$, $N^B = 320$ and $N^C = N^D = 160$ reduced jackknife bins and generated $K = 10000$ bootstrap samples.

5.3 Numerical results

In the following, we describe in detail the analysis of the lattice data from Ref. [129], which was conducted in this work.

5.3.1 Gluelump masses at finite lattice spacing

We define an effective mass, which is a common and straightforward approach to numerically extract the mass from the asymptotic temporal behavior of the correlation function $C_{\mathcal{R}^{PC}}(t)$ (5.19),

$$m^{e,s}_{\text{eff};\mathcal{R}^{PC}}(t) = \frac{1}{a}\ln\left(\frac{C^{e,s}_{\mathcal{R}^{PC}}(t)}{C^{e,s}_{\mathcal{R}^{PC}}(t+a)}\right). \tag{5.20}$$

Thus, in the limit of large temporal separations t, the effective mass approaches a plateau, which can be identified with the mass of the corresponding ground state

$$\lim_{t\to\infty} m^{e,s}_{\text{eff};\mathcal{R}^{PC}}(t) = m^{e,s}_{\mathcal{R}^{PC}}. \tag{5.21}$$

We assume that $m^{e,s}_{\mathcal{R}^{PC}}$ extracted at large but finite t corresponds to a single state in the sector $\mathcal{R}^{PC}$ and not to be obscured by contributions of different states with the same lattice quantum numbers but different continuum total angular momentum. This yields a gluelump mass $m^{e,s}_{\mathcal{R}^{PC}}$ for each representation $\mathcal{R}^{PC} \in \{A_1^{\pm\pm}, A_2^{\pm\pm}, E^{\pm\pm}, T_1^{\pm\pm}, T_2^{\pm\pm}\}$, each ensemble $e \in \{A, B, C, D\}$ and both unsmeared and HYP2-smeared temporal links indicated by $s \in \{\text{none}, \text{HYP2}\}$.
We obtain the gluelump mass by fitting a constant to $m^{e,s}_{\text{eff};\mathcal{R}^{PC}}(t)$ within the range $t'_{\text{min}} \leq t \leq t'_{\text{max}}$, where the effective mass shows a plateau within statistical errors. The procedure for the determination of the fit range is similar to the one used in Section 4.2 and reads as

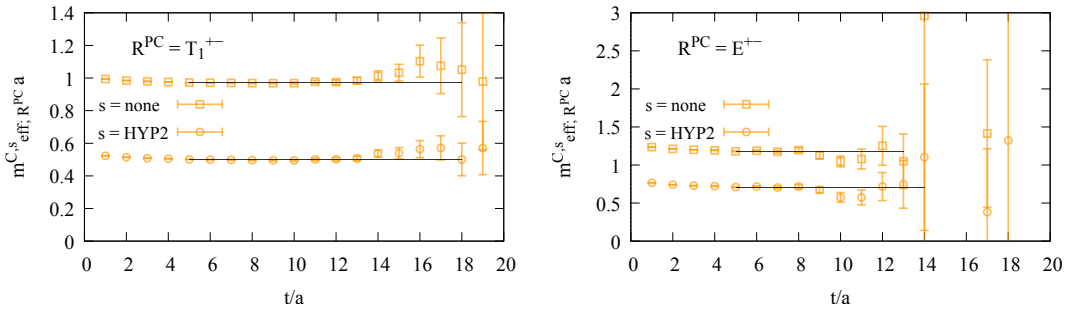

Figure 5.1: Exemplary plots of effective masses $m^{C,s}_{\text{eff};\mathcal{R}^{PC}}(t)a$. The horizontal gray bands depict the fitted plateau $m^{C,s}_{\mathcal{R}^{PC}}a$ and their width corresponds to the statistical error. (Left) $\mathcal{R}^{PC} = T_1^{+-}$, (right) $\mathcal{R}^{PC} = E^{++}$.

follows:

1. The lower bound of the fitting range t_{min} is defined as the smallest t, where the difference between the consecutive values of $m^{e,s}_{\text{eff};\mathcal{R}^{PC}}(t)a$ and $m^{e,s}_{\text{eff};\mathcal{R}^{PC}}(t+a)a$ is within 2σ.

2. t_{max} is the maximal t, where $C^{e,s}_{\mathcal{R}^{PC}}(t+a)$ has been computed, i.e. $t_{\text{max}} = 11a$, $19a$, $19a$, $19a$ for ensembles A, B, C, D, respectively.

3. Fits to $m^{e,s}_{\text{eff};\mathcal{R}^{PC}}(t)a$ are performed for all ranges $t'_{\text{min}} \le t \le t'_{\text{max}}$ satisfying:

$$t'_{\text{min}} \ge t_{\text{min}}\,, \qquad t'_{\text{max}} \le t_{\text{max}} \quad \text{and} \qquad t'_{\text{max}} - t'_{\text{min}} \ge 3a\,. \tag{5.22}$$

4. The fit yielding the longest plateau with $\chi^2_{\text{red}} \le 1$ is taken as the final result for $m^{e,s}_{\mathcal{R}^{PC}}a$, where the reduced χ^2 is calculated as

$$\chi^2_{\text{red}} = \frac{a}{t'_{\text{max}} - t'_{\text{min}}} \sum_{t=t'_{\text{min}},t'_{\text{min}}+a,\ldots,t'_{\text{max}}} \frac{\left(m^{e,s}_{\text{eff};\mathcal{R}^{PC}}(t)a - m^{e,s}_{\mathcal{R}^{PC}}a\right)^2}{\left(\sigma[m^{e,s}_{\text{eff};\mathcal{R}^{PC}}](t)a\right)^2} \tag{5.23}$$

with $\sigma[m^{e,s}_{\text{eff};\mathcal{R}^{PC}}](t)a$ denoting the statistical error of $m^{e,s}_{\text{eff};\mathcal{R}^{PC}}(t)a$.

This algorithm identifies gluelump masses from reliable plateaus in the effective masses at large t. The fitting range was manually adjusted to correct non-ideal selections in about ten percent of cases. We cross-check our results using a more conservative fit range, $t'_{\text{min}} + a \le t \le t'_{\text{max}}$. Results for both approaches agree within statistical errors indicating a reliable plateau extraction.

The quality of our lattice data is demonstrated in Figure 5.1, where we present two typical effective mass plots and the corresponding plateau fits for representations $\mathcal{R}^{PC} = T_1^{+-}$ (left plot) and $\mathcal{R}^{PC} = E^{++}$ (right plot), $e = C$ and both $s =$ none and $s =$ HYP2. The horizontal gray band represents the plateau fit result.

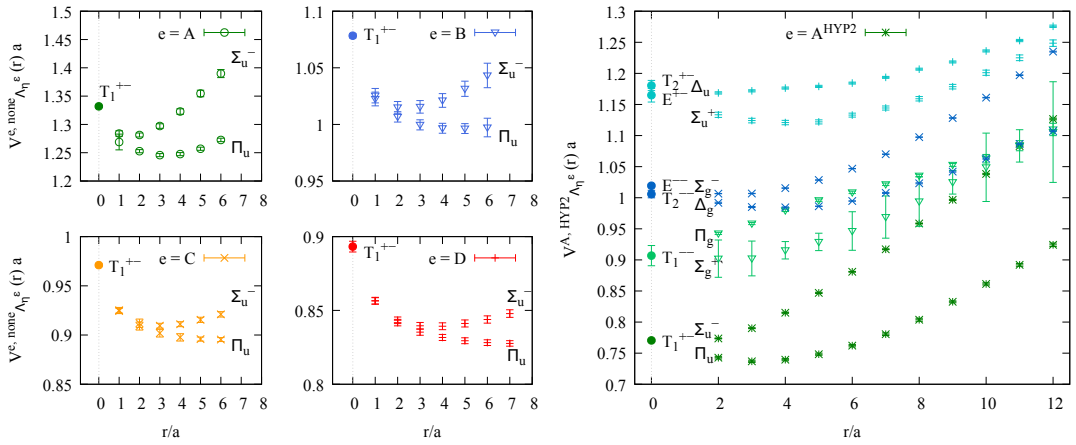

(a) (b)

Figure 5.2: (a) Hybrid static potentials $V^{e,\text{none}}_{\Lambda^\epsilon_\eta}(r)a$ with $\Lambda^\epsilon_\eta = \Pi_u, \Sigma^-_u$ for $r/a \geq 1$ and gluelump masses $m^{e,\text{none}}_{T_1^{+-}}a$ at $r/a = 0$.

(b) Hybrid static potentials $V^{A,\text{HYP2}}_{\Lambda^\epsilon_\eta}(r)a$ with $\Lambda^\epsilon_\eta = \Pi_u, \Sigma^-_u, \Sigma^{+\prime}_g, \Pi_g, \Delta_g, \Sigma^-_g, \Sigma^+_u, \Delta_u$ for $r/a \geq 2$ from Ref. [51] and gluelump masses $m^{A,\text{HYP2}}_{\mathcal{R}^{PC}}a$ with $\mathcal{R}^{PC} = T_1^{+-}, T_1^{--}, T_2^{--}, E^{--}, T_2^{+-}, E^{+-}$ at $r/a = 0$.

The lattice data for $\mathcal{R}^{PC} = A_2^{--}$ and unsmeared temporal links ($s = \text{none}$) is obscured by large statistical errors such that the identification of an effective mass plateau is impossible. Therefore, we do not report gluelump masses for this case and do not use the corresponding correlator data in the remainder of this work.

We summarize all resulting gluelump masses $m^{e,s}_{\mathcal{R}^{PC}}a$ for all 20 $\mathcal{R}^{PC}$ representations, the four ensembles and computations with unsmeared und with smeared temporal links in Table E.3.

5.3.2 Gluelumps and hybrid static potentials

The gluelump mass results $m^{e,s}_{\mathcal{R}^{PC}}a$ complement the hybrid static potential results $V^{e,s}_{\Lambda^\epsilon_\eta}a$ computed in the previous chapter and presented in Figure 4.2. The lowest gluelump with lattice quantum numbers T_1^{+-}, which is expected to correspond to the continuum gluelump with $J^{PC} = 1^{+-}$ [52, 127] (see Section 5.3.5), is associated to the two lowest hybrid static potentials with quantum numbers Π_u and Σ^-_u, as discussed before. In Figure 5.2a, we present the Π_u and Σ^-_u hybrid static potentials from all ensembles with unsmeared temporal links together with the corresponding T_1^{+-} gluelump mass at $r = 0$. The static potential data clearly approach the gluelump mass for vanishing quark-antiquark separation, demonstrating the expected degeneracy.

Ref. [51] computed even higher-lying hybrid static potentials for ensemble A and HYP2-smeared temporal links. These can be directly compared with our gluelump masses from ensemble A with $s = \text{HYP2}$. We compare the six lowest lattice gluelump masses, which are

expected to correspond to the four lowest continuum gluelump states (see Section 5.3.5), with the lattice hybrid static potentials in Figure 5.2b. The correspondence in the limit $r \to 0$ between higher lying hybrid static potentials and heavier gluelumps is also demonstrated, which was discussed for continuum quantum numbers in Section 5.1 and Table 5.1. This is an important cross-check of our results.

5.3.3 Continuum extrapolation

Lattice gluelump masses $m^{e,s}_{\mathcal{R}^{PC}}$ depend on the lattice spacing a. However, a direct extrapolation to $a = 0$ is not possible due to the inherent self-energy of the static adjoint color source, which diverges as $1/a$. Since this self-energy is identical for all gluelumps, it cancels in mass differences, making them finite in the continuum limit. As previously done by other authors, we use the lightest gluelump with lattice quantum numbers T_1^{+-} as a reference mass and define the gluelump mass splitting

$$\Delta m^{e,s}_{\mathcal{R}^{PC}} a = m^{e,s}_{\mathcal{R}^{PC}} a - m^{e,s}_{T_1^{+-}} a \,, \tag{5.24}$$

where the self-energy cancels.

We compute $\Delta m^{e,s}_{\mathcal{R}^{PC}} a$ for all 19 representations, the four ensembles and smeared and unsmeared temporal links. In Figure 5.3 we present these mass splittings $\Delta m^{e,s}_{\mathcal{R}^{PC}}$ in physical units as a function of a^2 for s = HYP2. Results from smeared and unsmeared temporal links are collected in Table E.4 and are mostly consistent, while the latter exhibit slightly larger statistical errors (see Figure E.1 in the Appendix).

As expected for the Wilson plaquette action, we observe a linear dependence on a^2 for the three smaller lattice spacings. To extrapolate to $a = 0$, we use the function

$$\Delta m^{\text{fit},s}_{\mathcal{R}^{PC}}(a) = \Delta m^{s}_{\mathcal{R}^{PC},\text{cont}} + c^{s}_{\mathcal{R}^{PC}} a^2 \tag{5.25}$$

and perform a two-parameters χ^2-minimizing fit for each representation $\mathcal{R}^{PC}$ including three data points. The fit parameter $\Delta m^{s}_{\mathcal{R}^{PC},\text{cont}}$ represents the continuum limit of the gluelump mass splitting, which is summarized in Table 5.2 and presented in Figure 5.3 at $a = 0$. The dashed lines in Figure 5.3 show the fit functions with mostly $\chi^2_{\text{red}} \approx 1$ indicating reasonable fits.

The data points from ensemble A deviate from the linear behavior. We extend our fit function by a term proportional to a^4 and include data points from ensemble A in the fits. The continuum gluelump mass splittings from this three-parameter fit are mostly consistent with the results of the previous fit. We use the differences to estimate the systematic error (the second of the two errors provided in Table 5.2).

The consistency between both fits supports the validity and stability of our continuum extrapolations. However, despite being the most straightforward approach to continuum extrapolated gluelump mass splitting, the above-presented method has some drawbacks. The continuum extrapolations are based on very few data points. Moreover, these data

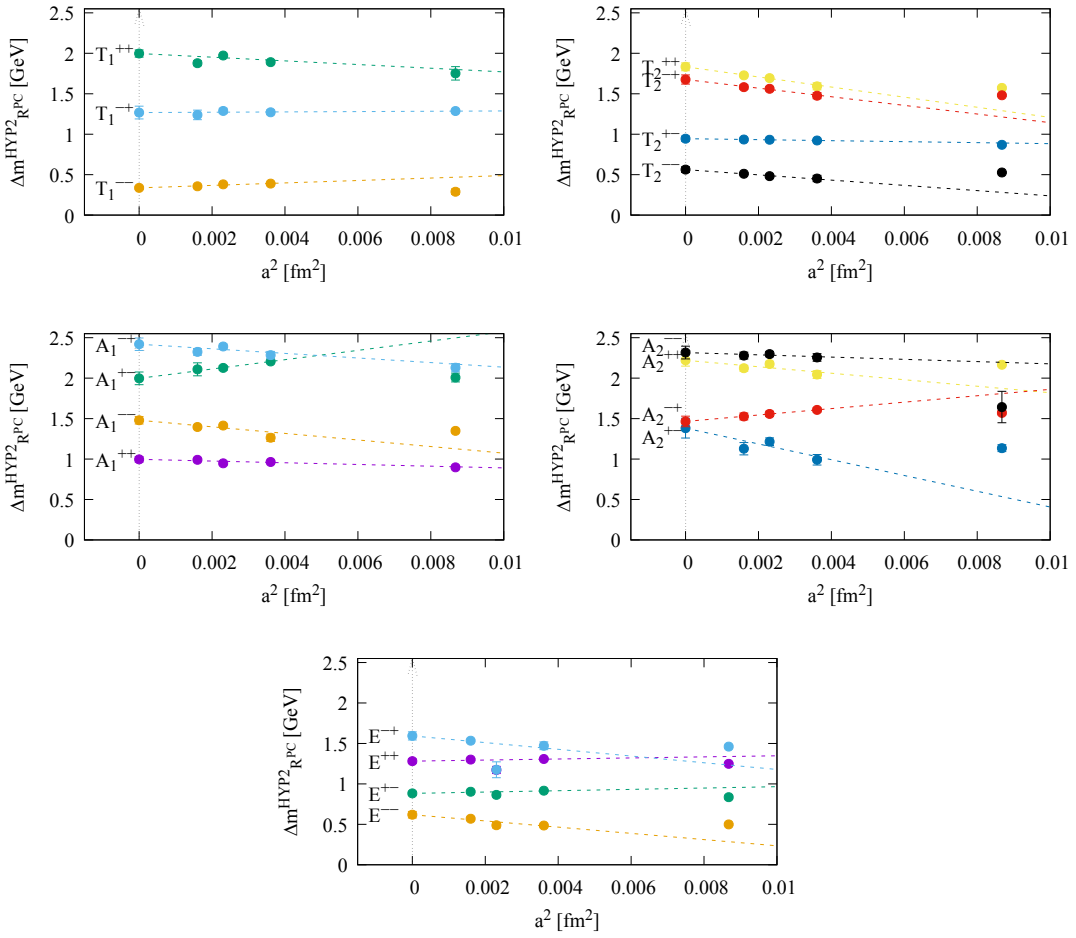

Figure 5.3: Continuum extrapolations of gluelump mass splittings $\Delta m^e_{\mathcal{R}^{PC}}$ for HYP2-smeared temporal links.

points also result from a plateau fit to few data points in the effective masses. Some effective masses exhibit large statistical errors, obscuring the fit or making a plateau identification difficult. We present a more elaborate method in the following to improve the quality and stability of our results.

Continuum extrapolated gluelump mass splittings from simultaneous fits to correlator data from several ensembles

The method we present here bases the results for continuum gluelump mass splittings on more data points than the abovementioned method. To this end, we define a ratio of correlation functions $C^{e,s}_{\mathcal{R}^{PC}}(t)$,

$$\tilde{C}^{e,s}_{\mathcal{R}^{PC}}(t) = \frac{C^{e,s}_{\mathcal{R}^{PC}}(t)}{C^{e,s}_{T_1^{+-}}(t)}\,, \tag{5.26}$$

$\mathcal{R}^{PC}$	$\Delta m^{\text{none}}_{\mathcal{R}^{PC},\text{cont}}$ [GeV]	$\Delta m^{\text{HYP2}}_{\mathcal{R}^{PC},\text{cont}}$ [GeV]
T_1^{++}	1.956(71)(86)	1.997(45)(39)
T_1^{+-}	0	0
T_1^{-+}	1.431(37)(39)	1.268(79)(6)
T_1^{--}	0.336(21)(30)	0.337(20)(33)
T_2^{++}	1.838(50)(35)	1.833(49)(33)
T_2^{+-}	0.940(34)(10)	0.945(32)(4)
T_2^{-+}	1.750(63)(44)	1.676(57)(40)
T_2^{--}	0.531(35)(0)	0.562(35)(36)
A_1^{++}	0.995(34)(3)	0.996(33)(3)
A_1^{+-}	2.223(40)(13)	1.997(79)(109)
A_1^{-+}	2.366(62)(126)	2.420(77)(31)
A_1^{--}	1.929(158)(320)	1.480(46)(8)
A_2^{++}	2.216(75)(24)	2.221(72)(29)
A_2^{+-}	1.659(127)(113)	1.382(123)(77)
A_2^{-+}	1.407(62)(83)	1.465(66)(45)
A_2^{--}	-	2.316(79)(103)
E^{++}	1.282(28)(14)	1.281(27)(12)
E^{+-}	0.881(24)(17)	0.882(24)(17)
E^{-+}	1.609(51)(54)	1.593(50)(47)
E^{--}	0.600(27)(29)	0.619(41)(40)

Table 5.2: Continuum extrapolated gluelump mass splittings $\Delta m^{s}_{\mathcal{R}^{PC},\text{cont}}$ derived from the gluelump masses in Table E.3 using a linear fit a^2 (see Eq. (5.25)). The first error represents the statistical error, while the second error accounts for systematic differences between extrapolations using a^2 and a^4 fits (see text for details).

such that the gluelump mass splitting $\Delta m^{e,s}_{\mathcal{R}^{PC}}$ as defined in Eq. (5.24) can be extracted from the exponential falloff of the correlator ratio at large times, i.e.

$$\lim_{t\to\infty} \tilde{C}^{e,s}_{\mathcal{R}^{PC}}(t) = A^{e,s}_{\mathcal{R}^{PC}} \exp\left(-\Delta m^{e,s}_{\mathcal{R}^{PC}} t\right). \tag{5.27}$$

The gluelump mass splitting $\Delta m^{e,s}_{\mathcal{R}^{PC}}$ has a lattice spacing dependence, which we expect to be linear in a^2 following our previous analysis. We incorporate the lattice spacing dependence into the fit function, which is given by

$$\tilde{C}^{\text{fit},e,s}_{\mathcal{R}^{PC}}(t) = A^{e,s}_{\mathcal{R}^{PC}} \exp\Big(-(\Delta m_{\mathcal{R}^{PC},\text{cont}} + c^{s}_{\mathcal{R}^{PC}} a^2) t \Big). \tag{5.28}$$

The fit parameter $\Delta m_{\mathcal{R}^{PC},\text{cont}}$ denotes the continuum gluelump mass splitting. In the continuum, gluelump mass splittings should be independent of the smearing method. Thus, we can use the data obtained with and without HYP2 smearing of temporal links not only for a cross-check but also to increase the number of data included in the fit. This results in a simultaneous 9-parameter fit to the correlator data from ensembles B, C and D for unsmeared and HYP2-smeared temporal links for each representation $\mathcal{R}^{PC}$. In general, the parameters $A^{e,s}_{\mathcal{R}^{PC}}$ and $c^{s}_{\mathcal{R}^{PC}}$ are different between HYP2 smearing (s = HYP2) and

no smearing ($s = \text{none}$) of temporal links. However, the parameters obtained from the fits appear to be equal within statistical errors between the unsmeared and HYP2-smeared data sets. Consequently, the number of fit parameters can be reduced and the resulting 5-parameter fit reads

$$\tilde{C}^{\text{fit},e,s}_{\mathcal{R}^{PC}}(t) = A^{e}_{\mathcal{R}^{PC}} \exp\Big(-(\Delta m_{\mathcal{R}^{PC},\text{cont}} + c_{\mathcal{R}^{PC}} a^2)t \Big). \tag{5.29}$$

In order to identify a reasonable fitting range for a fit of Eq. (5.29) to the correlator ratio data, we define a modified effective mass using the correlator ratios (5.26)

$$\tilde{m}^{e,s}_{\text{eff},\mathcal{R}^{PC}}(t) = \frac{1}{a} \ln\left(\frac{\tilde{C}^{e,s}_{\mathcal{R}^{PC}}(t)}{\tilde{C}^{e,s}_{\mathcal{R}^{PC}}(t+a)} \right). \tag{5.30}$$

Inspired by previous fit algorithms, the lower bound of the fitting range is set to the temporal extent, where the effective mass is consistent with a plateau within statistical errors. The details of determining the fit range $t_{\text{min}} \leq t \leq t_{\text{max}}$ are the following [57]:

1. For each e, s we define $t^{e,s}_{\text{min}} = \tilde{t} - a/2$ with $\tilde{t}$ denoting the smallest value of t, where the effective mass (5.30) satisfies $|\tilde{m}^{e,s}_{\text{eff},\mathcal{R}^{PC}}(t)a - \tilde{m}^{e,s}_{\text{eff},\mathcal{R}^{PC}}(t+a)a| < 2\sigma$.

2. t_{min} is set to the largest of those $t^{e,s}_{\text{min}}$. Consequently, the lower bound for the fit range is the same for all ensembles.

3. t_{max} is the largest t, where the correlation functions $C^{e,s}_{\mathcal{R}^{PC}}(t)$ have been computed.

The results of the fits are summarized in Table 5.3. We obtain $\chi^2_{\text{red}} = \mathcal{O}(1)$ indicating reasonable fits. For $\mathcal{R}^{PC} = A_2^{--}$ and data from unsmeared temporal links ($s = \text{none}$), no plateau in the effective mass was identified in the previous section. Including these data in the simultaneous fit of the correlator ratio results in $\chi^2_{\text{red}} \gg 1$. Thus, we exclude them and fit only HYP2-smeared data for $\mathcal{R}^{PC} = A_2^{--}$.

To test the stability of our continuum-extrapolated mass splittings, we repeat the fitting using a more conservative range $t'_{\text{min}} \leq t \leq t_{\text{max}}$. The modified lower bound t'_{min} is defined similarly to t_{min} but with a stricter plateau condition, i.e. $|\tilde{m}^{e,s}_{\text{eff},\mathcal{R}^{PC}}(t-a)a - \tilde{m}^{e,s}_{\text{eff},\mathcal{R}^{PC}}(t)a| < 2\sigma$. As a result, $t'_{\text{min}} > t_{\text{min}}$, leading to an increase in statistical errors of approximately 50%, as expected due to a worsening signal-to-noise ratio at larger t. However, the resulting mass splittings remain statistically consistent with those in Table 5.3, with no systematic shift due to excited-state contamination. Differences between the two fits are quoted as systematic errors (third error in Table 5.3).

Similar to our previous approach, we verify the stability of our continuum extrapolation by adding an a^4 term to the fit function (5.29),

$$\tilde{C}^{\text{fit},e,s}_{\mathcal{R}^{PC}}(t) = A^{e}_{\mathcal{R}^{PC}} \exp\Big(-(\Delta m_{\mathcal{R}^{PC},\text{cont}} + c_{\mathcal{R}^{PC}} a^2 + d_{\mathcal{R}^{PC}} a^4)t \Big). \tag{5.31}$$

We also include correlator data from ensemble A, which has the coarsest lattice spacing.

$\mathcal{R}^{PC}$	$\Delta m_{\mathcal{R}^{PC},\text{cont}}$ [GeV]	χ^2_{red}
T_1^{++}	1.793(94)(35)(42)	0.88
T_1^{-+}	1.213(59)(3)(24)	1.05
T_1^{--}	0.342(19)(22)(21)	0.43
T_2^{++}	1.771(85)(60)(35)	0.39
T_2^{+-}	0.966(29)(2)(13)	0.64
T_2^{-+}	1.638(73)(78)(30)	1.38
T_2^{--}	0.503(12)(5)(5)	1.34
A_1^{++}	0.979(26)(21)(14)	1.00
A_1^{+-}	2.088(51)(123)(36)	0.82
A_1^{-+}	2.354(53)(27)(106)	0.92
A_1^{--}	1.433(31)(31)(16)	0.91
A_2^{++}	2.210(66)(57)(38)	0.75
A_2^{+-}	1.376(128)(155)(60)	0.92
A_2^{-+}	1.496(32)(109)(21)	0.48
$A_2^{--\star}$	2.149(340)(7)(133)	1.34
E^{++}	1.258(19)(2)(15)	0.83
E^{+-}	0.858(21)(23)(18)	0.50
E^{-+}	1.511(162)(44)(81)	1.18
E^{--}	0.559(12)(44)(11)	0.87

* For $\mathcal{R}^{PC} = A_2^{--}$ we exclude correlator data obtained with unsmeared temporal links (s = none) from the fit .

Table 5.3: Continuum extrapolated gluelump mass splittings $\Delta m_{\mathcal{R}^{PC},\text{cont}}$ obtained from 5-parameter fits of the fit function (5.29) to correlator data from ensembles B, C and D. The first error is the statistical error, while the second error is a systematic error representing the difference between an a^2 and an a^4 ansatz for the continuum extrapolation, respectively, and the third error represents the systematic error coming from the choice of fitting range (see text for details).

The 19 resulting continuum-extrapolated gluelump mass splittings from these 7-parameter fits remain statistically consistent with those obtained from the 5-parameter fits. The differences between the two sets of results are quoted as systematic errors (the second of three errors in Table 5.3).

5.3.4 Comparison of gluelump mass splittings with literature

We compare our continuum-extrapolated gluelump mass splittings, $\Delta m_{\mathcal{R}^{PC}}$, with those from previous lattice studies [52, 127]. Figure 5.4 presents this comparison for the representations $\mathcal{R}^{PC} = T_1^{--}, T_2^{--}, A_1^{++}, A_2^{+-}, E^{+-}$, for which continuum extrapolations were also performed in Ref. [52]. Our results are presented as orange data points, which represent the values of $\Delta m_{\mathcal{R}^{PC},\text{cont}} + c_{\mathcal{R}^{PC}} a^2$ at our three smallest lattice spacings $a = 0.040\,\text{fm}$, $0.048\,\text{fm}$, $0.060\,\text{fm}$ (see Section 5.3.3, in particular Table 5.3). The results from Ref. [52] are shown as blue data points for three lattice spacings $a = 0.068\,\text{fm}$, $0.095\,\text{fm}$, $0.170\,\text{fm}$ along with a continuum extrapolation linear in a^2, similar to our method in Section 5.3.3. Since calculations in Ref. [52] were also performed in pure

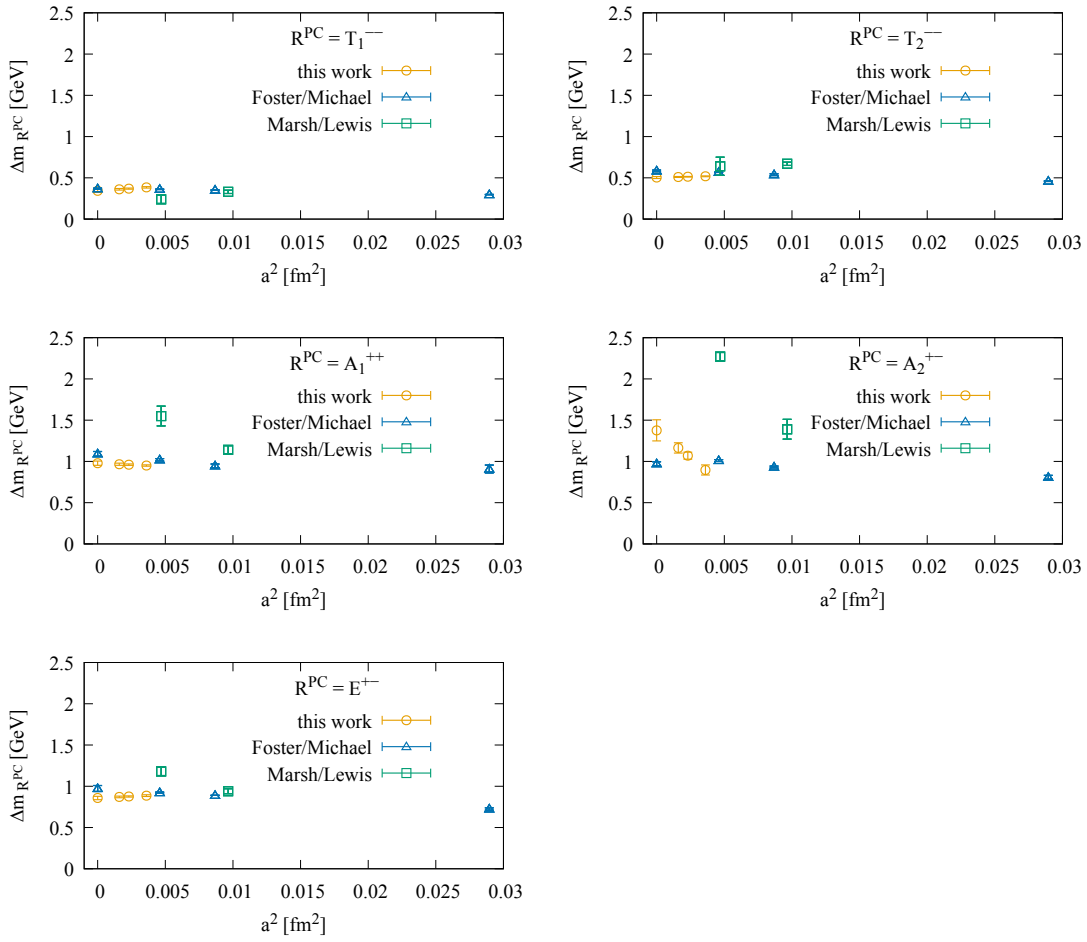

Figure 5.4: Comparison of our results for gluelump mass splittings to results from Refs. [52] (Foster/Michael) and Ref. [127] (Marsh/Lewis). Error bars represent exclusively statistical errors.

SU(3) gauge theory, its continuum-extrapolated mass splittings should, in principle, be directly comparable to ours. While the results exhibit qualitative agreement across all five representations, there are quantitative discrepancies of up to $\approx 30\%$. The differences likely originate from improvements in the extraction of results in our work. Our continuum mass splittings are obtained from a fit incorporating a large number of correlator data points, whereas Ref. [52] performed an extrapolation to $a = 0$ based on only three data points. Moreover, our calculations employ three significantly smaller lattice spacings, reducing discretization effects. Given these factors, we consider our continuum extrapolations more robust and reliable than those in Ref. [52].

Ref. [127] reports results at two lattice spacings, $a = 0.0685\,\text{fm}$, $0.0982\,\text{fm}$, but does not perform a continuum extrapolation. Unlike our study and Ref. [52], these calculations were performed in full QCD, including dynamical quarks, with a pion mass approximately 3.5 times heavier than its physical value. While both approaches introduce systematic

uncertainties, the qualitative agreement of the results is encouraging for the study of gluonic correlation functions such as the gluelump correlator.

5.3.5 Spin assignment

Assigning continuum spin to lattice gluelump mass splittings is challenging due to several factors. First, the lattice gluelump masses are classified by irreducible representations of a subgroup of the continuum symmetry group of gluelumps and, thus, do not have definite continuum spin J. Each continuum irreducible representation J decomposes into multiple representations of the lattice symmetry group. Consequently, each lattice representation receives contributions from an infinite number of continuum representations,

$$\begin{aligned} A_1 &\leftrightarrow 0, 4, 6, 8, \dots \\ T_1 &\leftrightarrow 1, 3, 4, 5, \dots \\ T_2 &\leftrightarrow 2, 3, 4, 5, \dots \\ E &\leftrightarrow 2, 4, 5, 6, \dots \\ A_2 &\leftrightarrow 3, 6, 7, 9, \dots \end{aligned} \tag{5.32}$$

(see e.g. Ref. [131]). Therefore, assigning the lowest allowed total angular momentum J to the lowest state in the representation $\mathcal{R}^{PC}$ might not always be correct. However, this can be checked because some $\mathcal{R}^{PC}$ include the same J and should, thus, be degenerate. In particular, $J = 2$ is the lowest angular momentum value in T_2 and E. Consequently, a degeneracy of the lattice gluelump masses is expected.
Secondly, different continuum states could have similar masses and contribute to the same lattice representation. Extraction of a plateau becomes difficult, or a fake plateau is seen in the effective mass and a mass is extracted that lies between the continuum states. This could be checked using several operators in the $\mathcal{R}^{PC}$ representation, which would resemble different continuum quantum numbers. In principle, computing a correlation matrix with those operators and solving a generalized eigenvalue problem (see e.g. Ref. [128]) would allow us to identify the competing continuum states. First attempts of finding appropriate gluelump operators have been made in the context of a bachelor's thesis [132], which might be helpful for future refinements.
Since we have a single operator for each cubic representation and cannot differentiate between different continuum total angular momenta, we adopt the reasonable strategy of assigning the lowest allowed J to the lowest state in $\mathcal{R}^{PC}$. The most plausible spin assignments are determined based on the results summarized in Table 5.3 and Figure 5.5, observed degeneracies and the expected hierarchy of angular momenta. The following discussion outlines the reasoning behind each spin assignment, as previously presented in Ref. [57]:

- A_1 states:
  - $A_1^{PC} \rightarrow$ probably $J = 0$:

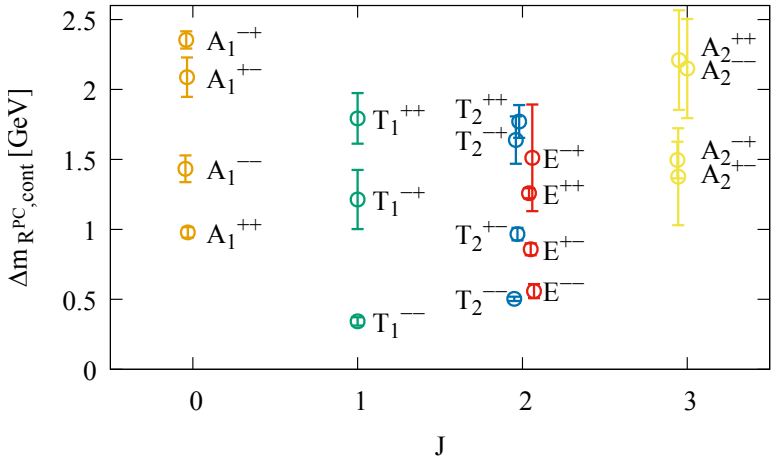

Figure 5.5: Summary of continuum extrapolated gluelump mass splittings. The horizontal axis indicates the lowest continuum total angular momentum J appearing in the corresponding representation of the cubic group. The error bars denote statistical and systematic errors.

The two lowest J values contained in A_1 are $J = 0$ and $J = 4$. Since higher angular momentum states are generally associated with larger energies, the lower-lying states in A_1 are naturally assigned $J = 0$. In particular, for the lighter A_1 states, A_1^{++} and A_1^{--}, no alternative assignment seems plausible.

- T_1 states:
  - T_1^{+-} and T_1^{--} $\rightarrow$ $J = 1$:
    The T_1 representation can contain $J = 1$ and $J = 3$, but the latter is also present in A_2. Since the energy levels for the corresponding A_2 states are significantly higher, it is reasonable to assign $J = 1$ to T_1^{+-} and T_1^{--} .
  - T_1^{-+} and T_1^{++} $\rightarrow$ $J = 1$ or $J = 3$:
    The energy level for T_1^{-+} and T_1^{++} are consistent with the energy level for A_2^{-+} and A_2^{++}, respectively, which suggests they may correspond to the same $J = 3$ state. However, the large uncertainty in both states allows for the possibility that they have $J = 1$, while A_2^{-+} and A_2^{++} have $J = 3$.

- T_2 and E states:
  - T_2^{--}, E^{--} $\rightarrow$ $J = 2$:
    Both representations contain $J = 2$ and their energy levels are degenerate within errors, indicating they likely correspond to the same state with $J = 2$. While a $J = 4$ assignment is theoretically possible, it is unlikely, as the $J = 3$ state (indicated by A_2^{--}) is already heavy and A_1^{--}, a lower bound for $J = 4$, lies significantly above the T_2^{--} and E^{--} energy levels.

  - T_2^{+-}, E^{+-} $\rightarrow$ $J = 2$:
    Follows the same reasoning as for T_2^{--}, E^{--} (see previous item).
  - E^{++} $\rightarrow$ $J = 2$ (excluding T_2^{++}):
    The T_2^{++} energy level is approximately 3σ above the E^{++} energy level, which is unexpected since all small J values in E^{++} are also present in T_2^{++}. This discrepancy could be a statistical fluctuation or indicate unfavorable overlaps in the T_2^{++} operator, possibly due to a large contribution from a heavy $J = 3$ state (the A_2^{++} energy level indicates that 3^{++} is quite heavy). Given this uncertainty, E^{++} is assigned $J = 2$, while T_2^{++} is excluded from the interpretation.
  - T_2^{-+}, E^{-+} $\rightarrow$ $J = 2$ (not inconsistent):
    The energy levels for T_2^{-+} and E^{-+} are degenerate within errors suggesting a common $J = 2$ state. However, their errors, particularly for E^{-+}, mean that other J assignments cannot be ruled out.

- A_2 states:
  - A_2^{PC} $\rightarrow$ $J = 3$ (most likely):
    The lowest possible J values in A_2 are $J = 3$ and $J = 6$. Following the same argument as previously for the A_1 states, the lower spin value is the more plausible assignment. For A_2^{-+} and A_2^{++}, this is further supported by our discussion of the T_1^{-+} and T_1^{++} states above, it suggests $J = 3$ for A_2^{-+} and A_2^{++}.

We can refine our analysis because we observed several degeneracies of lattice gluelump mass splittings, suggesting that they possibly correspond to the same continuum quantum number. We perform simultaneous fits to these lattice correlators using a single fit parameter for the continuum gluelump mass splitting $\Delta m_{\mathcal{R}^{PC},\text{cont}}$, combining two lattice representations results in a χ^2-minimizing 9-parameter fit of Eq. (5.29). Specifically, we obtain final results for $J^{PC} = 2^{+-}$, $J^{PC} = 2^{-+}$ and $J^{PC} = 2^{--}$ by combining fits for the corresponding lattice representations T_2^{+-} and E^{+-}, T_2^{-+} and E^{-+} and T_2^{--} and E^{--}, respectively. The resulting χ^2_{red} of $\mathcal{O}(1)$ confirm the reasonability of these combined fits. Our final results for gluelump mass splittings with quantum numbers J^{PC} are summarized in Table 5.4, where energy levels with plausible but unconfirmed continuum J assignments are shaded in gray.

5.4 Conversion of gluelump mass from the lattice to the RS scheme

As discussed in previous sections, the lattice results for gluelump masses, denoted as $m^{e,s}_{\mathcal{R}^{PC}} a$, include the self-energy of the static adjoint color source. This self-energy depends inversely on the lattice spacing a and diverges as $a \to 0$. Consequently, only mass

J^{PC}	$\Delta m_{J^{PC}}$ [GeV]	$\mathcal{R}^{PC}$	J^{PC}	$\Delta m_{J^{PC}}$ [GeV]	$\mathcal{R}^{PC}$
0^{++}	0.979(36)	A_1^{++}	2^{++}	1.258(24)	E^{++}
0^{+-}	2.088(138)	A_1^{+-}	2^{+-}	0.925(42)	T_2^{+-} & E^{+-} combined fit
0^{-+}	2.354(122)	A_1^{-+}	2^{-+}	1.664(256)	T_2^{-+} & E^{-+} combined fit
0^{--}	1.433(47)	A_1^{--}	2^{--}	0.523(11)	T_2^{--} & E^{--} combined fit
1^{++}	1.793(108)	T_1^{++}	3^{++}	2.210(95)	A_2^{++}
1^{+-}	0	–	3^{+-}	1.376(210)	A_2^{+-}
1^{-+}	1.213(64)	T_1^{-+}	3^{-+}	1.496(116)	A_2^{-+}
1^{--}	0.342(36)	T_1^{--}	3^{--}	2.149(340)	$A_2^{--\star}$

Table 5.4: Final results for gluelump mass splittings with quantum numbers J^{PC}. Errors include both statistical and systematic errors, added in quadrature. The column $\mathcal{R}^{PC}$ indicates from which cubic representation the result was taken. For $J = 2$ and $PC = +-, -+, --$, final results are obtained through combined fits (see text for details). Energy levels with plausible but unconfirmed continuum total angular momentum J assignments are shaded in gray.

differences, in which the self-energy contribution cancels out, yield meaningful continuum-limit results. As long as no continuum limit is performed, the lattice spacing a regulates the divergences.

Different renormalization schemes exist to address these divergences. The gradient flow method provides a promising approach on the lattice for handling self-energy contributions, which is explored in Ref. [133].

A standard renormalization scheme in perturbation theory is the Renormalon Subtraction (RS) scheme [134]. The RS scheme plays a critical role in the BOEFT, where specifically the gluelump mass $m_{T_1^{+-}}$ in this scheme at a scale $\nu_f = 2.5/r_0 \approx 1\,\text{GeV}$ serves as a key input parameter for the calculation of the heavy hybrid meson spectra [14]. The choice of $\nu_f = 2.5/r_0 \approx 1\,\text{GeV}$ is motivated by its role as a reasonable cutoff scale in the hierarchy of energy scales in the BOEFT [135]. Consequently, we aim to convert our precise lattice gluelump masses into the RS scheme. We specifically focus on converting the 1^{+-} lattice gluelump mass, as it served as the reference for our computed mass splittings in Section 5.3.3. The RS masses for higher gluelumps can then be derived using the precise continuum mass splittings in Table 5.2.

To perform this conversion, we follow the procedure outlined in Ref. [44], which utilized lattice data from Ref. [52]. Several improvements distinguish our approach from this earlier work. Our analysis, which has also been published in Ref. [57], benefits from more precise lattice data at smaller lattice spacings, improving the accuracy and reliability of the results (see Section 5.3.4 for a comparison). On the perturbative side, the running of the coupling in the $\overline{MS}$ scheme has been refined by one perturbative order. Moreover, we employ a more precise value of $\Lambda_{\overline{\text{MS}}}$, thereby reducing systematic uncertainties and increasing the overall precision of our conversion, as discussed further below.

The renormalon is the analog of the lattice self-energy of the static adjoint color charge in perturbation theory. A renormalon arises due to the factorial growth of expansion coefficients in perturbative series, leading to divergent behavior. The RS scheme mitigates this issue by subtracting the renormalon contribution, thus ensuring a more convergent and reliable result. In the following, we summarize the necessary equations from Refs. [44, 136, 137] in order to convert the lattice gluelump mass to the gluelump mass in the RS scheme.

The gluelump mass in the RS scheme, $\Lambda_B^{RS}(\nu_f)$, is related to the lattice gluelump mass, $\Lambda_B^L(a)$, through the perturbative conversion equation

$$\Lambda_B^{\mathrm{RS}}(\nu_f) = \Lambda_B^L(a) - \left(\delta\Lambda_B^L(a) + \delta\Lambda_B^{\mathrm{RS}}(\nu_f)\right). \tag{5.33}$$

Here, $\left(\delta\Lambda_B^L(a) + \delta\Lambda_B^{\mathrm{RS}}(\nu_f)\right)$ represents the perturbative corrections associated with the self-energy.

The lattice self-energy, $\delta\Lambda_B^L(a)$, is given by a perturbative expansion in the lattice coupling $\alpha_L(a)$

$$\delta\Lambda_B^L(a) = \frac{1}{a}\sum_{n=0}^{\infty} c_n^{(8,0)}(\alpha_L(a))^{n+1}. \tag{5.34}$$

The coefficients $c_n^{(8,0)}$ have been computed up to $n = 19$ in Refs. [136, 137]. The label $(8,0)$ refers to a static charge in the adjoint representation and applies to calculations using the standard Wilson plaquette action and a static propagator with unsmeared temporal links. Consequently, we can only utilize our lattice results obtained with unsmeared temporal links to maintain consistency with the perturbative formulas.

The RS scheme counterpart, $\delta\Lambda_B^{\mathrm{RS}}(\nu_f)$, is expressed in terms of the $\overline{\mathrm{MS}}$ coupling $\alpha_{\overline{\mathrm{MS}}}(\nu_f)$

$$\delta\Lambda_B^{\mathrm{RS}}(\nu_f) = \sum_{n=1}^{\infty} \nu_f \left(\tilde{V}_{s,n}^{\mathrm{RS}} - \tilde{V}_{o,n}^{\mathrm{RS}}\right)(\alpha_{\overline{\mathrm{MS}}}(\nu_f))^{n+1} \tag{5.35}$$

(see Ref. [44]). The coefficients $\tilde{V}_{s,n}^{\mathrm{RS}}$ and $\tilde{V}_{o,n}^{\mathrm{RS}}$ are known exactly for $n = 0, 1, 2$ and have been estimated for $n = 3, 4$ (see Table 2 in Ref. [44] and references therein).

The conversion via Equation (5.33) requires all terms to be known at the same order in the coupling. Therefore, the first step is to express the lattice coupling α_L in terms of the $\overline{\mathrm{MS}}$ coupling, $\alpha_{\overline{\mathrm{MS}}}$. Their relation is given as a perturbative expansion

$$\alpha_{\overline{\mathrm{MS}}} = \alpha_L(1 + \sum_{j=1}^{n} d_j \alpha_L^j). \tag{5.36}$$

The expansion coefficients are estimated up to $j = 3$. They are $d_1 = 5.883\ldots$, $d_2 = 43.407\ldots$ (see Refs. [44, 136] and references therein) and $d_3 = 352$ [136]. An inverted

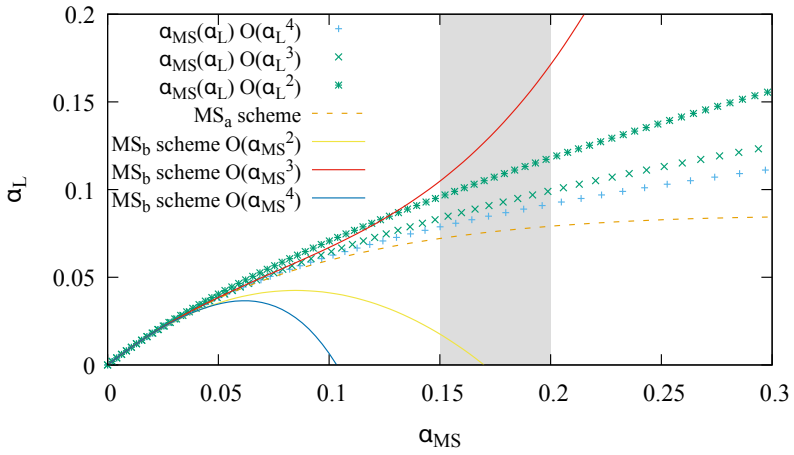

Figure 5.6: $\alpha_L(a)$ as a function of $\alpha_{\overline{\text{MS}}}(1/a)$. The three solid lines represent the polynomial expression (5.38) (or equivalently (5.39)) truncated at orders $n = 2, 3, 4$ in $\alpha_{\overline{\text{MS}}}$, with higher-order terms neglected. Similarly, the data points represent a polynomial expansion of $\alpha_{\overline{\text{MS}}}$ in terms of α_L, i.e. $\alpha_{\overline{\text{MS}}} = \alpha_L(1 + \sum_{j=0}^{n} d_j \alpha_L^j)$ up to $n = 1, 2, 3$, respectively (see Ref. [137] and references therein). The dashed line represents the $\overline{\text{MS}}_a$ conversion scheme (5.37). The shaded region highlights the range of $\alpha_{\overline{\text{MS}}}(1/a)$ corresponding to the lattice spacings $0.040\,\text{fm} \ldots 0.093\,\text{fm}$, as used in this work.

relation can be achieved in different ways. One approach, valid up to $j = 2$, is

$$\alpha_L(a) = \alpha_{\overline{\text{MS}}}(1/a) \frac{1}{1 + d_1 \alpha_{\overline{\text{MS}}}(1/a) + (d_2 - d_1^2)\alpha_{\overline{\text{MS}}}(1/a)} \,. \tag{5.37}$$

Alternatively,

$$\alpha_L(a) = \alpha_{\overline{\text{MS}}}(1/a) \Big(1 - d_1 \alpha_{\overline{\text{MS}}}(1/a) + (2d_1^2 - d_2)(\alpha_{\overline{\text{MS}}}(1/a))^2\Big) \,. \tag{5.38}$$

The first conversion scheme corresponds to the $\overline{\text{MS}}_a$ conversion scheme and the second equation represents the $\overline{\text{MS}}_b$ conversion scheme from Ref. [137]. The $\overline{\text{MS}}_b$ scheme can be further extended to incorporate the newly estimated d_3, yielding:

$$\begin{aligned} \alpha_L(a) = \alpha_{\overline{\text{MS}}}(1/a) \Big(1 &- d_1 \alpha_{\overline{\text{MS}}}(1/a) + (2d_1^2 - d_2)(\alpha_{\overline{\text{MS}}}(1/a))^2 \\ &+ (-5d_1^3 + 3d_1 d_2 - d_3)(\alpha_{\overline{\text{MS}}}(1/a))^3\Big) \,. \end{aligned} \tag{5.39}$$

Although both conversion schemes are valid in principle, they exhibit significant discrepancies and introduce systematic uncertainties at the typical scales used for this analysis. Figure 5.6 illustrates the difference between different conversions and truncations of the perturbative expansion of α_L in terms of $\alpha_{\overline{\text{MS}}}$. As expected, for small values of $\alpha_{\overline{\text{MS}}} \lesssim 0.05$, the different conversions agree. However, for larger values of $\alpha_{\overline{\text{MS}}}$, substantial deviations appear. The deviations are significant for the range $0.15 \lesssim \alpha_{\overline{\text{MS}}}(1/a) \lesssim 0.20$, correspond-

ing to lattice spacings in the range 0.040 fm . . . 0.093 fm, as used in this study (highlighted by the gray-shaded region in Figure 5.6).

Ref. [136] stated that the $\overline{\text{MS}}_a$ scheme was superior. However, Ref. [44] employed the $\overline{\text{MS}}_b$ scheme up to order $\alpha^3_{\overline{\text{MS}}}$. In alignment with their approach, we also adopt the $\overline{\text{MS}}_b$ scheme up to $\alpha^3_{\overline{\text{MS}}}$ in our calculations. Nevertheless, the systematic uncertainties associated with the conversion of α_L to $\alpha_{\overline{\text{MS}}}$ remain an open issue. Further refinement and validation of this conversion procedure through perturbative calculations would be essential for improving accuracy.

As a second step, we account for the running of the coupling when replacing $\alpha_L(a)$ with $\alpha_{\overline{\text{MS}}}(\nu_f)$ at a different scale $\nu_f \neq 1/a$. The β-function governs the running of the coupling via

$$\beta(\alpha_{\overline{\text{MS}}}(\mu)) = \frac{\mu}{\alpha_{\overline{\text{MS}}}(\mu)} \frac{d\alpha_{\overline{\text{MS}}}(\mu)}{d\mu} \,. \tag{5.40}$$

It can be expressed perturbatively as an expansion in $\alpha_{\overline{\text{MS}}}$

$$\beta(\alpha_{\overline{\text{MS}}}) = -2\beta_0 \sum_{i=0}^{4} \left(\frac{\alpha_{\overline{\text{MS}}}}{4\pi}\right)^{i+1} \frac{\beta_i}{\beta_0} \,, \tag{5.41}$$

with coefficients β_i determined up to five-loop order, $i = 4$ [138]. With the β-function, the running coupling $\alpha_{\overline{\text{MS}}}(\nu)$ can be expressed terms of powers of $\alpha_{\overline{\text{MS}}}(\mu)$ at a reference scale $\mu = \Lambda^{(0)}_{\overline{\text{MS}}}$, up to order $\alpha^2_{\overline{\text{MS}}}$ it reads

$$\alpha_{\overline{\text{MS}}}(\nu) = \alpha_{\overline{\text{MS}}}(\mu) \left\{ 1 + \frac{2\alpha_{\overline{\text{MS}}}(\mu)}{4\pi} \beta_0 \ln(\mu/\nu) \left[1 + \mathcal{O}\big(\alpha_{\overline{\text{MS}}}\big)\right] \right\} . \tag{5.42}$$

We will employ the five-loop running from Ref. [138] to compute numerical values for the $\overline{\text{MS}}$ coupling.

Having expressed the lattice coupling $\alpha_L(1/a)$ in terms of the $\overline{\text{MS}}$ coupling $\alpha_{\overline{\text{MS}}}(\mu)$ and incorporated the running of the coupling, we can now rewrite Eq. (5.33) as an expansion in $\alpha_{\overline{\text{MS}}}(\mu)$. Truncating this series at order $\alpha^3_{\overline{\text{MS}}}$ (denoted as NNNLO) yields the final conversion formula

$$\begin{aligned}
\Lambda^{\text{RS}}_B(\nu_f) = \Lambda^L_B(a) &- \frac{1}{a} c_0^{(8,0)} \alpha_{\overline{\text{MS}}}(\nu_f) \\
&+ \left(\frac{1}{a} c_1^{(8,0)} + \frac{1}{a} c_0^{(8,0)} \left[-d_1 + \frac{2\beta_0}{4\pi} \ln(\nu_f a) \right] + \nu_f \left(\tilde{V}^{\text{RS}}_{s,1} - \tilde{V}^{\text{RS}}_{o,1} \right) \right) (\alpha_{\overline{\text{MS}}}(\nu_f))^2 \\
&+ \left(\frac{1}{a} c_2^{(8,0)} + \frac{2}{a} c_1^{(8,0)} \left[-d_1 + \frac{2\beta_0}{4\pi} \ln(\nu_f a) \right] + \frac{1}{a} c_0^{(8,0)} \left[-d_2 + \frac{2\beta_1}{(4\pi)^2} \ln(\nu_f a) + d_1^2 \right] \right. \\
&\quad \left. + \frac{2}{a} c_0^{(8,0)} \left[-d_1 + \frac{2\beta_0}{4\pi} \ln(\nu_f a) \right]^2 + \nu_f \left(\tilde{V}^{\text{RS}}_{s,2} - \tilde{V}^{\text{RS}}_{o,2} \right) \right) (\alpha_{\overline{\text{MS}}}(\nu_f))^3 .
\end{aligned} \tag{5.43}$$

At order $\alpha^2_{\overline{\text{MS}}}$ (NNLO) this equation coincides with Eq. (70) in Ref. [44].

In Ref. [44] the coefficient $c_2^{(8,0)}$ appearing at NNNLO expression was estimated as $c_2^{(8,0)} = 193.8(2.8)$. More recent calculations provide a value of, $c_2^{(8,0)} = 193.2(3)$ [137]. We use

this up-to-date value, but its impact on the final result for the gluelump mass in the RS scheme is expected to be negligible due to the minimal difference.
Furthermore, we use the five-loop running coupling from Ref. [138] along with the updated value $r_0\Lambda^{(0)}_{\overline{\rm MS}} = 0.624(36)$ [101] and $r_0 = 0.5\,\text{fm}$ to compute numerical values for $\alpha_{\overline{\rm MS}}(1/a)$. In Table 5.5 we list both $\alpha_{\overline{\rm MS}}(1/a)$ and $\alpha_L(a)$ for the four lattice spacings used in our simulations $a = 0.040\,\text{fm}\,,\ 0.048\,\text{fm}\,,\ 0.060\,\text{fm}\,,\ 0.093\,\text{fm}$. The use of the five-loop running coupling represents an improvement over Ref. [44], which employed the four-loop running.

β	a in fm	$1/a$ in GeV	$\alpha_{\overline{\rm MS}}(1/a)$	$\alpha_L(a)$ (Eq. (5.38))
6.000	0.093	2.118	0.200	0.172
6.284	0.060	3.285	0.170	0.127
6.451	0.048	4.108	0.158	0.113
6.594	0.040	4.932	0.150	0.104

Table 5.5: $\alpha_{\overline{\rm MS}}(1/a)$ from the five-loop running coupling from Ref. [138] and $\alpha_L(a)$ according to Eq. (5.38) for the four lattice spacings used in our simulations.

We now use our computed gluelump mass values at the four lattice spacings, $a = 0.040\,\text{fm}\,,\ 0.048\,\text{fm}\,,\ 0.060\,\text{fm}\,,\ 0.093\,\text{fm}$, to determine the RS gluelump mass, $\Lambda_B^{\rm RS}(\nu_f = 1/a)$. Choosing $\nu_f = 1/a$ ensures that large logarithmic terms in the conversion formula are avoided. Figure 5.7 presents $\Lambda_B^{\rm RS}(1/a)$ at LO, NLO, NNLO and NNNLO for our four lattice spacings (colored data points). At LO, lattice and RS masses are identical $\Lambda_B^{\rm RS}(1/a) = \Lambda_B^L(a)$. The corresponding numerical values are listed in Table 5.6.
We compare our results with those from Ref. [44] (gray data points), which were derived using lattice data from Ref. [52] at coarser lattice spacings. Our converted results exhibit a convergence pattern similar to that observed in Ref. [44] and both data sets appear consistent.

a [fm]	$\Lambda_B^{\rm RS}(1/a) = \Lambda_B^L(a)$ LO	$\Lambda_B^{\rm RS}(1/a)$ NLO	$\Lambda_B^{\rm RS}(1/a)$ NNLO	$\Lambda_B^{\rm RS}(1/a)$ NNNLO	[GeV]
0.093	2.821(5)	0.798(5)	1.298(5)	1.167(5)	
0.060	3.541(7)	0.883(7)	1.440(7)	1.316(7)	
0.048	3.990(6)	0.902(6)	1.502(6)	1.378(6)	
0.040	4.429(8)	0.923(8)	1.568(8)	1.442(8)	

Table 5.6: $\Lambda_B^{\rm RS}(1/a)$ in GeV for our four lattice spacings at LO, NLO, NNLO and NNNLO. The errors are purely statistical.

To determine $\Lambda_B^{\rm RS}$ at the scale $\nu_f = 2.5/r_0 \approx 1\,\text{GeV}$, we adopt the procedure of Ref. [44]. The first step is to use the NNNLO expression (5.43) with $\nu_f = 1/a_{\rm min} = 1/0.040\,\text{fm}$ and to fit it to the lattice results at all four lattice spacings simultaneously to obtain the fit parameter $\Lambda_B^{\rm RS}(\nu_f = 1/0.040\,\text{fm})$. For ensembles A, B and C, we have $\nu_f \neq 1/a$, such that the logarithmic terms in Eq. (5.43) do not vanish. The resulting value of this fit is given

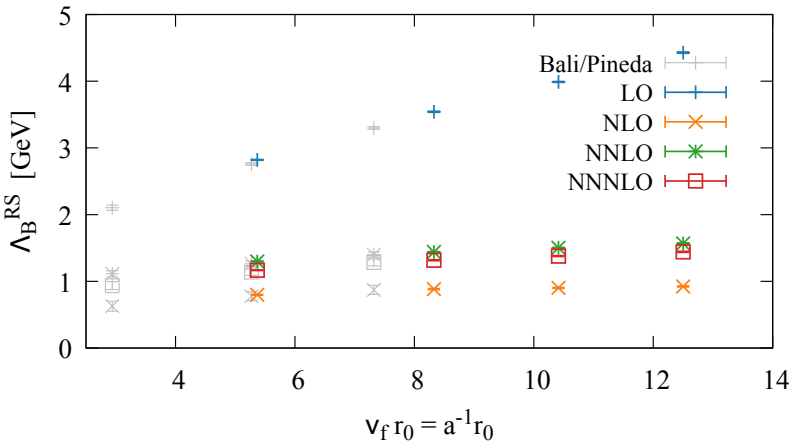

Figure 5.7: $\Lambda_B^{\mathrm{RS}}(1/a)$ for our four lattice spacings at LO, NLO, NNLO and NNNLO. The gray data points represent results from Ref. [44] (Bali/Pineda) for comparison.

by

$$\Lambda_B^{\mathrm{RS}}(\nu_f = 1/0.040\,\mathrm{fm} = 12.5/r_0) = 1.463(3)\,\mathrm{GeV}. \tag{5.44}$$

However, the relatively large reduced chi-square value $\chi^2_{\mathrm{red}} = 4.36$ suggests some tension among the four lattice spacings when combined with the perturbative conversion function. Possible reasons could be the large logarithmic terms from the separation of scales $\nu_f \neq 1/a$, truncation effects in the perturbative series, or lattice discretization errors, which are expected to scale as a^2. We assess the impact of excluding the coarsest lattice, $a = 0.093\,\mathrm{fm}$. The difference between the result, which is $\Lambda_B^{\mathrm{RS}}(\nu_f = 1/0.040\,\mathrm{fm}) = 1.460(4)\,\mathrm{GeV}$ with $\chi^2_{\mathrm{red}} = 5.89$, and the previous result is incorporated into the final systematic uncertainty (see the discussion at the end of this section). To address possible discretization errors, we perform an additional fit including an explicit a^2-correction term in Eq. (5.43). We include all four lattice spacings into this fit, which yields $\Lambda_B^{\mathrm{RS}}(\nu_f = 1/0.040\,\mathrm{fm}) = 1.454(6)\,\mathrm{GeV}$ with $\chi^2_{\mathrm{red}} = 4.94$. Again, we include the difference from Eq.(5.44) in the final systematic uncertainty. For comparison, a direct conversion of the lattice data point at the smallest lattice spacing results in $\Lambda_B^{\mathrm{RS}}(\nu_f = 1/0.040\,\mathrm{fm}) = 1.442(8)\,\mathrm{GeV}$, as presented in Figure 5.7 and Table 5.6. This result is slightly lower than the fit results.

For the propagation of the result at $\nu_f = 1/0.040\,\mathrm{fm} = 12.5/r_0$ to the specific scale $\nu'_f = 2.5/r_0 \approx 1\,\mathrm{GeV}$, we avoid errors from the large logarithms in the formulas above by using a different equation,

$$\Lambda_B^{\mathrm{RS}}(\nu'_f = 2.5/r_0) = \Lambda_B^{\mathrm{RS}}(\nu_f = 12.5/r_0) + \left(\delta\Lambda_B^{\mathrm{RS,PV}}(\nu_f) - \delta\Lambda_B^{\mathrm{RS,PV}}(\nu'_f)\right). \tag{5.45}$$

The choice of a useful prescription such as the Principal Value prescription to compute $\delta\Lambda_B^{\mathrm{RS}}$ is possible due to the cancellation of the renormalon in the difference $\delta\Lambda_B^{\mathrm{RS,PV}}(\nu_f) -$

$\delta\Lambda_B^{\mathrm{RS,PV}}(\nu_f')$. $\delta\Lambda_B^{\mathrm{RS,PV}}$ in the Principal Value prescription is computed via

$$\delta\Lambda_B^{\mathrm{RS,PV}}(\nu_f) = N_\Lambda \nu_f \alpha_{\overline{\mathrm{MS}}}(\nu_f) \sum_{s=0}^{\infty} c_s \left[D_{b-s}(-\frac{2\pi}{\beta_0 \alpha_{\overline{\mathrm{MS}}}(\nu_f)}) - 1 \right]. \tag{5.46}$$

This equation coincides with Eq. (61) in Ref. [44], when replacing N_m by N_Λ. We use the more recently determined value $N_\Lambda = -1.37(9)$ from Ref. [137]. The equation is evaluated with coefficients b and c_s [134, 139, 140], which read

$$b = \frac{\beta_1}{2\beta_0^2} \tag{5.47}$$

$$c_0 = 1 \tag{5.48}$$

$$c_1 = \frac{1}{4b\beta_0^3}\left(\frac{\beta_1^2}{\beta_0} - \beta_2\right) \tag{5.49}$$

$$c_2 = \frac{1}{b(b-1)} \frac{\beta_1^4 + 4\beta_0^3\beta_1\beta_2 - 2\beta_0\beta_1^2\beta_2 + \beta_0^2\left(-2\beta_1^3 + \beta_2^2\right) - 2\beta_0^4\beta_3}{32\beta_0^8}. \tag{5.50}$$

$D_b(-x)$ is a complex function which can be written as

$$D_b(-x) = -xe^{-x}x^b cos(\pi b)\Gamma(-b,0) + x(-x)^b e^{-x}\left[\Gamma(-b,0) - \Gamma(-b,-x)\right], \tag{5.51}$$

with the incomplete Γ function

$$\Gamma(b,x) = \int_x^\infty dt t^{b-1}e^{-t}. \tag{5.52}$$

The imaginary part cancels in the difference $\left(\delta\Lambda_B^{\mathrm{RS,PV}}(\nu_f) - \delta\Lambda_B^{\mathrm{RS,PV}}(\nu_f')\right)$.
Using Eq. (5.45) to propagate our result (5.44) determined from a fit to the lattice data to the specific scale $\nu_f' = 2.5/r_0 \approx 1\,\mathrm{GeV}$, we obtain

$$\Lambda_B^{\mathrm{RS}}(\nu_f = 2.5/r_0 \approx 1\,\mathrm{GeV}) = 0.857(3)\,\mathrm{GeV}. \tag{5.53}$$

The given error is a purely statistical uncertainty. With the more accurate lattice gluelump masses in our analysis, we could decrease the statistical error by a factor of 4 compared to the result from Ref. [44], which reads $\Lambda_B^{\mathrm{RS}}(\nu_f = 2.5/r_0 \approx 1\,\mathrm{GeV}) = 0.912(12)\,\mathrm{GeV}$.
The result is also subject to systematic uncertainties, which we summarize and compare to those reported in Ref. [44] in the following.
The uncertainty of $\Lambda_{\overline{\mathrm{MS}}}$ introduces an error in the running coupling. In Ref. [44], where the four-loop running coupling was used, it is estimated to be 0.04 GeV. Our analysis, which utilizes the five-loop running coupling and a more precise $\Lambda_{\overline{\mathrm{MS}}}$ value from Ref. [101] reduces this systematic error associated with $\Lambda_{\overline{\mathrm{MS}}}$ to 0.03 GeV.
Moreover, the result at $\nu_f = 1/0.040\,\mathrm{fm} = 12.5/r_0$ is derived from lattice gluelump masses at different scales including $1/a = 5.4/r_0$, $8.3/r_0$, $10.4/r_0$. The separation between these

scales to $\nu_f = 1/0.040\,\text{fm} = 12.5/r_0$ leads to systematic error due to the running of the coupling. We estimated this error by the difference to a fit incorporating only the three lattice gluelump masses at scales closest to $\nu_f = 1/0.040\,\text{fm} = 12.5/r_0$. The error estimate amounts to $\approx 0.003\,\text{GeV}$.

Lattice discretization errors proportional to a^2 present in the lattice gluelump masses are also a source for systematic errors. We account for these discretization errors by introducing a a^2 term in the fit of $\Lambda_B^{\text{RS}}(\nu_f = 1/0.040\,\text{fm})$, which differs from our main result by $\approx 0.01\,\text{GeV}$, thus estimating the systematic error due to discretization effects.

The perturbative conversion formula is only known up to NNNLO. To estimate the error from the truncation of the perturbative expansion, Ref. [44] considers the difference between the NNLO and NNNLO result, which in our case is $\approx 0.03\,\text{GeV}$. Additionally, the coefficients in the perturbative expressions introduce systematic error. Due to the 10% uncertainty in $N_{V_s} - N_{V_o}$, there is a systematic error contribution of $\approx 0.07\,\text{GeV}$ [44].

When summing all these systematic errors in the same way as in Ref. [44], our total systematic uncertainty amounts to $0.143\,\text{GeV}$. This is an improvement compared to the $0.205\,\text{GeV}$ systematic uncertainty reported in Ref. [44].

Our final result is

$$\Lambda_B^{\text{RS}}(\nu_f = 2.5/r_0 \approx 1\,\text{GeV}) = 0.857(3)(143)\,\text{GeV}, \tag{5.54}$$

where the first error is statistical and the second error is systematic. The systematic error is significantly larger than the statistical error associated with the lattice gluelump masses. Therefore, improvements on the perturbative side are necessary to enhance the precision of the 1^{+-} gluelump mass in the RS scheme.

For completeness, we also mention that in Ref. [44], a determination of $\Lambda_B^{\text{RS}}(\nu_f = 2.5/r_0 \approx 1\,\text{GeV})$ was conducted using the (hybrid) static potentials Σ_g^+, Π_u and Σ_u^-. The resulting value was reported as $\Lambda_B^{\text{RS}}(\nu_f = 2.5/r_0 \approx 1\,\text{GeV}) = [0.888 \pm 0.039(\text{latt.}) \pm 0.083(\text{th.}) \pm 0.032(\Lambda_{\overline{\text{MS}}})]\,\text{GeV}$, which is in agreement with our result presented in Eq. (5.54). This approach to determining the gluelump mass in the RS scheme could, in principle, also be repeated with our more accurate lattice results for the (hybrid) static potentials from Chapter 4. However, similar to the findings above, the accuracy of perturbative expressions currently is the limiting factor of precision.

5.5 Summary

In this chapter, we investigated 20 lattice gluelumps from pure SU(3) lattice gauge theory. The correspondence between gluelumps, representing the short-distance limit of hybrid static potentials, and multiplets of hybrid static potentials was discussed and confirmed through lattice data.

Throughout this chapter, we employed lattice correlator data from Ref. [129], computed on gauge link ensembles with four different lattice spacings, using both HYP2-smeared

and unsmeared temporal links. We extracted reliable gluelump masses for each lattice setup through plateau fits to the effective mass. Gluelump mass splittings were defined relative to the lowest-lying state in the T_1^{+-} representation. These mass splittings were extrapolated to $a = 0$, where we explicitly estimated systematic uncertainties arising from discretization effects. The results from smeared and unsmeared temporal links were found to be consistent.

To further improve the determination of continuum gluelump mass splittings, we introduced a superior approach utilizing a larger set of lattice data. By defining a correlator ratio with respect to the T_1^{+-} representation, we extracted continuum gluelump mass splittings via an exponential fit. Discretization effects proportional to a^2 and a^4 were accounted for and systematic uncertainties were carefully estimated. The chosen fit ranges were analyzed and we quantified the impact of different selections. Our final continuum results for 19 gluelump mass splittings are summarized in Table 5.3. These results show agreement with previous studies [52, 127] while achieving significantly improved accuracy.

Additionally, we carefully examined the identification of continuum spin quantum numbers for our lattice representations and refined the extracted gluelump masses based on observed degeneracy patterns. Our main results are presented in Table 5.4. However, the spin assignment of several states remains ambiguous and requires the inclusion of additional gluelump operators capable of distinguishing different continuum spin states. This needs to be addressed in future work.

As the gluelump mass in the Renormalon Subtraction (RS) scheme plays a crucial role in the determination of heavy hybrid meson masses within the Born-Oppenheimer Effective Field Theory [14], we converted our lattice result for $m_{T_1^{+-}}$ to the RS scheme, following the approach in Ref. [44]. Our final result is $\Lambda_B^{\mathrm{RS}}(\nu_f = 2.5/r_0 \approx 1\,\mathrm{GeV}) = 0.857(3)(143)\,\mathrm{GeV}$, where the first uncertainty is statistical and the second systematic. Due to our more precise gluelump lattice data and recent updates of perturbative parameters, we have improved regarding statistical and systematic uncertainties upon the commonly used estimate from Ref. [44], significantly reducing statistical and systematic uncertainties.

6 Hybrid spin-dependent and hybrid-quarkonium mixing potentials at order $(1/m_Q)^1$

In the previous chapters, we have considered the static limit of heavy hybrid mesons and neglected the spin of the heavy quarks. This simplifying approach is reasonable up to a certain point for bottom or charm quarks, whose masses ($m_b \approx 4.18\,\text{GeV}$ and $m_c \approx 1.27\,\text{GeV}$ in the $\overline{MS}$ scheme [3]) are significantly larger than the hadronic scale $\Lambda_{\overline{MS}} \approx 332\,\text{MeV}$ [141]. Corrections to this approximation appear in the expansion of the Born-Oppenheimer Effective Field Theory (BOEFT) Lagrangian (see Refs. [14–20]) and come in orders of the inverse heavy quark mass $1/m_Q$, as discussed in Chapter 3. Since quarks are spin-1/2 fermions, the spin of a quark-antiquark pair in a hybrid meson can couple to $S_{Q\bar{Q}} = 0$ or $S_{Q\bar{Q}} = 1$, influencing the quantum numbers J^{PC} of the (hybrid) meson and affecting its properties and mass spectrum. In the static approximation, we can only predict degenerate spin multiplets, but spin-dependent corrections in the expansion in $1/m_Q$ resolve this degeneracy.

While heavy quark spin-dependent corrections to the ordinary static potential arise at order $(1/m_Q)^2$, they appear already at order $(1/m_Q)^1$ for heavy hybrid mesons due to the coupling between heavy quark spin and non-zero gluon spin [15, 17, 18, 142]. A possible mixing between quarkonium and hybrid quarkonium is related to the heavy quark spin and is also an effect that appears with a factor of $(1/m_Q)^1$ in the BOEFT Lagrangian. This makes both kinds of spin-dependent effects particularly relevant for precision spectroscopy. Although order $(1/m_Q)^2$ corrections to the static quarkonium potential have been investigated with lattice field theory methods [76, 104, 143, 144], a first-principles computation of the next-to-leading order (NLO) corrections to hybrid potentials, which not only involve heavy quark spin-dependent parts, has not yet been performed. Previous studies of spin effects in hybrid mesons include early lattice NRQCD investigations [145, 146] as well as more recent full lattice QCD calculations of charmonium and bottomonium hybrids [11–13]. From the effective field theory approach, hybrid spin-dependent potentials have been explored in weakly coupled potential NRQCD (pNRQCD) at small quark-antiquark separations [17, 18]. In this framework, each correction is decomposed into a perturbative, distance-dependent part and a non-perturbative contribution expressed in terms of gluonic correlators. At large separations, QCD effective string theory describes these potentials [109, 110]. These approaches were used in Refs. [15, 23] to parametrize

hybrid potentials at NLO for short and long distances, combining pNRQCD predictions with QCD effective string theory. However, all of these studies rely on unknown non-perturbative parameters that require determination from lattice QCD.

A formulation of spin-dependent and hybrid-quarkonium mixing potentials in the BOEFT framework has recently been derived by matching to NRQCD without assumption on the quark-antiquark separation [15, 19]. These potentials can be expressed in terms of generalized Wilson loops with chromomagnetic insertions, making them accessible to lattice QCD calculations. The present chapter provides the first lattice field theory determination of these $(1/m_Q)^1$-spin-dependent potentials. Building on the techniques developed for hybrid static potentials in Chapter 4, our lattice calculation and analysis constitute a good starting point for future studies at multiple lattice spacings, with the ultimate goal of achieving a continuum limit extrapolation and renormalized results.

We begin by summarizing the key formulas for spin-dependent and hybrid-quarkonium mixing potentials at order $(1/m_Q)^1$ in the heavy quark mass expansion for the lowest hybrid mesons with gluon quantum numbers $\kappa^{PC} = 1^{+-}$, following Refs. [14–19]. The matching procedure between BOEFT and NRQCD relates the spin-dependent potentials to integral expressions involving generalized Wilson loops with chromomagnetic insertions [14–19]. By analytically integrating these expressions, we derive matrix elements suitable for evaluation in pure SU(3) lattice gauge theory. We investigate multiple methods to extract potential values and present results for the four $(1/m_Q)^1$-potentials V_{11}^{sa}, V_{10}^{sb}, $V_{\Sigma_u^-}^{\text{mix}}$ and $V_{\Pi_u}^{\text{mix}}$ at fixed gradient flow time and lattice spacing.

This work, including the underlying lattice calculations and data analysis, has been presented previously in Ref. [58].

6.1 Matrix form of spin-dependent potentials for $\kappa^{PC} = 1^{+-}$

The spin-dependent component of the hybrid potential in the Lagrangian at order $(1/m_Q)^1$ was introduced in Eq. (3.8). For the hybrid mesons under consideration, where the gluons possess quantum numbers $\kappa^{PC} = 1^{+-}$, it can be expressed as

$$\begin{aligned} V_{1^{+-}}^{(1),\mathrm{SD}\,n'A';nA}(\mathbf{r}) = {} & \mathcal{P}_{11}^{n'j} V_{11}^{sa}(r) \Big((\boldsymbol{S}_{Q\bar{Q}}^{p})^{A'A} \mathcal{P}_{10}^{pq} (\boldsymbol{S}_1^{q})^{jk} \Big) \mathcal{P}_{11}^{kn} \\ & + \mathcal{P}_{11}^{n'j} V_{10}^{sb}(r) \Big((\boldsymbol{S}_{Q\bar{Q}}^{p})^{A'A} \mathcal{P}_{11}^{pq} (\boldsymbol{S}_1^{q})^{jk} \Big) \mathcal{P}_{10}^{kn} + \mathcal{P}_{10}^{n'j} V_{01}^{sb}(r) \Big((\boldsymbol{S}_{Q\bar{Q}}^{p})^{A'A} \mathcal{P}_{11}^{pq} (\boldsymbol{S}_1^{q})^{jk} \Big) \mathcal{P}_{11}^{kn}, \end{aligned} \tag{6.1}$$

where the spin indices are explicitly written. The gluon spin-1 operator $(\boldsymbol{S}_1^q)^{jk} = -i\epsilon^{qjk}$ and the heavy quark spin operator $(\boldsymbol{S}_{Q\bar{Q}}^p)^{A'A}$ have three Cartesian x-, y- and z-components, $q = x, y, z$ and $p = x, y, z$, respectively.

The matrix $V_{1^{+-}}^{(1),\mathrm{SD}\,n'A';nA}$ is decomposed into radially symmetric potentials $V_{11}^{sa}(r)$, $V_{10}^{sb}(r)$ and $V_{01}^{sb}(r)$, where r is the heavy quark-antiquark separation. Time-reversal symmetry and hermiticity imply that $V_{10}^{sb} = V_{01}^{sb}$. Consequently, there are two independent hybrid spin-

dependent potentials, $V_{11}^{sa}(r)$ and $V_{10}^{sb}(r)$. The potential V_{11}^{sa} is associated with the term $\boldsymbol{S}_{Q\bar{Q}} \cdot \mathcal{P}_{10} \cdot \boldsymbol{S}_1 = \boldsymbol{S}_{Q\bar{Q}} \cdot (\mathbf{e}_r \otimes \mathbf{e}_r) \cdot \boldsymbol{S}_1$, thus, it is relevant when the gluon spin and heavy quark spin align along the quark-antiquark separation axis. Similarly, V_{10}^{sb} is proportional to $\boldsymbol{S}_{Q\bar{Q}} \cdot \mathcal{P}_{11} \cdot \boldsymbol{S}_1 = \boldsymbol{S}_{Q\bar{Q}} \cdot (1 - \mathbf{e}_r \otimes \mathbf{e}_r) \cdot \boldsymbol{S}_1$, thus, it is important when both the gluon spin and the heavy quark spin are orthogonal to the quark-antiquark separation axis.
The potential $V_{\text{mix}}^{n'n}$ appearing at order $(1/m_Q)^1$ in the Lagrangian (3.11), which is reponsible for the mixing of hybrid mesons with $\kappa^{PC} = 1^{+-}$ and ordinary quarkonium with $\kappa^{PC} = 0^{++}$, is decomposed into two independent, radially symmetric potentials

$$V_{\text{mix}}^{n'n}(\mathbf{r}) = V_{\Sigma_u^-}^{\text{mix}}(r)\mathcal{P}_{10}^{n'n} + V_{\Pi_u}^{\text{mix}}(r)\mathcal{P}_{11}^{n'n} \,. \tag{6.2}$$

$V_{\Sigma_u^-}^{\text{mix}}(r)$ denotes the component relevant for the spin components being aligned with the quark-antiquark separation axis and $V_{\Pi_u}^{\text{mix}}(r)$ is relevant for orthogonal orientation of the field spin components relative to the separation axis.
As already stated in the introduction, it is the main goal of this work to carry out the first lattice gauge theory computation of the four unknown next-to-leading order potentials, V_{11}^{sa}, V_{10}^{sb}, $V_{\Sigma_u^-}^{\text{mix}}$ and $V_{\Pi_u}^{\text{mix}}$. To achieve this, we require suitable expressions for a lattice evaluation of these potentials, which are presented in the following sections.

6.2 Spin-dependent potentials for $\kappa^{PC} = 1^{+-}$ in terms of matrix elements

6.2.1 Matching between BOEFT and NRQCD

The hybrid spin-dependent and hybrid-quarkonium mixing potentials of interest are determined by matching NRQCD and BOEFT correlators at order $(1/m_Q)^1$. In the following, we outline a matching calculation at order $(1/m_Q)^0$ and order $(1/m_Q)^1$ to introduce the notation relevant for the final expressions of the hybrid spin-dependent and hybrid-quarkonium mixing potentials. The matching calculation was conducted in Ref. [19] for the hybrid spin-dependent potentials and in Ref. [15] for the hybrid-quarkonium mixing potentials. We specifically focus on the case of gluon quantum numbers $\kappa^{PC} = 1^{+-}$ related to the lowest heavy hybrid mesons. Further details on the matching procedure for non-relativistic effective field theories can be found in Refs. [15, 17–19] and references therein.
The equivalence between NRQCD and BOEFT up to a given order in the expansion is imposed by matching the NRQCD quarkonium (hybrid) operator and the quarkonium (hybrid) field in the BOEFT in the large time limit, i.e.

$$\lim_{T\to\infty} \mathcal{O}_{\kappa^{PC}}(\mathbf{r}, \mathbf{R}, T) = \sqrt{Z_{\kappa^{PC}}}\Psi_{\kappa^{PC}}(\mathbf{r}, \mathbf{R}, T) \,. \tag{6.3}$$

Here, $\mathbf{r} = \mathbf{r}_1 - \mathbf{r}_2$ and $\mathbf{R} = (\mathbf{r}_1 + \mathbf{r}_2)/2$ denote the relative and center-of-mass coordinate of the heavy quark-antiquark pair, respectively. $\Psi_{\kappa^{PC}}(\mathbf{r}, \mathbf{R}, T)$ represents the (hybrid)

quarkonium field in the BOEFT, while $Z_{\kappa^{PC}}$ is a normalization constant. The operator $\mathcal{O}_{\kappa^{PC}}$ corresponds to a suitable NRQCD interpolating operator for a (hybrid) quarkonium state with gluon spin quantum numbers κ^{PC}. An interpolating operator for ordinary quarkonium is given by

$$\mathcal{O}_{0^{++}} = \mathcal{O}_{\Sigma_g^+} = \bar{Q}(\mathbf{r}_2)U(\mathbf{r}_2;\mathbf{r}_1)Q(\mathbf{r}_1)\,. \tag{6.4}$$

Here, $U(\mathbf{r}_2;\mathbf{r}_1)$ denotes a straight Wilson line connecting $\mathbf{r}_2$ and $\mathbf{r}_1$. The NRQCD correlator is expanded around the static limit, meaning that Q and $\bar{Q}$ denote a static quark and static antiquark, respectively. Corrections to the static limit are incorporated by an expansion of the correlator in terms of $1/m_Q$. A simple interpolating operator for the lowest quarkonium hybrid may be

$$\mathcal{O}_{1^{+-}} = \bar{Q}(\mathbf{r}_2)U(\mathbf{r}_2;\mathbf{R})\mathbf{B}(\mathbf{R})U(\mathbf{R};\mathbf{r}_1)Q(\mathbf{r}_1)\,, \tag{6.5}$$

where the chromomagnetic field ($\mathbf{B}_i = -\epsilon_{ijk}F_{jk}/2$) creates a gluonic excitation with $\kappa^{PC} = 1^{+-}$ (see e.g. Ref. [14]).

The matching procedure imposes equality between the BOEFT correlator and the NRQCD correlator order by order in the inverse heavy quark mass expansion. At order $(1/m_Q)^0$ and for arbitrary gluon spin, the matching equation takes the form

$$\sqrt{Z_{\kappa^{PC}}}e^{-itV^{(0)}_{\kappa^{PC}}(\mathbf{r})}\sqrt{Z^\dagger_{\kappa^{PC}}} = \lim_{t\to\infty}\langle\Omega|\mathcal{O}^\dagger_{\kappa^{PC}}(r,T/2)\mathcal{O}_{\kappa^{PC}}(r,-T/2)|\Omega\rangle\,. \tag{6.6}$$

The left-hand side results from evaluating the BOEFT correlator, which includes the static potential $V^{(0)}_{\kappa^{PC}}$ at this order. The right-hand side corresponds to the leading order term in the expansion of the NRQCD correlator around the static limit. It is equivalent to a Wilson loop correlation function (see Section 2.3), with creation and annihilation operators for a gluonic excitation with κ^{PC}.

At next-to-leading order, order $(1/m_Q)^1$, the matching equation for the spin-dependent terms is given by [19]

$$\begin{aligned}&\sqrt{Z_{\kappa^{PC}}}\frac{1}{T}\int_{-T/2}^{T/2}dt' e^{-i(T/2-t')V^{(0)}_{\kappa^{PC}}(\mathbf{r})}V^{(1),\,\mathrm{SD}}_{\kappa^{PC}}(\mathbf{r})e^{-i(t'+T/2)V^{(0)}_{\kappa^{PC}}(\mathbf{r})}\sqrt{Z^\dagger_{\kappa^{PC}}}\\ &= -\lim_{T\to\infty}\frac{c_F}{T}\int_{-T/2}^{T/2}dt'\mathbf{S}_{QQ}\cdot\langle\Omega|\mathcal{O}^\dagger_{\kappa^{PC}}(r,T/2)g\mathbf{B}(t',\mathbf{r}_1)\mathcal{O}_{\kappa^{PC}}(r,-T/2)|\Omega\rangle\,.\end{aligned} \tag{6.7}$$

$\langle\Omega|\mathcal{O}^\dagger_{\kappa^{PC}}(r,T/2)g\mathbf{B}(t',\mathbf{r}_1)\mathcal{O}_{\kappa^{PC}}(r,-T/2)|\Omega\rangle$ represents a generalized Wilson loop, which is a Wilson loop with a chromomagnetic field insertion $\mathbf{B}$ at position $(t',\mathbf{r}_1)$ on one of the temporal lines of the Wilson loop.

We omitted the spin indices in the above equations for better readability. In fact, these expressions are matrix-valued equations for the potentials $V^{(0)}_{\kappa^{PC}}(\mathbf{r}) = V^{(0)\,n'n}_{\kappa^{PC}}(\mathbf{r})$ and $V^{(1),\mathrm{SD}}_{\kappa^{PC}}(\mathbf{r}) = V^{(1),\mathrm{SD}\,n'A';nA}_{\kappa^{PC}}$. The potential matrices have been decomposed in Eqs. (3.3) and (3.8) employing the projection matrices $\mathcal{P}_{\kappa\Lambda} \equiv \mathcal{P}^{n'n}_{\kappa\Lambda}$, which project onto irreducible

representations of the dihedral group $D_{\infty h}$. The projection matrices $\mathcal{P}_{\kappa\Lambda}$ (3.4) are defined as $\mathcal{P}^{n'n}_{\kappa\Lambda} = \sum_{\lambda=\pm\Lambda} P^{n'}_{\kappa\lambda} P^{\dagger n}_{\kappa\lambda}$ where $P_{\kappa\lambda}$ are the normalized eigenfunctions of the gluon spin operator $\mathbf{S}^2_\kappa$ and $\mathbf{S}_\kappa \hat{\mathbf{r}}$, with $\hat{\mathbf{r}}$ denoting the quark-antiquark separation axis, i.e. they fulfill $\mathbf{S}^2_\kappa P_{\kappa\lambda} = \kappa(\kappa+1) P_{\kappa\lambda}$ and $\mathbf{S}_\kappa \hat{\mathbf{r}} P_{\kappa\lambda} = \lambda P_{\kappa\lambda}$ [147].
We now focus again on gluon spin quantum numbers $\kappa^{PC} = 1^{+-}$. Since the irreducible representations of $D_{\infty h}$ are labeled by Λ^ϵ_η in this work, we introduce projection vectors $P_{1\Lambda^\epsilon_\eta}$, such that $\mathcal{P}^{n'n}_{1\Pi} \equiv \mathcal{P}^{n'n}_{11} = \sum_{\Lambda^\epsilon_\eta = \Pi^+_u, \Pi^-_u} P^{n'}_{1\Lambda^\epsilon_\eta} P^{\dagger n}_{1\Lambda^\epsilon_\eta}$ and $\mathcal{P}^{n'n}_{1\Sigma} \equiv \mathcal{P}^{n'n}_{10} = P^{n'}_{1\Sigma^-_u} P^{\dagger n}_{1\Sigma^-_u}$ give the projection matrices as defined earlier. These projection vectors relate to $P_{1\lambda}$ via

$$P_{1\Pi^+_u} = \frac{-i}{\sqrt{2}} (P_{1-1_u} - P_{1+1_u}) \quad , \quad P_{1\Pi^-_u} = \frac{-1}{\sqrt{2}} (P_{1-1_u} + P_{1+1_u}) \quad , \quad P_{1\Sigma^-_u} = -iP_{10_u} \, . \tag{6.8}$$

Now, we can expand the interpolating operator for the lowest quarkonium hybrid in terms of representations Λ^ϵ_η

$$\mathcal{O}_{1^{+-}} = \sum_{\Lambda^\epsilon_\eta = \Pi^\pm_u, \Sigma^-_u} P^\dagger_{\Lambda^\epsilon_\eta} \mathcal{O}_{\Lambda^\epsilon_\eta} \, , \tag{6.9}$$

where

$$\mathcal{O}_{\Lambda^\epsilon_\eta} = \bar{Q}(\mathbf{r}_2) U(\mathbf{r}_2; \mathbf{R}) \mathcal{B}_{\Lambda^\epsilon_\eta}(\mathbf{R}) U(\mathbf{R}; \mathbf{r}_1) Q(\mathbf{r}_1) \tag{6.10}$$

is an interpolating operator that creates a state with definite quantum numbers Λ^ϵ_η.
For the remainder of the calculation, we place the quark and antiquark at fixed positions along the z-axis, choosing $\mathbf{r}_1 = (0,0,r/2)$ and $\mathbf{r}_2 = (0,0,-r/2)$, without loss of generality. Note that we adopt a simplified notation, where $\mathbf{r}$ is denoted as $r \equiv (0,0,r)$. In the cartesian basis representation, the projection vectors $P_{1\Lambda^\epsilon_\eta}$, as defined here, are given by

$$P_{1\Pi^+_u} = \begin{pmatrix} -i \\ 0 \\ 0 \end{pmatrix} , \, P_{1\Pi^-_u} = \begin{pmatrix} 0 \\ i \\ 0 \end{pmatrix} , \, P_{1\Sigma^-_u} = \begin{pmatrix} 0 \\ 0 \\ -i \end{pmatrix} . \tag{6.11}$$

Consequently,

$$\mathcal{B}_{\Sigma^-_u} = -iB_z \quad , \quad \mathcal{B}_{\Pi^+_u} = -iB_x \quad , \quad \mathcal{B}_{\Pi^-_u} = +iB_y \, . \tag{6.12}$$

Finally, the matching equations can be decomposed into separate equations for the radially symmetric potentials at each order in $1/m_Q$. At leading order, order $(1/m_Q)^0$, this results in

$$V_{\Lambda^\epsilon_\eta}(r) = \lim_{T\to\infty} \frac{i}{T} \ln\Big(\mathcal{P}^{n'n}_{1\Lambda} \langle \Omega | \mathcal{O}^{\dagger,n}_{1^{+-}}(r, T/2) \mathcal{O}^{n'}_{1^{+-}}(r, -T/2) | \Omega \rangle \Big) \, . \tag{6.13}$$

Using Eq. (6.9), the ordinary and lowest hybrid static potentials are determined from

$$V_{\Sigma_g^+}(r) = \lim_{T\to\infty} \frac{i}{T} \ln\Big(\langle\Omega|\mathcal{O}^\dagger_{\Sigma_g^+}(r,T/2)\mathcal{O}_{\Sigma_g^+}(r,-T/2)|\Omega\rangle\Big) \tag{6.14}$$

$$V_{\Pi_u}(r) = \lim_{T\to\infty} \frac{i}{T} \ln\left(\sum_{\Lambda_\eta^\epsilon=\Pi_u^+,\Pi_u^-} \langle\Omega|\mathcal{O}^\dagger_{\Lambda_\eta^\epsilon}(r,T/2)\mathcal{O}_{\Lambda_\eta^\epsilon}(r,-T/2)|\Omega\rangle\right) \tag{6.15}$$

$$V_{\Sigma_u^-}(r) = \lim_{T\to\infty} \frac{i}{T} \ln\Big(\langle\Omega|\mathcal{O}^\dagger_{\Sigma_u^-}(r,T/2)\mathcal{O}_{\Sigma_u^-}(r,-T/2)|\Omega\rangle\Big)\,. \tag{6.16}$$

Thus, the static potential is given by the logarithm of a Wilson loop correlation function in the large time limit.

At next-to-leading order, order $(1/m_Q)^1$, the matching equation (6.7) decomposes into separate matching equations for the spin-dependent potentials $V_{11}^{sa}(r)$ and $V_{10}^{sb}(r)$ (see Ref. [19] for details on the decomposition)

$$\begin{aligned} V_{11}^{sa}(r) =& -c_F \lim_{T\to\infty} \frac{1}{T} \frac{\mathrm{Tr}\left[\mathcal{P}_{11}\right]}{\left[\mathcal{P}_{11}^{n'n}\langle\Omega|\mathcal{O}^{\dagger,n}_{1^{+-}}\mathcal{O}^{n'}_{1^{+-}}|\Omega\rangle\right]}\times \\ & \int_{-T/2}^{+T/2} dt \frac{\left[\left(\left(\mathbf{S}_1^i\right)^{kl}\mathcal{P}_{10}^{ij}\right)\cdot\left(\mathcal{P}_{11}^{lq}\langle\Omega|\mathcal{O}^{\dagger,q}_{1^{+-}}g\mathbf{B}^j(t,+r/2)\mathcal{O}^p_{1^{+-}}|\Omega\rangle\mathcal{P}_{11}^{pk}\right)\right]}{\mathrm{Tr}\left[(\mathbf{S}_1\cdot\mathcal{P}_{10})\cdot(\mathcal{P}_{11}\mathbf{S}_1\mathcal{P}_{11})\right]} \end{aligned} \tag{6.17}$$

$$\begin{aligned} V_{10}^{sb}(r) =& -\frac{c_F}{2} \lim_{T\to\infty} \frac{V_{\Pi_u}(r)-V_{\Sigma_u^-}(r)}{\sin\Big((V_{\Pi_u}(r)-V_{\Sigma_u^-}(r))\frac{T}{2}\Big)}\times \\ & \sqrt{\frac{\mathrm{Tr}\left[\mathcal{P}_{11}\right]\ \mathrm{Tr}\left[\mathcal{P}_{10}\right]}{\left[\mathcal{P}_{11}^{n'n}\langle\Omega|\mathcal{O}^{\dagger,n}_{1^{+-}}\mathcal{O}^{n'}_{1^{+-}}|\Omega\rangle\right]\left[\mathcal{P}_{11}^{m'm}\langle\Omega|\mathcal{O}^{\dagger,m}_{1^{+-}}\mathcal{O}^{m'}_{1^{+-}}|\Omega\rangle\right]}}\times \\ & \int_{-T/2}^{+T/2} dt \frac{\left[\left(\left(\mathbf{S}_1^i\right)^{kl}\mathcal{P}_{11}^{ij}\right)\cdot\left(\mathcal{P}_{11}^{lq}\langle\Omega|\mathcal{O}^{\dagger,q}_{1^{+-}}g\mathbf{B}^j(t,+r/2)\mathcal{O}^p_{1^{+-}}|\Omega\rangle\mathcal{P}_{10}^{pk}\right)\right]}{\mathrm{Tr}\left[(\mathbf{S}_1\cdot\mathcal{P}_{11})\cdot(\mathcal{P}_{11}\mathbf{S}_1\mathcal{P}_{11})\right]}\,. \end{aligned} \tag{6.18}$$

To simplify these equations further, the action of the gluon spin operator $\mathbf{S}_1$ on the projection matrices must be evaluated, which is detailed in Appendix D together with the evaluation of the traces.

The final integral matching expressions for the spin-dependent potentials in terms of the irreducible representations Λ_η^ϵ read

$$\begin{aligned} V_{11}^{sa}(r) =& -ic_F \lim_{T\to\infty} \frac{1}{T} \\ & \int_{-T/2}^{+T/2} dt \frac{\langle\Omega|\mathcal{O}^\dagger_{\Pi_u^-}gB_z(t,+r/2)\mathcal{O}_{\Pi_u^+}|\Omega\rangle - \langle\Omega|\mathcal{O}^\dagger_{\Pi_u^+}gB_z(t,+r/2)\mathcal{O}_{\Pi_u^-}|\Omega\rangle}{\langle\Omega|\mathcal{O}^\dagger_{\Pi_u^+}\mathcal{O}_{\Pi_u^+}|\Omega\rangle + \langle\Omega|\mathcal{O}^\dagger_{\Pi_u^-}\mathcal{O}_{\Pi_u^-}|\Omega\rangle}\,, \end{aligned} \tag{6.19}$$

and

$$V_{10}^{sb}(r) = \frac{ic_F}{2} \lim_{T\to\infty} \frac{V_{\Pi_u}(r) - V_{\Sigma_u^-}(r)}{2\sin\left((V_{\Pi_u}(r) - V_{\Sigma_u^-}(r))\frac{T}{2}\right)} \int_{-T/2}^{T/2} dt \frac{\langle\Omega|\mathcal{O}^\dagger_{\Pi_u^+} gB_y(t,+r/2)\mathcal{O}_{\Sigma_u^-}|\Omega\rangle + \langle\Omega|\mathcal{O}^\dagger_{\Pi_u^-} gB_x(t,+r/2)\mathcal{O}_{\Sigma_u^-}|\Omega\rangle}{\sqrt{\frac{1}{2}\left(\langle\Omega|\mathcal{O}^\dagger_{\Pi_u^+}\mathcal{O}_{\Pi_u^+}|\Omega\rangle + \langle\Omega|\mathcal{O}^\dagger_{\Pi_u^-}\mathcal{O}_{\Pi_u^-}|\Omega\rangle\right)\langle\Omega|\mathcal{O}^\dagger_{\Sigma_u^-}\mathcal{O}_{\Sigma_u^-}|\Omega\rangle}}. \tag{6.20}$$

These equations are equivalent to those in Ref. [19], where a slightly different notation is used. The correlators in the numerator, which constitute the generalized Wilson loops, involve two hybrid operators with different Λ_η^ϵ, which were selected by the projectors. The chromomagnetic field component is inserted in between and the insertion position is integrated over.

The matching procedure was conducted in Ref. [15] for the hybrid-quarkonium mixing potentials. After analogous calculations, the final matching equations for the hybrid-quarkonium mixing potentials in terms of the irreducible representations Λ_η^ϵ are

$$V_{\Pi_u}^{\text{mix}}(r) = \frac{ic_F}{4m_Q} \lim_{T\to\infty} \frac{V_{\Pi_u}(r) - V_{\Sigma_g^+}(r)}{2\sin\left(V_{\Pi_u}(r) - V_{\Sigma_g^+}(r))\frac{T}{2}\right)} \int_{-T/2}^{T/2} dt \frac{\langle\Omega|\mathcal{O}^\dagger_{\Sigma_g^+} gB_x(t,+r/2)\mathcal{O}_{\Pi_u^+}|\Omega\rangle - \langle\Omega|\mathcal{O}^\dagger_{\Sigma_g^+} gB_y(t,+r/2)\mathcal{O}_{\Pi_u^-}|\Omega\rangle}{\sqrt{\langle\Omega|\mathcal{O}^\dagger_{\Sigma_g^+}\mathcal{O}_{\Sigma_g^+}|\Omega\rangle\,\frac{1}{2}(\langle\Omega|\mathcal{O}^\dagger_{\Pi_u^+}\mathcal{O}_{\Pi_u^+}|\Omega\rangle + \langle\Omega|\mathcal{O}^\dagger_{\Pi_u^-}\mathcal{O}_{\Pi_u^-}|\Omega\rangle)}}, \tag{6.21}$$

$$V_{\Sigma_u^-}^{\text{mix}}(r) = \frac{ic_F}{2m_Q} \lim_{T\to\infty} \frac{V_{\Sigma_u^-} - V_{\Sigma_g^+}}{2\sin\left(V_{\Sigma_u^-} - V_{\Sigma_g^+})\frac{T}{2}\right)} \int_{-T/2}^{T/2} dt \frac{\langle\Omega|\mathcal{O}^\dagger_{\Sigma_g^+} gB_z(t,+r/2)\mathcal{O}_{\Sigma_u^-}|\Omega\rangle}{\sqrt{\langle\Omega|\mathcal{O}^\dagger_{\Sigma_g^+}\mathcal{O}_{\Sigma_g^+}|\Omega\rangle\,\langle\Omega|\mathcal{O}^\dagger_{\Sigma_u^-}\mathcal{O}_{\Sigma_u^-}|\Omega\rangle}}. \tag{6.22}$$

These equations correspond to those derived in Ref. [15], where we only adjusted the notation to the one used in this work. The correlators in the numerator, the generalized Wilson loops, for the hybrid-quarkonium mixing potentials include one ordinary quarkonium operator and one hybrid operator. The resulting expressions are integrals over the temporal insertion position of the chromomagnetic field in the generalized Wilson loops in the large time limit. However, these expressions are not suited for lattice computations. In the next section, we exploit the large time limit and analytically perform the integration to relate the potentials to matrix elements, which can be extracted from lattice calculations of hybrid Wilson loops with chromomagnetic field insertions.

6.2.2 Spectral decomposition and integral evaluation

For the integration of the spin-dependent potentials we employ the spectral decomposition of the correlators

$$\begin{aligned}
&\langle\Omega|\mathcal{O}^\dagger_{\Lambda^\epsilon_\eta}(r,T/2)B_k(t,+r/2)\mathcal{O}_{\Lambda^{\epsilon\prime}_\eta}(r,-T/2)|\Omega\rangle \\
&\quad=\sum_n\sum_m\langle\Omega|\mathcal{O}^\dagger_{\Lambda^\epsilon_\eta}\left|n,\Lambda^\epsilon_\eta\right\rangle\left\langle m,\Lambda^{\epsilon\prime}_\eta\right|\mathcal{O}_{\Lambda^{\epsilon\prime}_\eta}|\Omega\rangle\left\langle n,\Lambda^\epsilon_\eta\right|B_k\left|m,\Lambda^{\epsilon\prime}_\eta\right\rangle(r) \\
&\qquad e^{-(V_{n,\Lambda^\epsilon_\eta}(r)+V_{m,\Lambda^{\epsilon\prime}_\eta}(r))T/2}e^{+(V_{n,\Lambda^\epsilon_\eta}(r)-V_{m,\Lambda^{\epsilon\prime}_\eta}(r))t} \qquad (6.23)\\
&\langle\Omega|\mathcal{O}^\dagger_{\Lambda^\epsilon_\eta}(r,T/2)\mathcal{O}_{\Lambda^{\epsilon\prime}_\eta}(r,-T/2)|\Omega\rangle \\
&\quad=\sum_n\langle\Omega|\mathcal{O}^\dagger_{\Lambda^\epsilon_\eta}\left|n,\Lambda^\epsilon_\eta\right\rangle\left\langle n,\Lambda^\epsilon_\eta\right|\mathcal{O}_{\Lambda^\epsilon_\eta}|\Omega\rangle e^{-V_{n,\Lambda^\epsilon_\eta}(r)T}\,, \qquad (6.24)
\end{aligned}$$

where sets of normalized static eigenstates $\left|n,\Lambda^\epsilon_\eta\right\rangle$ were inserted. The large time limit selects the ground state since excited states become exponentially suppressed due to their larger energy. The normalized ground state of a static quark and antiquark separated by r is defined as

$$\left|0,\Lambda^\epsilon_\eta\right\rangle=\lim_{T\to\infty}\frac{e^{-hT}\mathcal{O}_{\Lambda^\epsilon_\eta}|\Omega\rangle}{\left|e^{-hT}\mathcal{O}_{\Lambda^\epsilon_\eta}|\Omega\rangle\right|}\,, \qquad (6.25)$$

where $\mathcal{O}_{\Lambda^\epsilon_\eta}$ are the interpolating operators as definied in Eqs. (6.10) and (6.12). Consequently, the overlap factors $\langle\Omega|\mathcal{O}^\dagger_{\Lambda^\epsilon_\eta}|n,\Lambda^\epsilon_\eta\rangle=\langle n,\Lambda^\epsilon_\eta|\mathcal{O}_{\Lambda^\epsilon_\eta}|\Omega\rangle$ are positive and real. However, it is important to note that trial states created by an alternative interpolating operator may have a relative phase compared to the ground state defined above.
Using the spectral decomposition and taking the large-time limit, the integrals in the matching equations (6.19) to (6.22) can be evaluated analytically. This leads to explicit expressions for the spin-dependent potentials at order $(1/m_Q)^1$ in terms of ground-state matrix elements

$$V^{sa}_{11}(r)=\frac{igc_F}{2}\left(\left\langle0,\Pi^+_u\right|B_z(r/2)\left|0,\Pi^-_u\right\rangle(r)-\left\langle0,\Pi^-_u\right|B_z(r/2)\left|0,\Pi^-_u\right\rangle(r)\right) \qquad (6.26)$$

$$V^{sb}_{10}(r)=\frac{igc_F}{2}\left(\left\langle0,\Pi^+_u\right|B_y(r/2)\left|0,\Sigma^-_u\right\rangle(r)+\left\langle0,\Pi^-_u\right|B_x(r/2)\left|0,\Sigma^-_u\right\rangle(r)\right) \qquad (6.27)$$

$$V^{\mathrm{mix}}_{\Pi_u}(r)=\frac{igc_F}{4m_Q}\left(\left\langle0,\Sigma^+_g\right|B_x(r/2)\left|0,\Pi^+_u\right\rangle(r)-\left\langle0,\Sigma^+_g\right|B_y(r/2)\left|0,\Pi^-_u\right\rangle(r)\right) \qquad (6.28)$$

$$V^{\mathrm{mix}}_{\Sigma^-_u}(r)=\frac{igc_F}{2m_Q}\left\langle0,\Sigma^+_g\right|B_z(r/2)\left|0,\Sigma^-_u\right\rangle(r). \qquad (6.29)$$

To transform the insertion position of the chromomagnetic field from $+r/2$ to $-r/2$, we exploit the behavior of the matrix elements under a $\mathcal{P}\circ\mathcal{C}$ transformation, which reads $\left\langle0,\Lambda^\epsilon_\eta\right|B_j(-r/2)\left|0,\Lambda^{\epsilon\prime}_\eta\right\rangle=-\eta\eta'\left\langle0,\Lambda^\epsilon_\eta\right|B_j(+r/2)\left|0,\Lambda^{\epsilon\prime}_\eta\right\rangle$. Additionally, we apply a time reversal transformation under which the matrix elements behave like $\left\langle0,\Lambda^\epsilon_\eta\right|B_j(+r/2)\left|0,\Lambda^{\epsilon\prime}_\eta\right\rangle=-\left\langle0,\Lambda^{\epsilon\prime}_\eta\right|B_j(+r/2)\left|0,\Lambda^\epsilon_\eta\right\rangle$. Applying these transformations,

we obtain the final expressions for the hybrid spin-dependent and hybrid-quarkonium mixing potentials in terms of matrix elements, which we extract from lattice calculations in the following sections

$$V_{11}^{sa}(r) = \frac{igc_F}{2}\big(\langle 0,\Pi_u^-|\, B_z(-r/2)\,|0,\Pi_u^+\rangle\,(r) - \langle 0,\Pi_u^-|\, B_z(-r/2)\,|0,\Pi_u^+\rangle\,(r)\big) \tag{6.30}$$

$$V_{10}^{sb}(r) = \frac{igc_F}{2}\big(\langle 0,\Sigma_u^-|\, B_y(-r/2)\,|0,\Pi_u^+\rangle\,(r) + \langle 0,\Sigma_u^-|\, B_x(-r/2)\,|0,\Pi_u^-\rangle\,(r)\big) \tag{6.31}$$

$$V_{\Pi_u}^{\mathrm{mix}}(r) = \frac{igc_F}{4m_Q}\big(\langle 0,\Sigma_g^+|\, B_x(-r/2)\,|0,\Pi_u^+\rangle\,(r) - \langle 0,\Sigma_g^+|\, B_y(-r/2)\,|0,\Pi_u^-\rangle\,(r)\big) \tag{6.32}$$

$$V_{\Sigma_u^-}^{\mathrm{mix}}(r) = \frac{igc_F}{2m_Q}\langle 0,\Sigma_g^+|\, B_z(-r/2)\,|0,\Sigma_u^-\rangle\,(r). \tag{6.33}$$

It is important to note that Eqs. (6.30) to (6.33) depend on the choice of operators $\mathcal{B}_{\Lambda_\eta^\epsilon}$, as dictated by Eqs. (6.25) and (6.10). A different choice of operators $\mathcal{B}_{\Lambda_\eta^\epsilon}$ may lead to sign changes or introduce phase factors in Eqs. (6.30) to (6.33). This consideration will be particularly relevant for defining suitable lattice creation operators in the subsequent sections.

6.3 Lattice computation

6.3.1 Extraction of matrix elements from generalized Wilson loops

We aim to compute the hybrid spin-dependent and hybrid-quarkonium mixing potentials via the corresponding matrix elements, see Equations (6.30)-(6.33). To obtain these matrix elements, we calculate ratios of Wilson loop-like correlation functions, which asymptotically approach the desired values in the large-time limit. We define the correlator ratio as follows

$$\begin{aligned} &R^{B_k}_{\Lambda_\eta^\epsilon\Lambda_\eta^{\epsilon\prime}}(t;r,T) \\ &= W^{B_k}_{\Lambda_\eta^\epsilon\Lambda_\eta^\epsilon}(t;r,T)\left(\frac{1}{W_{\Lambda_\eta^\epsilon}(r,T)W_{\Lambda_\eta^{\epsilon\prime}}(r,T)}\right)^{1/2}\left(\frac{W_{\Lambda_\eta^{\epsilon\prime}}(r,T/2-t)W_{\Lambda_\eta^\epsilon}(r,T/2+t)}{W_{\Lambda_\eta^\epsilon}(r,T/2-t)W_{\Lambda_\eta^{\epsilon\prime}}(r,T/2+t)}\right)^{1/2}. \end{aligned} \tag{6.34}$$

Here, $W_{\Lambda_\eta^\epsilon}(r,T)$ denotes the familiar (hybrid) Wilson loop correlation function of hybrid trial states for quantum numbers Λ_η^ϵ (see Chapter 4),

$$W_{\Lambda_\eta^\epsilon}(r,T) = \langle\Omega|(O^{\mathrm{lattice}}_{\Lambda_\eta^\epsilon})^\dagger(r,T/2)O^{\mathrm{lattice}}_{\Lambda_\eta^\epsilon}(r,-T/2)|\Omega\rangle, \tag{6.35}$$

where the lattice operators $O^{\mathrm{lattice}}_{\Lambda_\eta^\epsilon}(r,T)$ are discussed in the following subsection. $W^{B_k}_{\Lambda_\eta^\epsilon\Lambda_\eta^{\epsilon\prime}}(t;r,T)$ is the generalized Wilson loop with different (hybrid) creation and annihilation operators and a chromomagnetic insertion along one of the temporal lines of the

Wilson loop,

$$W^{B_k}_{\Lambda^\epsilon_\eta \Lambda^{\epsilon\prime}_\eta}(t;r,T) = \langle\Omega|(O^{\text{lattice}}_{\Lambda^\epsilon_\eta})^\dagger(r,T/2)B^{\text{lattice}}_k(-r/2,t)O^{\text{lattice}}_{\Lambda^{\epsilon\prime}_\eta}(r,-T/2)|\Omega\rangle\,. \tag{6.36}$$

$B^{\text{lattice}}_k(-r/2,t)$ with $k=x,y,z$ is the lattice chromomagnetic field, which is inserted on the temporal line of the Wilson loop at spatial position $-r/2 \equiv (0,0,-r/2)$ and temporal position t. We discretize it on the lattice with the common clover-leaf discretization, i.e.

$$B^{\text{lattice}}_l = \frac{\epsilon_{lmn}}{2}\left(\Pi_{mn} - \Pi^\dagger_{mn}\right) = -igB_l\,, \tag{6.37}$$

where the clover-leaf plaquette is defined as

$$\Pi_{mn} = \frac{1}{4}\Big(P_{m,n} + P_{n,-m} + P_{-m,-n} + P_{-n,m}\Big). \tag{6.38}$$

The chromomagnetic field is always placed at spatial position $-r/2$ in the Wilson loop, which is consistent with Eqs. (6.30) to (6.33). So, we omit the spatial argument in the remainder of this work.

$t=0$ denotes the center of the Wilson loops on the temporal axis. For odd temporal extension T, the midpoint of the temporal line lies between two lattice sites, while for even T, it coincides with a lattice site. Consequently, valid insertion positions for the chromomagnetic field are $t/a = \ldots, -1,\ 0,\ 1, \ldots$ for even T and $t/a = \ldots, -3/2,\ -1/2,\ 1/2,\ 3/2, \ldots$ for odd T. At $t=0$, the chromomagnetic field is symmetrically inserted between the two spatial transporters of the Wilson loop. For $t<0$, the field is closer to the transporter at $-T/2$, while for $t>0$, it is closer to the one at $T/2$.

We defined the correlator ratio (6.34) so that it asymptotically approaches the matrix element of interest in the large time limit. This can be proven by inserting the spectral decomposition of the Wilson loops, Eqs. (6.24) and (6.23). As $T\to\infty$, excited-state contributions are exponentially suppressed and the ground state dominates. The first square root in the denominator of Eq. (6.34) cancels the overlap factors $\langle\Omega|(O^{\text{lattice}}_{\Lambda^\epsilon_\eta})^\dagger\left|0,\Lambda^\epsilon_\eta\right\rangle$ and $\left\langle 0,\Lambda^{\epsilon\prime}_\eta\right| O^{\text{lattice}}_{\Lambda^{\epsilon\prime}_\eta}|\Omega\rangle$ along with the exponential T-dependence in the dominating term from the spectral decomposition. Similarly, the second square root eliminates the residual t-dependence. In the large T-limit, the so-defined correlator ratio (6.34) approaches a plateau

$$\lim_{T\to\infty} R^{B_k}_{\Lambda^\epsilon_\eta \Lambda^{\epsilon\prime}_\eta}(t;r,T) = \left\langle 0,\Lambda^\epsilon_\eta\right| B^{\text{lattice}}_k \left|0,\Lambda^{\epsilon\prime}_\eta\right\rangle(r) = -ig\left\langle 0,\Lambda^\epsilon_\eta\right| B_k \left|0,\Lambda^{\epsilon\prime}_\eta\right\rangle(r). \tag{6.39}$$

The asymptotic value of this ratio directly yields the matrix element of interest, which depends on the spatial separation of the static quark and antiquark r but is independent of the temporal insertion position t.

For finite T, the leading contamination from excited states in Eq. (6.39) is expected to arise from the Wilson loops in the second square root. The dominant excited-state contamination comes from the Wilson loop with Λ^ϵ_η with the smallest energy gap between the ground

state and the first excited state and the shortest temporal extent, $T/2 - |t|$. As a result, excited-state contamination is less suppressed in ratios with $t \neq 0$, so we expect that they reach the plateau slightly later than those with $t = 0$. However, for sufficiently large T, all ratios eventually converge to the same plateau, corresponding to the desired ground-state matrix element. Thus, it is beneficial to incorporate ratios with different t into the analysis. This approach enhances the signal by increasing statistics while providing some control on systematic uncertainties from excited states.
Besides the definition in Eq. (6.34), other ratio formulations could also be used to extract the matrix elements. Later, we introduce an alternative approach and compare it to the ratio method discussed here.

6.3.2 Lattice creation operators and their phase

The interpolating operators/creation operators defined in Eqs. (6.10) and (6.12) are not ideal for use in the lattice Wilson loops due to their relatively poor ground-state overlap. In Chapter 4, we already employed optimized lattice creation operators from Ref. [51] to compute Wilson loops and precisely extract the hybrid static potentials Π_u and Σ_u^-. These optimized operators, as defined in Eqs. (4.3) and (4.4), consist of a weighted sum of properly rotated non-trivially shaped paths of gauge links. This structure enhances the ground-state overlap compared to chromomagnetic field components as operators. Consequently, we adopt the optimized lattice operators for the computation of spin-dependent potentials as well. The hybrid Wilson loops are, thus, computed on the lattice from Eq. (4.2). Accordingly, the generalized Wilson loop is computed on the lattice from

$$\begin{aligned} &W^{B_k}_{\Lambda_\eta^\epsilon \Lambda_\eta^{\epsilon\prime}}(t; r, T) \\ &\quad = \Big\langle \mathrm{Tr}\Big(a_{S',\Lambda_\eta^{\epsilon\prime}}(-r/2, r/2; -T/2) U(r/2; -T/2, T/2) \Big(a_{S,\Lambda_\eta^\epsilon}(-r/2, r/2; T/2) \Big)^\dagger \\ &\qquad U(-r/2; T/2, t) B_k^{\text{lattice}}(-r/2, t) U(-r/2; t, -T/2) \Big) \Big\rangle_U , \end{aligned} \tag{6.40}$$

where the creation operators $a_{S,\Lambda_\eta^\epsilon}(-r/2, r/2; T/2)$ are defined in Eq. (4.4) and $\langle \ldots \rangle_U$ denotes the average on the ensemble of gauge link configurations.
As before, we apply APE smearing to the spatial links, as it significantly increases the ground-state overlap. The smearing parameters are chosen following the calculations in Chapter 4.
The shape of the gauge-link path S, which serves as the fundamental building block of the lattice creation operators in Eq. (4.4), defines the structure of the creation operator for the quantum numbers Λ_η^ϵ. Similar to Chapter 4, we choose $S = S_{\mathrm{IV},2}$ for $\Lambda_\eta^\epsilon = \Sigma_u^-$ and $S = S_{\mathrm{III},1}$ for $\Lambda_\eta^\epsilon = \Pi_u^+$. In order for $\mathcal{O}^{\text{lattice}}_{\Pi_u^+}$ and $\mathcal{O}^{\text{lattice}}_{\Pi_u^-}$ to have the same structure, we use for Π_u^- $S = R(-\pi/2) S_{\mathrm{III},1}$, which is a counterclockwise $\pi/2$ rotation of the insertion $S_{\mathrm{III},1}$ with respect to the z axis. It is important to note that an operator, which we label with $\mathcal{O}^{\text{lattice},2}_{\Pi_u^+}$, built for Π_u^- using the non-rotated insertion $S_{\mathrm{III},1}$, has a different operator

structure than $\mathcal{O}^{\text{lattice}}_{\Pi_u^+}$. Even though this alternative operator also generates states with quantum numbers Π_u^-, it generates smaller ground-state overlap and was, thus, only used for numerical cross-checks and not for the final results.
To ensure consistency with Eq. (6.25), the lattice operators $\mathcal{O}^{\text{lattice}}_{\Lambda_\eta^\epsilon}$ must be defined such that they satisfy the condition

$$\left|0,\Lambda_\eta^\epsilon\right\rangle = \lim_{T\to\infty} \frac{e^{-hT}\mathcal{O}^{\text{lattice}}_{\Lambda_\eta^\epsilon}|\Omega\rangle}{\left|e^{-hT}\mathcal{O}^{\text{lattice}}_{\Lambda_\eta^\epsilon}|\Omega\rangle\right|}, \tag{6.41}$$

where $|0,\Lambda_\eta^\epsilon\rangle$ is identical to the ground state defined in Eq. (6.25). As we already discussed, defining $|0,\Lambda_\eta^\epsilon\rangle$ here with a relative phase to the first definition in Eq. (6.25) would lead to an inconsistency with Eqs. (6.30)-(6.33). In order to ensure consistency, we replace the lattice operators with

$$\mathcal{O}^{\text{lattice}}_{\Lambda_\eta^\epsilon} \;\to\; \underbrace{\left(\lim_{T\to\infty} \frac{\langle\Omega|(\mathcal{O}^{\text{lattice}}_{\Lambda_\eta^\epsilon})^\dagger e^{-hT}\mathcal{O}_{\Lambda_\eta^\epsilon}|\Omega\rangle}{\left|\langle\Omega|(\mathcal{O}^{\text{lattice}}_{\Lambda_\eta^\epsilon})^\dagger e^{-hT}\mathcal{O}_{\Lambda_\eta^\epsilon}|\Omega\rangle\right|}\right)}_{=\alpha_{\Lambda_\eta^\epsilon}} \mathcal{O}^{\text{lattice}}_{\Lambda_\eta^\epsilon}, \tag{6.42}$$

where $\alpha_{\Lambda_\eta^\epsilon}$ is the relative phase between $\mathcal{O}_{\Lambda_\eta^\epsilon}$ and $\mathcal{O}^{\text{lattice}}_{\Lambda_\eta^\epsilon}$, which takes values of either $+1$ or -1. The phase depends on the exact shape of $\mathcal{O}^{\text{lattice}}_{\Lambda_\eta^\epsilon}$.
In order to determine the relative phase, we compute the $\alpha_{\Lambda_\eta^\epsilon}$ using $\mathcal{O}^{\text{lattice}}_{\Lambda_\eta^\epsilon}$ as defined in Eqs. (4.3) and (4.4) and $\mathcal{O}_{\Lambda_\eta^\epsilon}$ as given in Eqs. (6.10) and (6.12). Numerical results show that $\alpha_{\Sigma_g^+} = \alpha_{\Sigma_u^-} = \alpha_{\Pi_u^+} = \alpha_{\Pi_u^-} = +1$. A graphical analysis of the operator structure can further support this. By projecting the operators $a_{S;\Lambda_\eta^\epsilon}$ onto the plane of the associated chromomagnetic field $\mathcal{B}_{\Lambda_\eta^\epsilon}$, we observe consistent orientation between the operator projection and the plaquettes forming the chromomagnetic field operator. Specifically, projecting the operator $a_{S_{III,1};\Pi_u^+}$ onto the yz-plane shows alignment with the plaquettes that constitute $\mathcal{B}_{\Pi_u^+} \sim B_x^{\text{lattice}}$. Similarly, $a_{S_{III,1};\Pi_u^-}$, when projected onto the xz-plane, displays the same orientation to $\mathcal{B}_{\Pi_u^-} \sim -B_y^{\text{lattice}}$, as expected. Lastly, $a_{S_{IV,2};\Sigma_u^-}$ shows a matching orientation with $\mathcal{B}_{\Sigma_u^-} \sim B_z^{\text{lattice}}$.

6.3.3 Lattice setup

We perform the first direct lattice calculation of hybrid spin-dependent potentials $V_{11}^{sa}(r)$, $V_{10}^{sb}(r)$, $V_{\Sigma_u^-}^{\text{mix}}(r)$ and $V_{\Pi_u}^{\text{mix}}(r)$. To this end, we employ one of the four SU(3) lattice gauge ensembles used in the previous chapters, specifically ensemble B, which has a lattice spacing of $a = 0.060\,\text{fm}$ (see Table 4.3 for details). By employing ensemble B, we obtain lattice data for these potentials at intermediate quark-antiquark separations, making this ensemble a solid starting point to explore their behavior. Furthermore, this setup serves as a foundation for future studies aiming at continuum-extrapolated results.
In previous chapters, we have employed the multilevel algorithm [77] to reduce statistical

errors. In this chapter, we use another promising method, the gradient flow [68], which has already been applied for related correlators in Refs. [71, 74–76] (see also Section 2.4.3). We employ an implementation of the gradient flow algorithm carried out in the context of Refs. [76, 106].

The gradient flow serves as a smearing procedure, in which the gauge fields are smeared over a sphere of radius $r_f = \sqrt{8t_f}$ and, thus, reduces significantly undesired ultraviolet (UV) fluctuations. In order to avoid discretization effects from overlapping gauge links in the Wilson loop, we ensure that the separation of operators in both the temporal and spatial directions is larger than $2r_f$. Specifically, for (hybrid) Wilson loops without an insertion along the temporal line, the constraint for its spatial and temporal extents reads $r, T \geq 2r_f$. For Wilson loops with an insertion, we require the smallest distance between the operator and the inserted field to be sufficiently large, which translates to $T/2 - |t| \geq 2r_f$, where t denotes the insertion position (see Eq. (6.36)). Additionally, for chromomagnetic insertions extending along the separation axis, we impose the constraint $r \geq 2r_f + a$.

We compute the correlators at several flow times in the range $0 \leq t_f/a^2 \leq 1.445$. These flow times correspond to flow radius range of $0 \leq r_f/a \leq 3.4$. The larger the flow radius, the better the signal-to-noise ratio. However, due to discretization effects, the reliable region of lattice results for the potentials is restricted. We present results for a representative flow radius $r_f/a = 1.8$ in the following. This choice is justified by the conclusions on the gradient flow dependence of our results made in Section 6.4.2.

The gradient flow is also a useful renormalization scheme for the correlators of interest involving chromomagnetic field insertions [148]. For the potentials (6.30) to (6.33) to be finite, the divergent chromomagnetic matrix elements $\langle 0, \Lambda_\eta^\epsilon | B_k | 0, \Lambda_\eta^{\epsilon\prime} \rangle (r)$ are multiplied with a matching coefficient c_F. The matching coefficients $c_F(t_f, \mu)$ are known for the conversion from gradient flow as a renormalization scheme with scale t_f to the $\overline{\text{MS}}$ scheme with the renormalization scale μ up to one-loop order [73, 74]. Thus, given results of the matrix element at several lattice spacings and flow times, the product of matching coefficient and matrix element can be extrapolated to the continuum at fixed flow times. Performing a continuum extrapolation of flowed observables with chromomagnetic insertions is particularly advantageous, as the convergence is expected to be significantly improved compared to non-flowed observables. After this extrapolation, any remaining dependence on the flow time can be removed by an additional flow time extrapolation to $t_f \to 0$.

In this work, we explore the gradient flow procedure for calculating hybrid spin-dependent potentials at a single lattice spacing. Our results demonstrate that the chosen setup, in combination with gradient flow, is promising. They suggest that our calculations and analysis can be extended to multiple lattice spacings and flow times in future studies. This extension will allow for a precise continuum and zero-flow time extrapolation.

6.4 Numerical results

6.4.1 Potentials at finite lattice spacing and flow radius

In the following, we present correlator ratios $R^{B_k}_{\Lambda_\eta^\epsilon \Lambda_\eta^{\epsilon\prime}}(t;r,T)$ defined in Eq. (6.34) computed at lattice spacing $a = 0.060\,\mathrm{fm}$ and flow radius $r_f/a = 1.8$ and discuss the methods used to extract the corresponding potentials.

We exploit translational and rotational symmetry in our calculations. Precisely, correlators involving $\mathcal{O}^{\mathrm{lattice}}_{\Pi_u^+}$ and $\mathcal{O}^{\mathrm{lattice}}_{\Pi_u^-}$, which correspond to the same potential (see Eq. (6.31) and (6.32)) and are related by rotational symmetry, are averaged.

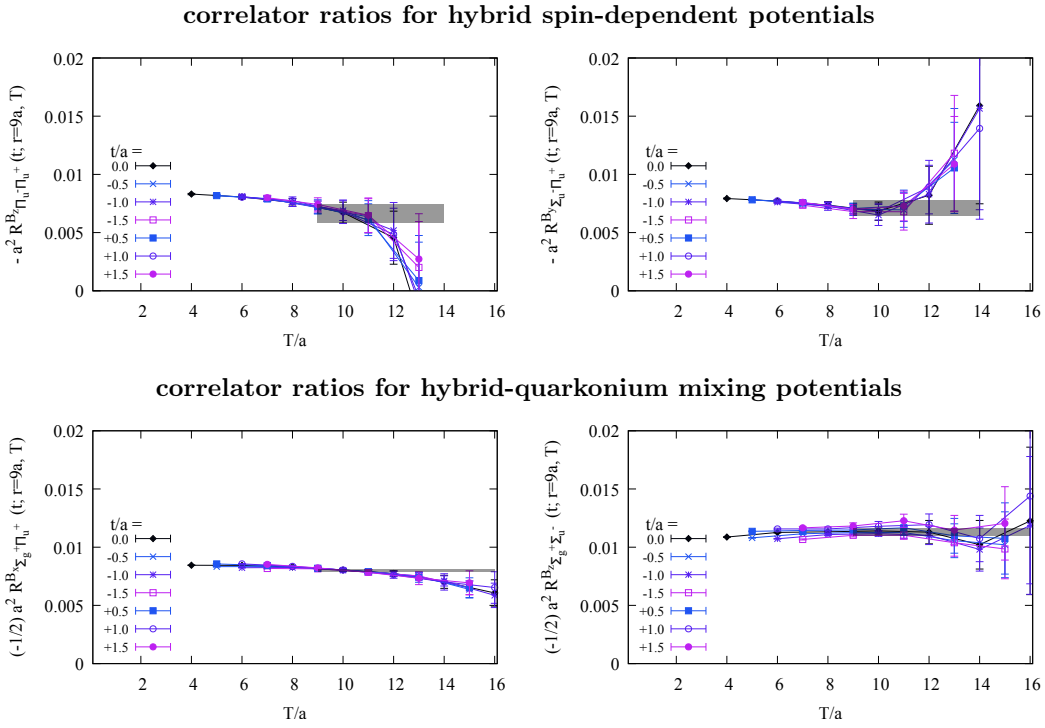

Figure 6.1: Correlator ratios $-R^{B_z}_{\Pi_u^-\Pi_u^+}(t;r=9a,T)$, $-R^{B_y}_{\Sigma_u^-\Pi_u^+}(t;r=9a,T)$, $-(1/2)R^{B_x}_{\Sigma_g^+\Pi_u^+}(t;r=9a,T)$ and $-(1/2)R^{B_z}_{\Sigma_g^+\Sigma_u^-}(t;r=9a,T)$ in units of the lattice spacing $a = 0.060\,\mathrm{fm}$ at flow radius $r_f/a = 1.8$. The prefactors -1 and $-1/2$ were chosen such that the asymptotic values at large T correspond to $V_{11}^{sa}(r=9a)/c_F$ (top left), $V_{10}^{sb}(r=9a)/c_F$ (top right), $V^{\mathrm{mix}}_{\Sigma_u^-}(r=9a)m_Q/c_F$ (bottom left) and $V^{\mathrm{mix}}_{\Pi_u}(r=9a)m_Q/c_F$ (bottom right), see Eqs. (6.39) and (6.30) to (6.33). Each gray band represents a fit of a constant to data points fulfilling both $T/2-|t|\geq 2r_f$ and $9a \leq T \leq T_{\mathrm{max}}$.

In Figure 6.1 we show the relevant ratios $R^{B_k}_{\Lambda_\eta^\epsilon \Lambda_\eta^{\epsilon\prime}}(t;r,T)$ for the four hybrid spin-dependent and hybrid-quarkonium mixing potentials. The ratios are presented as functions of T for the exemplary spatial separation of $r = 9a = 0.54\,\mathrm{fm}$. We consider several temporal positions of the chromomagnetic field insertion $t/a = -3/2,\ -1,\ -1/2,\ 0,\ +1/2,\ +1,\ +3/2$.

The ratios with different t/a approach their asymptotic values in the computed range of T/a, although ratios with $t \neq 0$ exhibit observable excited-state contributions and tend to reach their plateau slightly later. Moreover, excited-state contributions are more pronounced in the ratios related to hybrid spin-dependent potentials (top row of Figure 6.1) than in those related to hybrid-quarkonium mixing potentials (bottom row). The reason is that the operator for the trivial, non-excited gluon configuration Σ_g^+ generates a larger ground-state overlap compared to hybrid operators. This behavior is explained by the more complex gluon configurations of hybrid states, which are more challenging to approximate using lattice operators. These configurations have been studied in detail in Refs. [49, 149]. The asymptotic values of the ratios as shown in Figure 6.1 correspond directly to the potentials $V_{11}^{sa}(r)/c_F$, $V_{10}^{sb}(r)/c_F$, $V_{\Sigma_u^-}^{\text{mix}}(r)m_Q/c_F$ and $V_{\Pi_u}^{\text{mix}}(r)m_Q/c_F$ (see Eqs. (6.30) to (6.33)). We extract these values by fitting a constant to the available set of ratios, which includes multiple values of t. The range of T included in the fit is constrained by the gradient flow radius r_f. We exclude ratios where $T/2 - |t| < 2r_f$ to avoid overlapping effects. In the following, we explore different methods for determining the fit range $T_{\text{min}} \leq T \leq T_{\text{max}}$.

In all approaches, the upper bound, T_{max}, is set to maintain a moderate noise-to-signal ratio, significantly below unity. We adopt $T_{\text{max}}/a = 14$ for hybrid spin-dependent potentials, while for hybrid-quarkonium mixing potentials, we set $T_{\text{max}}/a = 16$.

The starting point for the determination of T_{min} is a fit algorithm, which is inspired by the one used in previous chapters. The lower bound $T_{\text{min}}(t, r)$ was chosen as the smallest T, where $|R^{B_k}_{\Lambda_\eta^\epsilon \Lambda_\eta^{\epsilon\prime}}(t; r, T) - R^{B_k}_{\Lambda_\eta^\epsilon \Lambda_\eta^{\epsilon\prime}}(t; r, T + a)| < 2\sigma[R^{B_k}_{\Lambda_\eta^\epsilon \Lambda_\eta^{\epsilon\prime}}](t; r, T + a)$ with $\sigma[R^{B_k}_{\Lambda_\eta^\epsilon \Lambda_\eta^{\epsilon\prime}}]$ denoting the statistical error.

Most ratios satisfy this plateau criterion already at the smallest T fulfilling $T/2 - |t| \geq 2r_f$. With these $T_{\text{min}}(t, r)$, we obtain reasonable fits indicated by reduced χ^2 values of order 1. Typically, $T_{\text{min}}(t = 0, r)/a = 8$, though, for example, for $V_{10}^{sb}(r)$ the algorithm selects $T_{\text{min}}(t = 0, r)/a = 10$ for $3 \leq r/a \leq 7$. Consequently, the resulting potential shows a large variation of statistical uncertainties between neighboring potential data points, which is not due to a change in the data quality but the abrupt change in $T_{\text{min}}(t, r)$. To address this issue, we investigated an alternative approach in which a fixed T_{min} is applied uniformly across all values of t and r, ensuring more consistent statistical uncertainties. We test three different values for the fixed lower bound, $T_{\text{min}}/a = 8$, $T_{\text{min}}/a = 9$ and $T_{\text{min}}/a = 10$. The extracted potential values obtained with $T_{\text{min}}/a = 8$ and $T_{\text{min}}/a = 9$ are found to agree, with a slight trend that the potentials determined using $T_{\text{min}}/a = 9$ are slightly lower than those extracted at $T_{\text{min}}/a = 8$. Moreover, $T_{\text{min}}/a = 10$ does not significantly alter the central values of the extracted potentials but led to a noticeable increase in statistical errors. Based on these findings, we conclude that using $T_{\text{min}}/a = 9$ represents an optimal choice, balancing the need for stable statistical uncertainties. This choice ensures consistency across different values of r and facilitates a smoother interpolation or parametrization of the extracted potentials.

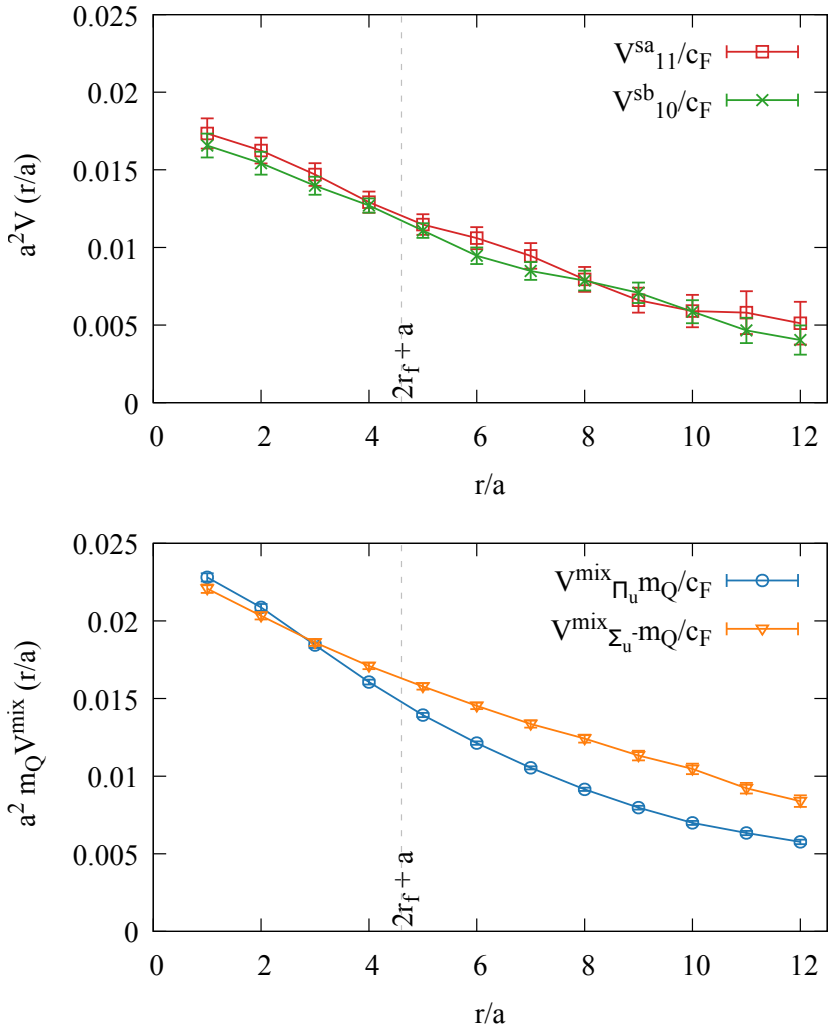

Figure 6.2: Hybrid spin-dependent potentials $V_{11}^{sa}(r)/c_F$ and $V_{10}^{sb}(r)/c_F$ (left) and hybrid-quarkonium mixing potentials $V_{\Sigma_u^-}^{\text{mix}}(r)m_Q/c_F$ and $V_{\Pi_u}^{\text{mix}}(r)m_Q/c_F$ (right) in units of the lattice spacing $a = 0.060\,\text{fm}$ at flow radius $r_f = \sqrt{8t_f} = 1.8\,a$.

The final results for the potentials, obtained using this refined fitting procedure, are presented as a function of the quark-antiquark separation in Figure 6.2 and are summarized in Tables E.5 and E.6.

Alternative ratio method

Beyond the ratio defined in Eq. (6.34), alternative approaches can be used to extract the matrix elements in Eqs. (6.30)-(6.33). One such alternative is the following ratio

$$R^{B_k}_{2;\Lambda_\eta^\epsilon\Lambda_\eta^{\epsilon\prime}}(t;r,T) = \frac{W^{B_k}_{\Lambda_\eta^\epsilon\Lambda_\eta^{\epsilon\prime}}(t;r,T)}{W_{\Lambda_\eta^\epsilon}(r,T/2-t)W_{\Lambda_\eta^{\epsilon\prime}}(r,T/2+t)}\,. \tag{6.43}$$

In the limit $T \to \infty$, this ratio approaches

$$R^{B_k}_{2;\Lambda^\epsilon_\eta \Lambda^{\epsilon\prime}_\eta}(t;r,T) \to_{T\to\infty} \frac{\left\langle 0,\Lambda^\epsilon_\eta\right| B^{\text{lattice}}_k \left|0,\Lambda^{\epsilon\prime}_\eta\right\rangle(r)}{\left\langle 0,\Lambda^\epsilon_\eta\right| O^{\text{lattice}}_{\Lambda^\epsilon_\eta}|\Omega\rangle\langle\Omega|(O^{\text{lattice}}_{\Lambda^{\epsilon\prime}_\eta})^\dagger \left|0,\Lambda^{\epsilon\prime}_\eta\right\rangle}\,. \tag{6.44}$$

The quality of the alternative ratios and their plateaus is comparable to those shown in Figure 6.1.

Since the ground-state overlaps $\langle 0,\Lambda^\epsilon_\eta|O^{\text{lattice}}_{\Lambda^\epsilon_\eta}|\Omega\rangle = \langle\Omega|(O^{\text{lattice}}_{\Lambda^\epsilon_\eta})^\dagger|0,\Lambda^\epsilon_\eta\rangle$ are positive, as ensured by Eq. (6.41), we can extract them from a single exponential fit of $W_{\Lambda^\epsilon_\eta}(r,T)$ and $W_{\Lambda^{\epsilon\prime}_\eta}(r,T)$ in the large time limit with the fit function $W_{\Lambda^\epsilon_\eta}(r,T) = \left(\langle 0,\Lambda^\epsilon_\eta|O^{\text{lattice}}_{\Lambda^\epsilon_\eta}|\Omega\rangle\right)^2 e^{-V_{0,\Lambda^\epsilon_\eta}(r)T}$. This alternative ratio provides an independent way to verify the matrix elements extracted using the primary method discussed in the previous section. The asymptotic values of the alternative Wilson loop correlator ratio (see Eq. (6.44)) are extracted from a plateau fit in the large T range, similar to the method discussed earlier. Once the overlap factors are obtained, the matrix elements are obtained by multiplying the plateau values with the corresponding ground-state overlaps. The results are statistically consistent with those obtained from the ratio in Eq. (6.34). The consistency of the extracted values further validates the reliability of our primary method and confirms that systematic uncertainties are well under control.

6.4.2 Flow time dependence of correlator ratios and matrix elements

One of the key benefits of the gradient flow is the significant enhancement in the signal quality of correlators. This improvement is demonstrated in Figure 6.3, where we plot

$$S(t;r,T) = \frac{\Delta R^{B_x}_{\Sigma_g^+\Pi_u^+}(t;r,T)\Big|_{t_f}}{\Delta R^{B_x}_{\Sigma_g^+\Pi_u^+}(t;r,T)\Big|_{t_f=0}}, \tag{6.45}$$

which represents the statistical error of $R^{B_x}_{\Sigma_g^+\Pi_u^+}(t;r,T)$ at flow time $t_f \geq 0$ normalized by its statistical error at $t_f = 0$. The dependence on t_f is shown for several values of T with fixed $t = 0$ and $r/a = 9$. The statistical errors are drastically reduced by the gradient flow, with the most significant improvement for $t_f/a^2 \geq 0.4$ or $r_f/a \geq 1.8$.

On the one hand, the larger the flow time t_f and, thus, the flow radius r_f, the smaller the relative error of the correlator ratio. On the other hand, a larger flow radius shifts the reliable range of T and r to significantly larger separations because, as discussed earlier, discretization errors may arise due to the overlapping of smeared operators. In particular, when the distance between two operators is smaller than $2r_f$ systematic errors introduced by the flow radius become sizable. For instance, this effect is noticeable for $T \lesssim 2r_f$ in the effective potentials for ordinary and hybrid static potentials at small T/a. Discretization effects for $r \lesssim 2r_f$ are illustrated in Figure 6.4, where we show the difference of ordinary static potential data at several flow radii from a fit of the non-flowed data of the ordinary

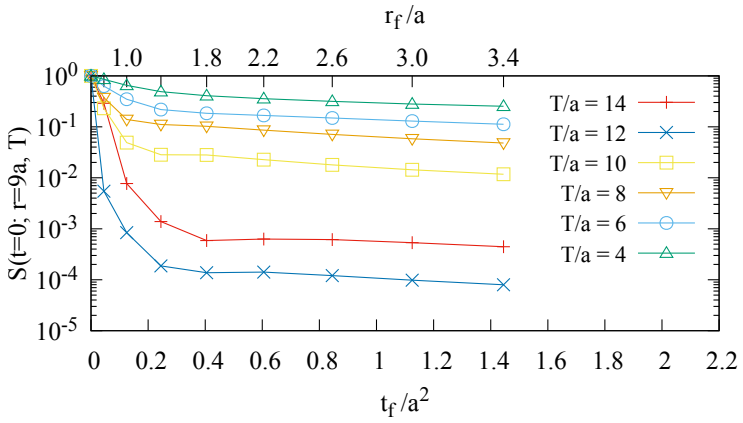

Figure 6.3: Relative error $S(t=0; r=9a, T)$ as defined in Eq. (6.45) as function of the flow time t_f/a^2 for several T.

static potential. The data points coincide only for $r \geq 2r_f$. Below this bound, discretization effects due to overlapping flowed operators lead to distortions from the non-flowed potential result. Potential data for $r < 2r_f$ should be interpreted with caution to ensure a reliable analysis. In the previous section, we presented results for an intermediate flow radius of $r_f/a = 1.8$ to balance signal improvement and data reliability. This choice ensures a significant reduction of statistical error while maintaining an acceptable range of lattice data for the analysis of potentials.

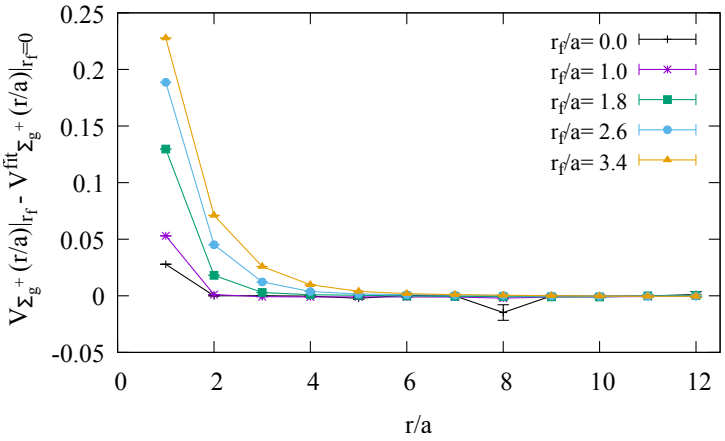

Figure 6.4: Difference between flowed and non-flowed ordinary static potential $V_{\Sigma_g^+}(r/a)|_{r_f} - V^{\text{fit}}_{\Sigma_g^+}(r/a)|_{r_f/a=0}$ as a function of r/a for different flow radii r_f. $V^{\text{fit}}_{\Sigma_g^+}(r/a)|_{r_f=0}$ has been obtained from a fit of the Cornell potential to the lattice data $V_{\Sigma_g^+}(r/a)$ at flow radius $r_f/a = 0$ in the range $2a \leq r \leq 11a$.

Data at multiple lattice spacings are currently unavailable, preventing a continuum limit $a \to 0$. Nonetheless, we analyze the flow time dependence of the matrix elements. The flow time dependence of the matrix elements $\langle 0, \Pi_u^- | \, B_z^{\text{lattice}} \, | 0, \Pi_u^+ \rangle \, (r)$, $\langle 0, \Sigma_u^- | \, B_y^{\text{lattice}} \, | 0, \Pi_u^+ \rangle \, (r)$,

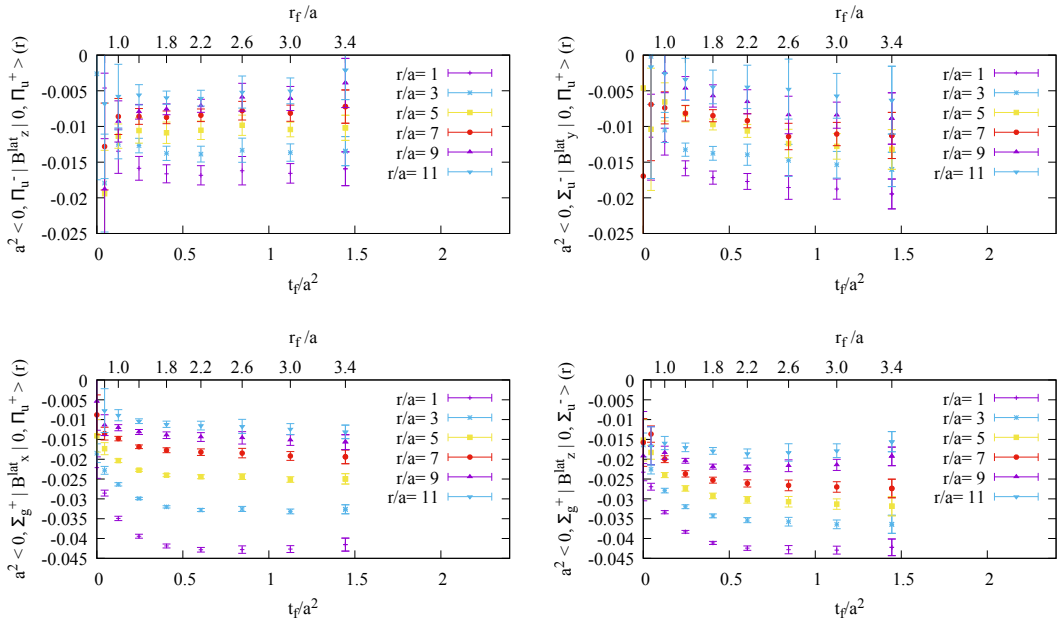

Figure 6.5: The matrix elements $a^2 \langle 0, \Pi_u^- | B_z^{\text{lattice}} | 0, \Pi_u^+ \rangle (r)$ (top left), $a^2 \langle 0, \Sigma_u^- | B_y^{\text{lattice}} | 0, \Pi_u^+ \rangle (r)$ (top right), $a^2 \langle 0, \Sigma_g^+ | B_x^{\text{lattice}} | 0, \Pi_u^+ \rangle (r)$ (bottom left) and $a^2 \langle 0, \Sigma_g^+ | B_z^{\text{lattice}} | 0, \Sigma_u^- \rangle (r)$ (bottom right) for selected separations r as functions of the flow time t_f/a^2.

$\langle 0, \Sigma_g^+ | B_x^{\text{lattice}} | 0, \Pi_u^+ \rangle (r)$ and $\langle 0, \Sigma_g^+ | B_z^{\text{lattice}} | 0, \Sigma_u^- \rangle (r)$ for several fixed r as a function of the flow time is displayed in Figure 6.5. These matrix elements are directly related to the potentials $V_{11}^{sa}(r)$, $V_{10}^{sb}(r)$, $V_{\Sigma_u^-}^{\text{mix}}(r)$ and $V_{\Pi_u}^{\text{mix}}(r)$ up to a multiplicative factor, namely the matching coefficient $c_F(t_f, \mu)$. Assuming discretization effects are small, the matrix elements exhibit a relatively weak flow-time dependence. From perturbation theory, one expects that a logarithmic dependence should be canceled by the logarithmic flow-time dependence of $c_F(t_f, \mu)$, which is known up to one-loop order [73, 74]. These findings suggest that a combined continuum limit and zero-flow-time extrapolation is feasible once computations are performed at multiple lattice spacings. Related studies [71, 74–76, 148, 150] have explored different methods for continuum and zero-flow-time extrapolations for related observables. These techniques could be applied to our results in future work, enabling the determination of fully renormalized hybrid spin-dependent potentials suitable for precise parametrizations.

6.4.3 Comparison with parametrizations in the literature

The presented lattice data correspond to the hybrid spin-dependent potentials $V^{sa}(r)$ and $V^{sb}(r)$ as well as the hybrid-quarkonium mixing potentials $V_{\Pi_u}^{\text{mix}}(r) m_Q/2$ and $V_{\Sigma_u^-}^{\text{mix}}(r) m_Q/2$, up to a multiplicative constant c_F (see Eqs. (6.30))-(6.33)) and possible minor systematic effects arising from the finite lattice spacing a and finite flow time t_f. These first-principles

lattice gauge theory computations provide a crucial initial insight into spin-dependent corrections, including hybrid-quarkonium mixing with ordinary quarkonium. Moreover, they demonstrate the feasibility of a more precise extraction of these potentials. While a combined continuum-limit and zero-flow-time extrapolation remains a necessary future step, the current lattice results are expected to be close to that limit within the given precision. Since these are the first lattice field theory results that directly determine these potentials for quark-antiquark separations $0.30\,\text{fm} \lesssim r \lesssim 0.72\,\text{fm}$, we want to compare them exemplarily to existing parametrizations in the literature. This is not intended as a rigorous comparison, as further steps remain necessary, but rather as an illustration of how our lattice study enables possible improvements in heavy hybrid meson mass predictions previously performed in Refs. [15,17,18,23].

In the literature, spin effects in the heavy hybrid meson spectra due to hybrid spin-dependent and hybrid quarkonium mixing potentials have been explored using a combination of approaches. The short-distance behavior of the potentials can be derived from potential non-relativistic QCD (pNRQCD). For instance, the short-distance multipole expansion of $V^{sa}_{1^+11}(r)$ and $V^{sb}_{1^+10}(r)$ with non-perturbative parameters has been given in Eqs. (3.9) and (3.10) [17,18]. These non-perturbative parameters are expressed in terms of r-independent gluonic correlators in Ref. [17,18] but have not been calculated yet. Thus, they were estimated through fits to existing charmonium hybrid meson spectrum data in Refs [17,18] and subsequently, predictions have been extended to the bottomonium sector. For $r \to 0$, the hybrid spin-dependent potentials are expected to be degenerate. The short-distance prediction for the hybrid-quarkonium mixing potentials [15] reads

$$V^{\text{mix}}_{\Pi_u}(r) = V^{\text{mix}}_{\Sigma_u^-}(r) = \frac{\pm c_F \lambda^2}{m_Q}\,. \tag{6.46}$$

with an unknown sign and parameter λ.

In Refs. [15,23], interpolating functions for the potentials were employed, which incorporate the expected long-distance behavior of the potentials from QCD effective string theory, which are given by

$$V^{sa}_{1^+11}(r) = -\frac{2c_F\pi^2 g\Lambda'''}{\sigma}\frac{1}{r^3} \tag{6.47}$$

$$V^{sb}_{1^+10}(r) = \mp\frac{c_F g\Lambda'\pi^2}{\sqrt{\pi\sigma}}\frac{1}{r^2} \tag{6.48}$$

$$V^{\text{mix}}_{\Pi_u}(r) = \frac{\pi^{3/2} g\Lambda' c_F}{2m_Q\sqrt{\sigma}r^2} \tag{6.49}$$

$$V^{\text{mix}}_{\Sigma_u^-}(r) = \frac{-\pi^2 g\Lambda''' c_F}{m_Q\sigma r^3}\,. \tag{6.50}$$

The long-distance behavior includes parameters such as the string tension σ, which can, in principle, be fixed through a fit to available lattice data for the ordinary static potential. Other parameters as $g\Lambda'$ and $g\Lambda'''$ can be fixed using lattice data for quarkonium spin-

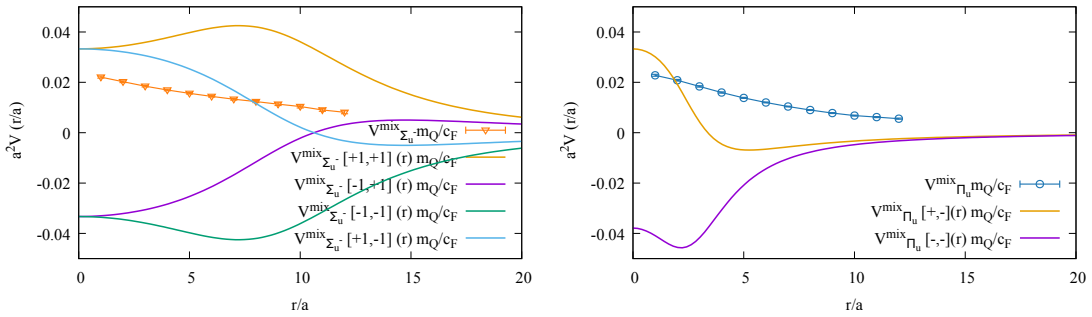

Figure 6.6: Lattice field theory results for $V^{\text{mix}}_{\Pi_u}(r)m_Q/c_F$ and $V^{\text{mix}}_{\Sigma_u^-}(r)m_Q/c_F$ at fixed lattice spacing $a = 0.060\,\text{fm}$, compared to variants of interpolating functions (6.51).

dependent potentials, though only up to an unknown sign. The parameter λ and the sign in Eq. (6.46) were varied in Ref. [15] to explore their impact on heavy hybrid meson spectra.

As an illustrative example, Figure 6.6 presents our lattice results for $V^{\text{mix}}_{\Pi_u}(r)m_Q/c_F$ and $V^{\text{mix}}_{\Sigma_u^-}(r)m_Q/c_F$ alongside interpolating functions from Ref. [15], which are given by

$$V^{\text{mix}}_{\Pi_u}[\pm-](r) = \frac{c_F\lambda^2}{m_Q}\left(\frac{\pm 1 - \frac{r^2}{r_\Pi^2}}{1+\frac{r^4}{r_\Pi^4}}\right) \qquad r_\Pi = \left(\frac{\left|g\Lambda'\pi^{3/2}\right|}{2\lambda^2\sigma^{1/2}}\right)^{1/2} \tag{6.51}$$

$$V^{\text{mix}}_{\Sigma_u^-}[\pm\pm](r) = \frac{c_F\lambda^2}{m_Q}\left(\frac{\pm 1 \pm \frac{r^2}{r_\Sigma^2}}{1+\frac{r^5}{r_\Sigma^5}}\right) \qquad r_\Sigma = \left(\frac{\left|g\Lambda'''\pi^2\right|}{\lambda^2\sigma}\right)^{1/3}, \tag{6.52}$$

with $g\Lambda' = -59\,\text{MeV}$, $g\Lambda''' = \pm 230\,\text{MeV}$, determined from a lattice data fit of spin potentials for heavy quarkonium, and $\lambda = 600\,\text{MeV}$, which was chosen because it creates the largest mixing of the explored values. However, none of these interpolating variants with the chosen parameters closely match our lattice results as demonstrated by Figure 6.6 while the qualitative behavior of the predictions seems to agree with our lattice data.

Given the uncertainties in the values and signs of non-perturbative parameters, which are difficult to constrain using existing lattice QCD data, we believe our direct lattice computation of hybrid spin-dependent and hybrid-quarkonium mixing potentials from generalized Wilson loops will provide more precise estimates and will help to resolve open questions about these potentials.

Techniques developed for parametrizations and removal of discretization errors in the hybrid static potentials (as outlined in Chapter 4) might be extended to the hybrid potentials at order $(1/m_Q)^1$ calculated with gradient flow, enabling precise parametrizations of the spin-dependent potentials. As discussed earlier, once renormalized results are available, the resulting hybrid spin-dependent potentials will contribute to sophisticated predictions of heavy hybrid meson masses.

6.5 Summary

In this chapter, we investigated the hybrid spin-dependent and hybrid-quarkonium mixing potentials at order $(1/m_Q)^1$ derived in the BOEFT using first-principles lattice gauge theory calculations. These potentials play a crucial role in understanding the hyperfine splitting in heavy hybrid meson spectra and their mixing with conventional quarkonia.
We specified the expressions for the hybrid spin-dependent potentials in the $\kappa^{PC} = 1^{+-}$ sector. We outlined the matching between the BOEFT and NRQCD and worked out the potentials in terms of matrix elements by analytical integration of the matching expressions. The lattice computation of these potentials was then discussed in detail. We outlined the methodology for extracting matrix elements from generalized Wilson loops and explained how to construct lattice creation operators, incorporating appropriate phase factors, to compute the corresponding potentials. The specifics of the lattice setup, including the choice of gradient flow time, were discussed in detail.
Our numerical results provide the first direct lattice field theory determination of the hybrid spin-dependent and hybrid-quarkonium mixing potentials at order $(1/m_Q)^1$ for quark-antiquark separations in the range $0.30\,\text{fm} \leq r \leq 0.72\,\text{fm}$. We analyzed these potentials at finite lattice spacing and flow radius and studied the flow-time dependence of correlator ratios and matrix elements. Although a full continuum and zero-flow-time extrapolation were beyond the scope of this work, our results suggest that these are feasible when the calculations are extended to several smaller and larger lattice spacings.
While predictions for the potentials exist in the literature, where unknown, non-perturbative parameters can partly be fixed by existing lattice data for the hybrid charmonium spectra or spin-dependent potentials for quarkonium, direct lattice computation of the hybrid spin-dependent potentials are important to reduce uncertainties and improve theoretical predictions of heavy hybrid meson spectra.
To conclude, this work represents a significant advancement in studying spin-dependent effects in the heavy hybrid meson spectrum. The methodology developed here sets the stage for future studies with improved precision, including continuum-limit, renormalization and zero-flow time extrapolation of the computed potentials and parametrizations.

7 Conclusions

This thesis has enhanced and extended the range of precise results for hybrid meson potentials at the leading and next-to-leading order in the Born-Oppenheimer Effective Field Theory (BOEFT) by employing pure SU(3) lattice gauge theory calculations with lattice spacings as small as 0.04 fm. We computed the hybrid static potentials Π_u and Σ_u^- with unprecedented accuracy and provided parametrizations consistent with the continuum limit (see Section 4.6 for a detailed summary). Our results extend the available lattice data to smaller separations and improve the precision of mass predictions for the lowest heavy hybrid mesons within the BOEFT.

Additionally, we extracted a spectrum of 19 continuum-extrapolated gluelump mass splittings with total angular momentum up to $J = 3$ and displayed their connection to the short-distance limit of hybrid static potentials (see Section 5.5). Although our lattice results significantly improve previous studies, the conversion to renormalized gluelump masses in the RS scheme, which directly affect hybrid meson mass predictions, remains limited by the precision of perturbative expressions.

We also performed an exploratory study of the hybrid spin-dependent potentials $V^{sa}(r)/c_F$ and $V^{sb}(r)/c_F$ as well as for the hybrid-quarkonium mixing potentials $V^{\text{mix}}_{\Pi_u}(r)m_Q/c_F$ and $V^{\text{mix}}_{\Sigma_u^-}(r)m_Q/c_F$ at order $(1/m_Q)^1$ in the BOEFT. We related these potentials to matrix elements, which can be obtained from generalized Wilson loops suitable for lattice evaluation. Through this, we were able to provide the first lattice results for heavy quark spin-dependent corrections to hybrid static potentials (see Section 6.5 for a detailed summary). These findings represent an important step towards clarifying open questions regarding the hyperfine splitting and mixing with ordinary quarkonium in the spectrum of heavy hybrid mesons. A combined $a \to 0$ and $r_f \to 0$ extrapolation remains mandatory for rigorous renormalized continuum results.

Systematic uncertainties such as volume effects from the finite lattice volume and topological freezing were carefully addressed and excluded. By utilizing multiple lattice data ensembles, we quantified and effectively eliminated discretization effects from the lattice data for hybrid static potentials (see Section 4.3), gluelump mass splittings (see Section 5.3.3) and the renormalized RS gluelump mass (see Section 5.4). These strategies may also be applied to hybrid spin-dependent potentials at order $(1/m_Q)^1$ once lattice data at several lattice spacings is available.

While our study was conducted in pure gauge theory without dynamical quarks, which is a simplifying approximation introducing an unclear systematic uncertainty, lattice computations of hybrid static potentials from Ref. [38] suggest that omitting dynamical quarks

leads to no statistically significant deviations. Moreover, the inclusion of dynamical quarks would introduce several multiparticle states consisting of light pions and ordinary quarkonium below the hybrid state of interest. These states could lead to systematic errors in the results and avoiding contamination from them is rather difficult. In pure gauge theory, such multiparticle states are limited to states involving ordinary quarkonium and a relatively heavy glueball. These states only affect the potentials at very small separations (as discussed in Section 4.4.3) and can be safely neglected for this work.

Future work should focus on extending lattice calculations to smaller lattice spacings and larger volumes. This would allow making contact to string-like descriptions as e.g. in Ref. [15, 23, 112, 114] at large r and to higher-order perturbation theory at small r similar to Ref. [113], to enhance the description of the potentials. However, achieving fine lattices with large volumes is computationally demanding due to critical slowing down. Master field simulations [151] offer a promising approach to overcome this challenge, such that volume effects from topological freezing are avoided. Additionally, applying the gradient flow method to hybrid static potentials and gluelumps may provide an effective strategy for improving precision, extracting higher-lying hybrid static potentials with similar accuracy and achieving renormalization.

Overall, this work successfully enhances the range and accuracy of results for heavy hybrid meson potentials and contributes essential inputs for refined theoretical predictions of heavy quark spin effects and heavy hybrid meson masses within the BOEFT framework.

A Error analysis

This appendix outlines the methods used throughout this work for the statistical error analysis in Monte Carlo simulations. These were already described and used in Refs. [55, 57, 58]. We employ the jackknife and bootstrap methods to estimate statistical errors, ensuring reliable results.

To eliminate correlations in Monte Carlo time, measurements on consecutively generated gauge link configurations from ensemble e are combined into N^e bins.

For results from individual ensembles, we employ the jackknife method starting at the level of correlation functions. For the data points of the correlation function of interest $C^e(t)$, statistical errors are determined via a standard jackknife analysis. From N^e reduced jackknife samples $C_j^{e,\text{jackknife}}(t)$ the error is computed as

$$\sigma_{C^e}(t) = \left(\frac{N^e - 1}{N^e} \sum_{j=1}^{N^e} \left(C_j^{e,\text{jackknife}}(t) - \bar{C}^e(t) \right)^2 \right)^{1/2}, \tag{A.1}$$

where $\bar{C}^e(t)$ denotes the result for the full sample. Quantities derived from the correlation function, O^e, such as the effective potentials $V^e_{\text{eff};\Lambda^\epsilon_\eta}(r,T)$, gluelump correlator ratios $\tilde{C}^{e,s}_{\mathcal{R}^{PC}}(t)$ or the correlator ratios $R^{B_k}_{\Lambda^\epsilon_\eta \Lambda^{\epsilon\prime}_\eta}(t;r,T)$ related to hybrid spin-dependent potentials, are calculated on each reduced jackknife sample and the error is computed analogously to Eq. (A.1).

For cases where results from different ensembles are combined, such as for the parametrization of static potentials in Section 4.3 or continuum gluelump mass splittings in Section 5.3.3, the bootstrap method is employed. This approach is more practical than continuing with the jackknife method due to a large number of reduced jackknife samples, i.e. for fits in Section 4.3 this would amount to $N^A \times N^B \times N^C \times N^D \times N^{A^{\text{HYP2}}}$, and the corresponding huge computational effort.

Reduced jackknife samples for the quantity of interest O^e must be inflated

$$O^e_j = \bar{O}^e + (N^e - 1)\left(O^{e,\text{jackknife}}_j - \bar{O}^e \right). \tag{A.2}$$

From the inflated samples O^e_j, a bootstrap sample is generated by randomly selecting N^e data points for each ensemble, where the same inflated sample may be selected more than once. This procedure is applied to the static potential $V^e_{\Lambda^\epsilon_\eta}(r)$ for the parametrization in Section 4.3, the gluelump mass splittings $\Delta m^e_{\mathcal{R}^{PC}}$ or gluelump correlator ratio $\tilde{C}^{e,s}_{\mathcal{R}^{PC}}(t)$ for the fits in Section 5.3.3. The bootstrap error of the derived quantity Q is given by the

standard deviation of the bootstrap samples, i.e.

$$\sigma_Q = \left(\frac{1}{K} \sum_{k=1}^{K} \left(Q_k - \bar{Q} \right)^2 \right)^{1/2}. \tag{A.3}$$

Here, Q_k denotes the result on the k-th bootstrap sample and $\bar{Q}$ the result on the full sample. Q may be one of the fit parameters extracted from the fits in Section 4.3 and Section 5.3.3. K, the number of bootstrap samples, has to be chosen sufficiently large, such that ΔQ is essentially independent of K. Throughout this work, $K = 10000$ bootstrap samples are used.

B SU(2) gauge field ensembles

In the following, we summarize details on generated SU(2) gauge field ensembles [53, 117, 152]. We generated three ensembles of gauge link configurations with gauge couplings $\beta = 2.85, 2.70, 2.50$. We relate the lattice spacing a to the scale t_0 using a parametrization of $\ln(t_0/a^2)$ determined in Ref. [153] via the gradient flow. Physical units are then introduced by setting $\sqrt{8t_0} = 0.3010\,\text{fm}$, which corresponds to $r_0 = 0.5\,\text{fm}$. The details of the gauge link ensembles are summarized in Table B.1. The three lattice volumes are approximately $L^3 \times T \approx (1.3\,\text{fm})^3 \times (1.3\,\text{fm})$. For the investigation of finite volume effects in Section 2.6.3, additional ensembles with both smaller and larger lattice volumes at gauge couplings $\beta = 3.00, 2.85, 2.70, 2.50$ were generated.

ensemble	β	a in fm [153]	$(L/a)^3 \times T/a$	N_{sim}	N_{total}	N_{or}	N_{therm}	N_{sep}	N_{meas}
a	2.50	0.078	$16^3 \times 16$	20	40000	0	10000	100	6000
b	2.70	0.041	$32^3 \times 32$	20	25000	0	10000	100	3000
c	2.85	0.026	$48^3 \times 48$	20	25000	0	10000	200	1500

Table B.1: Gauge link ensembles for gauge group SU(2).

C Different formulations of the hybrid-quarkonium mixing potential at order $(1/m_Q)^1$

In Section 3.1.2 we introduce the hybrid-quarkonium mixing Lagrangian for gluon spin $\kappa = 1$ in a notation that aligns with the one used in Refs. [19, 23], which reads

$$\mathcal{L}_{\text{mixing}} = 2V_{\text{mix}}^{n'n}\Big(\Psi_{0^{++}}^{n'\dagger}\Psi_{1^{+-}}^{n0} + \Psi_{0^{++}}^{0\dagger}\Psi_{1^{+-}}^{nn'} + \text{H.c.}\Big). \tag{C.1}$$

In Ref. [15], where the hybrid-quarkonium mixing potential was derived, a different notation is used. There, the quarkonium field is denoted by $S = S_0 + \sigma^k S_1^k$ and the hybrid field is denoted by $H^j = H_0^j + \sigma^k H_1^{jk}$. The subscripts 0 and 1 stand for the heavy quark pair spin $S_{Q\bar{Q}}$ and the superscripts denote the three components of the gluon or heavy quark spin 1 case. For clarity, we have in our notation $\Psi_{0^{++}}^0 = S_0$, $\Psi_{0^{++}}^A = S_1^j$, if $A = j$. For the hybrid field $\Psi_{1^{+-}}^{n0} = H_0^n$ and $\Psi_{1^{+-}}^{nA} = H_1^{nj}$, if $A = j$. The BOEFT Lagrangian for the fields S and H^j reads [15]

$$\mathcal{L} = \underbrace{\text{tr}\left(S^\dagger\left(i\partial_t - h_S\right)S\right)}_{=\mathcal{L}_{\text{quarkonium}}} + \underbrace{\text{tr}\left(H^{n'\dagger}\left(i\delta^{n'n}\partial_t - h_H^{n'n}\right)H^n\right)}_{=\mathcal{L}_{\text{hybrids}}} + \underbrace{\text{tr}\left(S^\dagger V_{\text{mix}}^{n'n}\{\sigma^{n'}, H^n\} + \text{H.c.}\right)}_{=\mathcal{L}_{\text{mixing}}}. \tag{C.2}$$

h_S and h_H denote the order $(1/m_Q)^0$ Hamiltonian for quarkonium and hybrid quarkonium, respectively,

$$h_S(\mathbf{r}) = -\frac{\Delta_{\mathbf{r}}}{m_Q} + V_{\Sigma_g^+}(r) \tag{C.3}$$

$$\begin{aligned} h_H^{n'n}(\mathbf{r}) &= -\frac{\Delta_{\mathbf{r}}}{m_Q}\delta^{n'n} + \sum_{\Lambda_\eta^\epsilon = \Sigma_u^-, \Pi_u} V_{\Lambda_\eta^\epsilon}(r)\mathcal{P}_{1\Lambda}^{n'n} = \\ &= -\frac{\Delta_{\mathbf{r}}}{m_Q}\delta^{n'n} + V_{\Sigma_u^-}(r)\Big(\mathbf{e}_r \otimes \mathbf{e}_r\Big)^{n'n} + V_{\Pi_u}(r)\Big(1 - \mathbf{e}_r \otimes \mathbf{e}_r\Big)^{n'n}. \end{aligned} \tag{C.4}$$

Each term in tr(...) in Eq. (C.2) is a 2×2 matrix and tr(...) denotes the trace with respect to these 2×2 matrices. The term $\mathcal{L}_{\text{mixing}}$ in the Lagrangian (C.2) describes hybrid-quarkonium mixing, which is either formulated in terms of the fields $\Psi_{\kappa^{PC}}$ as in Eq. (3.11) or in terms of the fields S and H^j as in Eq. (C.2).

D Evaluation of traces in the matching expressions for hybrid spin-dependent potentials

In this appendix, we give details on the evaluation of traces of spin matrices and projection vectors occurring in the matching expressions for hybrid spin-dependent potentials, Eqs. (6.17) and (6.18).
The projection matrices $\mathcal{P}_{\kappa\Lambda}$ (3.4) projecting onto an irreducible representation $\Lambda_\eta^\epsilon \in D_{\infty h}$ are either expanded in terms of the normalized eigenfunctions $P_{\kappa\lambda}$ of the gluon spin operator $\mathbf{S}_\kappa^2$ and $\mathbf{S}_\kappa \hat{\mathbf{r}}$ or the projection vectors $P_{\kappa\Lambda_\eta^\epsilon}$ (see Section 6.2.1). For $\kappa^{PC} = 1^{+-}$, the relevant projection matrices are

$$\mathcal{P}_{11} \equiv \mathcal{P}_{1\Pi_u} = P_{1\Pi_u^+} P_{1\Pi_u^+}^\dagger + P_{1\Pi_u^-} P_{1\Pi_u^-}^\dagger = P_{+1_u} P_{+1_u}^\dagger + P_{-1_u} P_{-1_u}^\dagger \tag{D.1}$$

$$\mathcal{P}_{10} \equiv \mathcal{P}_{1\Sigma_u^-} = P_{1\Sigma_u^-} P_{1\Sigma_u^-}^\dagger = P_{10_u} P_{10_u}^\dagger . \tag{D.2}$$

For the calculation of the matching equations in Section 6.2.1, we can assume that the quark-antiquark separation axis is the z-axis. In particular, in the cartesian basis representation and with the quark-antiquark pair being separated along the z-axis, the projection vectors $P_{1\lambda_\eta}$ are given by

$$P_{1\pm 1_u} = \mp \frac{1}{\sqrt{2}} \begin{pmatrix} 1 \\ \pm i \\ 0 \end{pmatrix} \quad , \quad P_{10_u} = \begin{pmatrix} 0 \\ 0 \\ 1 \end{pmatrix} . \tag{D.3}$$

The projection vectors $P_{1\Lambda_\eta^\epsilon}$ are related to $P_{1\lambda_\eta}$ via

$$\begin{aligned} P_{1\Pi_u^+} &= \frac{-i}{\sqrt{2}} \left(P_{1-1_u} - P_{1+1_u} \right) \\ P_{1\Pi_u^-} &= \frac{-1}{\sqrt{2}} \left(P_{1-1_u} + P_{1+1_u} \right) \\ P_{1\Sigma_u^-} &= -i P_{10_u} . \end{aligned} \tag{D.4}$$

Consequently, in the cartesian basis representation and with the quark-antiquark pair being

separated along the z-axis, the projection vectors $P_{1\Lambda^{\varepsilon}_{\eta}}$ are represented by

$$P_{1\Pi^{+}_{u}} = \begin{pmatrix} -i \\ 0 \\ 0 \end{pmatrix}, \; P_{1\Pi^{-}_{u}} = \begin{pmatrix} 0 \\ i \\ 0 \end{pmatrix}, \; P_{1\Sigma^{-}_{u}} = \begin{pmatrix} 0 \\ 0 \\ -i \end{pmatrix}. \tag{D.5}$$

Eqs. (6.17) and (6.18) involve several expressions given by traces of spin operators and projection matrices. These expressions can be evaluated by considering that a cartesian component of the spin operator $\mathbf{S}_1$ acts on a projection vector $P_{1\lambda_\eta}$ as follows [147]

$$S_1^x P_{1+1_u} = \frac{1}{\sqrt{2}} P_{10_u} \qquad S_1^y P_{1+1_u} = \frac{i}{\sqrt{2}} P_{10_u} \qquad S_1^z P_{1+1_u} = P_{1+1_u} \tag{D.6}$$

$$S_1^x P_{1-1_u} = \frac{1}{\sqrt{2}} P_{10_u} \qquad S_1^y P_{1-1_u} = \frac{-i}{\sqrt{2}} P_{10_u} \qquad S_1^z P_{1-1_u} = -P_{1-1_u} \tag{D.7}$$

$$S_1^x P_{10_u} = \frac{1}{\sqrt{2}} (P_{1-1_u} + P_{1+1_u}) \qquad S_1^y P_{10_u} = \frac{i}{\sqrt{2}} (P_{1-1_u} - P_{1+1_u}) \qquad S_1^z P_{10_u} = 0\,. \tag{D.8}$$

Consequently, the occurring traces involving no correlation functions can be computed straightforwardly, resulting in [19]

$$\mathrm{Tr}\left[\mathcal{P}_{11}\right] = 2 \tag{D.9}$$

$$\mathrm{Tr}\left[(\mathbf{S}_1 \cdot \mathcal{P}_{10}) \cdot (\mathcal{P}_{11} \mathbf{S}_1 \mathcal{P}_{11})\right] = 2 \tag{D.10}$$

$$\mathrm{Tr}\left[\mathcal{P}_{10}\right] = 1 \tag{D.11}$$

$$\mathrm{Tr}\left[(\mathbf{S}_1 \cdot \mathcal{P}_{11}) \cdot (\mathcal{P}_{11} \mathbf{S}_1 \mathcal{P}_{10})\right] = 2\,. \tag{D.12}$$

Exemplarily for the traces involving correlation functions, we work out the numerator in Eq. (6.17) given by $\mathrm{Tr}\left[(\mathbf{S}_1 \mathcal{P}_{10}) \cdot \left(\mathcal{P}_{11} \langle \Omega | \mathcal{O}^{\dagger}_{1^+_-} g \mathbf{B} \mathcal{O}_{1^+_-} | \Omega \rangle \mathcal{P}_{11}\right)\right]$,

$$\begin{aligned} &\mathrm{Tr}\left[(\mathbf{S}_1 \mathcal{P}_{10}) \cdot \left(\mathcal{P}_{11} \langle \Omega | \mathcal{O}^{\dagger}_{1^+_-} g \mathbf{B} \mathcal{O}_{1^+_-} | \Omega \rangle \mathcal{P}_{11}\right)\right] \\ &\quad = \left(\left(\mathbf{S}_1^i\right)^{kl} \mathcal{P}_{10}^{ij} \right) \cdot \left(\mathcal{P}_{11}^{lq} \langle \Omega | \mathcal{O}^{\dagger,q}_{1^+_-} g \mathbf{B}^j \mathcal{O}^{p}_{1^+_-} | \Omega \rangle \mathcal{P}_{11}^{pk} \right), \end{aligned} \tag{D.13}$$

with $\left(\mathbf{S}_1^i \mathcal{P}_{10}^{ij}\right) \mathbf{B}^j = \begin{pmatrix} S_1^x \\ S_1^y \\ S_1^z \end{pmatrix} \begin{pmatrix} 0 \\ 0 \\ 1 \end{pmatrix} (0,0,1) \begin{pmatrix} B_x \\ B_y \\ B_z \end{pmatrix} = S_1^z B_z,$

$$= \left(S_1^z\right)^{kl} \cdot \left(\mathcal{P}_{11}^{lq} \langle \Omega | \mathcal{O}^{\dagger,q}_{1^+_-} g B_z \mathcal{O}^{p}_{1^+_-} | \Omega \rangle \mathcal{P}_{11}^{pk} \right) \tag{D.14}$$

$$= \left(S_1^z\right)^{kl} \cdot \left(\left(P^{l}_{1+1_u} P^{\dagger,q}_{1+1_u} + P^{l}_{1-1_u} P^{\dagger,q}_{1-1_u} \right) \langle \Omega | \mathcal{O}^{\dagger,q}_{1^+_-} g B_z \mathcal{O}^{p}_{1^+_-} | \Omega \rangle \mathcal{P}_{11}^{pk} \right). \tag{D.15}$$

The spin operator S_1^z acts on the projection vectors according to Eqs. (D.6)-(D.8), which

yields

$$\left(P^{k}_{1+1_u}P^{\dagger,q}_{1+1_u} - P^{k}_{1-1_u}P^{\dagger,q}_{1-1_u}\right)\langle\Omega|\mathcal{O}^{\dagger,q}_{1+-}gB_z\mathcal{O}^{p}_{1+-}|\Omega\rangle\mathcal{P}^{pk}_{11}\,. \tag{D.16}$$

The aim is to to express the correlators in terms of $\Lambda^{\epsilon}_{\eta}$ representations of the operators. Therefore, we replace the projection vectors $P_{1\lambda_\eta}$ with $P_{1\Lambda^{\epsilon}_{\eta}}$ according to Eq. (D.4), resulting in

$$i\left(P^{k}_{1\Pi^{-}_u}P^{\dagger,q}_{1+\Pi^{+}_u} - P^{k}_{1\Pi^{+}_u}P^{\dagger,q}_{1\Pi^{-}_u}\right)\langle\Omega|\mathcal{O}^{\dagger,q}_{1+-}gB_z\mathcal{O}^{p}_{1+-}|\Omega\rangle\mathcal{P}^{pk}_{11} \tag{D.17}$$

$$=i\left(P^{k}_{1\Pi^{-}_u}P^{\dagger,q}_{1+\Pi^{+}_u} - P^{k}_{1\Pi^{+}_u}P^{\dagger,q}_{1\Pi^{-}_u}\right)\langle\Omega|\mathcal{O}^{\dagger,q}_{1+-}gB_z\mathcal{O}^{p}_{1+-}|\Omega\rangle\left(P^{p}_{1\Pi^{+}_u}P^{\dagger,k}_{1\Pi^{+}_u} + P^{p}_{1\Pi^{-}_u}P^{\dagger,k}_{1\Pi^{-}_u}\right)\,. \tag{D.18}$$

Due to the trace and the orthonormality of the projection vectors, the expression simplifies to

$$= iP^{\dagger,q}_{1+\Pi^{+}_u}\langle\Omega|\mathcal{O}^{\dagger,q}_{1+-}gB_z\mathcal{O}^{p}_{1+-}|\Omega\rangle P^{p}_{1\Pi^{-}_u} - iP^{\dagger,q}_{1\Pi^{-}_u}\langle\Omega|\mathcal{O}^{\dagger,q}_{1+-}gB_z\mathcal{O}^{p}_{1+-}|\Omega\rangle P^{p}_{1\Pi^{+}_u}\,. \tag{D.19}$$

Using the expansion of the operator $\mathcal{O}_{1+-}$ in terms of $\Lambda^{\epsilon}_{\eta}$ representations (6.9), we finally arrive at

$$\begin{aligned}&\mathrm{Tr}\left[(\mathbf{S}_1\mathcal{P}_{10})\cdot\left(\mathcal{P}_{11}\langle\Omega|\mathcal{O}^{\dagger}_{1+-}g\mathbf{B}\mathcal{O}_{1+-}|\Omega\rangle\mathcal{P}_{11}\right)\right]\\ &= i\langle\Omega|\mathcal{O}^{\dagger}_{\Pi^{-}_u}gB_z\mathcal{O}_{\Pi^{+}_u}|\Omega\rangle - i\langle\Omega|\mathcal{O}^{\dagger}_{\Pi^{+}_u}gB_z\mathcal{O}_{\Pi^{-}_u}|\Omega\rangle\,,\end{aligned} \tag{D.20}$$

which is the final result for the numerator in Eq. 6.19

E Summary of lattice field theory results

E.1 SU(3) lattice field theory data for the Σ_g^+, Π_u and Σ_u^- static potentials

In Table E.1, we list $V^e_{\Lambda^\epsilon_\eta}(r)a$, the bare lattice data points in units of the lattice spacing (see Section 4.2). In Table E.2 we list $\tilde{V}^e_{\Lambda^\epsilon_\eta}(r)$, the lattice data points defined in Eqs. (4.18) and (4.19), where the self-energy as well as lattice discretization errors at tree-level and proportional to a^2 are removed.

ensemble	r/a	$V^e_{\Sigma_g^+}\, a$	$V^e_{\Pi_u}\, a$	$V^e_{\Sigma_u^-}\, a$
A	1	0.411038(27)	1.2697(139)	1.2841(48)
	2	0.596753(62)	1.2527(28)	1.2813(35)
	3	0.699138(134)	1.2457(27)	1.2972(41)
	4	0.772857(238)	1.2476(27)	1.3228(48)
	5	0.835109(387)	1.2570(28)	1.3547(58)
	6	0.891807(601)	1.2726(30)	1.3898(71)
B	1	0.365472(9)	1.0222(63)	1.0253(64)
	2	0.512961(19)	1.0067(46)	1.0150(52)
	3	0.584400(40)	0.9996(45)	1.0155(56)
	4	0.629977(73)	0.9966(44)	1.0212(61)
	5	0.664972(117)	0.9963(43)	1.0315(67)
	6	0.694703(175)	0.9973(82)	1.0432(76)
C	1	0.345081(4)	0.9245(28)	0.9248(29)
	2	0.478535(11)	0.9091(40)	0.9120(43)
	3	0.540198(26)	0.9019(39)	0.9095(25)
	4	0.577592(47)	0.8976(37)	0.9110(25)
	5	0.604988(76)	0.8959(21)	0.9154(26)
	6	0.627360(111)	0.8954(20)	0.9210(28)
D	1	0.329925(2)	0.8556(24)	0.8557(24)
	2	0.453884(7)	0.8417(22)	0.8433(22)
	3	0.509466(16)	0.8353(21)	0.8396(23)
	4	0.542058(29)	0.8317(21)	0.8393(23)
	5	0.565146(46)	0.8295(20)	0.8412(24)
	6	0.583422(68)	0.8282(19)	0.8438(25)
	7	0.598894(93)	0.8276(19)	0.8479(26)
A^{HYP2}	2	0.116648(13)	0.7427(21)	0.7737(7)
	3	0.206462(31)	0.7369(18)	0.7901(8)
	4	0.275767(60)	0.7395(17)	0.8151(9)
	5	0.336546(114)	0.7483(18)	0.8469(10)
	6	0.392896(184)	0.7621(19)	0.8809(6)
	7	0.446512(289)	0.7805(21)	0.9171(7)
	8	0.498474(446)	0.8037(24)	0.9586(8)
	9	0.549517(680)	0.8326(15)	0.9966(9)
	10	0.599980(1032)	0.8613(19)	1.0382(11)
	11	0.649218(1563)	0.8920(23)	1.0831(13)
	12	0.696191(2361)	0.9243(28)	1.1266(15)

Table E.1: Bare lattice data points for the Σ_g^+, Π_u and Σ_u^- static potentials in units of the lattice spacing (see Section 4.2).

ensemble	r/a	r [fm]	$\tilde{V}^e_{\Sigma_g^+}$ [GeV]	$\tilde{V}^e_{\Pi_u}$ [GeV]	$\tilde{V}^e_{\Sigma_u^-}$ [GeV]
A	1	0.0931	−0.46677(6)	1.2484(295)	1.2502(102)
	2	0.1863	−0.1033(24)	1.2245(73)	1.2541(76)
	3	0.2794	0.0929(24)	1.2122(76)	1.2903(91)
	4	0.3726	0.2428(24)	1.2169(78)	1.3454(108)
	5	0.4657	0.3726(24)	1.2372(81)	1.4131(127)
	6	0.5589	0.4919(25)	1.2703(84)	1.4876(154)
B	1	0.0600	−0.76257(3)	1.2715(200)	1.2687(210)
	2	0.1201	−0.3254(26)	1.2318(150)	1.2465(170)
	3	0.1801	−0.1227(24)	1.2127(149)	1.2521(183)
	4	0.2402	0.0174(24)	1.2039(147)	1.2719(199)
	5	0.3002	0.1292(24)	1.2035(147)	1.3061(220)
	6	0.3603	0.2256(24)	1.2067(270)	1.3449(246)
C	1	0.0480	−0.93421(2)	1.2979(110)	1.2930(118)
	2	0.0960	−0.4459(28)	1.2489(168)	1.2525(180)
	3	0.1441	−0.2326(24)	1.2241(165)	1.2472(108)
	4	0.1921	−0.0910(24)	1.2082(159)	1.2551(112)
	5	0.2401	0.0176(24)	1.2015(95)	1.2737(116)
	6	0.2881	0.1079(24)	1.1999(93)	1.2968(122)
D	1	0.0400	−1.09060(1)	1.3332(112)	1.3266(109)
	2	0.0800	−0.5520(30)	1.2754(108)	1.2776(113)
	3	0.1200	−0.3260(25)	1.2497(109)	1.2653(116)
	4	0.1600	−0.1796(24)	1.2337(106)	1.2655(118)
	5	0.2000	−0.0706(24)	1.2234(104)	1.2753(122)
	6	0.2400	0.0176(24)	1.2173(101)	1.2888(127)
	7	0.2800	0.0930(24)	1.2148(99)	1.3088(133)
A^{HYP2}	2	0.1863	−0.1112(24)	1.2267(58)	1.2573(51)
	3	0.2794	0.0928(23)	1.2126(56)	1.2904(51)
	4	0.3726	0.2430(24)	1.2178(58)	1.3430(53)
	5	0.4657	0.3727(24)	1.2364(61)	1.4102(54)
	6	0.5589	0.4923(26)	1.2654(66)	1.4822(52)
	7	0.6520	0.6059(28)	1.3045(72)	1.5588(52)
	8	0.7452	0.7159(32)	1.3538(79)	1.6467(53)
	9	0.8383	0.8240(37)	1.4148(74)	1.7273(54)
	10	0.9315	0.9308(44)	1.4757(79)	1.8153(55)
	11	1.0246	1.0351(54)	1.5407(85)	1.9104(58)
	12	1.1178	1.1345(69)	1.6090(91)	2.0026(61)

Table E.2: Lattice data points defined in Eqs. (4.18) and (4.19), where the self-energy as well as lattice discretization errors at tree-level and proportional to a^2 are removed (using Fit 1), for the Σ_g^+, Π_u and Σ_u^- static potentials in units of GeV (physical units are introduced by setting $r_0 = 0.5\,\mathrm{fm}$).

E.2 SU(3) lattice field theory data for gluelumps

E.2.1 Lattice gluelump masses for all ensembles and unsmeared and HYP2 smeared temporal links

$\mathcal{R}^{PC}$	$m_{\mathcal{R}^{PC}}^{A,\text{none}}\, a$	$m_{\mathcal{R}^{PC}}^{B,\text{none}}\, a$	$m_{\mathcal{R}^{PC}}^{C,\text{none}}\, a$	$m_{\mathcal{R}^{PC}}^{D,\text{none}}\, a$	$m_{\mathcal{R}^{PC}}^{A,\text{HYP2}}\, a$	$m_{\mathcal{R}^{PC}}^{B,\text{HYP2}}\, a$	$m_{\mathcal{R}^{PC}}^{C,\text{HYP2}}\, a$	$m_{\mathcal{R}^{PC}}^{D,\text{HYP2}}\, a$
T_1^{++}	2.144(44)	1.633(17)	1.451(3)	1.279(6)	1.598(39)	1.155(7)	0.980(3)	0.828(6)
T_1^{+-}	1.332(2)	1.078(2)	0.971(2)	0.898(2)	0.771(2)	0.580(2)	0.500(1)	0.448(2)
T_1^{-+}	1.936(7)	1.464(9)	1.292(5)	1.173(3)	1.378(6)	0.966(9)	0.813(8)	0.699(12)
T_1^{--}	1.474(9)	1.195(3)	1.062(3)	0.970(2)	0.907(16)	0.698(3)	0.592(3)	0.520(2)
T_2^{++}	2.071(9)	1.560(14)	1.382(3)	1.248(4)	1.513(9)	1.064(13)	0.912(3)	0.798(4)
T_2^{+-}	1.735(9)	1.360(5)	1.198(5)	1.087(4)	1.181(8)	0.860(5)	0.726(4)	0.637(4)
T_2^{-+}	2.030(8)	1.489(26)	1.351(6)	1.222(4)	1.470(8)	1.029(11)	0.880(6)	0.768(6)
T_2^{--}	1.576(2)	1.211(14)	1.096(3)	1.001(2)	1.019(2)	0.717(12)	0.617(6)	0.551(2)
A_1^{++}	1.753(8)	1.371(5)	1.201(6)	1.099(3)	1.194(7)	0.873(5)	0.730(6)	0.648(3)
A_1^{+-}	2.276(27)	1.748(6)	1.486(8)	1.351(4)	1.718(26)	1.251(6)	1.017(7)	0.875(16)
A_1^{-+}	2.159(108)	1.794(6)	1.551(7)	1.370(9)	1.776(24)	1.275(14)	1.082(7)	0.919(9)
A_1^{--}	1.966(10)	1.416(27)	1.314(4)	1.211(38)	1.407(10)	0.964(14)	0.844(4)	0.731(3)
A_2^{++}	2.351(6)	1.700(15)	1.500(8)	1.328(8)	1.793(6)	1.202(14)	1.029(8)	0.878(7)
A_2^{+-}	1.887(8)	1.371(23)	1.288(6)	1.133(17)	1.306(20)	0.881(20)	0.795(12)	0.676(16)
A_2^{-+}	2.069(13)	1.580(4)	1.351(8)	1.205(9)	1.512(12)	1.069(8)	0.879(8)	0.757(9)
A_2^{--}	-	-	-	-	1.546(91)	1.266(15)	1.059(8)	0.910(8)
E^{++}	1.917(9)	1.477(3)	1.255(11)	1.162(3)	1.359(8)	0.978(3)	0.785(11)	0.711(3)
E^{+-}	1.726(12)	1.356(3)	1.181(6)	1.081(2)	1.165(11)	0.858(3)	0.710(6)	0.631(2)
E^{-+}	2.014(10)	1.521(15)	1.255(25)	1.209(3)	1.460(9)	1.027(15)	0.785(24)	0.759(3)
E^{--}	1.563(6)	1.227(7)	1.089(9)	1.010(2)	1.006(6)	0.727(6)	0.619(8)	0.563(5)

Table E.3: Lattice gluelump masses $m_{\mathcal{R}^{PC}}^{e,s}\, a$ in units of the lattice spacing obtained from fits to effective mass plateaus (see Section 5.3.1). The row corresponding to the lightest gluelump with $\mathcal{R}^{PC} = T_1^{+-}$ is shaded in gray.

E.2.2 Gluelump mass splittings for all ensembles and unsmeared and HYP2 smeared temporal links

$\mathcal{R}^{PC}$	$\Delta m^{A,\text{none}}_{\mathcal{R}^{PC}}\, a$	$\Delta m^{B,\text{none}}_{\mathcal{R}^{PC}}\, a$	$\Delta m^{C,\text{none}}_{\mathcal{R}^{PC}}\, a$	$\Delta m^{D,\text{none}}_{\mathcal{R}^{PC}}\, a$
T_1^{++}	0.812(44)	0.555(17)	0.480(3)	0.381(6)
T_1^{+-}	0	0	0	0
T_1^{-+}	0.604(7)	0.386(9)	0.321(5)	0.276(3)
T_1^{--}	0.142(9)	0.118(3)	0.091(3)	0.072(2)
T_2^{++}	0.739(9)	0.482(14)	0.411(3)	0.350(4)
T_2^{+-}	0.403(9)	0.282(5)	0.227(4)	0.189(4)
T_2^{-+}	0.698(8)	0.411(26)	0.380(6)	0.325(4)
T_2^{--}	0.244(3)	0.133(14)	0.125(2)	0.103(2)
A_1^{++}	0.421(8)	0.293(5)	0.230(5)	0.201(4)
A_1^{+-}	0.944(27)	0.670(6)	0.515(8)	0.453(4)
A_1^{-+}	0.828(108)	0.716(6)	0.580(7)	0.472(9)
A_1^{--}	0.634(10)	0.338(27)	0.343(4)	0.313(38)
A_2^{++}	1.019(6)	0.622(15)	0.529(8)	0.430(8)
A_2^{+-}	0.555(8)	0.294(22)	0.317(6)	0.235(17)
A_2^{-+}	0.737(13)	0.502(4)	0.380(8)	0.308(9)
A_2^{--}	-	-	-	-
E^{++}	0.585(9)	0.399(3)	0.284(11)	0.264(3)
E^{+-}	0.394(12)	0.279(4)	0.210(6)	0.183(3)
E^{-+}	0.682(10)	0.443(15)	0.284(25)	0.311(4)
E^{--}	0.231(6)	0.149(6)	0.118(9)	0.112(2)

$\mathcal{R}^{PC}$	$\Delta m^{A,\text{HYP2}}_{\mathcal{R}^{PC}}\, a$	$\Delta m^{B,\text{HYP2}}_{\mathcal{R}^{PC}}\, a$	$\Delta m^{C,\text{HYP2}}_{\mathcal{R}^{PC}}\, a$	$\Delta m^{D,\text{HYP2}}_{\mathcal{R}^{PC}}\, a$
T_1^{++}	0.827(39)	0.575(7)	0.480(3)	0.381(6)
T_1^{+-}	0	0	0	0
T_1^{-+}	0.607(6)	0.387(9)	0.313(8)	0.251(12)
T_1^{--}	0.136(16)	0.119(3)	0.092(3)	0.072(2)
T_2^{++}	0.743(9)	0.484(13)	0.412(3)	0.350(4)
T_2^{+-}	0.410(8)	0.281(5)	0.227(4)	0.189(4)
T_2^{-+}	0.699(8)	0.449(11)	0.380(6)	0.321(6)
T_2^{--}	0.249(2)	0.138(12)	0.117(5)	0.104(2)
A_1^{++}	0.424(7)	0.293(5)	0.231(5)	0.201(4)
A_1^{+-}	0.948(26)	0.671(6)	0.518(7)	0.428(16)
A_1^{-+}	1.005(24)	0.695(14)	0.582(7)	0.471(9)
A_1^{--}	0.636(9)	0.384(14)	0.344(4)	0.283(3)
A_2^{++}	1.022(6)	0.622(14)	0.529(8)	0.430(7)
A_2^{+-}	0.536(20)	0.302(20)	0.296(11)	0.229(15)
A_2^{-+}	0.741(11)	0.489(8)	0.379(8)	0.309(9)
A_2^{--}	0.776(91)	0.687(14)	0.559(8)	0.462(9)
E^{++}	0.589(9)	0.398(3)	0.285(11)	0.264(3)
E^{+-}	0.394(11)	0.279(4)	0.210(6)	0.183(3)
E^{-+}	0.690(9)	0.448(15)	0.286(24)	0.311(4)
E^{--}	0.235(6)	0.148(6)	0.119(8)	0.115(4)

Table E.4: Gluelump mass splittings $\Delta m^{e,s}_{\mathcal{R}^{PC}}\, a$ in units of the lattice spacing obtained by subtracting the lattice gluelump masses from Table E.3 (see Section 5.3.3). $\Delta m^{e,s}_{T_1^{+-}} = 0$ by definition (see Eq. (5.24)), because we use $m^{e,s}_{T_1^{+-}}$ as reference mass.

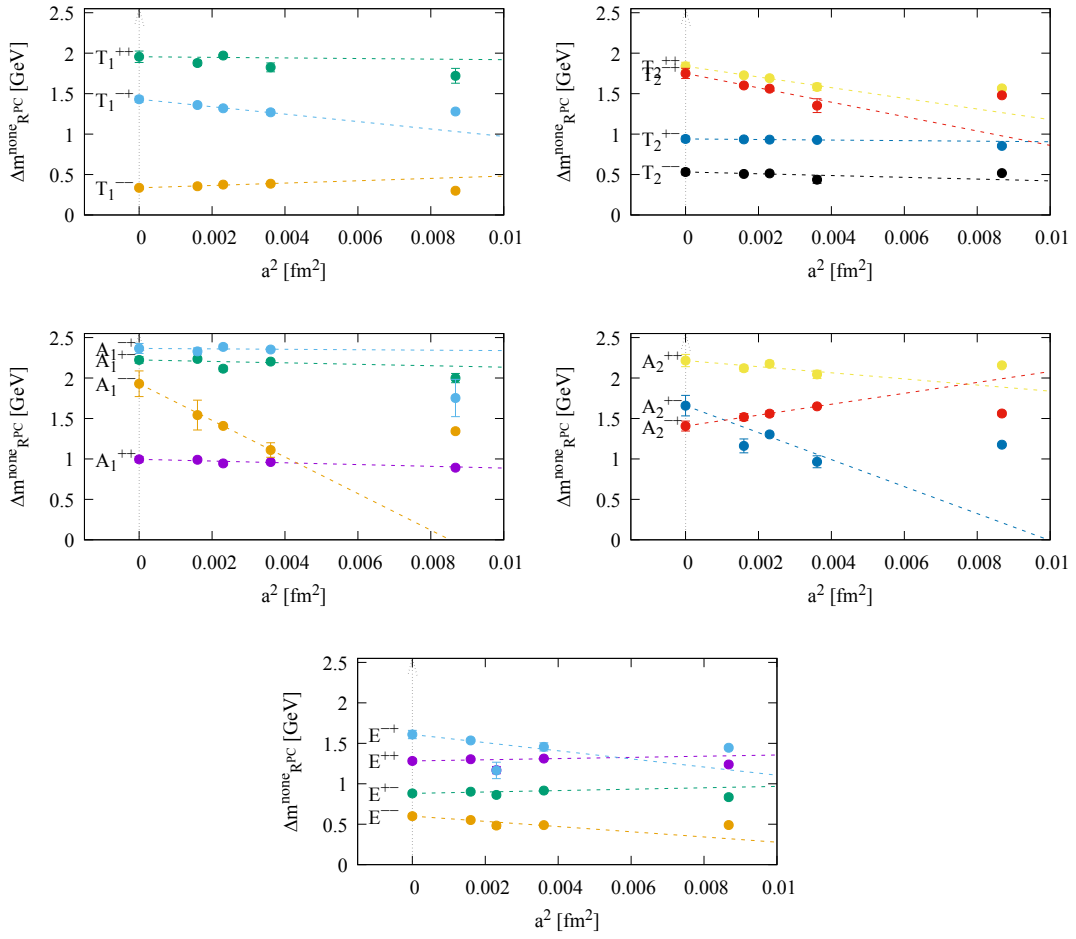

Figure E.1: Continuum extrapolations of gluelump mass splittings $\Delta m_{\mathcal{R}^{PC}}$ for unsmeared temporal links.

E.3 SU(3) lattice field theory data for hybrid spin-dependent and hybrid-quarkonium mixing potentials at $\mathcal{O}(1/m_Q)$

method	$T_{\min}(t,r)$	$T_{\min}/a = 8$	$T_{\min}/a = 9$	$T_{\min}/a = 10$
r/a	$a^2 V_{11}^{sa}(r) m_Q/c_F$			
1	0.01766(58)	0.01766(58)	0.01734(97)	0.01728(131)
2	0.01653(49)	0.01653(49)	0.01624(83)	0.01631(118)
3	0.01505(46)	0.01505(46)	0.01470(73)	0.01465(102)
4	0.01346(44)	0.01346(44)	0.01291(68)	0.01256(94)
5	0.01205(43)	0.01205(43)	0.01147(66)	0.01104(91)
6	0.01093(44)	0.01093(44)	0.01060(71)	0.01044(101)
7	0.00970(48)	0.00970(48)	0.00945(82)	0.00941(117)
8	0.00834(49)	0.00834(49)	0.00794(80)	0.00773(106)
9	0.00716(50)	0.00716(50)	0.00660(81)	0.00614(107)
10	0.00638(63)	0.00638(63)	0.00590(104)	0.00550(138)
11	0.00589(84)	0.00589(84)	0.00580(138)	0.00583(183)
12	0.00512(91)	0.00512(91)	0.00512(138)	0.00527(177)

method	$T_{\min}(t,r)$	$T_{\min}/a = 8$	$T_{\min}/a = 9$	$T_{\min}/a = 10$
r/a	$a^2 V_{10}^{sb}(r)/c_F$			
1	0.01726(43)	0.01726(43)	0.01657(77)	0.01596(119)
2	0.01622(43)	0.01622(43)	0.01543(74)	0.01468(112)
3	0.01397(58)	0.01479(35)	0.01397(58)	0.01312(88)
4	0.01270(46)	0.01336(29)	0.01270(46)	0.01204(70)
5	0.01087(54)	0.01178(31)	0.01108(47)	0.01037(70)
6	0.00921(62)	0.01018(35)	0.00947(53)	0.00871(80)
7	0.00829(66)	0.00915(35)	0.00849(57)	0.00776(88)
8	0.00828(39)	0.00828(39)	0.00786(64)	0.00752(92)
9	0.00724(41)	0.00724(41)	0.00708(66)	0.00711(95)
10	0.00606(50)	0.00606(50)	0.00586(74)	0.00576(102)
11	0.00499(54)	0.00499(54)	0.00465(81)	0.00415(115)
12	0.00452(59)	0.00443(61)	0.00403(94)	0.00338(138)

Table E.5: Hybrid spin-dependent potentials $V_{11}^{sa}(r)/c_F$ and $V_{10}^{sb}(r)/c_F$ in units of the lattice spacing $a = 0.060\,\text{fm}$ at flow radius $r_f = \sqrt{8t_f} = 1.8\,a$. The four columns correspond to the four fitting variants discussed in Section 6.4.1. Our main results were obtained by setting $T_{\min}/a = 9$ and are shaded in gray. Potential values with separations $r \lesssim 2r_f + a = 4.6\,a$ should be taken with caution due to possible operator overlapping effects.

method	$T_{\min}(t,r)$	$T_{\min}/a = 8$	$T_{\min}/a = 9$	$T_{\min}/a = 10$
r/a	$a^2 V^{\text{mix}}_{\Pi_u}(r) m_Q/c_F$			
1	0.02284(18)	0.02284(18)	0.02281(26)	0.02276(34)
2	0.02092(15)	0.02092(15)	0.02087(22)	0.02082(29)
3	0.01852(13)	0.01852(13)	0.01844(19)	0.01838(24)
4	0.01615(11)	0.01615(11)	0.01606(16)	0.01599(20)
5	0.01403(9)	0.01403(9)	0.01394(14)	0.01386(18)
6	0.01221(7)	0.01221(7)	0.01213(11)	0.01206(15)
7	0.01062(7)	0.01062(7)	0.01054(10)	0.01045(13)
8	0.00928(7)	0.00928(7)	0.00915(11)	0.00905(14)
9	0.00797(12)	0.00813(9)	0.00797(12)	0.00786(15)
10	0.00699(13)	0.00716(9)	0.00699(13)	0.00687(16)
11	0.00634(14)	0.00648(9)	0.00634(14)	0.00624(17)
12	0.00591(10)	0.00591(10)	0.00577(15)	0.00564(19)

method	$T_{\min}(t,r)$	$T_{\min}/a = 8$	$T_{\min}/a = 9$	$T_{\min}/a = 10$
r/a	$a^2 V^{\text{mix}}_{\Sigma_u^-}(r) m_Q/c_F$			
1	0.02211(18)	0.02211(18)	0.02208(27)	0.02203(35)
2	0.02041(17)	0.02041(17)	0.02033(24)	0.02024(30)
3	0.01872(15)	0.01872(15)	0.01861(22)	0.01850(27)
4	0.01720(14)	0.01720(14)	0.01710(21)	0.01700(26)
5	0.01589(14)	0.01589(14)	0.01578(21)	0.01568(26)
6	0.01462(15)	0.01462(15)	0.01453(21)	0.01446(26)
7	0.01344(16)	0.01344(16)	0.01336(24)	0.01330(30)
8	0.01247(17)	0.01247(17)	0.01242(26)	0.01238(34)
9	0.01133(19)	0.01133(19)	0.01133(31)	0.01133(43)
10	0.01051(21)	0.01051(21)	0.01047(34)	0.01042(45)
11	0.00934(22)	0.00934(22)	0.00922(34)	0.00910(44)
12	0.00860(24)	0.00860(24)	0.00839(37)	0.00820(50)

Table E.6: Hybrid-quarkonium mixing potentials $V^{\text{mix}}_{\Sigma_u^-}(r) m_Q/c_F$ and $V^{\text{mix}}_{\Pi_u}(r) m_Q/c_F$ in units of the lattice spacing $a = 0.060\,\text{fm}$ at flow radius $r_f = \sqrt{8t_f} = 1.8\,a$. The four columns correspond to the four fitting variants discussed in Section 6.4.1. Our main results were obtained by setting $T_{\min}/a = 9$ and are shaded in gray. Potential values with separations $r \lesssim 2r_f + a = 4.6\,a$ should be taken with caution due to possible operator overlapping effects.

References

[1] M. Gell-Mann, "A Schematic Model of Baryons and Mesons," *Phys. Lett.* **8** (1964) 214–215.

[2] G. Zweig, *An SU(3) model for strong interaction symmetry and its breaking. Version 2*, pp. 22–101. 2, 1964.

[3] **Particle Data Group** Collaboration, S. Navas *et al.*, "Review of particle physics," *Phys. Rev. D* **110** no. 3, (2024) 030001.

[4] **Belle** Collaboration, S. K. Choi *et al.*, "Observation of a narrow charmonium-like state in exclusive $B^{\pm} \to K^{\pm}\pi^{+}\pi^{-}J/\psi$ decays," *Phys. Rev. Lett.* **91** (2003) 262001, arXiv:hep-ex/0309032.

[5] **Quarkonium Working Group** Collaboration, N. Brambilla *et al.*, "Heavy Quarkonium Physics," arXiv:hep-ph/0412158.

[6] N. Brambilla *et al.*, "Heavy Quarkonium: Progress, Puzzles, and Opportunities," *Eur. Phys. J. C* **71** (2011) 1534, arXiv:1010.5827 [hep-ph].

[7] N. Brambilla *et al.*, "QCD and Strongly Coupled Gauge Theories: Challenges and Perspectives," *Eur. Phys. J. C* **74** no. 10, (2014) 2981, arXiv:1404.3723 [hep-ph].

[8] N. Brambilla, S. Eidelman, C. Hanhart, A. Nefediev, C.-P. Shen, C. E. Thomas, A. Vairo, and C.-Z. Yuan, "The XYZ states: experimental and theoretical status and perspectives," *Phys. Rept.* **873** (2020) 1–154, arXiv:1907.07583 [hep-ex].

[9] H.-X. Chen, W. Chen, X. Liu, Y.-R. Liu, and S.-L. Zhu, "An updated review of the new hadron states," *Rept. Prog. Phys.* **86** no. 2, (2023) 026201, arXiv:2204.02649 [hep-ph].

[10] K. G. Wilson, "Confinement of Quarks," *Phys. Rev. D* **10** (1974) 2445–2459.

[11] **Hadron Spectrum** Collaboration, L. Liu, G. Moir, M. Peardon, S. M. Ryan, C. E. Thomas, P. Vilaseca, J. J. Dudek, R. G. Edwards, B. Joo, and D. G. Richards, "Excited and exotic charmonium spectroscopy from lattice QCD," *JHEP* **07** (2012) 126, arXiv:1204.5425 [hep-ph].

[12] **Hadron Spectrum** Collaboration, G. K. C. Cheung, C. O'Hara, G. Moir, M. Peardon, S. M. Ryan, C. E. Thomas, and D. Tims, "Excited and exotic

charmonium, D_s and D meson spectra for two light quark masses from lattice QCD," *JHEP* **12** (2016) 089, arXiv:1610.01073 [hep-lat].

[13] L. Gayer, S. M. Ryan, and D. J. Wilson, "Highly excited B, B_s and B_c meson spectroscopy from lattice QCD," arXiv:2408.02126 [hep-lat].

[14] M. Berwein, N. Brambilla, J. Tarrús Castellà, and A. Vairo, "Quarkonium Hybrids with Nonrelativistic Effective Field Theories," *Phys. Rev. D* **92** no. 11, (2015) 114019, arXiv:1510.04299 [hep-ph].

[15] R. Oncala and J. Soto, "Heavy Quarkonium Hybrids: Spectrum, Decay and Mixing," *Phys. Rev.* **D96** no. 1, (2017) 014004, arXiv:1702.03900 [hep-ph].

[16] N. Brambilla, G. a. Krein, J. Tarrús Castellà, and A. Vairo, "Born-Oppenheimer approximation in an effective field theory language," *Phys. Rev. D* **97** no. 1, (2018) 016016, arXiv:1707.09647 [hep-ph].

[17] N. Brambilla, W. K. Lai, J. Segovia, J. Tarrús Castellà, and A. Vairo, "Spin structure of heavy-quark hybrids," *Phys. Rev. D* **99** no. 1, (2019) 014017, arXiv:1805.07713 [hep-ph]. [Erratum: Phys.Rev.D 101, 099902 (2020)].

[18] N. Brambilla, W. K. Lai, J. Segovia, and J. Tarrús Castellà, "QCD spin effects in the heavy hybrid potentials and spectra," *Phys. Rev. D* **101** no. 5, (2020) 054040, arXiv:1908.11699 [hep-ph].

[19] J. Soto and J. Tarrús Castellà, "Nonrelativistic effective field theory for heavy exotic hadrons," *Phys. Rev. D* **102** no. 1, (2020) 014012, arXiv:2005.00552 [hep-ph].

[20] M. Berwein, N. Brambilla, A. Mohapatra, and A. Vairo, "One Born−Oppenheimer Effective Theory to rule them all: hybrids, tetraquarks, pentaquarks, doubly heavy baryons and quarkonium," arXiv:2408.04719 [hep-ph].

[21] J. Soto and J. Tarrús Castellà, "Effective QCD string and doubly heavy baryons," *Phys. Rev. D* **104** (2021) 074027, arXiv:2108.00496 [hep-ph].

[22] J. Tarrús Castellà, "Heavy meson thresholds in Born-Oppenheimer effective field theory," *Phys. Rev. D* **106** no. 9, (2022) 094020, arXiv:2207.09365 [hep-ph].

[23] J. Soto and S. T. Valls, "Hyperfine splittings of heavy quarkonium hybrids," *Phys. Rev. D* **108** no. 1, (2023) 014025, arXiv:2302.01765 [hep-ph].

[24] L. A. Griffiths, C. Michael, and P. E. L. Rakow, "Mesons with excited glue," *Phys. Lett. B* **129** (1983) 351–356.

[25] N. A. Campbell, L. A. Griffiths, C. Michael, and P. E. L. Rakow, "Mesons with excited glue from SU(3) lattice gauge theory," *Phys. Lett. B* **142** (1984) 291–293.

[26] N. A. Campbell, A. Huntley, and C. Michael, "Heavy Quark Potentials and Hybrid Mesons From SU(3) Lattice Gauge Theory," *Nucl. Phys. B* **306** (1988) 51–62.

[27] S. Perantonis, A. Huntley, and C. Michael, "Static potentials from pure SU(2) lattice gauge theory," *Nuclear Physics* **326** (1989) 544–556.

[28] C. Michael and S. J. Perantonis, "Potentials and glueballs at large beta in SU(2) pure gauge theory," *J. Phys. G* **18** (1992) 1725–1736.

[29] S. Perantonis and C. Michael, "Static potentials and hybrid mesons from pure SU(3) lattice gauge theory," *Nucl. Phys. B* **347** (1990) 854–868.

[30] K. Juge, J. Kuti, and C. Morningstar, "Gluon excitations of the static quark potential and the hybrid quarkonium spectrum," *Nucl. Phys. B Proc. Suppl.* **63** (1998) 326–331, arXiv:hep-lat/9709131.

[31] M. J. Peardon, "Coarse lattice results for glueballs and hybrids," *Nucl. Phys. B Proc. Suppl.* **63** (1998) 22–27, arXiv:hep-lat/9710029.

[32] K. J. Juge, J. Kuti, and C. J. Morningstar, "A Study of hybrid quarkonium using lattice QCD," *AIP Conf. Proc.* **432** no. 1, (1998) 136–139, arXiv:hep-ph/9711451.

[33] C. Morningstar, K. J. Juge, and J. Kuti, "Gluon excitations of the static quark potential," in *3rd International Conference in Quark Confinement and Hadron Spectrum (Confinement III)*, pp. 179–182. 6, 1998. arXiv:hep-lat/9809015.

[34] C. Michael, "Hadronic spectroscopy from the lattice: Glueballs and hybrid mesons," *Nucl. Phys. A* **655** (1999) c12, arXiv:hep-ph/9810415.

[35] C. Michael, "Quarkonia and hybrids from the lattice," *PoS* (1999) hf8/001, arXiv:hep-ph/9911219 [hep-ph].

[36] K. Juge, J. Kuti, and C. Morningstar, "Ab initio study of hybrid anti-b g b mesons," *Phys. Rev. Lett.* **82** (1999) 4400–4403, arXiv:hep-ph/9902336.

[37] K. J. Juge, J. Kuti, and C. J. Morningstar, "The heavy hybrid spectrum from NRQCD and the Born-Oppenheimer approximation," *Nucl. Phys. Proc. Suppl.* **83** (2000) 304–306, arXiv:hep-lat/9909165 [hep-lat].

[38] **TXL, T(X)L** Collaboration, G. S. Bali, B. Bolder, N. Eicker, T. Lippert, B. Orth, P. Ueberholz, K. Schilling, and T. Struckmann, "Static potentials and glueball masses from QCD simulations with Wilson sea quarks," *Phys. Rev. D* **62** (2000) 054503, arXiv:hep-lat/0003012.

[39] C. Morningstar, "Gluonic excitations in lattice QCD: A brief survey," *AIP Conf. Proc.* **619** no. 1, (2002) 231–240, arXiv:nucl-th/0110074.

[40] K. J. Juge, J. Kuti, and C. Morningstar, "Fine structure of the QCD string spectrum," *Phys. Rev. Lett.* **90** (2003) 161601, arXiv:hep-lat/0207004.

[41] K. J. Juge, J. Kuti, and C. Morningstar, "The heavy quark hybrid meson spectrum in lattice QCD," *AIP Conf. Proc.* **688** no. 1, (2003) 193–207, arXiv:nucl-th/0307116.

[42] C. Michael, "Exotics," *Int. Rev. Nucl. Phys.* **9** (2004) 103–126, arXiv:hep-lat/0302001.

[43] C. Michael, "Hybrid mesons from the lattice," arXiv:hep-ph/0308293.

[44] G. S. Bali and A. Pineda, "QCD phenomenology of static sources and gluonic excitations at short distances," *Phys. Rev. D* **69** (2004) 094001, arXiv:hep-ph/0310130.

[45] K. J. Juge, J. Kuti, and C. Morningstar, "Excitations of the static quark-antiquark system in several gauge theories,". https://www.worldscientific.com/doi/abs/10.1142/9789812702845_0017.

[46] P. Wolf and M. Wagner, "Lattice study of hybrid static potentials," *J. Phys. Conf. Ser.* **599** no. 1, (2015) 012005, arXiv:1410.7578 [hep-lat].

[47] C. Reisinger, S. Capitani, O. Philipsen, and M. Wagner, "Computation of hybrid static potentials in SU(3) lattice gauge theory," *EPJ Web Conf.* **175** (2018) 05012, arXiv:1708.05562 [hep-lat].

[48] P. Bicudo, M. Cardoso, and N. Cardoso, "Colour fields of the quark-antiquark excited flux tube," *EPJ Web Conf.* **175** (2018) 14009, arXiv:1803.04569 [hep-lat].

[49] P. Bicudo, N. Cardoso, and M. Cardoso, "Color field densities of the quark-antiquark excited flux tubes in SU(3) lattice QCD," *Phys. Rev. D* **98** no. 11, (2018) 114507, arXiv:1808.08815 [hep-lat].

[50] C. Reisinger, S. Capitani, L. Müller, O. Philipsen, and M. Wagner, "Computation of hybrid static potentials from optimized trial states in SU(3) lattice gauge theory," *PoS* **LATTICE2018** (2018) 054, arXiv:1810.13284 [hep-lat].

[51] S. Capitani, O. Philipsen, C. Reisinger, C. Riehl, and M. Wagner, "Precision computation of hybrid static potentials in SU(3) lattice gauge theory," *Phys. Rev. D* **99** no. 3, (2019) 034502 arXiv:1811.11046 [hep-lat].

[52] **UKQCD** Collaboration, M. Foster and C. Michael, "Hadrons with a heavy color adjoint particle," *Phys. Rev. D* **59** (1999) 094509, arXiv:hep-lat/9811010.

[53] C. Riehl and M. Wagner, "Hybrid static potentials in SU(2) lattice gauge theory at short quark-antiquark separations," in *Asia-Pacific Symposium for Lattice Field Theory*. 8, 2020. arXiv:2008.12216 [hep-lat].

[54] C. Schlosser and M. Wagner, "Computing hybrid static potentials at short quark-antiquark separations from fine lattices in SU(3) Yang-Mills theory," *PoS* **LATTICE2021** (2022) 147, arXiv:2108.05222 [hep-lat].

[55] C. Schlosser and M. Wagner, "Hybrid static potentials in SU(3) lattice gauge theory at small quark-antiquark separations," *Phys. Rev. D* **105** no. 5, (2022) 054503, arXiv:2111.00741 [hep-lat].

[56] C. Schlosser, S. Köhler, and M. Wagner, "Lattice field theory results for hybrid static potentials at short quark-antiquark separations and their parametrization," *PoS* **LATTICE2022** (2023) 083, arXiv:2211.00489 [hep-lat].

[57] J. Herr, C. Schlosser, and M. Wagner, "Gluelump masses and mass splittings from SU(3) lattice gauge theory," *Phys. Rev. D* **109** no. 3, (2024) 034516, arXiv:2306.09902 [hep-lat].

[58] C. Schlosser and M. Wagner, "Hybrid spin-dependent and hybrid-quarkonium mixing potentials at order $(1/m_Q)^1$ from SU(3) lattice gauge theory," *Phys. Rev. D* **111** (2025) 074504, arXiv:2501.08844 [hep-lat].

[59] C. Gattringer and C. B. Lang, "Quantum chromodynamics on the lattice," *Lect. Notes Phys.* **788** (2010) 1–343.

[60] H. J. Rothe, *Lattice Gauge Theories*. WORLD SCIENTIFIC, 4th ed., 2012. https://www.worldscientific.com/doi/abs/10.1142/8229.

[61] T. DeGrand and C. DeTar, *Lattice Methods for Quantum Chromodynamics*. WORLD SCIENTIFIC, 2006. https://www.worldscientific.com/doi/abs/10.1142/6065.

[62] K. G. Wilson, "Confinement of quarks," *Phys. Rev. D* **10** (Oct, 1974) 2445–2459.

[63] O. Philipsen, C. Pinke, A. Sciarra, and M. Bach, "CL^{2}QCD - Lattice QCD based on OpenCL," *PoS* **LATTICE2014** (2014) 038, arXiv:1411.5219 [hep-lat].

[64] **APE** Collaboration, M. Albanese *et al.*, "Glueball Masses and String Tension in Lattice QCD," *Phys. Lett. B* **192** (1987) 163–169.

[65] A. Hasenfratz, R. Hoffmann, and F. Knechtli, "The Static potential with hypercubic blocking," *Nucl. Phys. B Proc. Suppl.* **106** (2002) 418–420, arXiv:hep-lat/0110168.

[66] **ALPHA** Collaboration, M. Della Morte, S. Durr, J. Heitger, H. Molke, J. Rolf, A. Shindler, and R. Sommer, "Lattice HQET with exponentially improved statistical precision," *Phys. Lett. B* **581** (2004) 93–98, arXiv:hep-lat/0307021. [Erratum: Phys.Lett.B 612, 313–314 (2005)].

[67] M. Della Morte, A. Shindler, and R. Sommer, "On lattice actions for static quarks," *JHEP* **08** (2005) 051, arXiv:hep-lat/0506008.

[68] M. Lüscher, "Properties and uses of the Wilson flow in lattice QCD," *JHEP* **08** (2010) 071, arXiv:1006.4518 [hep-lat]. [Erratum: JHEP03,092(2014)].

[69] A. Bazavov and T. Chuna, "Efficient integration of gradient flow in lattice gauge theory and properties of low-storage commutator-free Lie group methods," arXiv:2101.05320 [hep-lat].

[70] C. Alexandrou, A. Athenodorou, K. Cichy, A. Dromard, E. Garcia-Ramos, K. Jansen, U. Wenger, and F. Zimmermann, "Comparison of topological charge definitions in Lattice QCD," *Eur. Phys. J. C* **80** no. 5, (2020) 424, arXiv:1708.00696 [hep-lat].

[71] L. Altenkort, O. Kaczmarek, L. Mazur, and H.-T. Shu, "Color-electric correlation functions under gradient flow," *PoS* **LATTICE2019** (2019) 204, arXiv:1912.11248 [hep-lat].

[72] N. Brambilla, V. Leino, J. Mayer-Steudte, and A. Vairo, "Static force from generalized Wilson loops on the lattice using the gradient flow," *Phys. Rev. D* **109** no. 11, (2024) 114517, arXiv:2312.17231 [hep-lat].

[73] N. Brambilla and X.-P. Wang, "Off-lightcone Wilson-line operators in gradient flow," *JHEP* **06** (2024) 210, arXiv:2312.05032 [hep-ph].

[74] L. Altenkort, D. de la Cruz, O. Kaczmarek, G. D. Moore, and H.-T. Shu, "Lattice B-field correlators for heavy quarks," *Phys. Rev. D* **109** no. 11, (2024) 114505, arXiv:2402.09337 [hep-lat].

[75] V. Leino, N. Brambilla, J. Mayer-Steudte, and A. Vairo, "The static force from generalized Wilson loops using gradient flow," *EPJ Web Conf.* **258** (2022) 04009, arXiv:2111.10212 [hep-lat].

[76] M. Eichberg and M. Wagner, "Relativistic corrections to the static potential from generalized Wilson loops at finite flow time," *PoS* **LATTICE2023** (2024) 068, arXiv:2311.06560 [hep-lat].

[77] M. Luscher and P. Weisz, "Locality and exponential error reduction in numerical lattice gauge theory," *JHEP* **09** (2001) 010, arXiv:hep-lat/0108014.

[78] N. Brambilla, V. Leino, O. Philipsen, C. Reisinger, A. Vairo, and M. Wagner, "Lattice gauge theory computation of the static force," arXiv:2106.01794 [hep-lat].

[79] R. Sommer, "A New way to set the energy scale in lattice gauge theories and its applications to the static force and alpha-s in SU(2) Yang-Mills theory," *Nucl. Phys. B* **411** (1994) 839–854, arXiv:hep-lat/9310022.

[80] R. Sommer, "Scale setting in lattice QCD," *PoS* **LATTICE2013** (2014) 015, arXiv:1401.3270 [hep-lat].

[81] M. Lüscher, "Two particle states on a torus and their relation to the scattering matrix," *Nucl. Phys. B* **354** (1991) 531–578.

[82] **ALPHA** Collaboration, S. Schaefer, R. Sommer, and F. Virotta, "Critical slowing down and error analysis in lattice QCD simulations," *Nucl. Phys.* **B845** (2011) 93–119, arXiv:1009.5228 [hep-lat].

[83] T. Schäfer and E. V. Shuryak, "Instantons in QCD," *Rev. Mod. Phys.* **70** (Apr, 1998) 323–425, https://link.aps.org/doi/10.1103/RevModPhys.70.323.

[84] R. Brower, S. Chandrasekharan, J. W. Negele, and U. Wiese, "QCD at fixed topology," *Phys. Lett. B* **560** (2003) 64–74, arXiv:hep-lat/0302005.

[85] S. Aoki, H. Fukaya, S. Hashimoto, and T. Onogi, "Finite volume QCD at fixed topological charge," *Phys. Rev. D* **76** (2007) 054508, arXiv:0707.0396 [hep-lat].

[86] W. Bietenholz, C. Czaban, A. Dromard, U. Gerber, C. P. Hofmann, H. Mejía-Díaz, and M. Wagner, "Interpreting Numerical Measurements in Fixed Topological Sectors," *Phys. Rev.* **D93** no. 11, (2016) 114516, arXiv:1603.05630 [hep-lat].

[87] P. de Forcrand, M. Garcia Perez, and I.-O. Stamatescu, "Topology of the SU(2) vacuum: A Lattice study using improved cooling," *Nucl. Phys. B* **499** (1997) 409–449, arXiv:hep-lat/9701012.

[88] M. Luscher, "Volume Dependence of the Energy Spectrum in Massive Quantum Field Theories. 1. Stable Particle States," *Commun. Math. Phys.* **104** (1986) 177.

[89] C. J. Morningstar and M. J. Peardon, "The Glueball spectrum from an anisotropic lattice study," *Phys. Rev.* **D60** (1999) 034509, arXiv:hep-lat/9901004 [hep-lat].

[90] P. Weisz, "Continuum limit improved lattice action for pure Yang-Mills theory (I)," *Nucl. Phys. B* **212** (1983) 1–17.

[91] A. Hasenfratz and F. Knechtli, "Flavor symmetry and the static potential with hypercubic blocking," *Phys. Rev. D* **64** (2001) 034504, arXiv:hep-lat/0103029.

[92] M. Luscher and P. Weisz, "Coordinate space methods for the evaluation of Feynman diagrams in lattice field theories," *Nucl. Phys. B* **445** (1995) 429–450, arXiv:hep-lat/9502017.

[93] S. Necco and R. Sommer, "The N(f) = 0 heavy quark potential from short to intermediate distances," *Nucl. Phys. B* **622** (2002) 328–346, arXiv:hep-lat/0108008.

[94] S. Köhler, "Methods of tree-level improvement of the static potential in SU(2) lattice Yang-Mills theory," Bachelor's Thesis, Goethe University, July, 2022. https://itp.uni-frankfurt.de/~mwagner/theses/BA_Koehler.pdf.

[95] C. Michael, "The Running coupling from lattice gauge theory," *Phys. Lett. B* **283** (1992) 103–106, arXiv:hep-lat/9205010.

[96] M. Born and R. Oppenheimer, "Zur Quantentheorie der Molekeln," *Annalen der Physik* **389** no. 20, (1927) 457–484.

[97] S. Godfrey and N. Isgur, "Mesons in a relativized quark model with chromodynamics," *Phys. Rev. D* **32** (Jul, 1985) 189–231, https://link.aps.org/doi/10.1103/PhysRevD.32.189.

[98] P. Guo, A. P. Szczepaniak, G. Galata, A. Vassallo, and E. Santopinto, "Heavy quarkonium hybrids from Coulomb gauge QCD," *Phys. Rev. D* **78** (2008) 056003, arXiv:0807.2721 [hep-ph].

[99] E. Braaten, C. Langmack, and D. H. Smith, "Born-Oppenheimer Approximation for the XYZ Mesons," *Phys. Rev. D* **90** no. 1, (2014) 014044, arXiv:1402.0438 [hep-ph].

[100] N. Brambilla, A. Pineda, J. Soto, and A. Vairo, "Potential NRQCD: An Effective theory for heavy quarkonium," *Nucl. Phys. B* **566** (2000) 275, arXiv:hep-ph/9907240.

[101] **Flavour Lattice Averaging Group (FLAG)** Collaboration, Y. Aoki *et al.*, "FLAG Review 2021," *Eur. Phys. J. C* **82** no. 10, (2022) 869, arXiv:2111.09849 [hep-lat].

[102] C. Anzai, M. Prausa, A. V. Smirnov, V. A. Smirnov, and M. Steinhauser, "Color octet potential to three loops," *Phys. Rev. D* **88** no. 5, (2013) 054030, arXiv:1308.1202 [hep-ph].

[103] A. Pineda and A. Vairo, "The QCD potential at O $(1/m^2)$: Complete spin dependent and spin independent result," *Phys. Rev. D* **63** (2001) 054007, arXiv:hep-ph/0009145. [Erratum: Phys.Rev.D 64, 039902 (2001)].

[104] Y. Koma and M. Koma, "Spin-dependent potentials from lattice QCD," *Nucl. Phys. B* **769** (2007) 79–107, arXiv:hep-lat/0609078.

[105] C. Peset, A. Pineda, and J. Segovia, "P-wave heavy quarkonium spectrum with next-to-next-to-next-to-leading logarithmic accuracy," *Phys. Rev. D* **98** no. 9, (2018) 094003, arXiv:1809.09124 [hep-ph].

[106] M. Eichberg and M. Wagner, "Computing $1/m_Q$ and $1/m_Q^2$ corrections to the static potential with lattice gauge theory using gradient flow," in *41st International Symposium on Lattice Field Theory*. 11, 2024. arXiv:2411.11640 [hep-lat].

[107] P. Hasenfratz, R. R. Horgan, J. Kuti, and J. M. Richard, "The effects of colored glue in the QCD motivated bag of heavy quark-antiquark systems," *Phys. Lett. B* **95** (1980) 299–305.

[108] E. Braaten, C. Langmack, and D. H. Smith, "Selection Rules for Hadronic Transitions of XYZ Mesons," *Phys. Rev. Lett.* **112** (2014) 222001, arXiv:1401.7351 [hep-ph].

[109] M. Luscher and P. Weisz, "Quark confinement and the bosonic string," *JHEP* **07** (2002) 049, arXiv:hep-lat/0207003.

[110] M. Luscher and P. Weisz, "String excitation energies in SU(N) gauge theories beyond the free-string approximation," *JHEP* **07** (2004) 014, arXiv:hep-th/0406205.

[111] R. Höllwieser, F. Knechtli, T. Korzec, M. J. Peardon, and J. A. Urrea-Niño, "Hybrid static potentials from Laplacian eigenmodes," *PoS* **LATTICE2023** (2024) 073, arXiv:2401.09453 [hep-lat].

[112] A. Sharifian, N. Cardoso, and P. Bicudo, "Eight very excited flux tube spectra and possible axions in SU(3) lattice gauge theory," *Phys. Rev. D* **107** no. 11, (2023) 114507, arXiv:2303.15152 [hep-lat].

[113] F. Karbstein, M. Wagner, and M. Weber, "Determination of $\Lambda_{\overline{\rm MS}}^{(n_f=2)}$ and analytic parametrization of the static quark-antiquark potential," *Phys. Rev. D* **98** no. 11, (2018) 114506, arXiv:1804.10909 [hep-ph].

[114] F. Alasiri, E. Braaten, and A. Mohapatra, "Born-Oppenheimer potentials for SU(3) gauge theory," *Phys. Rev. D* **110** no. 5, (2024) 054029, arXiv:2406.05123 [hep-ph].

[115] Y. Koma, M. Koma, and H. Wittig, "Relativistic corrections to the static potential at O(1/m) and O($1/m^2$)," *PoS* **LATTICE2007** (2007) 111, arXiv:0711.2322 [hep-lat].

[116] A. Vairo, "Quarkonia: a theoretical frame," 2009. arXiv:0912.4422 [hep-ph].

[117] C. Riehl, "Hybrid static potentials at small lattice spacings and possible glueball decay," Master's Thesis, Goethe University, September, 2019. https://itp.uni-frankfurt.de/~mwagner/theses/MA_Riehl.pdf.

[118] A. Athenodorou and M. Teper, "SU(N) gauge theories in 3+1 dimensions: glueball spectrum, string tensions and topology," arXiv:2106.00364 [hep-lat].

[119] **Particle Data Group** Collaboration, M. Tanabashi *et al.*, "Review of Particle Physics," *Phys. Rev. D* **98** no. 3, (2018) 030001.

[120] S. Perantonis and C. Michael, "Static potentials and hybrid mesons from pure su(3) lattice gauge theory," *Nuclear Physics B* **347** no. 3, (1990) 854 – 868. http://www.sciencedirect.com/science/article/pii/055032139090386R.

[121] **ATLAS** Collaboration, "Generation and Simulation of R-Hadrons in the ATLAS Experiment," tech. rep., CERN, Geneva, 2019. https://cds.cern.ch/record/2676309.

[122] G. Karl and J. E. Paton, "Gluelump spectrum in the bag model," *Phys. Rev. D* **60** (1999) 034015, arXiv:hep-ph/9904407.

[123] P. Guo, A. P. Szczepaniak, G. Galata, A. Vassallo, and E. Santopinto, "Gluelump spectrum from Coulomb gauge QCD," *Phys. Rev. D* **77** (2008) 056005, arXiv:0707.3156 [hep-ph].

[124] F. Buisseret, "Gluelump model with transverse constituent gluons," *Eur. Phys. J. A* **38** (2008) 233–238, arXiv:0808.2399 [hep-ph].

[125] Y. A. Simonov, "Gluelump spectrum in the QCD string model," *Nucl. Phys. B* **592** (2001) 350–368, arXiv:hep-ph/0003114.

[126] V. Mathieu, C. Semay, and F. Brau, "Casimir scaling, glueballs and hybrid gluelumps," *Eur. Phys. J. A* **27** (2006) 225–230, arXiv:hep-ph/0511210.

[127] K. Marsh and R. Lewis, "A lattice QCD study of generalized gluelumps," *Phys. Rev. D* **89** no. 1, (2014) 014502, arXiv:1309.1627 [hep-lat].

[128] R. Höllwieser, F. Knechtli, T. Korzec, M. J. Peardon, L. Struckmeier, and J. A. Urrea-Niño, "Hybrid static potentials and gluelumps on $N_f = 3 + 1$ ensembles," *PoS* **LATTICE2024** (2025) 102, arXiv:2501.15670 [hep-lat].

[129] J. Herr, "Computation of gluelump masses for hybrid static potentials in SU(3) lattice gauge theory using the multilevel algorithm," Master's Thesis, Goethe University, May, 2022. https://itp.uni-frankfurt.de/~mwagner/theses/MA_Herr.pdf.

[130] I. H. Jorysz and C. Michael, "The field configurations of a static adjoint source in SU(2) lattice gauge theory," *Nucl. Phys. B* **302** (1988) 448–470.

[131] R. C. Johnson, "Angular momentum on a lattice," *Phys. Lett. B* **114** (1982) 147–151.

[132] M. Heydaripoor, "Identifizierung des Gesamtdrehimpulses von Gluelumps in Gittereichtheorie," Bachelor's Thesis, Goethe University Frankfurt am Main, August, 2023. https://itp.uni-frankfurt.de/~mwagner/theses.html

[133] V. Leino, "Adjoint chromoelectric and -magnetic correlators with gradient flow," *PoS* **LATTICE2023** (2024) 385, arXiv:2401.06733 [hep-lat].

[134] A. Pineda, "Determination of the bottom quark mass from the Upsilon(1S) system," *JHEP* **06** (2001) 022, arXiv:hep-ph/0105008.

[135] A. Pineda, "The Static potential: Lattice versus perturbation theory in a renormalon based approach," *J. Phys. G* **29** (2003) 371–385, arXiv:hep-ph/0208031.

[136] G. S. Bali, C. Bauer, A. Pineda, and C. Torrero, "Perturbative expansion of the energy of static sources at large orders in four-dimensional SU(3) gauge theory," *Phys. Rev. D* **87** (2013) 094517, arXiv:1303.3279 [hep-lat].

[137] G. S. Bali, C. Bauer, and A. Pineda, "The static quark self-energy at $O(\alpha^{20})$ in perturbation theory," *PoS* **LATTICE2013** (2014) 371, arXiv:1311.0114 [hep-lat].

[138] P. A. Baikov, K. G. Chetyrkin, and J. H. Kühn, "Five-Loop Running of the QCD coupling constant," *Phys. Rev. Lett.* **118** no. 8, (2017) 082002, arXiv:1606.08659 [hep-ph].

[139] M. Beneke, "More on ambiguities in the pole mass," *Phys. Lett. B* **344** (1995) 341–347, arXiv:hep-ph/9408380.

[140] M. Beneke, "Renormalons," *Phys. Rept.* **317** (1999) 1–142, arXiv:hep-ph/9807443.

[141] **Particle Data Group** Collaboration, R. L. Workman *et al.*, "Review of Particle Physics," *PTEP* **2022** (2022) 083C01.

[142] J. Soto, "Heavy Quarkonium Hybrids," *Nucl. Part. Phys. Proc.* **294-296** (2018) 87–94, arXiv:1709.08038 [hep-ph].

[143] G. S. Bali, K. Schilling, and A. Wachter, "Complete O (v^2) corrections to the static interquark potential from SU(3) gauge theory," *Phys. Rev. D* **56** (1997) 2566–2589, arXiv:hep-lat/9703019.

[144] Y. Koma, M. Koma, and H. Wittig, "Nonperturbative determination of the QCD potential at O(1/m)," *Phys. Rev. Lett.* **97** (2006) 122003, arXiv:hep-lat/0607009.

[145] T. Burch, K. Orginos, and D. Toussaint, "Determining hybrid content of heavy quarkonia using lattice nonrelativistic QCD," *Nucl. Phys. B Proc. Suppl.* **106** (2002) 382–384, arXiv:hep-lat/0110001.

[146] **MILC** Collaboration, T. Burch and D. Toussaint, "Hybrid configuration content of heavy S wave mesons," *Phys. Rev. D* **68** (2003) 094504, arXiv:hep-lat/0305008.

[147] D. A. Varshalovich, A. N. Moskalev, and V. K. Khersonskii, *Quantum Theory of Angular Momentum*. WORLD SCIENTIFIC, 1988. https://www.worldscientific.com/doi/pdf/10.1142/0270.

[148] **TUMQCD** Collaboration, V. Leino, N. Brambilla, O. Philipsen, C. Reisinger, A. Vairo, and M. Wagner, "The static force from generalized Wilson loops," *PoS* **LATTICE2021** (2022) 585, arXiv:2111.07916 [hep-lat].

[149] L. Müller, O. Philipsen, C. Reisinger, and M. Wagner, "Hybrid static potential flux tubes from SU(2) and SU(3) lattice gauge theory," *Phys. Rev. D* **100** no. 5, (2019) 054503, arXiv:1907.01482 [hep-lat].

[150] M. Eichberg and M. Wagner, "Computing $1/m_Q$ and $1/m_Q^2$ corrections to the static potential with lattice gauge theory using gradient flow," *PoS* **LATTICE2024** (2024) 117.

[151] M. Lüscher, "Stochastic locality and master-field simulations of very large lattices," *EPJ Web Conf.* **175** (2018) 01002, arXiv:1707.09758 [hep-lat].

[152] C. Schlosser and M. Wagner, "SU(3) hybrid static potentials at small quark-antiquark separations from fine lattices," *SciPost Phys. Proc.* **6** (2022) 009, arXiv:2112.01911 [hep-lat].

[153] T. Hirakida, E. Itou, and H. Kouno, "Thermodynamics for pure SU(2) gauge theory using gradient flow," *PTEP* **2019** no. 3, (2019) 033B01, arXiv:1805.07106 [hep-lat].

Acknowledgments

First and foremost, I would like to thank my supervisor, Marc Wagner. Since my bachelor's thesis, he has always offered valuable guidance while allowing me the freedom to pursue my academic interests. His trust and support have played a crucial role in shaping my academic journey.
I am also grateful for the colleagues I have met and the helpful interactions that have enriched this journey. In particular, I want to thank Christian Reisinger for providing his multilevel code and Michael Eichberg for making his gradient flow code available.
Moreover, I am profoundly thankful for the support of my family. Above all, I am especially grateful to my husband, whose encouragement and patience have been invaluable.

Calculations on the GOETHE-NHR and on the FUCHS-CSC high-performance computers of the Goethe University Frankfurt were conducted for this research. I would like to thank HPC-Hessen, funded by the State Ministry of Higher Education, Research and the Arts, for the HPC infrastructure.
This thesis was written independently. ChatGPT (OpenAI, 2024, version ChatGPT-4, https://chat.openai.com) and Grammarly (https://app.grammarly.com) were used solely as auxiliary tools for linguistic revisions. I confirm that my creative input predominates in this work.

GOETHE
UNIVERSITÄT
FRANKFURT AM MAIN